ENABLING HIGH-PRESSURE OPERATION WITH WATER FOR THE PISTON-CYLINDER INTERFACE IN AXIAL PISTON MACHINES

by

Meike Ernst

A Dissertation

Submitted to the Faculty of Purdue University

In Partial Fulfillment of the Requirements for the degree of

Doctor of Philosophy

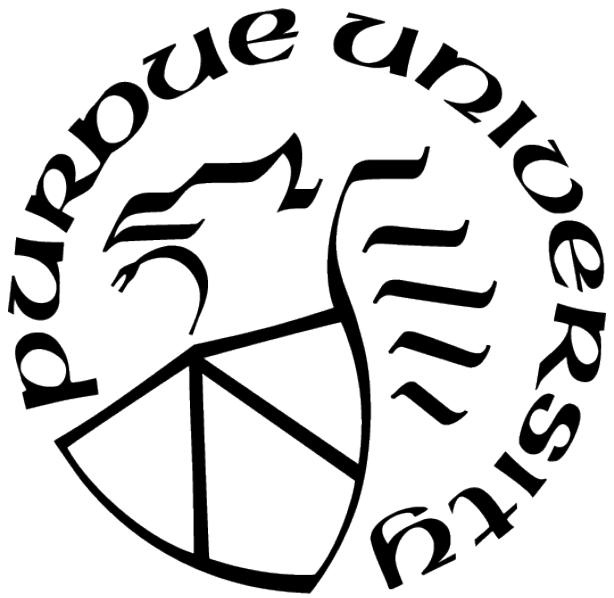

School of Mechanical Engineering

West Lafayette, Indiana

May 2021

THE PURDUE UNIVERSITY GRADUATE SCHOOL
STATEMENT OF COMMITTEE APPROVAL

Dr. Andrea Vacca, Chair

School of Mechanical Engineering

Dr. Farshid Sadeghi

School of Mechanical Engineering

Dr. Arezoo Ardekani

School of Mechanical Engineering

Dr. John Lumkes

School of Agricultural and Biological Engineering

Approved by:

Dr. Nicole L. Key

For my family, especially my sisters: Divya, Eimii, Hiral, Karen, Maria, and Mrudula

ACKNOWLEDGMENTS

I would like to thank Dr. Vacca, Dr. Ivantysynova, and the entire team at the Maha Fluid Power Research Center for the wealth of guidance, support, and friendship that have made my PhD such a rich experience. In particular, I would like to thank Dr. Ivantysynova for the opportunity to join the Maha Fluid Power Research Center, and for her spirited guidance and uncontainable excitement for my research topic. Simultaneously, I would like to extend my deepest thank you to Dr. Vacca, who generously opted to take on the challenging role of PhD advisor for the students left behind when Dr. Ivantysynova passed away; I deeply appreciate not only the sacrifices in time and energy he made in taking on this responsibility, but also his drive to create new learning and career opportunities for his students, and to go above and beyond his duties in giving them advice, inspiration and direction— to be not just an advisor to us, but, despite the difficult circumstances, a great advisor.

I would like to thank Dr. Enevoldsen, Dr. Kolb, and the rest of the team in the Danfoss High Pressure Pump Division in Nordborg, for the exciting opportunity to implement and physically test my research. This has been a learning experience that I will always value, and I look forward to seeing where the insights gained from our joint efforts will lead pump design in the future. I would also like to thank the USDA for sponsoring part of the work in this dissertation.

Special thanks go out to Marco Zecchi, Andrew Schenk, Daniel Mizell, Lizhi Shang, Paul Kalbfleisch and Rene Chacon, who have been the most dedicated and patient tutors to me— and to Dr. Sadeghi and Dr. Crossley, whose unmistakable passion for teaching has imparted on me not only much of the fundamental knowledge upon which this work is built, but the propulsive desire to learn more. I would also like to thank the Maha staff, especially Susan Gauger and David Johnson, for always putting the smile on my face that I needed to get me through the day. I am grateful for all friends and family who encouraged and believed in me, and for the wonderful time I had at Maha. Finally, I would like to thank my PhD committee: Dr. Vacca, Dr. Sadeghi, Dr. Ardekani, and Dr. Lumkes.

TABLE OF CONTENTS

LIST OF TABLES

LIST OF FIGURES

ABBREVIATIONS

APMSPD	Axial piston machine of swash plate design
DC	Displacement chamber
IDC	Inner dead center
ODC	Outer dead center

NOMENCLATURE

a_{K}	Piston axial acceleration
A_{r}	Area of the smallest cross-section fluid traverses in going from the DC to port or vice versa
C_{p}	Specific heat
d_{K}	Piston diameter
F_{aK}	Force due to the axial acceleration of the piston
F_{DK}	Force on the piston due to the difference between DC and case pressure
F_{SK}	Swash plate reaction force to the piston pushing on the swash plate
F_{SKy}	y-Component of F_{SK}
F_{TG}	Force due to viscous friction in the slipper-swash plate interface
F_{TK}	Force due to viscous friction in the piston-cylinder interface
$F_{\omega\mathrm{K}}$	Force on the piston due to the centrifugal effect
h	Film thickness
H_{K}	Piston stroke
K	Bulk modulus
l_{F}	Guide length
m_{K}	Piston mass
p	Pressure
p_{Case}	Case pressure
p_{DC}	DC pressure
p_{HP}	Pressure in the high-pressure port
p_{LP}	Pressure in the low-pressure port
Q_{HPr}	Flow rate of fluid passing from the high-pressure port into the DC
Q_{LPr}	Flow rate of fluid passing from the low-pressure port into the DC
Q_{r}	Flow rate of fluid passing from the port into the DC, or visa versa
Q_{SB}	Flow rate of fluid leaking from the cylinder block-valve plate interface
Q_{SG}	Flow rate of fluid exiting the piston orifice at the piston head
Q_{SK}	Flow rate of fluid leaking from the piston-cylinder interface

R_b	Axial piston machine pitch radius
R_Z	Cylinder bore (or bushing) inner diameter
s_K	Distance the piston head has traveled along the z-axis from ODC
T	Temperature
u	$\hat{x}$ component of the fluid velocity
$\hat{u}$	Fluid velocity in the $\hat{x}$-direction
$\hat{u}_\mathrm{K}$	Piston surface circumferential velocity
v	$\hat{y}$ component of the fluid velocity
$\hat{v}$	Fluid velocity in the $\hat{y}$-direction
$\hat{v}_\mathrm{K}$	Piston surface axial velocity
v_K	Piston axial speed
$\vec{V}$	Fluid velocity vector
V_i	Derived displacement volume
w	$\hat{z}$ component of the fluid velocity

α_D	Orifice discharge coefficient
β	Swashplate angle
$\triangle h$	Change in film thickness from elastic deformations of the solid bodies
$\triangle p$	Pressure difference between the DC and pump case
λ	Thermal conductivity
μ	Viscosity
ρ	Density
φ	Shaft angle
Φ_D	Viscous dissipation
ω	Pump speed

ABSTRACT

Water is inflammable, non-toxic, environmentally friendly— desirable traits, for a hydraulic fluid. However, its extremely low viscosity diminishes the load-bearing and sealing capacity of lubricating interfaces. Case in point: axial piston machines of swash plate design are compact, highly efficient positive displacement machines at the heart of hydraulic systems in forestry, construction, aerospace, and agricultural equipment, as well as industrial applications (presses, etc.); however, the three main lubricating interfaces decisive to the performance of such units in terms of both component life and efficiency are challenged by the use of water as working fluid. Especially during high-pressure operation, this low-viscosity lubricant can cause the these interfaces to fail in carrying the imposed load, resulting in severe wear, or even pump failure. The piston-cylinder interface is particularly challenging to design for water because it stands under obligation to carry the heavy side load that acts on the pistons of these machines, which increases with operating pressure. Furthermore, the architecture of axial piston machines of swash plate design does not allow this interface to be hydrostatically balanced.

Through the development of a methodology that separates the fluid pressure fields of the three main lubricating interfaces of axial piston machines into their hydrostatic and hydrodynamic components, the present work enables a direct comparison of these interfaces in terms of how they support load [1]. A case study of a 75 cc unit running on hydraulic oil conducted via this methodology at three different operating conditions (low pressure/low speed, low pressure/high speed, and high pressure/low speed) demonstrates that in the piston-cylinder interface, the force from hydrostatic pressure reaches such high magnitudes over the high-pressure stroke that *less* than half of it is needed to counter the load. The excess force from hydrostatic pressure then becomes the load. Consequentially, hydrodynamic pressure must counter a force from hydrostatic pressure that exceeds the original load. In the other two interfaces, by contrast, over half the load is being carried by hydrostatic pressure, thus significantly diminishing the amount of hydrodynamic pressure the interfaces are required to generate in order to achieve full load support. Moreover, nearly all of the moment on the

piston is countered by hydrodynamic pressure, while less than half of the moment on the block is countered by hydrodynamic pressure, and the moment on the slipper is negligible by comparison.

While this case study only investigates one pump, it shows how critical hydrodynamic pressure can be to load support in the piston-cylinder interface. The use of a low-viscosity fluid, e.g. water, reduces the hydrodynamic pressure that is generated in this interface, which, at challenging operating conditions, can lead to metal-to-metal contact. However, the performance of the interface can be improved via micro surface shaping, i.e. by giving the surface of the piston, or the bore that it moves through, a shape on the order of microns in height. The aim of present work is to pursue design trends leading to surface shapes that will enable this interface to function at higher pressures than currently achievable.

This pursuit takes the form of systematic virtual design studies, an optimization procedure, and an algorithm developed specifically for tailoring the bore surfaces through which the pistons travel to piston tilt and deformation. From this emerges not only a set of design trends corresponding to the dimensions of two particularly powerful types of micro surface shaping, but also a profound insight into the behavior of the water-lubricated piston-cylinder interface fluid film, and how that behavior can be manipulated by changing the component surfaces that constitute its borders. Furthermore, in collaboration with Danfoss High Pressure Pumps, a physical prototype of a 444 cc axial piston pump with surface shaping generated via the aforementioned algorithm has been constructed and tested, achieving a total pump efficiency roughly 3% higher than that achievable by the commercial unit that the geometry of the prototype is based on [2], [3].

1. INTRODUCTION

Viscosity: in tribological interfaces, the lubricant's inherent internal friction governs both *power loss* and *load support*— respectively markers of efficiency and functionality that can serve to peg the performance of an interface's design. The investigation at hand takes these markers as guides in its pursuit of design solutions for the piston-cylinder interface of APMSPD (axial piston machines of swash plate design), specifically during high-pressure operation when using a rather famous low-viscosity hydraulic fluid: *water*. APMSPD are positive displacement machines— pumps, motors— of particular import in modern hydraulics. Their efficiency, as well as their capacity for high pressure and variable displacement operation [4], have conferred on them a well-justified popularity; applications span construction, agricultural and forest machinery, and aerospace systems.

In these applications, the prevalent working fluid is traditional hydraulic oil. The present work, however, focuses entirely on the use of water as hydraulic fluid. This is because water holds a number of advantages over oil in the context of this utilization. For a start: it

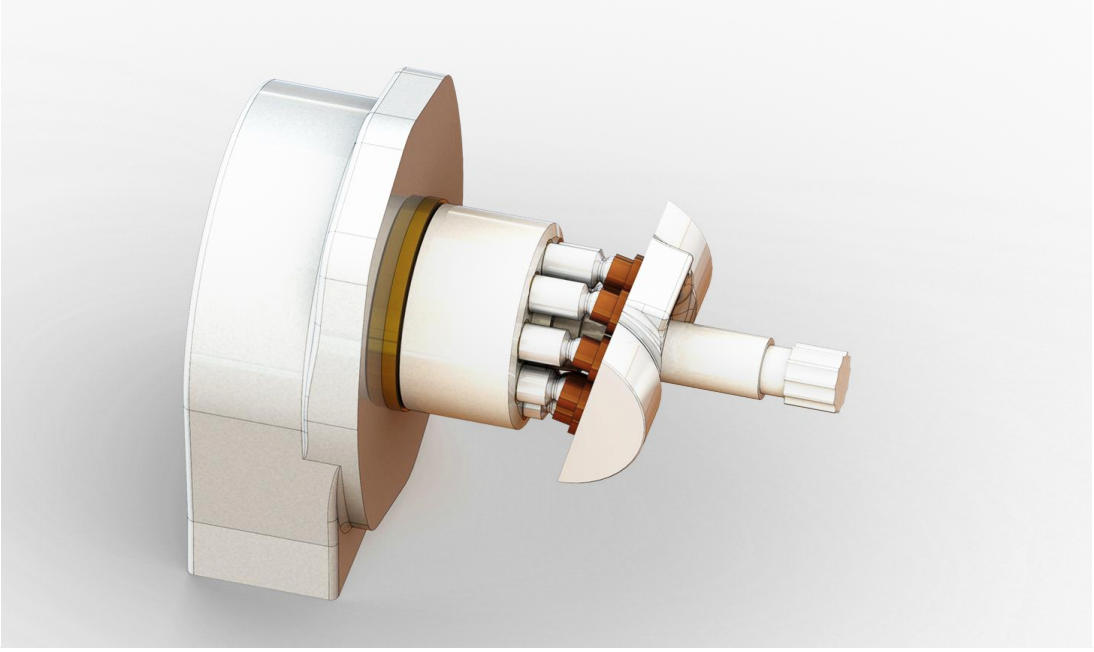

Figure 1.1. Axial piston machine of swash plate design.

is cheap, abundant, green, and comes with incredibly short health hazards documentation. Moreover, it has a high heat capacity and thermal conductivity; consequently, water as a working fluid allows hydraulic circuits to be temperature regulated by less powerful cooling systems than those required when running with oil [5]. Water is fireproof, id est the associated insurance costs are more economical [6]. Water is immune to the aging process that causes performance loss in plant-based oils over time [7]. These benefits of water have driven, and continue to drive, its re-emergence as a hydraulic fluid across a diverse repertoire of applications.

Current applications of water hydraulics technology include fire-fighting, industrial cleaning, paper mills, desalination, mining, injection molding, etc. [6]. The success of modern water hydraulics components, including APMSPD, in these applications suggests that their repertoire should be extended to dominate the applications listed earlier: construction, agricultural and forest machinery, etc. This, in conjunction with the ambition to deliver the highest achievable performance in the more stereotypical water hydraulics systems, creates a great demand for APMSPD that are able to operate in what Ruble [8] categorizes as the high-pressure regime: 300+ bar— but especially for mid- to large-sized units, the industry struggles to push the operating pressure of these machines much past 160 bar [9].

One of the major roadblocks in this effort faces is water's viscosity, which is low enough to endanger the bearing and sealing functions of the tribological interfaces in APMSPD. Failure to bear the imposed load results in excessive component wear/damage, and failure to seal properly, in excessive power loss. The piston-cylinder tribological interface in APMSPD exemplifies this in utter severity, specifically at high-pressure operating conditions, because it is subject to a large side load that increases with operating pressure— and because it requires hydrodynamic pressure to carry that load [10]. Hydrodynamic pressure, i.e. the pressure generated through the relative motion of the surfaces that form the interface, diminishes as the viscosity decreases, rendering the use of water as a lubricant particularly dangerous for the piston-cylinder interface. Ergo, this interface is the chosen object of study: the intent is to investigate how its design should be changed in address of the aforementioned problems.

For reasons best understood after an introduction to APMSPD, the design strategy investigated in this body of research is the imposition of a surface shape, only microns in height, on the surfaces that border the piston-cylinder interface fluid film. On account of the high pressure regime being examined, and the poor load-carrying capacity of water, testing a large number of such shapes experimentally in the context of extensive design studies (risking machine damage/failure with every trial) is prohibitively expensive and unsafe. Therefore, a predominantly computational approach is taken. Designs for the piston-cylinder interface are tested by simulating the behavior of this fluid film with FSTI, a non-isothermal fluid-structure-thermal interaction model of the main lubricating interfaces in APMSPD developed at the Maha Fluid Power Research Center. Using this interface model, the effect of surface shaping on the piston-cylinder interface is investigated in several design studies and an optimization study, culminating in the development of a novel algorithm for generating effective surface shapes, and the experimental testing of such a shape in collaboration with the Danfoss High Pressure Pump Division.

In concise overview:

Research Objective. The research objective is to expose trends and develop methods in piston-cylinder interface design that lead to full load support and minimal power loss at the fluid film for APMSPD running in the high-pressure regime, with water as the hydraulic fluid.

Research Approach. The described objective is pursued via the following steps:

1. Compare the roles of hydrodynamic and hydrostatic pressure to load support in the three main lubricating interfaces of APMSPD in order to establish why the design of the piston-cylinder interface, in particular, can be so challenging.

2. Conduct large-scale simulation studies with the aforementioned interface model in order to investigate the design trends associated with two powerful forms of surface shaping: the concave bore surface shape, which gives the surfaces of the bores through which the piston moves the lengthwise cross-section of a circular arc, and the barrel piston

surface shape, which gives the piston running surface the lengthwise cross-section of a circular arc.

3. Develop an algorithm that outperforms these surface shapes by generating designs specifically tailored to how the pistons of a particular unit "sit" and deform in their bores during operation.

4. In collaboration with Danfoss, experimentally test the output of that algorithm in a physical prototype.

Thesis structure. Table 1.1 outlines the structure in which the results of the described research approach will be presented.

Table 1.1. Chapter overview.

Ch.	*Summary*
2	Introduction to APMSPD
3	Introduction to the piston-cylinder interface model
4	The contributions of hydrodynamic and hydrostatic pressure to load support in the three main lubricating interfaces of APMSPD
5	State of the art
6	Baseline simulation results (i.e. no surface shaping)
7	Simulation results for the concave bore and barrel piston surface shapes
8	Response surface algorithm for piston-cylinder interface design
9	·Algorithm for generating high-performance bore surface shapes tailored to piston tilt and deformation ·Experimental testing of surface shape generated using this algorithm
10	Conclusions

The next chapter provides an introduction to the basic architecture of APMSPD, their principle of operation, the lubricating interface of interest, the aforementioned piston side load, and surface shaping as a design solution. For a more detailed description of APMSPD that encompasses and surpasses the background knowledge required for this particular work, please refer to [4].

2. THE PISTON-CYLINDER INTERFACE

2.1 Introduction to APMSPD

As already stated, APMSPD are displacement machines; they function as pumps and/or motors in hydraulic circuits. Fig. 2.1 illustrates a typical APMSPD construction. In this architecture, a rotating drive shaft turns a "cylinder block." This causes the pistons sitting within the bores of said block to move in circles about its central axis, denoted as the z-axis in Fig. 2.1; ball joints connect these pistons to "slippers," and the slippers sit up against an angled swash plate. The swash plate's angle is key: it links a piston's traversal of its circular path around the z-axis with an axial movement into, and out of, the cylinder block.

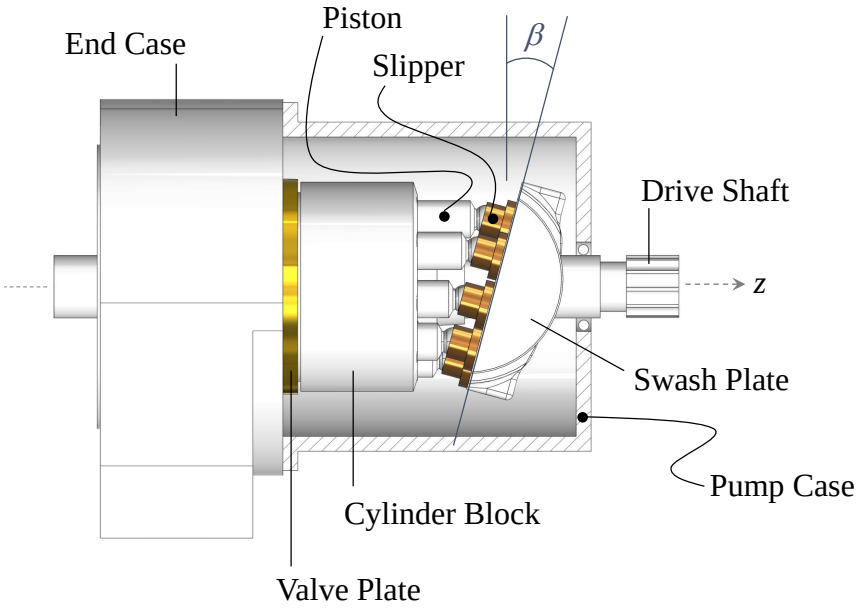

Figure 2.1. APMSPD components (coordinate system based on [11]).

Fig. 2.2 provides an overview of how that movement displaces fluid in such a machine. Moving out of the block over the first half of a drive shaft revolution, a piston leaves behind a void that, on account of its low pressure, pulls in fluid from an inlet port located inside the end case. The hollow space inside the cylinder block behind each piston into which this fluid enters is known as the DC (displacement chamber). Moving back into the block during the second half of the drive shaft revolution, the piston forces fluid inside the DC to exit into

an outlet port, also located within the end case. In this way, fluid is pumped from the inlet port to the outlet port. The inlet and outlet ports can be at the same pressure, in which case the APMSPD simply displaces fluid— or, as is the case in many hydraulic systems, the fluid can be pumped from a low-pressure inlet to a high-pressure outlet. The present work focuses on the latter.

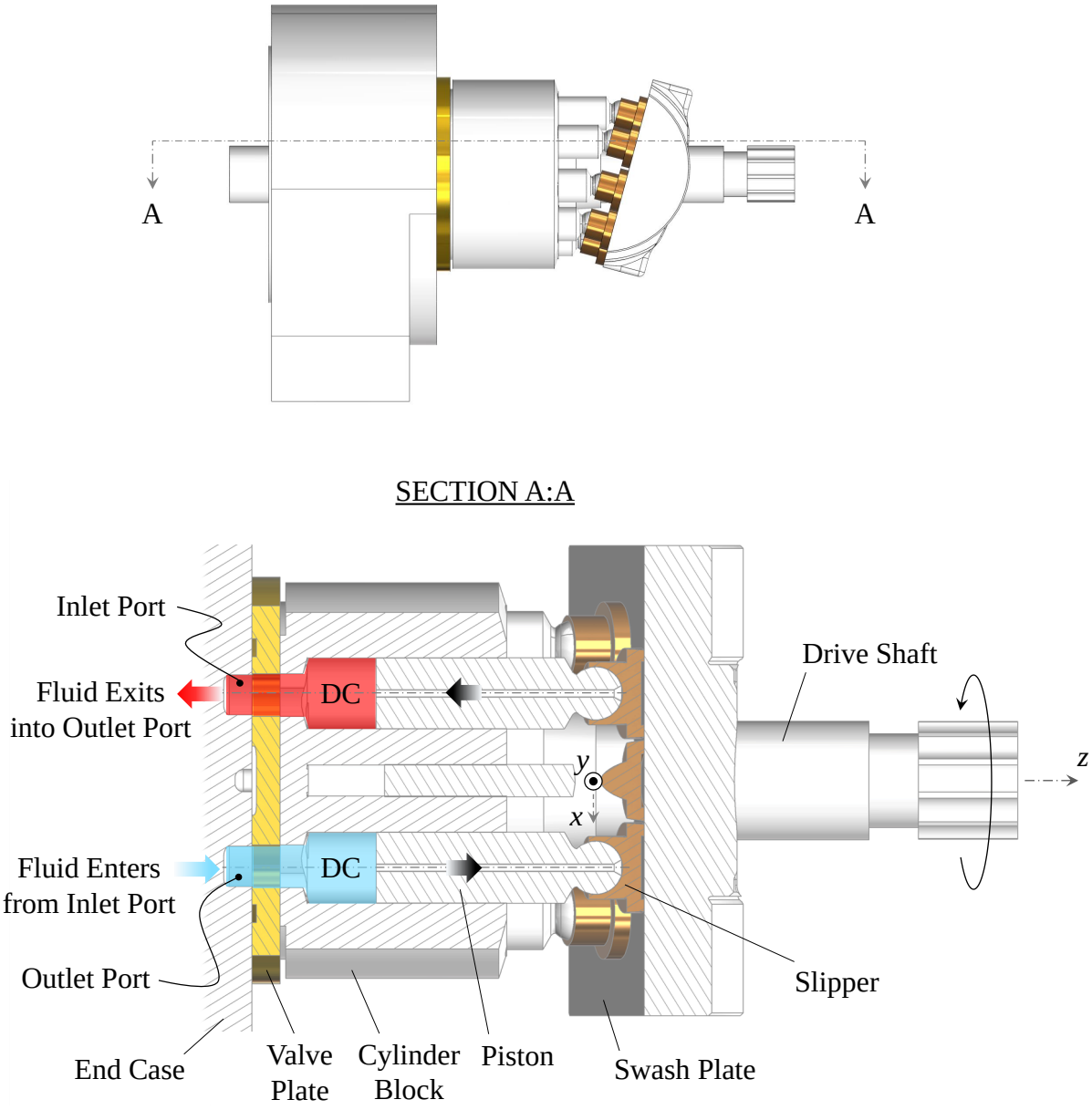

Figure 2.2. Cross-section of an APMSPD.

While the investigation to be presented here makes use of a unit of the described architecture, some notable variations in pump design do exist. For example, APMSDP can be made slipper-less, in which case the pistons are directly supported by the swash plate [4]. Or: instead of rotating the cylinder block and keeping the swash plate still, it is possible to invert the kinematics— turn the swash plate and hold the block still. Regardless, efficiency and lifespan of the machine are heavily dependent on the design of its lubricating interfaces.

2.2 The Tribological Interfaces of APMSPD

In order for the pumping/motoring mechanisms to work as described, the swash plate, slippers (if present), pistons, cylinder block, and valve plate must exercise relative motion. In APMSPD, three main tribological interfaces preside over this motion: the cylinder block-valve plate interface, the piston-cylinder interface, and the slipper-swash plate interface, all shown in Fig. 2.3 [10]. These interfaces have two functions. First, they have a sealing function that serves to minimize the amount of hydraulic fluid leaking through interface, from

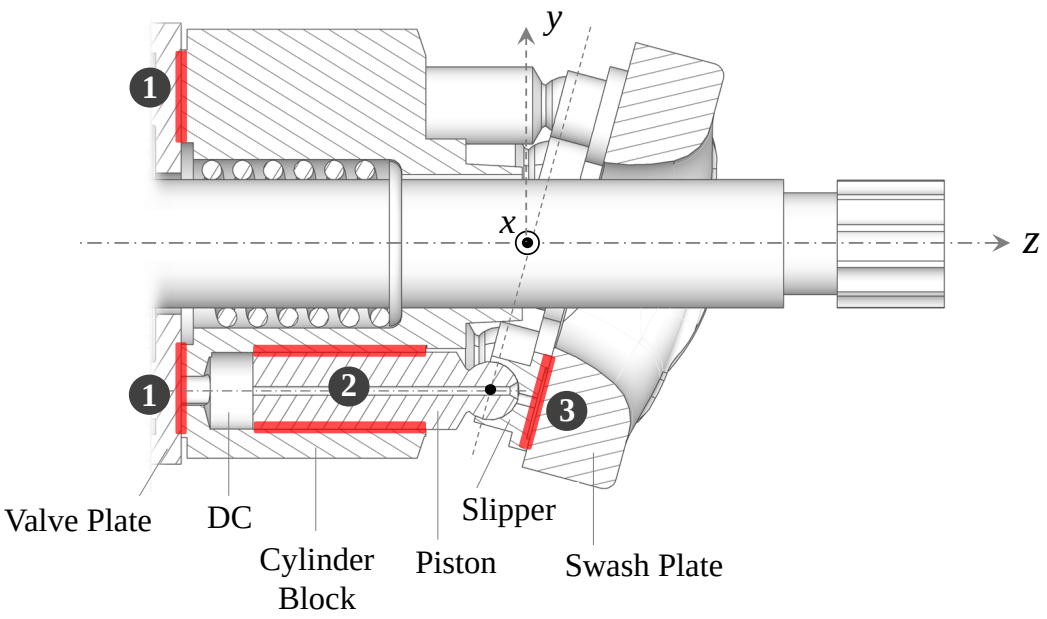

Figure 2.3. 1) Cylinder block-valve plate interface, 2) piston-cylinder interface, 3) slipper-swash plate interface (image based on [10]).

the DCs into the pump case. Second, they have a bearing function that serves to minimize wear and mixed friction, and to prevent unit failure by eliminating solid contact between components.

Low-viscosity fluids, e.g. water, perform these functions poorly; they lack the internal friction between molecules needed to keep the fluid from slipping through the interface fast, and they lack in their ability to build the hydrodynamic pressure that prevents metal-to-metal contact. As already stated in the previous chapter, the piston-cylinder interface is the chosen subject of study because it is an especially pronounced example of these problems— a point that Ch. 4 will further elaborate on. This interface is the fluid film between a piston, and the cylinder block bore within which it moves— unless the APMSPD was designed with a bushing inside the cylinder block bore, in which case the piston-cylinder interface is the fluid film between the piston and the *bushing* bore within which it moves. In either case this film is only microns to tens of microns thick— yet indisputably decisive to the performance of an APMSPD.

2.3 Shaft Angle

Study of the piston-cylinder interface requires having a measure of its angular position. This is because the interface not only moves as the cylinder block rotates— it changes behavior in terms of the leakage, friction, pressure distribution, etc. associated with the fluid film. These behavioral changes come from the fact that the load imposed on the interface (discussed in the next section) changes with that angular position [10]. The position of the interface is tied to the position of the bushing/the cylinder block bore through which the corresponding piston moves; adopting the convention used by [4], the angular position, φ, is defined in the present work as shown in Fig. 2.4.

The figure depicts a valve plate, which sits between the cylinder block and end case in an APMSPD (refer back to Fig. 2.1), and is stationary (does not rotate with the block); its purpose is to regulate the flow into, and out of, the ports. Fig. 2.4 shows two openings in this plate, marked in red and blue— one of them connects the DCs passing over it to the

inlet port, while the other connects them to the outlet port. (Depending on pump design, each of these openings can be subdivided into multiple openings.)

In order to determine φ for a particular piston-bore set, the valve plate should be viewed as illustrated. The x- and y-axis intersect at the center axis of the cylinder block. The x-axis falls within the total angular range spanned by the valve plate opening(s) that connect to the high-pressure port (this may be either the inlet or the outlet port, depending on whether the APMSPD is pumping or motoring), while the y-axis passes through ODC (outer dead center): the angular position at which the piston of interest has moved furthest out of the cylinder block. In this setup, φ is the angle from the y-axis to the center axis of the cylinder block bore of interest, measured clockwise about the z-axis.

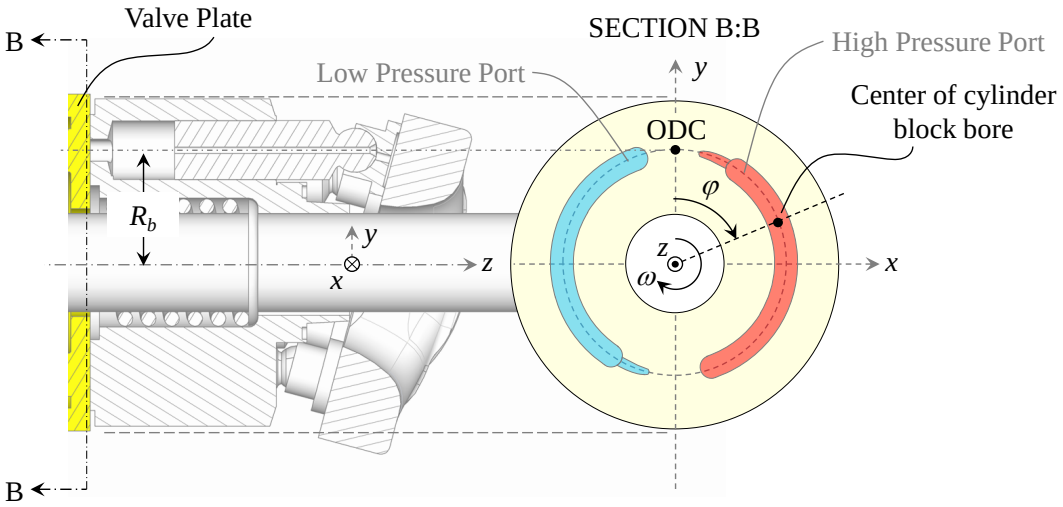

Figure 2.4. Shaft angle.

2.4 External Forces Acting on APMSPD Pistons

The load that the piston-cylinder interface must carry is the "side load" mentioned in the introduction; an understanding of the forces acting on the pistons in APMSPD sheds light on its origins. Fig. 2.5 (a) and (b) illustrate these forces, except those due to pressure buildup within the fluid film (which depend strongly on the interface's exact geometry). Of those

shown— F_{DK}, $F_{\omega\mathrm{K}}$, F_{TK}, F_{TG}, and F_{aK}— F_{DK} tends to be the largest; it is the force acting on the flat end of the piston because of the pressure difference between the DC and the pump case. Fig. 2.5 (c) gives an example of how the DC pressure that sets the magnitude of this force changes over the course of a shaft revolution. As can be seen, the DC first connects to the high-pressure port, then to the low-pressure port; accordingly, the pressure rises at the start of the revolution, and then drops near $\varphi = 180°$. In contrast, pump case pressure, i.e. the other pressure defining F_{DK}, is roughly constant over a shaft turn— and much lower in magnitude (commonly on the order of 1 bar).

Although F_{DK} is a dominant contributor to the side load, it is not the sole contributor. The others are: $F_{\omega\mathrm{K}}$, the force generated due to the centrifugal effect, F_{TK}, the force due to viscous friction in the piston-cylinder interface, F_{TG}, the force due to viscous friction in the slipper-swash plate interface, and F_{aK}, the force due to the acceleration of the piston in the axial direction [4].

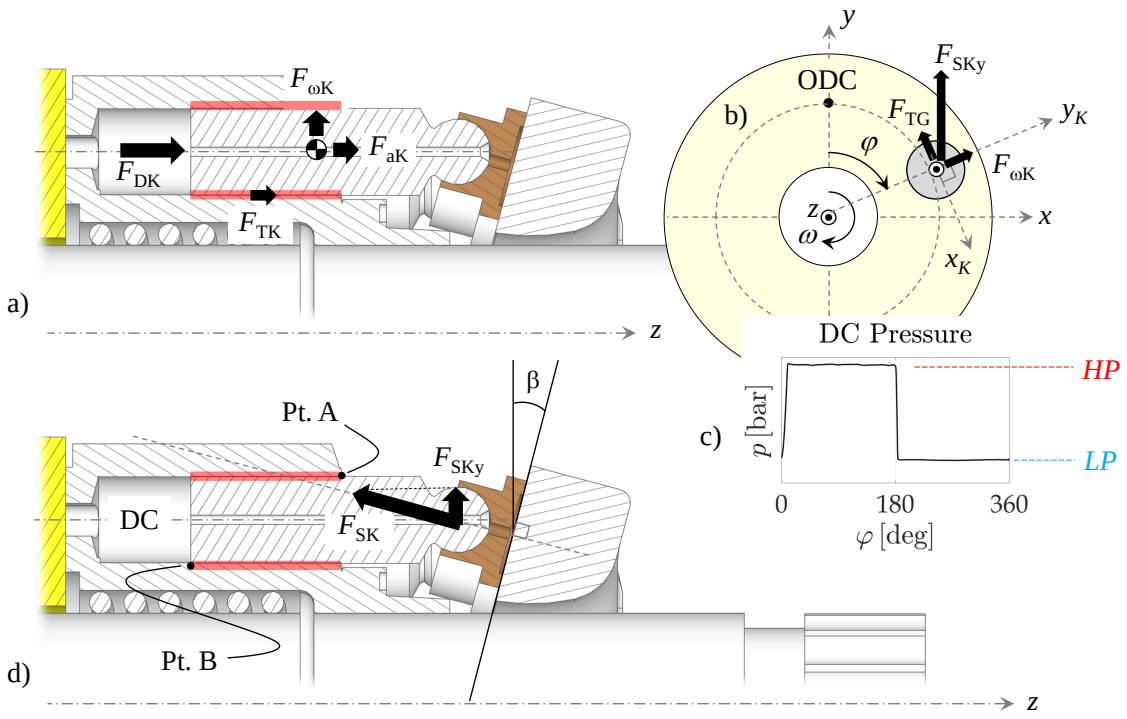

Figure 2.5. External forces acting on the piston (left), and DC pressure as a function of φ (right). Image based on [4].

Together, F_{DK}, F_{aK}, and F_{TK} evoke a reaction force from the swash plate, F_{SK} [4]:

$$F_{\mathrm{SK}} = -\frac{(F_{\mathrm{DK}} + F_{\mathrm{TK}} + F_{\mathrm{aK}})}{cos(\beta)} \tag{2.1}$$

This reaction force, shown in Fig. 2.5 (d), has a component along the y-axis, denoted F_{SKy}:

$$F_{\mathrm{SKy}} = -F_{\mathrm{SK}} sin(\beta) = (F_{\mathrm{DK}} + F_{\mathrm{TK}} + F_{\mathrm{aK}}) tan(\beta) \tag{2.2}$$

The forces F_{SKy}, $F_{\omega\mathrm{K}}$, and F_{TG}, along with forces due to fluid pressure buildup in the piston-cylinder interface, cause the piston's central axis to move away from, and tilt with respect to, the corresponding cylinder block bore's central axis. The load comprising these forces is dangerous— especially because the moment it creates, which causes the piston to tilt within its bore, can result in solid contact. Due to this tilt, a piston-bore collision typically takes place near the ends of the guide length (the axial extent of the interface), in the vicinity of what Fig. 2.5 labels Point A and Point B.

F_{TG} tends to be small, leaving the piston tilt to be set mainly by F_{SKy} and $F_{\omega\mathrm{K}}$. According to Eq. 2.2, F_{SKy} grows with F_{DK}— for this reason, it is demanding to design the piston-cylinder interface such as to avert solid contact during high-pressure operation, when F_{DK} is large for a piston connected to the high-pressure port. In a functional, post wear-in phase APMSPD, the aforementioned hard collision of the piston with its surrounding bore is prevented by the forces arising from the fluid pressure distribution within the piston-cylinder lubricating interface. Key to this is the hydrodynamic pressure buildup generated where the piston comes close to the bore— but this pressure buildup decreases in magnitude when the viscosity of the lubricating fluid is lowered; hence the difficulty with high pressure operation *when the hydraulic fluid is water.*

The force F_{SKy} is key in this problem; its component F_{DK} can be computed as follows:

$$F_{\mathrm{DK}} = \frac{\pi {d_{\mathrm{K}}}^2 (p_{\mathrm{DC}} - p_{\mathrm{Case}})}{4} = \frac{\pi {d_{\mathrm{K}}}^2 \triangle p}{4} \tag{2.3}$$

Here, d_{K} is the piston diameter, p_{DC} is DC pressure, p_{Case} is the pressure inside the pump case, and $\triangle p = p_{\mathrm{DC}} - p_{\mathrm{Case}}$.

F_{aK} is simply piston mass times acceleration:

$$F_{\mathrm{aK}} = m_{\mathrm{K}} a_{\mathrm{K}} \tag{2.4}$$

Expressing the acceleration at a particular shaft angle in terms of s_{K}, i.e. the position of the piston head's center at that angle relative to its position at ODC, measured along the z-axis [4]:

$$a_{\mathrm{K}} = \frac{dv_{\mathrm{K}}}{dt} = \left(\frac{dv_{\mathrm{K}}}{d\varphi}\right)\left(\frac{d\varphi}{dt}\right) = \omega\frac{dv_{\mathrm{K}}}{d\varphi} \tag{2.5}$$

$$v_{\mathrm{K}} = \frac{ds_{\mathrm{K}}}{dt} = \left(\frac{ds_{\mathrm{K}}}{d\varphi}\right)\left(\frac{d\varphi}{dt}\right) = \omega\frac{ds_{\mathrm{K}}}{d\varphi} \tag{2.6}$$

$$=> F_{\mathrm{aK}} = (m_{\mathrm{K}})(\omega^2)\left(\frac{d^2 s_{\mathrm{K}}}{d\varphi^2}\right) \tag{2.7}$$

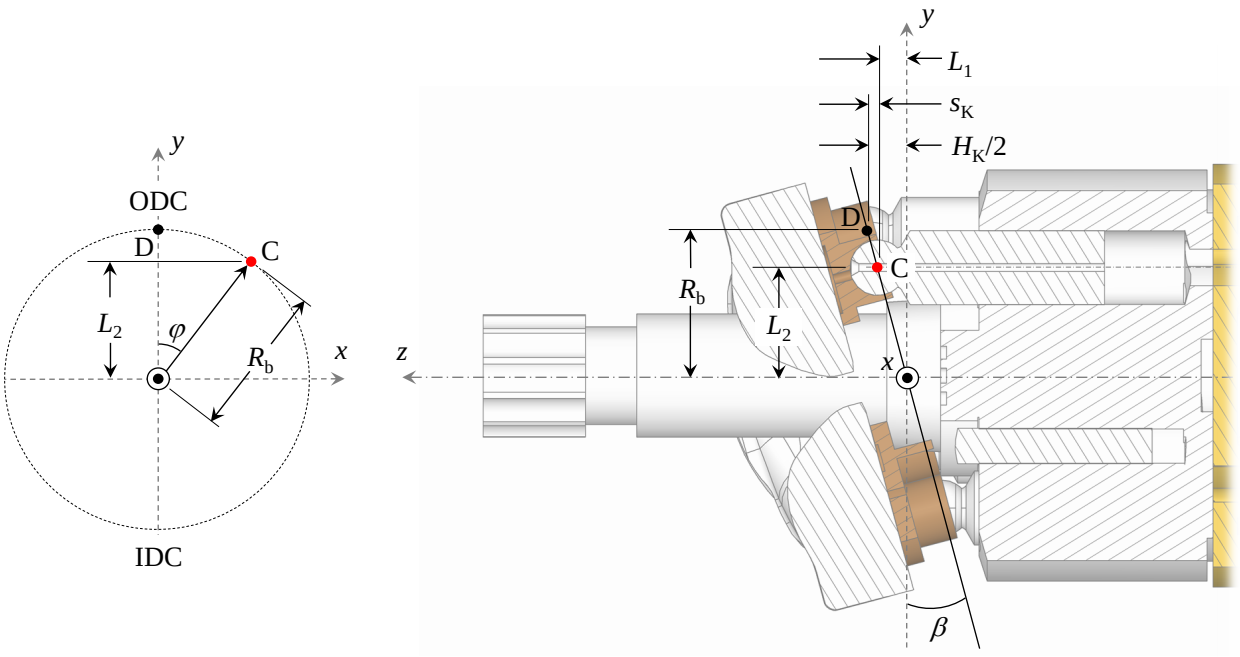

Figure 2.6. Cross-section of an APMSPD for the derivation of s_K.

s_K can be derived from Fig. 2.6, showing a piston at an angular position φ, with the center of its head at Pt. C. Pt. D is the position of the center of that same piston's head at ODC. Thus, s_K is the difference between the z-coordinates of Pt. C and Pt.D. The z-coordinate of Pt. C is the distance L_1, and the z-coordinate of Pt. D is half of the piston's stroke, H_K:

$$s_K = L_1 - \frac{H_K}{2} \tag{2.8}$$

The distance L_1 can be derived from the distance L_2 (see the right-hand image of Fig. 2.6):

$$L_1 = L_2 tan(\beta) \tag{2.9}$$

L_2, in turn, can be derived from the pitch radius R_b (see the left-hand image of Fig. 2.6):

$$L_2 = R_b cos(\varphi) \tag{2.10}$$

$$=> s_K = R_b cos(\varphi) tan(\beta) - \frac{H_K}{2} \tag{2.11}$$

Lastly, from the right-hand image of Fig. 2.6 [4]:

$$H_K = 2R_b tan(\beta) \tag{2.12}$$

$$\therefore s_K = -R_b tan(\beta)(1 - cos(\varphi)) \tag{2.13}$$

$$=> F_{aK} = -(m_K + m_G)(\omega^2)\,(R_b tan(\beta) cos(\varphi)) \tag{2.14}$$

Taking eq. 2.3 and 2.14 into account, it can be seen that F_{SKy} depends on F_{TK}, p_{DC}, p_{Case}, d_K, m_K, m_G, ω, R_b, and β. However, because F_{aK} and F_{TK} are typically small compared to F_{DK}, F_{SKy} is most heavily influenced by p_{DC}, p_{Case}, β, and d_K.

It is possible to decrease F_{SKy} by decreasing β, but this lessens the unit's displacement (the volume of fluid that the APMSPD can move from the inlet port to the outlet port per shaft revolution). An effort may be made to compensate for that lost displacement by

increasing the pitch radius R_b, which, according to Eq. 2.12, increases the piston stroke; however, increasing R_b makes the unit less compact. It is also possible to decrease F_{SKy} by decreasing d_K, but that lessens the displacement as well. In this case, since pistons of smaller diameter take up less space in the cylinder block, an effort may be made to compensate for lost displacement by increasing the number of pistons in the APMSPD— however, as structural integrity must be maintained, this is difficult to do without increasing R_b, and thereby again compromising pump compactness.

Lastly, a number of machine architectures have been developed that could be employed in APMSPD in order to drastically reduce the side load (to be discussed in more detail in Ch. 5). Though these designs may present a solution for some applications, they either render the pump bulky (constitute a packaging problem for applications with space constraints), introduce components that can cause violent machine failure if they malfunction, place a high side load on the drive shaft bearings, or are only implementable for tandem units. This creates demand for a more versatile solution.

2.5 Surface Shaping as a Design Solution

In order to evade the described disadvantages associated with large-scale geometric modifications to a unit, the present work addresses the objective stated in the introduction via micro surface shaping. In the context of piston-cylinder interface design, micro surface shaping refers to giving the surfaces that form the interface a shape, on the order of microns in height— i.e. on the same order of magnitude as the thickness of the fluid film. A surface shape can be imposed on the running surface of a piston (the surface that will be in contact with the fluid film during operation), and/or the surface of the bore through which that piston travels (see Fig. 2.7).

By changing the film thickness, the imposition of a surface shape *changes the pressure field within the interface*; this is what makes surface shaping such an effective design tool: by changing the pressure field, it can adjust the balance of the forces and moments acting on the piston, thereby relieving the piston's need to directly push against the solid surface of

its surrounding bore for support. In précis, an ideal surface shape changes the pressure field such as to counter the negative effects of the piston's side load.

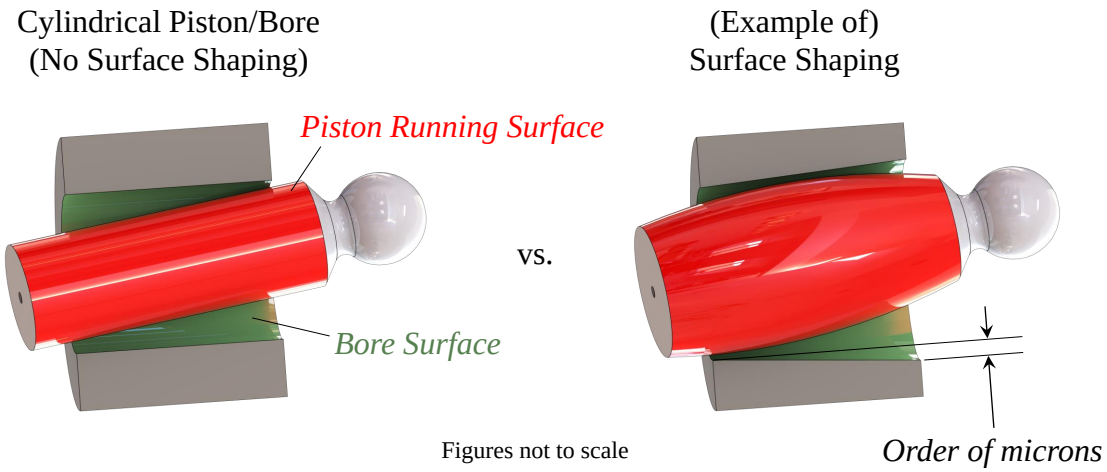

Figure 2.7. Micro surface shaping concept overview.

For standard units, with cylindrical pistons and bores, surface shaping happens automatically during the wear-in process: the piston and bore surfaces scrape away at each other, until the resulting pressure field supports the load. However, when employing the low-viscosity fluid water under extreme operating conditions, as is the objective of the current work, the wear-in process may be so brutal as to cause severe component damage (scoring, distortion, etc.), without bringing the piston and bore surfaces to converge to a form that is conducive to load support. Furthermore, even if the shaping produced during the wear-in phase provides full load support, it may cause the piston-cylinder interface to incur more power loss (more leakage and/or more viscous friction) than another design that is also able to achieve full load support.

Moreover, depending on the materials used, and the imperfections present therein, the wear-in shaping may vary from one interface to the next, thereby introducing additional elements

of uncertainty and inconsistency into the pump design process. Lastly, relying on wear-in to render the unit operational restricts the choice of material pairings for the interface-forming components to those that facilitate favorable shaping. This can preclude the use of materials that are cheaper, have better corrosion resistance, or may be more environmentally friendly to produce/dispose of. All of these problems can be avoided by pre-shaping the surfaces during the pump manufacturing process; the present work therefore pursues the design of surface shaping that is machined into the relevant surfaces *before* starting the machine for the first time.

3. INTERFACE MODEL

Uncovering trends that chart a path, through the infinity of possible design concepts, towards the best-performing micro surface shape(s) for a given piston-cylinder interface, requires being able to determine how the behavior of that interface transforms in response to the imposition of such a shape. For this, FSTI, a state of the art fluid-structure-thermal interaction model developed at the Maha Fluid Power Research Center, is employed. The full model can simulate the behavior of all three main tribological interfaces in APMSPD; the design studies in subsequent chapters, however, exclusively make use of its piston-cylinder interface module, developed by Dr. M. Pelosi, Dr. D. Mizell and Dr. L. Shang. In order to enable a more complete understanding of the simulation results to be presented later, a basic overview of this module will now be provided. For more information on the module and its experimental validation, please refer to [10], [12]–[16].

3.1 Groundwork: The Pressure Module

p_{DC}, the DC pressure, is a key parameter in simulating the piston-cylinder interface, because it sets the magnitude of F_{DK}, one of the largest components of F_{SKy}. Through its contribution to this force, p_{DC} dictates, to a substantial degree, the micro-motion of a piston within its bore. The interface module takes this pressure as an input; hence, it is computed (for each DC) as a function of shaft angle prior to starting the interface module. This is done by the "pressure module" of FSTI: a lumped parameter model (see [17], [18] for details) based in the work of Wieczorek and Ivantysynova [19]. In this model, the control volume associated with a DC, shown in red in Fig. 3.1, is assumed to have a uniform pressure. The pressure change in the i$^{\mathrm{th}}$ DC with time is described by the equation [4]:

$$\frac{dp_{\mathrm{DCi}}}{dt} = \frac{K}{V_{\mathrm{i}}}\left(Q_{\mathrm{ri}} - Q_{\mathrm{SKi}} - Q_{\mathrm{SBi}} - Q_{\mathrm{SGi}} - \frac{dV_{\mathrm{i}}}{dt}\right) \tag{3.1}$$

K is the bulk modulus, V_{i} is the derived displacement volume, Q_{ri} is the flow rate of fluid passing from the port into the DC or visa versa, Q_{SGi} is the flow rate of fluid exiting the piston orifice at the piston head, and Q_{SKi} and Q_{SBi} are the flow rates of fluid leaking into the pump

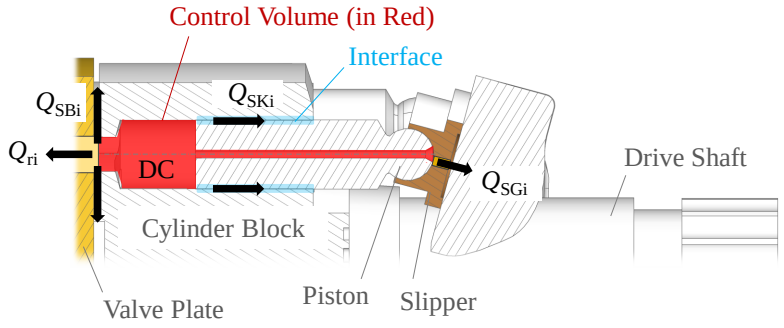

Figure 3.1. Control volume (image based on Ivantysyn and Ivantysynova (2003)).

case from the piston-cylinder and cylinder block-valve plate interfaces, respectively. Q_{SGi}, Q_{SKi}, and Q_{SBi} can be neglected for the purposes of computing p_{DCi} [18]. That leaves Q_{ri} [18]:

$$Q_{\mathrm{ri}} = Q_{\mathrm{rLPi}} + Q_{\mathrm{rHPi}} \tag{3.2}$$

Here, Q_{rLPi} is the flow rate of fluid passing from the low-pressure port into the DC, and Q_{rHPi} is the flow rate of fluid passing from the DC into the high-pressure port. Assuming turbulent flow, both of these terms can be expressed as functions of p_{DCi} through the orifice equation [4], [18]:

$$Q_{\mathrm{LPri}} = \alpha_{\mathrm{DLP}} A_{\mathrm{rLPi}} \sqrt{\frac{2|p_{\mathrm{DCi}} - p_{\mathrm{LP}}|}{\rho}} sgn(p_{\mathrm{DCi}} - p_{\mathrm{LP}}) \tag{3.3}$$

$$Q_{\mathrm{HPri}} = \alpha_{\mathrm{DHP}} A_{\mathrm{rHPi}} \sqrt{\frac{2|p_{\mathrm{DCi}} - p_{\mathrm{HP}}|}{\rho}} sgn(p_{\mathrm{DCi}} - p_{\mathrm{HP}}) \tag{3.4}$$

α_{D} is the orifice discharge coefficient, and A_{r} is the area of the smallest cross-section of the fluid volume (cross-section taken perpendicular to a streamline) that starts in the DC, and ends in the port that DC connects to at a particular shaft angle. As can be seen now, EQ.3.1 relates p_{DCi} to its time derivative; it is an ODE (ordinary differential equation). The pressure module sets up such an ODE for each displacement chamber, and solves the resulting system of ODEs via a Runge-Kutta scheme [18]— thus obtaining p_{DCi} as a function of shaft angle (e.g. Fig. 2.5 c).

3.2 The Piston-Cylinder Interface Module

Fig. 3.2 gives an overview of the piston-cylinder interface module of FSTI. For a given APMSPD, this module simulates the behavior of *one* piston-cylinder interface over a full shaft revolution, under the assumption that all other piston-cylinder interfaces in the unit have the same geometry as that one. It is also assumed that the APMSPD has reached steady-state operation (FSTI does not simulate startup conditions). The module's outermost code loop calculates the temperatures and elastic thermal deformations of the solid bodies that border, and/or are capable of deforming, the piston-cylinder interface: the piston, the cylinder block, and, if present, the bushing sitting inside of the cylinder block bore [10]. Both the temperatures and the thermal deformations are obtained using a finite element method [10], [14].

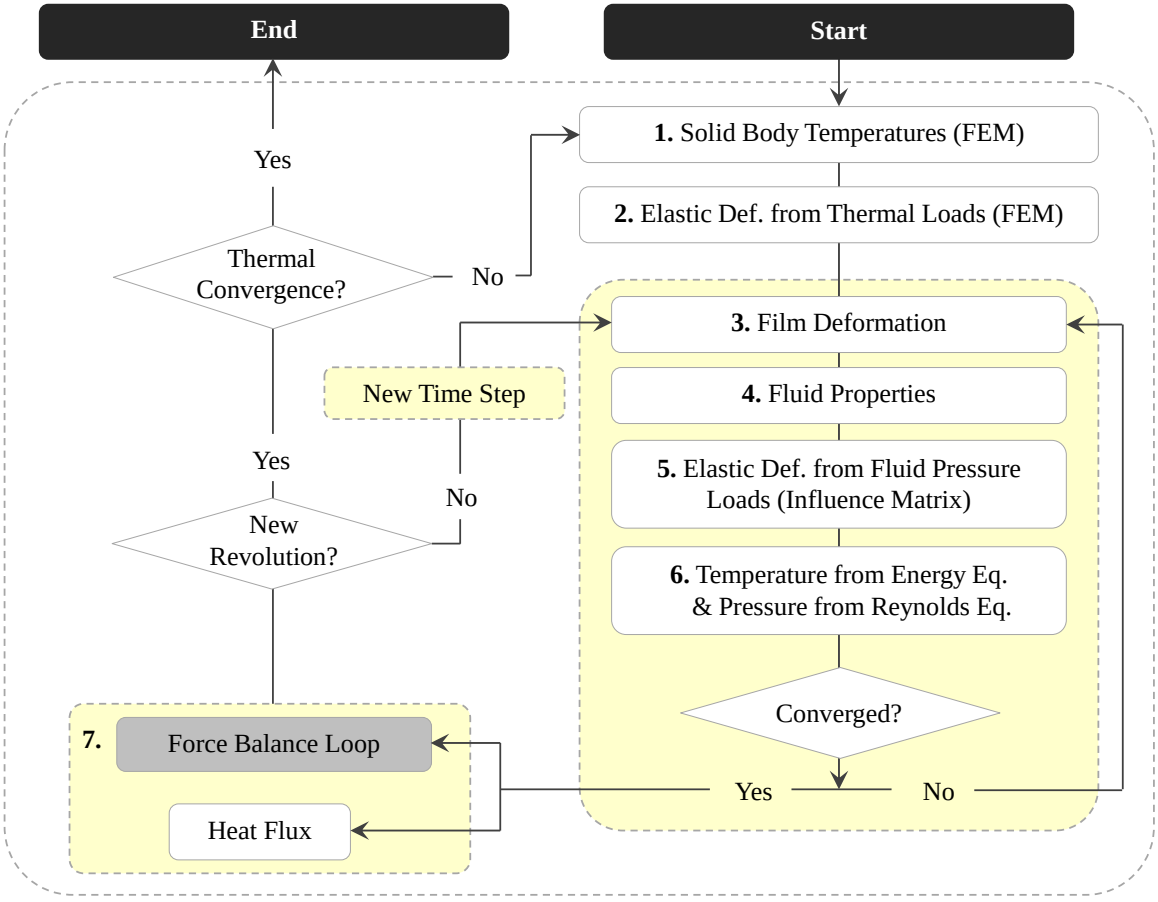

Figure 3.2. FSTI (image based on [10])

These solid body temperatures and thermal deformations are computed only once for the shaft revolution being simulated, under the assumption that they will not change significantly with time over the course of that revolution (the duration of one shaft turn is typically on the order of thousandths to hundredths of a minute— too brief to justify the immense computational expense of modeling the time-dependency of these parameters). The inner loop encompassing steps 3. to 7., however, is devoted to parameters that *are* significantly time-dependent; this loop is completed at every time step.

It begins by updating the fluid film deformation, and the fluid properties within the interface, at the time step being examined [10]. Then, it proceeds to compute the elastic deformations of the aforementioned solid bodies due to the pressure exerted on them by the fluid film. This is done using an influence matrix method: prior to running FSTI, point loads are applied to the solid bodies. The deformation of each body in response to each point load is stored, and when FSTI runs, the stored deformations are scaled and superimposed in accordance with how the corresponding point loads must be scaled and superimposed in order to form the simulated pressure load acting on the solid bodies at the interface.

Once the solid body pressure deformations have been computed in this way, the pressure field within the fluid film is determined using the Reynolds equation, and the temperature field using the energy equation— both to be explained in detail later. These two equations mark the end of the loop formed by steps 3.-6., which repeats itself until the temperature and pressure fields converge. At that point, the temperature field is used to compute the heat flux from the fluid film to the adjacent solid bodies (see step 7.).

In addition, the code enters a force balance loop that computes, via a Newton-Raphson solver, the squeeze velocity (velocity of the piston towards the bore) needed in order to achieve a balance between the force and moment generated by the fluid film pressure, and the other external forces and moments acting on the piston. This velocity is computed at two control points on the piston's central axis: one at either end of the guide length. Once the squeeze motion has been determined, the module repeats steps 3.-7. for the next time step.

When the shaft revolution is complete, the module uses an average of the heat fluxes obtained in step 7. at all the simulated time steps to update the solid body temperatures, and the revolution is re-simulated using these values. The simulation finishes when steps 1.-7. have run through at least five iterations, and convergence has been achieved for the average heat fluxes corresponding to the piston and bore, as well as the energy dissipation and leakage values. The energy dissipation and leakage must each converge to within 5%, while the avg. heat fluxes, being parameters that strongly simplify a highly complex heat transfer problem, to 10%.

3.3 FSTI Coordinate Systems

As stated, the pressure and temperature fields spanning the fluid film are calculated using the Reynolds and energy equations, respectively [10]. In order to do that, the fluid film around the piston is "unwrapped," and then subjected to the aforementioned equations in Cartesian coordinates. This is illustrated in Fig. 3.3: the fluid film in image (a) is unwrapped into the

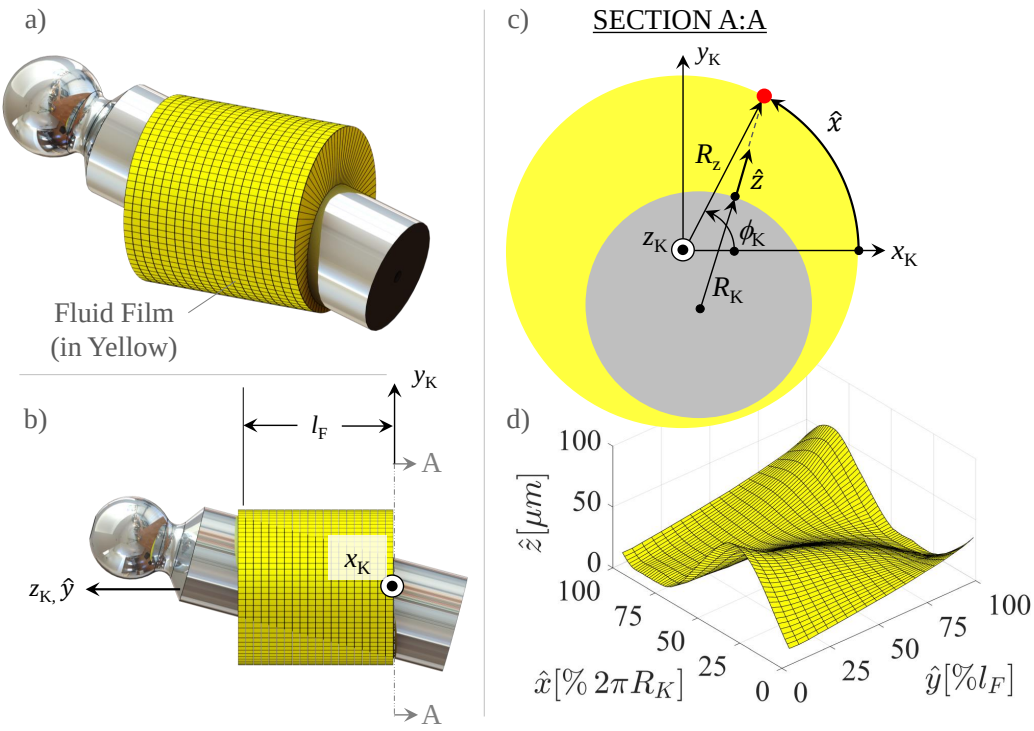

Figure 3.3. $\hat{x} - \hat{y} - \hat{z}$ coordinate system (images based on [10]).

Cartesian $\hat{x} - \hat{y} - \hat{z}$ coordinate system of image (d); the axes of that coordinate system are depicted in images (b) and (c).

In defining the $\hat{x} - \hat{y} - \hat{z}$ coordinate system, it is necessary to first introduce the $x - y - z$ coordinate system— the global coordinate system that already made a brief appearance in the shaft angle section of Ch. 2. This system is shown in Fig. 3.4; it is defined such that the z-axis is the central axis of the cylinder block, and its positive direction points towards the swash plate [11]. The origin of this coordinate system is the intersection point of the z-axis with Plane C, the plane that lies parallel to the swash plate surface, and passes through all the piston head centers. The y-axis is oriented such that it passes through ODC in the positive direction, and the x-axis is oriented such that it falls within the total angular range spanned by the valve plate opening(s) connecting to the high-pressure port.

The $x - y - z$ (global) coordinate system is stationary— but based on its layout, a second, rotating system can be defined. Fig. 3.3 shows the $x_K - y_K - z_K$ coordinate system; here, it can be seen that its origin is located on the center axis of the cylinder block bore (of the

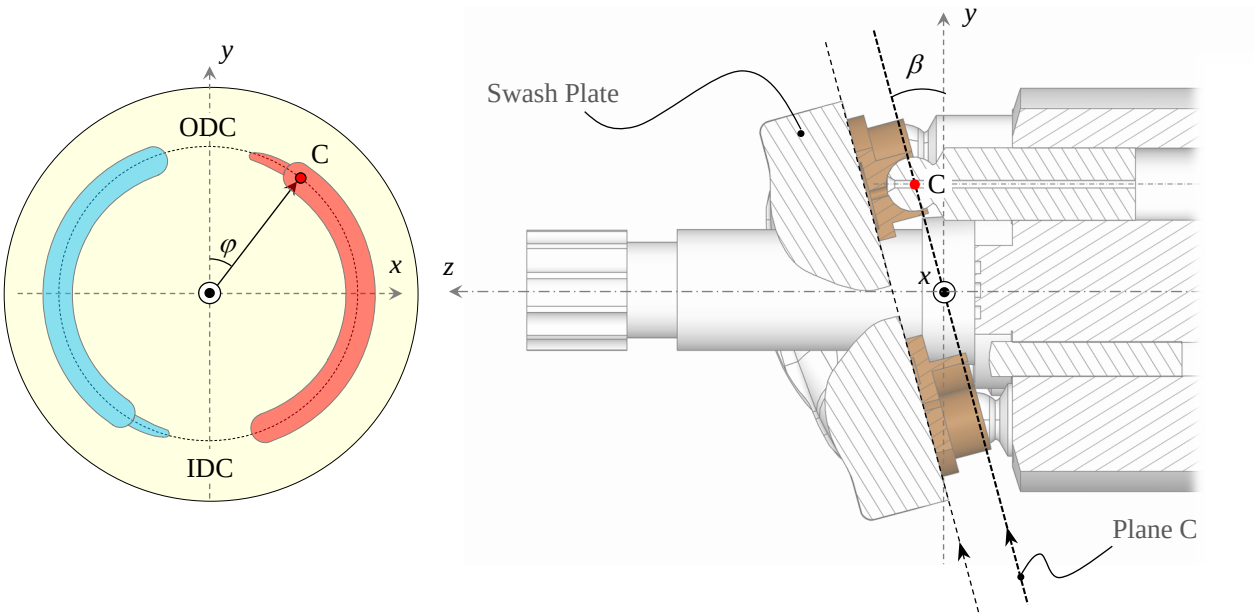

Figure 3.4. $x - y - z$ coordinate system (image based on [10]).

interface being modeled), at the end of the guide length bordering the DC [10]. Its positive z_K-axis lies on the bore's center axis, and points away from the DC. As can be observed from the top-down view of the cylinder block provided in Fig. 3.5, the y_K-axis lies on a line that moves radially outward from the center axis of the block, and passes through the origin of the $x_K - y_K - z_K$ system, denoted Pt. E. As the cylinder block turns, the bores move—and the position of Pt. E changes. Consequentially, the y_K-axis moves; Fig. 3.5 shows the orientation of this axis for four different shaft angles. Viewing the cylinder block in the orientation of these images (with the x-axis pointing to the right), the positive x_K-axis is located 90°clockwise from the y_K-axis.

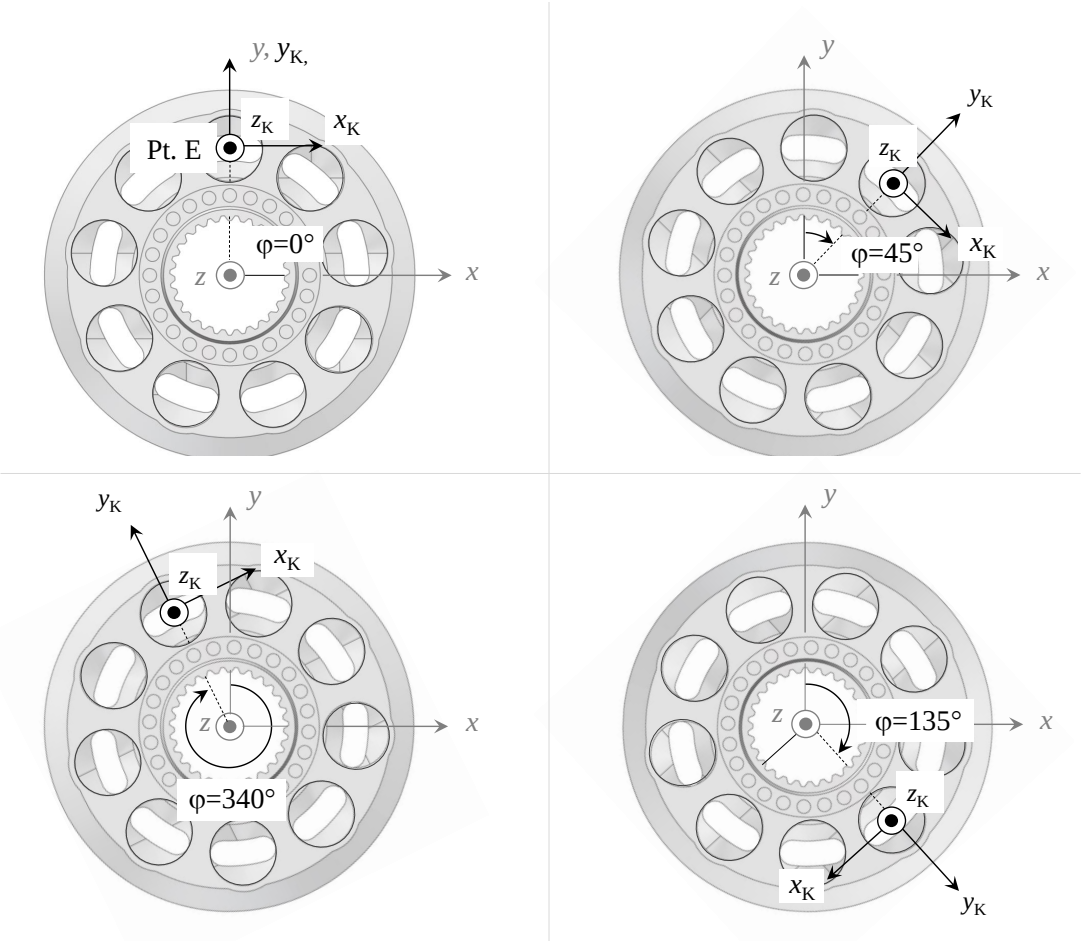

Figure 3.5. $x_K - y_K - z_K$ coordinate system.

Now, with the $x_K - y_K - z_K$ coordinate system in hand, the $\hat{x} - \hat{y} - \hat{z}$ system can be easily defined. The $\hat{y}$-axis is identical to the z_K axis, including its zero point. The $\hat{x}$-axis, on the other hand, has its zero point where the positive x_K-axis intersects the cylinder bore (or inner bushing) wall. When viewed with the x_K-axis pointing to the right, as in image (c) of Fig. 3.3, the positive $\hat{x}$-axis moves counterclockwise around the circumference of the interface. Finally, the $\hat{z}$-axis has its zero point on the piston surface, and moves radially outwards, along a line perpendicular to that surface.

3.4 Reynolds Equation: Obtaining the Pressure Field in the Fluid Film

Both, the Reynolds and the energy equation employed in FSTI, are written within the frame of the $\hat{x} - \hat{y} - \hat{z}$ coordinate system described. The Reynolds equation states the relationship between fluid pressure, density, viscosity, and velocity— as it exists in the viscous flow of a thin film; the general form of the relationship between these parameters for a Newtonian fluid (not necessarily moving within a thin film) is given by the Navier-Stokes equation [10]:

$$\frac{\partial \rho \vec{V}}{\partial t} + \vec{\nabla} \cdot \rho \vec{V} \vec{V} - \vec{\nabla} \cdot (\mu \vec{\nabla} \vec{V}) = -\vec{\nabla} p \tag{3.5}$$

Pelosi [10] tailored this equation to model the piston-cylinder interface by making the following simplifying assumptions:

Table 3.1. Assumptions.

1.	Steady state $\left(\frac{\partial(\rho \vec{V})}{\partial t} = 0\right)$
2.	Inertia effects « viscous effects
3.	Pressure is not a function of $\hat{z}$
4.	Velocity gradients in the $\hat{x}$- and $\hat{y}$-directions are orders of magnitude less than those in the $\hat{z}$-direction
5.	Velocity in the z-direction is negligible
6.	Stretch effects in the piston/bore materials are negligible

Taking assumptions 1.-4. into account, EQ. 3.5 becomes:

$$\vec{\nabla} p = \vec{\nabla} \cdot (\mu \vec{\nabla} \vec{V}) \tag{3.6}$$

where $\vec{V}$ is the three-dimensional fluid velocity vector:

$$\vec{V} = \begin{pmatrix} u \\ v \\ w \end{pmatrix} \tag{3.7}$$

The Reynolds equation is constructed by solving this simplified Navier Stokes equation for the velocity components u and v (w is negligible— assumption 5., Table 3.1), inserting the results into the continuity equation, and integrating [20]. The continuity equation is shown below— it states the conservation of mass within a fluid:

$$\int_0^h \left(\frac{\partial \rho}{\partial t} + \frac{\partial (\rho u)}{\partial x} + \frac{\partial (\rho v)}{\partial y} + \frac{\partial (\rho w)}{\partial z} \right) \partial z = 0 \tag{3.8}$$

Combining the continuity equation with the Navier-Stokes equation in the aforesaid manner yields a Reynolds equation of the following form [10], [14]:

$$\begin{aligned} 0 = &\underbrace{-\nabla \cdot \left(\frac{\rho h^3}{12\mu} \nabla p \right)}_{1.} + \underbrace{\frac{1}{2} \left(\frac{\partial (\rho h (\hat{u}_\mathrm{B} + \hat{u}_\mathrm{K}))}{\partial \hat{x}} + \frac{\partial (\rho h (\hat{v}_\mathrm{B} + \hat{v}_\mathrm{K}))}{\partial \hat{y}} \right)}_{2.} + \underbrace{\rho (\hat{w}_\mathrm{B} - \hat{w}_\mathrm{K})}_{3.} \\ &\underbrace{- \left(\rho \hat{u}_\mathrm{B} \frac{\partial h_\mathrm{B}}{\partial \hat{x}} + \rho \hat{v}_\mathrm{B} \frac{\partial h_\mathrm{B}}{\partial \hat{y}} \right) + \left(\rho \hat{u}_\mathrm{K} \frac{\partial h_\mathrm{K}}{\partial \hat{x}} + \rho \hat{v}_\mathrm{K} \frac{\partial h_\mathrm{K}}{\partial \hat{y}} \right)}_{4.} + \underbrace{h \frac{\partial \rho}{\partial t}}_{5.} \end{aligned} \tag{3.9}$$

Here, $h = h(\hat{x}, \hat{y})$ is the film thickness at a point $(\hat{x}, \hat{y})$ in the fluid grid, measured along the $\hat{z}$-axis. $h_\mathrm{B} = h_\mathrm{B}(\hat{x}, \hat{y})$ is the $\hat{z}_\mathrm{S}$-coordinate of the bore surface at a point $(\hat{x}, \hat{y})$— where the $\hat{z}_\mathrm{S}$-axis is identical to the $\hat{z}$-axis, except that its zero point is located on a reference plane that lies between the piston and bore surfaces (see Fig. 3.6). Similarly, h_K is the $\hat{z}_\mathrm{S}$-coordinate of the *piston* surface at a point $(\hat{x}, \hat{y})$. $\hat{u}_\mathrm{B}$, $\hat{v}_\mathrm{B}$, and $\hat{w}_\mathrm{B}$ are the bore surface's $\hat{x}$, $\hat{y}$, and $\hat{z}$ velocity components, respectively, and $\hat{u}_\mathrm{K}$, $\hat{v}_\mathrm{K}$, and $\hat{w}_\mathrm{K}$ are the piston surface's $\hat{x}$, $\hat{y}$, and $\hat{z}$ velocity components, respectively.

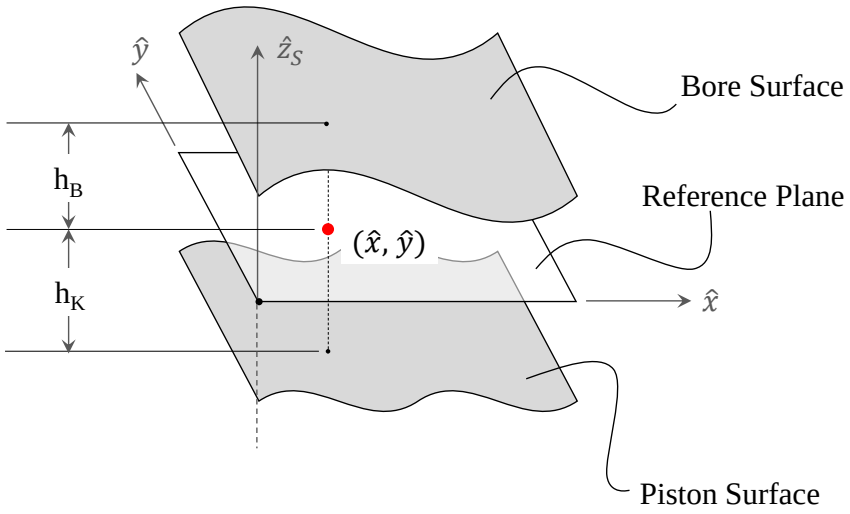

Figure 3.6. h_B and h_K (image based on[15]).

Term 1 in Eq. 3.9 is the poiseuille term of the Reynolds equation, representing the flow due to the pressure gradients within the fluid film; term 2. is the couette term, representing the flow due to viscous shear [20]. Term 3 is the normal squeeze term, which describes the pressure buildup resulting from the piston and bore surfaces moving towards each other (along the $\hat{z}$-axis). Term 4. also describes a form of squeeze motion: translational squeeze. This term expresses how pressure builds due to changes in film thickness when the surfaces bordering the fluid film are non-flat and/or non-parallel, and are moving past each other in the $\hat{x}$- and/or $\hat{y}$- directions. Finally, term 5. constitutes the effect of the fluid's expansion or contraction as a result of changes in density.

The equation can be greatly simplified by considering three important points. The first is that term 2. can be expanded out into three terms: a density wedge term, a stretch term, and a physical wedge term, respectively accounting for changes in the density, in the velocity of the surfaces bordering the fluid, and in the fluid film height [20].

That is:

$$\underbrace{\frac{1}{2}\left(\frac{\partial(\rho h(\hat{u}_{\mathrm{B}}+\hat{u}_{\mathrm{K}}))}{\partial\hat{x}}+\frac{\partial(\rho h(\hat{v}_{\mathrm{B}}+\hat{v}_{\mathrm{K}}))}{\partial\hat{y}}\right)}_{2.}=\underbrace{\left(\frac{h(\hat{u}_{\mathrm{B}}+\hat{u}_{\mathrm{K}})}{2}\frac{\partial\rho}{\partial\hat{x}}+\frac{h(\hat{v}_{\mathrm{B}}+\hat{v}_{\mathrm{K}})}{2}\frac{\partial\rho}{\partial\hat{y}}\right)}_{2.\ \mathrm{a})}$$
$$+\underbrace{\left(\frac{\rho h}{2}\left(\frac{\partial(\hat{u}_{\mathrm{B}}+\hat{u}_{\mathrm{K}})}{\partial\hat{x}}+\frac{\partial(\hat{v}_{\mathrm{B}}+\hat{v}_{\mathrm{K}})}{\partial\hat{y}}\right)\right)}_{2.\ \mathrm{b})}+\underbrace{\left(\frac{\rho(\hat{u}_{\mathrm{B}}+\hat{u}_{\mathrm{K}})}{2}\frac{\partial h}{\partial\hat{x}}+\frac{\rho(\hat{v}_{\mathrm{B}}+\hat{v}_{\mathrm{K}})}{2}\frac{\partial h}{\partial\hat{y}}\right)}_{2.\ \mathrm{c})} \tag{3.10}$$

2.a) is the density wedge term, 2.b) the stretch term, and 2.c) the physical wedge term. The physical wedge term is a critical contributor to hydrodynamic pressure buildup. The stretch term, on the other hand, is negligible when modeling the piston-cylinder interface (assumption 6., Table3.1). Omitting this stretch term, term 2. becomes:

$$\frac{1}{2}\left(\frac{\partial(\rho h(\hat{u}_{\mathrm{B}}+\hat{u}_{\mathrm{K}}))}{\partial\hat{x}}+\frac{\partial(\rho h(\hat{v}_{\mathrm{B}}+\hat{v}_{\mathrm{K}}))}{\partial\hat{y}}\right)=\frac{(\hat{u}_{\mathrm{B}}+\hat{u}_{\mathrm{K}}+\hat{v}_{\mathrm{B}}+\hat{v}_{\mathrm{K}})}{2}\nabla(\rho h) \tag{3.11}$$

The second important point concerns the squeeze motion of the fluid film. Traditionally, the translational and normal squeeze are calculated separately, in the form given by terms 3. and 4. of EQ. 3.9 [15]. Pelosi (see [10]) obtains the translational squeeze in his model from the piston kinematics, from the piston's eccentricity, inclination, and surface profile, and from the solid body thermal deformations at the interface; he obtains normal squeeze from the piston's micro motion. However, this approach fails to capture the squeeze that results from changes in the fluid-pressure-induced elastic deformations of the solid bodies surrounding the interface [14], [15]. To include this effect, Shang [15] proposed to describe the squeeze effect as the difference in gap height between the current and previous time steps.

$$\text{Squeeze term}: \quad \rho\left(\frac{h_{\mathrm{c}}-h_{\mathrm{p}}}{t_{\mathrm{c}}-t_{\mathrm{p}}}\right) \tag{3.12}$$

h_c is the current film thickness at a particular point in the fluid grid, h_p is the film thickness at the same point in the fluid grid at the previous time step, and t_c and t_p are the current and previous time steps, respectively. This expression can replace terms 3. and 4. of EQ. 3.9, yielding a simpler, yet more realistic model of squeeze motion in the fluid film.

The third important point to consider is that the piston-cylinder interface module of FSTI considers the bore to be stationary, i.e. $\hat{u}_B = \hat{v}_B = \hat{w}_B = 0$. Implementing the three changes described, the Reynolds equation becomes [15]:

$$0 = \underbrace{-\nabla \cdot \left(\frac{\rho h^3}{12\mu}\nabla p\right)}_{1.} + \underbrace{\frac{(\hat{u}_K + \hat{v}_K)\nabla(\rho h)}{2}}_{2.} + \underbrace{h\frac{\partial \rho}{\partial t}}_{5.} - \underbrace{\rho\left(\frac{h_c - h_p}{t_c - t_p}\right)}_{7.} \tag{3.13}$$

This is the Reynolds equation utilized by the piston-cylinder interface module of FSTI—implemented in finite volume form. Only when the film thickness falls below $h_{min} = 0.1\mu$m, and the fluid film's behavior can no longer be resolved with a grid size resulting in a reasonable computational time, h is saturated to h_{min}, and a modified version of EQ. 3.13 is used: it simulates a parallel gap in the regions covered by such low film thickness [14]. In either case, because of the assumptions that pressure is not a function of $\hat{z}$, and that velocity in the $\hat{z}$-direction is negligible (see Table 3.1), the fluid film modeled by the Reynolds equation can be— and is— discretized into a *2-D* Cartesian grid [10]. The fluid properties required to solve the equation for the fluid film pressure field (viscosity, density, and bulk modulus) are computed by FSTI as a function of temperature and pressure using an interpolation created from measurement data. In the case of water as a hydraulic fluid, a polynomial interpolation based on NIST data [21].

3.5 The Film Thickness, h

The film thickness of the lubricating interface, h, that appears in the Reynolds equation is calculated as follows [10], [22]:

$$h(z_K, \phi_K) = \sqrt{(R_Z cos(\phi_K) - x_m(z_K))^2 + (R_Z sin(\phi_K) - y_m(z_K))^2} - R_K + \triangle h, \tag{3.14}$$

$$\text{where:} \quad x_m(z_K) = \frac{(e_3 - e_1)}{l_F} z_K + e_1, \quad \text{and} \quad y_m(z_K) = \frac{(e_4 - e_2)}{l_F} z_K + e_1 \tag{3.15}$$

The inner cylinder block bore/bushing radius, R_Z, and the angle ϕ_K, are illustrated in Fig. 3.3. $\triangle h$ is the change in film thickness from elastic deformation of the solid bodies due to pressure and temperature effects [10]. The eccentricities e_1,e_2,e_3, and e_4, are shown in

Fig. 3.7— they describe the deviation of the piston's center axis from the center axis of the cylinder block bore/bushing at either end of the guide length; e_1 and e_3 are the deviations along the x_K-axis, and e_2 and e_4 are the deviations along the y_K-axis [22]. The eccentricities e_1 and e_2 are measured at the end of the guide length adjacent to the DC (Section A-A), while e_3 and e_4 are measured at the end of the guide length nearest the swash plate (Section B-B).

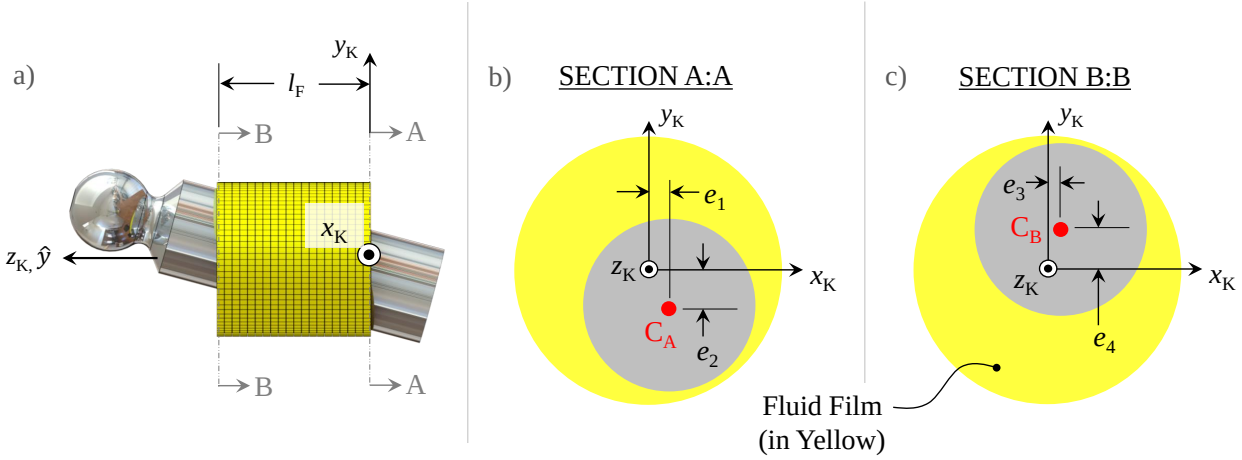

Figure 3.7. Eccentricities e_1, e_2, e_3, and e_4. Image based on [22].

3.6 Energy Equation: Obtaining the Temperature Field in the Fluid Film

The temperature field of the piston-cylinder interface fluid film is obtained by solving the energy equation (below); it states the relationship between H— the enthalpy of a given control volume at the current time step— and H_0, the enthalpy of that same control volume at the previous time step [23]:

$$H = H_0 + \triangle H, \tag{3.16}$$

$$\text{where : } \begin{cases} H = (h_e)(m) \\ H_0 = (h_{e_0})(m_0) \\ \triangle H = \left(\underbrace{\left(\frac{\partial h_e}{\partial t}\right)(m_0) + (h_{e,in})(\dot{m}_{in}) - (h_{e,out})(\dot{m}_{out})}_{1.} + \underbrace{\mu \Phi_D dV}_{2.} + \underbrace{\sum_i \lambda_i (\nabla T)_i A_i}_{3.} \right) dt \end{cases} \tag{3.17}$$

As can be seen from the equations above, H is the product of the mass m of a given control volume, and the specific enthalpy, h_{e}, defined as [23]:

$$h_{\mathrm{e}} = (h_{\mathrm{e}_0})(T_0) + \int_{T_0}^{T} (c_{\mathrm{p}0}) dT + \int_{p_0}^{p} \left(\frac{\partial v}{\partial T}\right) dp + \int_{\mathrm{p}0}^{p} v dp \tag{3.18}$$

The change in enthalpy from one time step to the next, $\triangle H$, consists of three terms: the first describes how the enthalpy changes due to mass flow into and out of a control volume, the second captures the influence of energy dissipation due to viscous flow, and the third is the enthalpy change caused by conduction at the faces of the control volume [23]. In Term 2., the source term Φ_D representing the heat produced through viscous dissipation is calculated as [10]:

$$\Phi_{\mathrm{D}} = \left(\frac{\partial \hat{u}}{\partial \hat{z}}\right)^2 + \left(\frac{\partial \hat{v}}{\partial \hat{z}}\right)^2 + \left(\frac{\partial \hat{w}}{\partial \hat{z}}\right)^2 \tag{3.19}$$

The assumption that the fluid velocity in the $\hat{z}$-direction is zero (made for the Reynolds equation earlier) is also upheld for the energy equation [23]; however, the change in temperature along the $\hat{z}$-direction is non-negligible. Hence, in contrast to the Reynolds equation, the energy equation is solved over a structured 3-D grid. Fig. 3.8 gives a magnified view of one of the control volumes that constitute this grid; the pressure and temperature of such a volume are taken to be the values at its centroid, P. From the energy equation described, the temperature of each control volume emerges as a function of the temperatures of its neighbors, and a source term, "s." The source term is a function of the fluid pressure of the control volume at the current and previous time steps, its temperature at the previous time step, and the pressure in the neighboring control volumes [23]:

$$\begin{cases} T_{\mathrm{P}} = f(T_{\mathrm{E}}, T_{\mathrm{N}}, T_{\mathrm{W}}, T_{\mathrm{S}}, T_{\mathrm{T}}, T_{\mathrm{B}}, s) \\ s = f(p_{\mathrm{P}_0}, p_{\mathrm{P}}, T_{\mathrm{P}_0}, p_{\mathrm{E}}, p_{\mathrm{N}}, p_{\mathrm{W}}, p_{\mathrm{S}}, p_{\mathrm{T}}, p_{\mathrm{B}}) \end{cases} \tag{3.20}$$

This approach to computing the fluid film temperature field in the piston-cylinder interface, developed by Shang [23], accounts for temperature changes arising from conduction, convection, heat generation due to compression losses resulting from the fluid pressure gradient, as

well as the effect of energy dissipation due to viscous friction. The solid body temperatures of the pistons, bushings (if present), and cylinder block constitute the boundary conditions for this thermal solver.

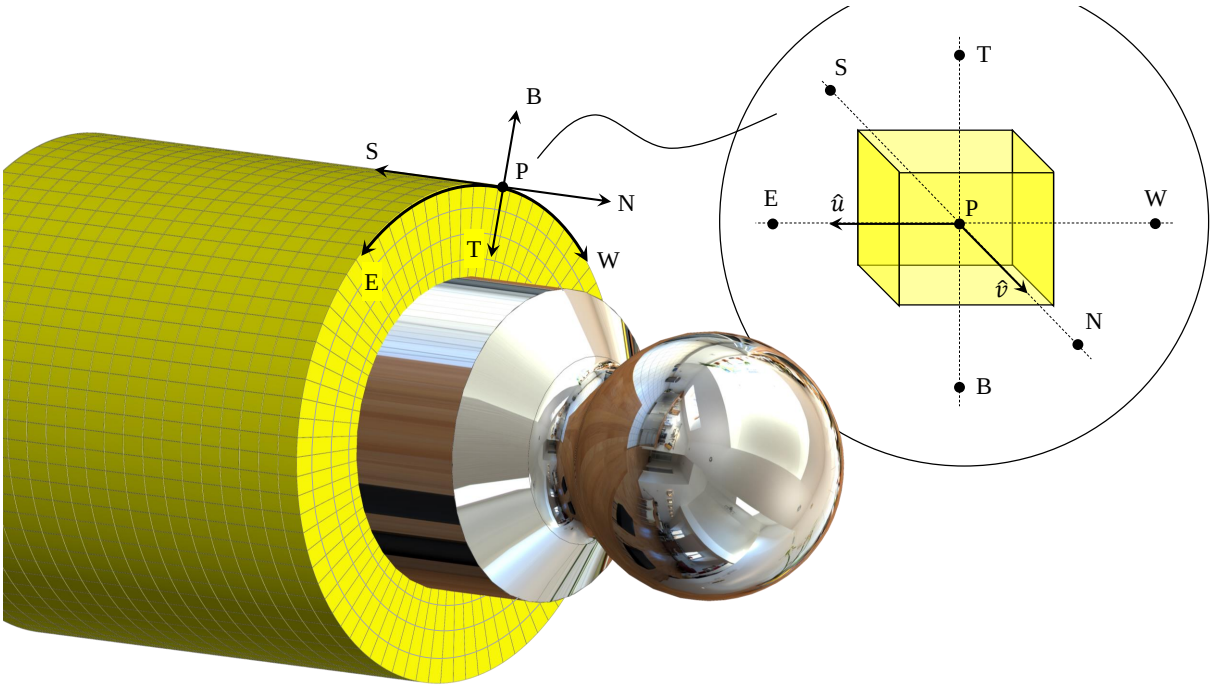

Figure 3.8. Fluid grid for the energy equation (image based on [10], [23]).

3.7 Solid Contact

If the pressure distribution within the fluid film between them does not balance the piston side load, the piston and cylinder bore (or bushing) surfaces come into contact. When the film thickness falls below $h_{\min}$, the piston-cylinder interface module of FSTI assumes the possibility of solid, metal-to-metal contact: the model imposes a stress, σ, on all elements of the 2-D Cartesian Reynolds equation computational grid with less than this minimum film thickness [14]. The stress imposed on each element is linearly proportional to the depth

of penetration of the piston surface beyond the $h = h_{\min}$ mark at the location of that element [14]:

$$\sigma(\mathrm{i}) = \begin{cases} C(h_{\min} - h(\mathrm{i})) & h(\mathrm{i}) \leq h_{\min} \\ 0 & h(\mathrm{i}) > h_{\min} \end{cases} \tag{3.21}$$

C is a constant, defined based on the piston radius, and the equivalent Young's modulus E' pertaining to the two surfaces in contact [14]:

$$C = \frac{2E}{R_{\mathrm{K}}}, \text{ where} : E = \frac{1}{\left(\frac{1-{v_{\mathrm{K}}}^2}{E_{\mathrm{K}}} + \frac{1-{v_{\mathrm{Z}}}^2}{E_{\mathrm{Z}}}\right)} \tag{3.22}$$

The piston-cylinder module computes the forces resulting from the imposed stress distribution at two control points: Pt. C_{A} and C_{B}, located on the piston's central axis at the DC and case ends of the interface, respectively— that is, at the end of the interface abutting the DC, and at the end of the interface open to the pump case, respectively (see Fig. 3.9) [14]. These are the same control points from which the eccentricity of the piston's center axis is calculated by the model. Let the x_{K}- and y_{K}- components of the contact stress resultant force at C_{A} be denoted F_{CK1} and F_{CK2}, and the x_{K}- and y_{K}- components of the force at C_{B}, F_{CK3} and F_{CK4} [14]:

$$\begin{cases} F_{CK1} = \int_0^{l_{\mathrm{F}}} \int_0^{2\pi} \sigma \, cos(\phi_{\mathrm{K}}) \left(1 - \frac{z_{\mathrm{K}}}{l_{\mathrm{F}}}\right) d\phi_{\mathrm{K}} dz_{\mathrm{K}} \\ F_{CK2} = \int_0^{l_{\mathrm{F}}} \int_0^{2\pi} \sigma \, sin(\phi_{\mathrm{K}}) \left(1 - \frac{z_{\mathrm{K}}}{l_{\mathrm{F}}}\right) d\phi_{\mathrm{K}} dz_{\mathrm{K}} \\ F_{CK3} = \int_0^{l_{\mathrm{F}}} \int_0^{2\pi} \sigma \, cos(\phi_{\mathrm{K}}) \frac{z_{\mathrm{K}}}{l_{\mathrm{F}}} d\phi_{\mathrm{K}} dz_{\mathrm{K}} \\ F_{CK4} = \int_0^{l_{\mathrm{F}}} \int_0^{2\pi} \sigma \, sin(\phi_{\mathrm{K}}) \frac{z_{\mathrm{K}}}{l_{\mathrm{F}}} d\phi_{\mathrm{K}} dz_{\mathrm{K}} \end{cases} \tag{3.23}$$

The two forces described by these components, one at each of the two control points, are "correction forces" that signal the possibility of metal-to-metal contact between the piston and bore in regions of minimum film thickness [14]. The force applied at the control point $\mathrm{C_A}$ (see Fig. 3.9) is the "DC end correction force", and the force applied the control point $\mathrm{C_B}$ is the "case end correction force". The larger they are, the more severe the predicted

solid contact is. Both forces are included in the force balance loop that constitutes step 7. of the piston-cylinder module in Fig. 3.2, thus contributing to the simulated micro motion of the piston within its bore.

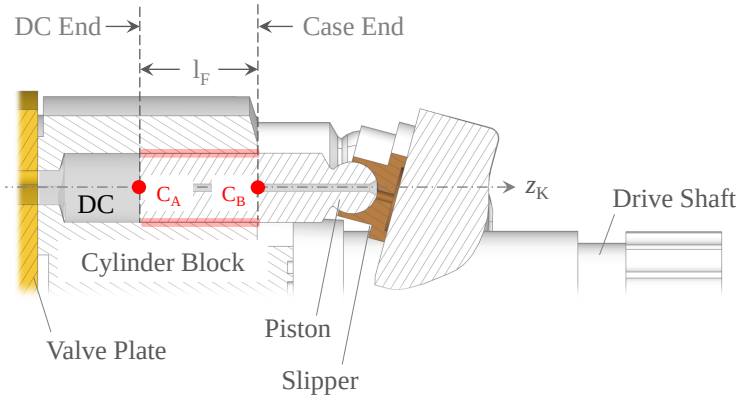

Figure 3.9. Control Points.

Because a computational grid fine enough to capture the exact behavior of the fluid film within regions of minimum film thickness ($h < h_{\min}$) is too computationally expensive, there may be load support within these regions that the parallel gap assumption made there does not capture [14]. However, considering water's low viscosity, it is unlikely that enough load support is generated within these regions to prevent contact. Thus, while the computation of large correction forces does not guarantee failure of the interface in a real pump, it does indicate that severe wear and/or component failure are *likely* to occur. The objective in design studies conducted using FSTI is therefore to find interface designs that eliminate these correction forces, i.e. designs guaranteed to prevent contact.

3.8 Losses at the Piston-Cylinder Interface

FSTI calculates leakage through the piston-cylinder interface as the velocity $\hat{v}$ integrated over the film thickness, and over the circumference of the single ring of fluid elements that is closest to midway between the DC and case ends of the interface.

More succinctly [10]:

$$Q_{\mathrm{SK}}(\varphi) = \int_0^{2\pi R_{\mathrm{K}}} \int_0^{h} \hat{v}(\varphi) d\hat{z} d\hat{x} \tag{3.24}$$

The leakage values presented for design studies in later chapters are time averages of the leakage over a full shaft revolution. Similarly, power loss is obtained as a time average of the integral of the mechanical dissipation $\mu\Phi_D$ over space (the entire fluid film). Lastly, the torque loss is taken to be a time average of the difference between the total energy dissipation and the energy dissipation due to leakage only, divided by the pump speed.

3.9 Friction Force

The friction force, F_{T}, is computed as the integral of the shear stress τ [10]:

$$F_{\mathrm{T}}(\varphi) = \int_A \tau(\varphi) dA, \tag{3.25}$$

where the shear stress of the fluid at the cylinder bore/bushing and piston surfaces is given by [10]:

$$\text{Cylinder shear stress: } \begin{cases} \tau_{\mathrm{F}\hat{x}} = \mu \dfrac{\partial \hat{u}}{\partial \hat{z}}\Big|_{\hat{z}=0} \\ \tau_{\mathrm{F}\hat{y}} = \mu \dfrac{\partial \hat{v}}{\partial \hat{z}}\Big|_{\hat{z}=0} \end{cases} \qquad \text{Piston shear stress: } \begin{cases} \tau_{\mathrm{F}\hat{x}} = \mu \dfrac{\partial \hat{u}}{\partial \hat{z}}\Big|_{\hat{z}=h} \\ \tau_{\mathrm{F}\hat{y}} = \mu \dfrac{\partial \hat{v}}{\partial \hat{z}}\Big|_{\hat{z}=h} \end{cases} \tag{3.26}$$

4. CONTRIBUTIONS OF HYDROSTATIC VS. HYDRODYNAMIC PRESSURE TO LOAD SUPPORT

A version of this chapter has been previously published in [1].

While the previous chapters lay out the premise of this work, arising from the viscosity of the hydraulic fluid under study, and the geometry of axial piston machines, and describe the interface model that is the key instrument of its methodology, the choice of investigating the piston-cylinder interface, rather than the slipper-swash plate or cylinder block-valve plate interfaces, remains to be addressed in full. To this end, a comparison of the three main APMSPD lubricating interfaces in terms of the contribution made by hydrostatic, versus hydrodynamic pressure to load support is in order. By separating the pressure fields of each of the three interfaces into these two components, and calculating how each of these components contributes to the load-carrying capacity of the fluid film, it can be seen what sets the piston-cylinder interface apart.

4.1 Methodology for Calculating the Hydrostatic and Hydrodynamic Components of APMSPD Interface Pressure Fields

Achieving such a separation requires a closer examination of the definition of these pressure components. Hydrostatic pressure is the pressure exerted by a stationary fluid— however, the hydrostatic component of a lubricating interface's fluid pressure field may be defined as either [1]:

A. The pressure field that would result if hydrodynamic pressure did not exist,

B. The component of the total fluid pressure field that is not generated by the movement of the lubricating fluid relative to the surfaces that form the interface.

The key difference between these two definitions arises from the fact that the hydrodynamic and hydrostatic components of fluid pressure interact [1]. Each component has an impact on the film thickness, which, in turn, affects the distribution of hydrodynamic pressure, and the generation of hydrodynamic pressure. If one component is calculated by omitting the

other, then the interaction between them is omitted. As will be seen shortly, that interaction is especially pronounced in the piston-cylinder interface. Definition B will therefore be pursued; this distinguishes the present work from the calculation of the hydrostatic pressure component in the cylinder-block valve plate interface presented by Zloto [24], the calculation of the hydrostatic pressure component in the slipper-swash plate interface presented by Koç and Hooke [25], and the dissection of the pressure fields in the lateral gaps of external gear machines into their hydrostatic and hydrodynamic components by Dhar and Vacca [26].

The methodology developed for this consists of three stages. For a given APMSPD, at a given operating condition, the first step is to simulate the behavior of all three lubricating interfaces over the course of one drive shaft revolution of the pump using FSTI [1]. This entails the use of not only the piston-cylinder interface module described in the previous chapter, but also the slipper-swash plate interface and cylinder block-valve plate modules developed by Schenk [27], [28] and Zecchi [11], [29]. The structure of these other two modules is similar to that of the piston-cylinder interface; for the purpose of this chapter, it is sufficient to know that like the piston-cylinder interface module, both output fluid pressure, fluid film thickness, and the dynamic viscosity of the fluid— and that, like the piston-cylinder interface module, in calculating these parameters, both take into account the temperature of the fluid film, as well as the elastic deformations due to thermal and pressure loading of the solid bodies that border each interface. The general form of the Reynolds equation employed by the interface model to solve for the pressure field of a lubricating interface at each simulated shaft angle is [28][1]:

$$\nabla \cdot \left(-\frac{\rho h^3}{12\mu} \nabla p \right) + \nabla \cdot \left(\frac{\rho h}{2} \left(\boldsymbol{V_a} + \boldsymbol{V_b} \right) \right) + \rho \boldsymbol{V_b} \cdot \nabla h_b - \rho \boldsymbol{V_a} \cdot \nabla h_a + \rho \frac{\partial h}{\partial t} = 0 \tag{4.1}$$

The pressure field output by the model at a given shaft angle consists of *both*, the hydrostatic and hydrodynamic components of pressure; let it be denoted p_t [1]. Let the fluid film thickness and dynamic viscosity corresponding to this field, which are also output by the model, respectively be denoted h_t and μ_t. The second stage of the developed methodology

[1]The expansion term included in the piston-cylinder interface module (term 5 from Eq. 3.9) is omitted here in order to allow for a fair comparison to the other two interfaces, whose modules neglect this term [11], [28].

calculates p_s, the hydrostatic component of the interface fluid pressure field, by solving the Reynolds equation with only its hydrostatic term, i.e. the Poiseuille term, using a finite volume scheme. In order to take into account the previously described interaction between hydrostatic and hydrodynamic pressure, when solving for p_s, the film thickness and viscosity are treated as constants, and are set to the values output by FSTI (h_t and μ_t). That is, their values correspond to the total pressure field [1]:

$$\nabla \cdot \left(\frac{\rho_t {h_t}^3}{\mu_t} \nabla p_s \right) = 0 \tag{4.2}$$

Integrating this over a control volume, and applying the divergence theorem [10]:

$$\int_A (\Gamma \nabla p_s) \cdot d\boldsymbol{A} = 0, \text{where } \Gamma = \rho_t {h_t}^3 / \mu_t \tag{4.3}$$

Discretizing the equation according to the grid structures and control volume stencil in Fig. 4.1, in the same manner employed by [10]:

$$a_e p_E + a_w p_W + a_n p_N + a_s p_S - a_P p_P = 0 \tag{4.4}$$

$$\text{where : } \begin{cases} a_e = \Gamma_e \frac{\Delta Y}{\delta X_e} \\ a_w = \Gamma_w \frac{\Delta Y}{\delta X_w} \\ a_n = \Gamma_n \frac{\Delta X_n}{\delta Y_n} \\ a_s = \Gamma_s \frac{\Delta X_s}{\delta Y_s} \\ a_P = \Gamma_e \frac{\Delta Y}{\delta X_e} + \Gamma_w \frac{\Delta Y}{\delta X_w} + \Gamma_n \frac{\Delta X_n}{\delta Y_n} + \Gamma_s \frac{\Delta X_s}{\delta Y_s} \end{cases} \tag{4.5}$$

Setting up this equation for each element in the fluid grid of an interface, appropriately modified at the boundaries (see [1] for details), generates a system of equations that can then be solved for the hydrostatic component of the fluid pressure field in that interface. With p_s known, the third stage of the developed methodology calculates the hydrodynamic component of the fluid pressure field, p_d, as the following difference [1]:

$$p_d = p_t - p_s \tag{4.6}$$

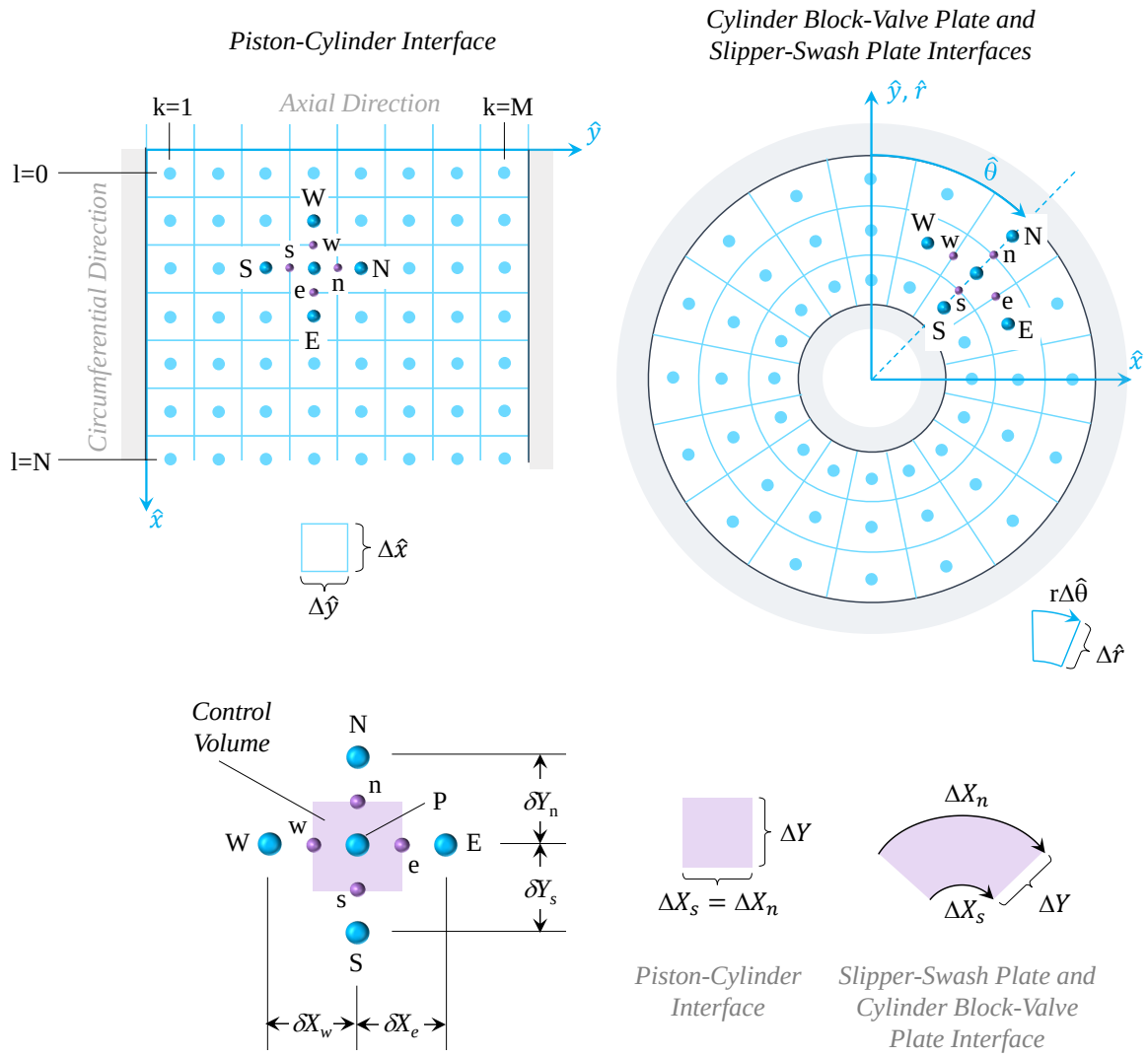

Figure 4.1. Fluid grid structure, as described in [10], [11], [30], for discretizing the Reynolds equation (top), and stencil for control volume (bottom) [1].

4.2 Calculating the Loads on the Piston, Slipper, and Block

Having separated the pressure field into its hydrostatic and hydrodynamic components, it is possible to calculate their contribution to load support at the interface in which they act. In order to make the interfaces comparable, the load forces and moments acting on the piston, slipper, and block, as well as the forces and moments due to fluid pressure in the lubricating interfaces that counter these loads, will be calculated in the coordinate systems shown in Fig. 4.2: the $x_{\mathrm{K,GC}} - y_{\mathrm{K,GC}} - z_{\mathrm{K,GC}}$ system for the piston, the $x_{\mathrm{G,GC}} - y_{\mathrm{G,GC}} - z_{\mathrm{G,GC}}$ system

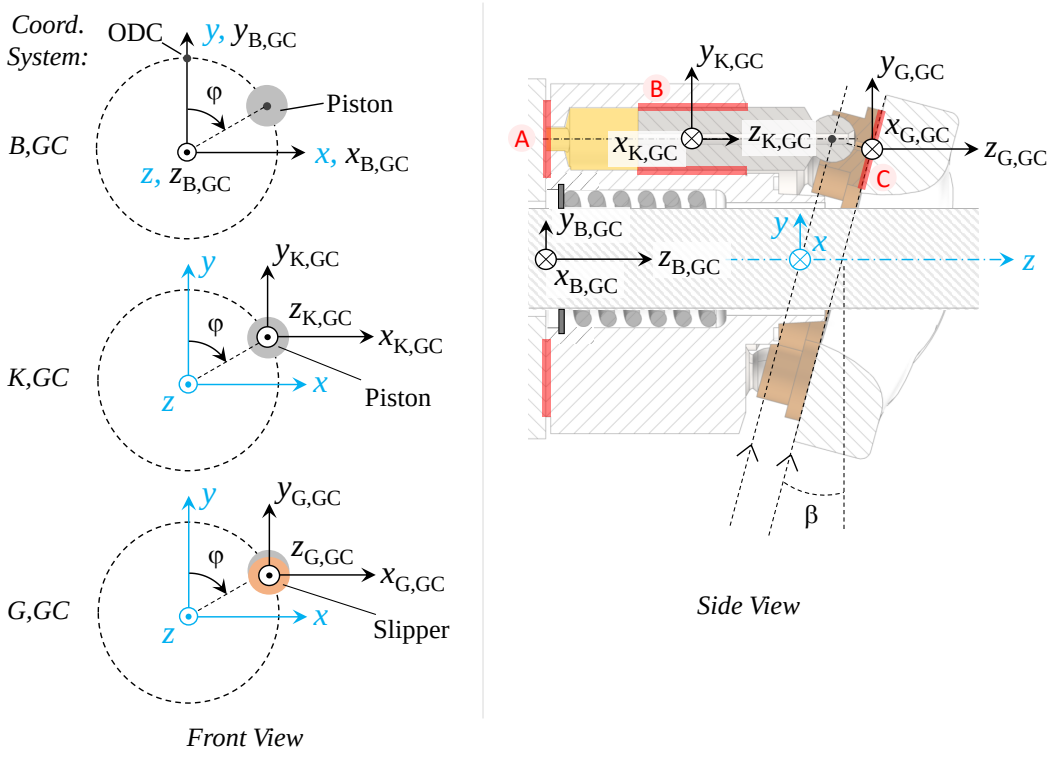

Figure 4.2. Coordinate systems for expressing the forces on the piston, slipper, and block [1].

for the slipper, and the $x_{B,GC} - y_{B,GC} - z_{B,GC}$ system for the block [1]. All three have the same orientation as the global pump coordinate system for FSTI described in the previous chapter, with their point of origin located at the center of the piston-cylinder, slipper-swash plate, and cylinder block-valve plate interfaces, respectively.

A brief overview of the load forces and moments acting on the pistons, slippers, and cylinder block of an APMSPD in these coordinate systems will now be provided (see [1]). It should be noted that while FSTI does not directly output the load in these coordinate systems, the load is calculated based on the components of, and information related to, the load that

is output by FSTI. The load on the piston can be expressed in the $x_{\mathrm{K,GC}} - y_{\mathrm{K,GC}} - z_{\mathrm{K,GC}}$ coordinate system as [1], [4], [10]:

$$\begin{cases} F_{\mathrm{l,K,xGC}} = F_{\omega\mathrm{K,xz}} + F_{\mathrm{TG,xz}} cos(\beta) \\ F_{\mathrm{l,K,yGC}} = F_{\mathrm{SKy}} + F_{\omega\mathrm{K,yz}} + F_{\mathrm{TG,yz}} cos(\beta) \\ M_{\mathrm{l,K,xGC}} = -(F_{\mathrm{SKy}})(l_1) - (F_{\omega\mathrm{K,yz}})(l_2) - F_{\mathrm{TG,yz}}(cos(\beta)(l_3) + sin(\beta)(l_4)) \\ M_{\mathrm{l,K,yGC}} = (F_{\omega\mathrm{K,xz}})(l_2) + (F_{\mathrm{TG,xz}})(cos(\beta) l_3) \end{cases} \tag{4.7}$$

$$\text{where} : \begin{cases} F_{\omega\mathrm{K,xz}} = F_{\omega\mathrm{K}} sin(\varphi) \\ F_{\omega\mathrm{K,yz}} = F_{\omega\mathrm{K}} cos(\varphi) \\ F_{\mathrm{TG,xz}} = -F_{\mathrm{TG}} cos(\varphi) \\ F_{\mathrm{TG,yz}} = F_{\mathrm{TG}} sin(\varphi) \\ F_{\mathrm{TG}} = \mu\omega R_{\mathrm{b}} / h_{\mathrm{G}} \left[\pi/4 \left({d_{\mathrm{outG}}}^2 - {d_{\mathrm{inG}}}^2 \right) \right] \end{cases} \tag{4.8}$$

The forces that generate this load have already been discussed in Ch. 2, and the moment arms, $l_1 - l_4$, are shown in Fig. 4.3 (a). Next, the load on the slipper can be expressed in the $x_{\mathrm{G,GC}} - y_{\mathrm{G,GC}} - z_{\mathrm{G,GC}}$ coordinate system as [1], [30]:

$$\begin{cases} F_{\mathrm{l,G,yGC}} = F_{\mathrm{l,G,yLC}} sin(\beta) \\ F_{\mathrm{l,G,zGC}} = -F_{\mathrm{l,G,zLC}} cos(\beta) \\ M_{\mathrm{l,G,xGC}} = (F_{\omega\mathrm{G}} cos(\varphi))(-l_5 + l_6) - (F_{\mathrm{TG,yz}})(cos(\beta) l_5 + sin(\beta) l_7) + M_{\mathrm{HD,x}} \\ M_{\mathrm{l,G,yGC}} = (F_{\omega\mathrm{G}} sin(\varphi))(l_5 - l_6) + (F_{\mathrm{TG,xz}})(cos(\beta) l_5) + M_{\mathrm{HD,y}} \end{cases} \tag{4.9}$$

$$\text{where} : \begin{cases} F_{\mathrm{l,G,zLC}} = F_{\mathrm{KS}} + F_{\mathrm{CG}} + F_{\mathrm{pG}} + F_{\mathrm{HD}} \\ F_{\mathrm{KS}} = -F_{\mathrm{SK}} \\ F_{\mathrm{CG}} = \pi p_{\mathrm{C}} \left(\left({d_{\mathrm{outG}}}^2 - {d_{\mathrm{DG}}}^2 \right) - \left({d_{\mathrm{K}}}^2 - {d_{\mathrm{DG}}}^2 \right) / cos(\beta) \right) / 4 \\ F_{\mathrm{pG}} = p_{\mathrm{G}} \pi {d_{\mathrm{inG}}}^2 / 4 \\ F_{\omega\mathrm{G}} = m_{\mathrm{G}} R_{\mathrm{b}} \omega^2 \end{cases} \tag{4.10}$$

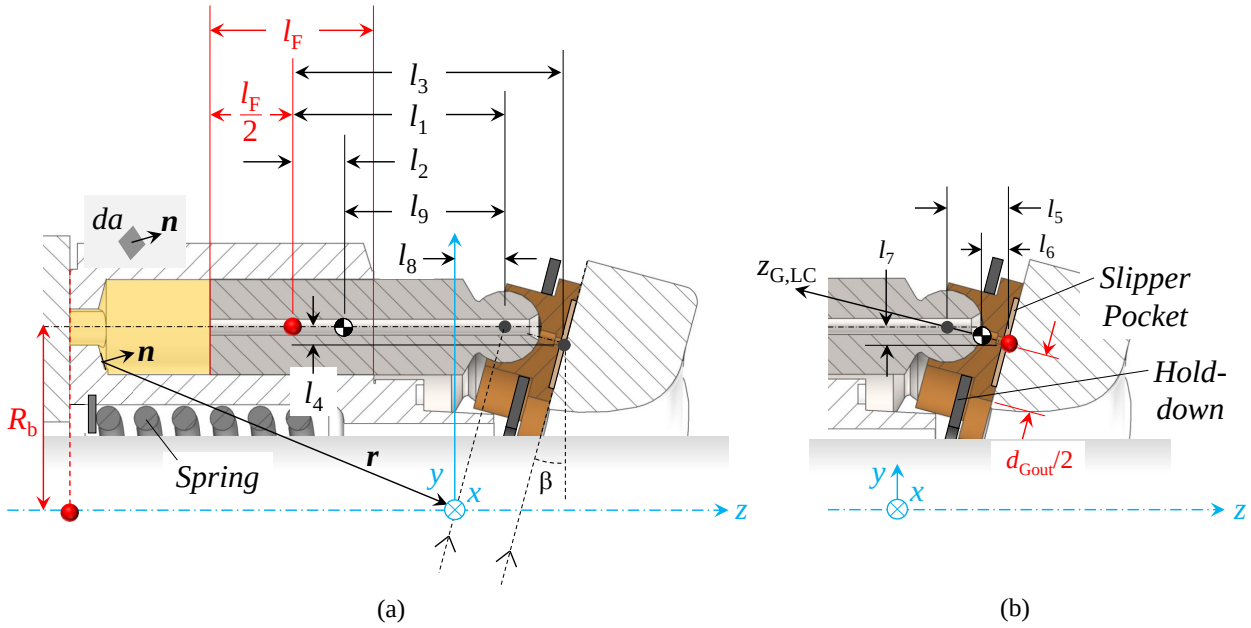

Figure 4.3. Moment arms $l_1 - l9$ (the origins of the $x_{K,GC} - y_{K,GC} - z_{K,GC}$, $x_{G,GC} - y_{G,GC} - z_{G,GC}$, and $x_{B,GC} - y_{B,GC} - z_{B,GC}$ coordinate systems are marked in red) [1].

Here, $F_{l,G,zLC}$ is the sum of the forces acting along the $z_{G,LC}$-axis shown in Fig. 4.3 (b) [1]. It consists of F_{KS}, which is simply the opposite of the force F_{SK} introduced in Ch. 2, F_{CG}, which is the force due to pressure in the pump case pushing down on the top of the slipper, F_{pG}, the force due to fluid pressure in the slipper pocket, and F_{HD}, the force of the hold-down mechanism acting on the slipper to prevent it from lifting too far off the swash plate during operation (this typically consists of a plate that is either fixed in place, or being pushed down onto the outer ledge of the slippers by a spring). Since neither F_{TG} (the force due to viscous friction in the slipper-swash plate interface) nor $F_{\omega G}$ (the force on the slipper due to the centrifugal effect) act at the center of the piston head, but are reacted at that point, both impose a moment on the slipper [30]. In addition to this, the slipper hold-down mechanism imposes the moments $M_{HD,x}$ and $M_{HD,y}$. The moment arms $l_5 - l_7$ are shown in Fig. 4.3 (b).

Finally, the load on the block can be expressed in the $x_{\mathrm{B,GC}} - y_{\mathrm{B,GC}} - z_{\mathrm{B,GC}}$ coordinate system as [1], [11]:

$$\begin{cases} F_{\mathrm{l,B,zGC}} = F_{\mathrm{S}} + F_{\mathrm{TB}} + F_{\mathrm{DB}} \\ M_{\mathrm{l,B,xGC}} = \sum_{\mathrm{i}=1}^{nK} \Big[p_{\mathrm{DC,i}} \Big(M^0_{\mathrm{DBx}} cos(\varphi_{\mathrm{i}}) + M^0_{\mathrm{DBy}} sin(\varphi_{\mathrm{i}}) \Big) \\ \qquad\qquad -(F_{\mathrm{SKy}})(l_7) - (F_{\omega\mathrm{K,yz}})(l_8) - (F_{\mathrm{TG,yz}})(l_7) \Big] \\ M_{\mathrm{l,B,yGC}} = \sum_{\mathrm{i}=1}^{nK} \Big[p_{\mathrm{DC,i}} \Big(-M^0_{\mathrm{DBx}} sin(\varphi_{\mathrm{i}}) + M^0_{\mathrm{DBy}} cos(\varphi_{\mathrm{i}}) \Big) + (F_{\mathrm{TG,xz}})(l_7) \Big] \end{cases} \tag{4.11}$$

$$\text{where} : \begin{cases} F_{\mathrm{TB}} = -\sum_{\mathrm{i}=1}^{nK} F_{\mathrm{TK,i}}, \ \text{where} F_{\mathrm{TK}} = \mu v_{\mathrm{K}} A_{\mathrm{K}} / c_{\mathrm{K,r}} \\ F_{\mathrm{DB}} = \sum_{\mathrm{i}=1}^{nK} p_{\mathrm{DC,i}} F^0_{\mathrm{DB}}, \ \text{where} F^0_{\mathrm{DB}} \approx \sum_{\mathrm{i}} da_{\mathrm{i}} \boldsymbol{n}_{\mathrm{i}} \cdot \boldsymbol{k} \\ M^0_{\mathrm{DB}} \approx \sum_{\mathrm{i}} \boldsymbol{r}_{\mathrm{i}} \times da_{\mathrm{i}} \boldsymbol{n}_{\mathrm{i}} \end{cases} \tag{4.12}$$

The forces acting on the block consist of F_{S}, the spring force that pushes the block against the valve plate to prevent lift-off during operation (see the spring in Fig. 4.3 (a)), F_{TB}, the force due to viscous friction in the piston-cylinder interfaces, and F_{DB}, the force due to DC pressure [11]. F_{TB} is calculated based on F_{TK}, which is approximated by the cylinder block-valve plate interface module of FSTI as the product of the viscosity μ, the piston speed v_{K}, and the area spanned by the piston running surface A_{K}, divided by the radial piston-bore clearance $c_{\mathrm{K,r}}$. F_{DB} is calculated by the module based on F^0_{DB}, the force due to DC pressure acting on a reference DC, subjected to 1 bar of pressure. Likewise, M_{DB}, the moment due to displacement chamber pressure, is modeled using a reference moment, M^0_{DB} (see Eq. 4.12). In addition to the moment from DC pressure, there are also moments on the block imposed by F_{SKy}, $F_{\omega\mathrm{K}}$, and F_{TG}.

4.3 Case Study

In order to provide insight on how the hydrostatic and hydrodynamic components of fluid pressure in the lubricating interfaces of a real pump contribute to load support for the piston, slipper, and block, a case study has been conducted on a 75 cc stock unit, running at the operating conditions listed in Table 4.1 [1]. The simulated pump geometry includes wear pro-

files on the surfaces of both the bores of the cylinder block bushings, and the slipper sealing land[2]. As this is a topic of interest to pump manufacturers and the fluid power community at large, the case study has been conducted with HLP-32 as the hydraulic fluid; however, as its findings speak toward the differing nature of the three main lubricating interfaces of APMSPD, it is also highly relevant to the design of pumps whose working fluid is water.

The results of this study are presented in Fig. 4.4 and Fig. 4.5, respectively showing how the forces and moments that constitute the load on the piston, slipper, and block are balanced by hydrostatic and hydrodynamic pressure at OCA-OCC [1]. This is done by plotting the percentage of the opposing force, i.e. the force generated by the pressure field of an interface that acts *in the direction opposite of the load force vector*, that comes from hydrostatic pressure ($F_{\text{ps,of}}$), and the percentage that comes from hydrodynamic pressure ($F_{\text{pd,of}}$). Also plotted is the percentage of the opposing force that exceeds the force required to counter the load ($F_{\text{pe,of}}$).

For example, the top plot in the left-hand column of Fig. 4.4 shows that over the high-pressures stroke of OC1, 100% of the opposing force comes from hydrostatic pressure, and none from hydrodynamic pressure, meaning that all of the load on the piston is being carried by hydrostatic pressure [1]. However, circa 60% of the opposing force is not needed to support the load. That is, the hydrostatic pressure is generating more force than needed to counter the load. In order to avoid metal-to-metal contact of the piston and bore, the excess force must be balanced by the hydrostatic pressure. Since the load only constitutes about 40% of the opposing force, because of the magnitude of the force from hydrostatic pressure,

[2]Based on profilometer measurements of these surfaces on the pump taken by Ashley Busquets [31] and Ashkan Darbani.

Table 4.1. Operating conditions for the case study [1].

OC	p_{out} *[bar]*	n *[rpm]*
A	125	1,000
B	125	3,000
C	325	1,000

the hydrodynamic pressure must counter a force that is greater than the original load. This is also the case for most of the high-pressure stroke at OCB, and all of the high-pressure stroke at OCC. For the slipper and block, by contrast, this is not the case: the load over the high-pressure stroke is supported by both, hydrodynamic and hydrostatic pressure, and the opposing force is not in excess of the load.

Moreover, as can be seen from Fig. 4.5, the piston-cylinder interface distinguishes itself from the slipper-swash plate and cylinder-block valve plate interfaces in that, over the majority of the drive shaft revolution at OCA-OCC, it carries over 80% of the moment acting on the piston with hydrodynamic pressure [1]. The cylinder block-valve plate interface carries less than half of the moment acting on the block with hydrostatic pressure, and while the slipper-swash plate interface does carry all of the moment acting on the slipper with hydrodynamic pressure over certain shaft angle ranges, the magnitude of that moment is negligible. Fig. 4.6 illustrates why the moment on the piston is predominantly countered by hydrodynamic pressure over the high-pressure stroke: the side load on the piston causes it to tilt, resulting in a circumferentially uneven hydrostatic pressure distribution. As can be seen, the moment that this pressure distribution generates about Point P runs in the same direction as the moment generated by the (typically) dominant component of the piston side load, F_{SKy}. This is why, provided $F_{\mathrm{SKy}} > F_{\omega\mathrm{K,yz}}$, the piston-cylinder interface cannot be hydrostatically balanced. Fig. 4.5 reflects this.

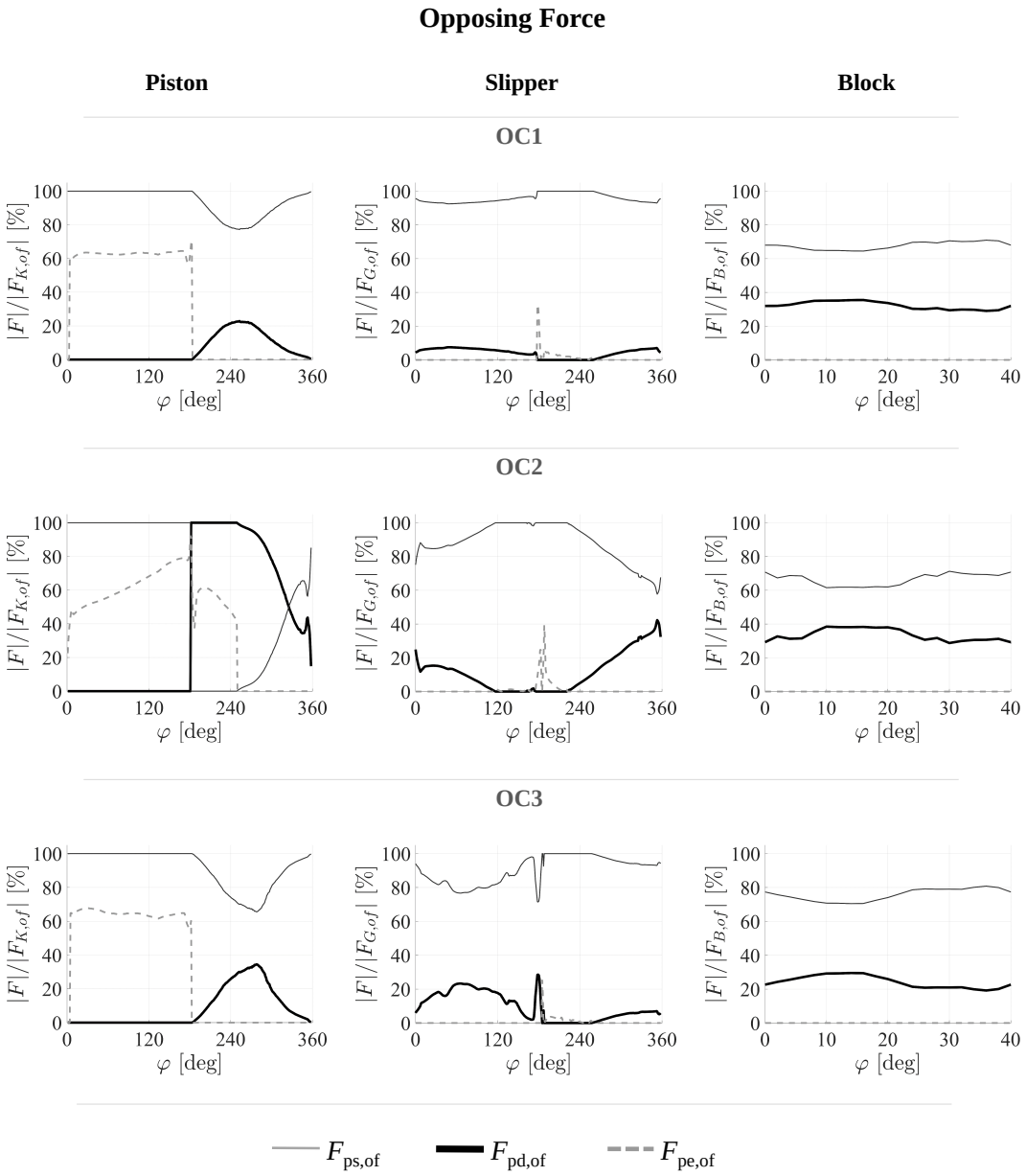

Figure 4.4. Hydrostatic, hydrodynamic, and excess components of opposing force vector [1].

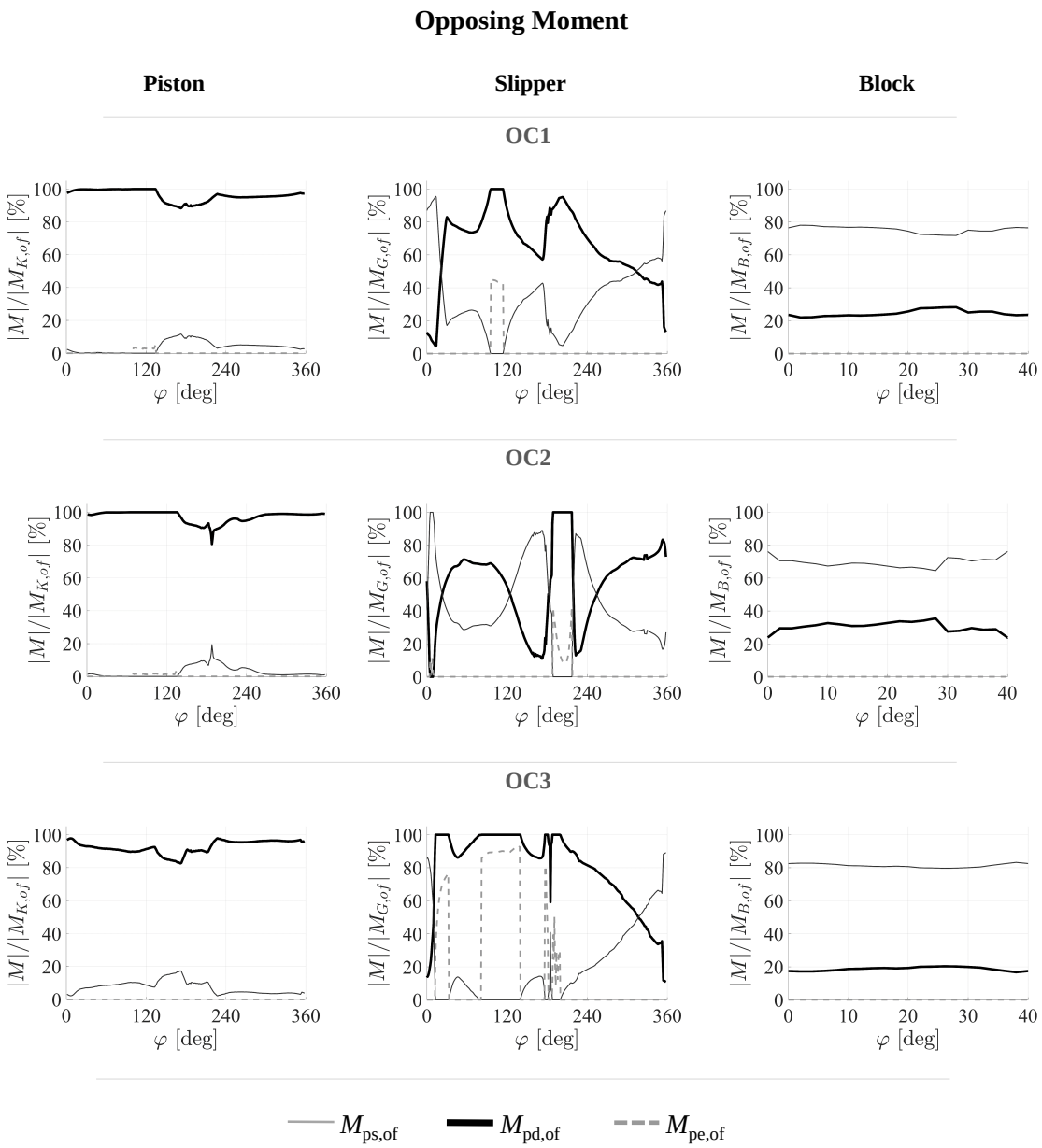

Figure 4.5. Hydrostatic, hydrodynamic, and excess components of opposing moment vector [1].

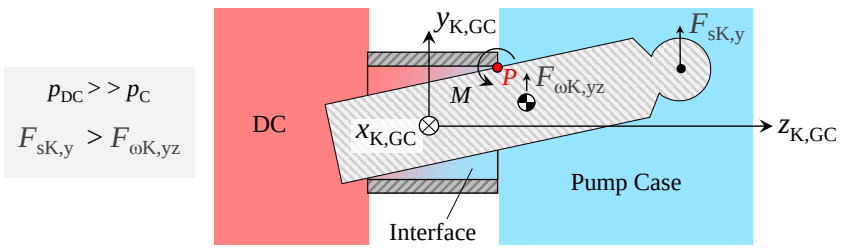

Figure 4.6. Moment on piston about Point P over the high-pressure stroke [1].

4.4 Summary/Conclusions vis-á-vis Hydrostatic vs. Hydrodynamic Pressure in APMSPD Lubricating Interfaces

A methodology has been developed to separate the pressure fields of the three main lubricating interfaces of APMSPD into their hydrostatic and hydrodynamic pressure components, and calculate the contribution that each of these components make to supporting the load imposed on the pistons, slippers, and block [1]. A case study was then conducted using a 75 cc stock unit, and HLP-32 as the working fluid, at three operating conditions: one at low pressure and low pump speed, one at low pressure and high pump speed, and one at high pump pressure and low pump speed.

Comparing the three interfaces over these operating conditions, it was seen that over the high-pressure stroke, the piston-cylinder interface counters the load imposed on the piston with hydrostatic pressure— but that the force from hydrostatic pressure exceeds the force needed to counter the load to such an extent that, especially at the two low-speed operating conditions, the hydrodynamic pressure has to counter a force larger than the original load [1]. This is not the case for the other two interfaces. Furthermore, the piston-cylinder interface carries over 80% of the moment acting on the piston with hydrodynamic pressure, whereas the cylinder block-valve plate interface carries less than half the moment on the block with hydrodynamic pressure, and the moment on the slipper is negligible at the studied operating conditions.

The results of the case study show that the piston-cylinder interface poses a unique design challenge, not only because it cannot be hydrostatically balanced, but because of the manner in which the hydrostatic and hydrodynamic components of pressure interact within this interface. For this reason, the present work focuses on the design of the piston-cylinder interface, rather than the slipper-swash plate or cylinder-block valve plate interfaces.

5. STATE OF THE ART

5.1 The Birth of Modern Water Hydraulics Technology

FSTI is a modern simulation tool, powerful enough to be employed by Chacon and Ivantysynova [32] as the clockwork of a prototyping methodology that enables the design of an APMSPD (component sizing, material selection, surface shaping for the lubricating interfaces) entirely in the virtual world, without experimental testing. Today, such a tool can be used to design the tribological interfaces of APMSPD for use with various hydraulic fluids; however, two hundred years ago, no such models were available. This was problematic because water, the hydraulic fluid of the time, generates a number of must-solve problems— among the most critical, the low load-carrying capacity and high leakage rate that result when this fluid is employed as a lubricant in a tribological interface. Further concerns include corrosion, microorganism (e.g. bacterial) growth, violent cavitation on account of water's high vapor pressure, a limited operating temperature range on account of water's high freezing point, and a more pronounced hammer effect than hydraulic oil on account of water's higher bulk modulus [6], [33]. Because the technical knowledge of the early 1900's did not provide effective solutions to these problems, the idea of two gentlemen, Williams and Janney, to use oil as the working fluid in a hydrostatic transmission— notably comprised of axial piston machines— took off [4].

Hydraulic systems could suddenly be rendered functional for an assortment of applications and operating conditions that had appeared out of reach when working with water. By the 1980's, however, "functional" was no longer sufficient, health and environmental concerns had shifted into public focus, and with the state of the art in engineering over eighty years further along, solutions to the problems of water hydraulics technology were moving into sight [6]. In the 1990's, modern tap water hydraulics began to crystallize in the form of new components and product lines that finally opened the door for operating conditions and applications which, in the days of Williams and Janney, had been unthinkable with that fluid. The renascent technology continues to evolve; yet, to date, the maximum operating pressure of most APMSD running on water stands at only 160 bar— with a few exceptions, e.g. the

55 cc pump from Mitsubishi and the 20 cc pump from Hytar Oy, both able to achieve 210 bar [9], [34]. To put this in perspective, the Series 90 axial piston pumps by Danfoss running on hydraulic oil, which have a higher maximum displacement than the Mitsubishi unit, can run at a working pressure of up to 450 bar [35]. One major obstacle to high-pressure operation is the inability of the water-lubricated piston-cylinder interface to sustain this condition, specifically in terms of providing sufficient support for the side load imposed on the pistons, without allowing for excessive leakage through the interface.

It should be noted that the side load on the pistons in APMSPD for a given operating condition will be lower for smaller units, because scaling down a unit decreases the diameter of its piston barrels, thus bringing down the magnitude of F_{DK}— and because scaling down decreases piston weight, thus bringing down $F_{\omega\mathrm{K}}$. This eases achieving high-pressure operation for the piston-cylinder interfaces of smaller machines, provided that they can be constructed with an adequately small piston-cylinder clearance, and provided that the advantage of their lower piston side load is not entirely undone by the disadvantage of a lower interface load support capacity (coming from having a smaller total area over which the piston-bore conformity suffices for high hydrodynamic pressure buildup). In other words, for very small units, the high pressure operation with water pursued in this work may already be achievable with the current state of art. However, a broad range of commercially available unit sizes continues to be challenged by this objective.

5.2 Materials Research as a Solution

One of the primary avenues through which a solution to this has been pursued is the choice of materials for the parts in relative motion at the piston-cylinder interface. This search for favorable material pairings, able to mitigate the problems of a low-viscosity fluid, is embodied by a growing collection of experimental studies. A typical example is the study by Huayong et al. in 2003 [36], detailing the construction and implementation of a test bench for comparing the performance of a 940 stainless steel piston paired with an Al_2O_3 ceramic cylinder block to the performance of the same stainless steel, paired with an F102 engineering plastics block. Emulating the piston-cylinder block interaction, for each material

combination, the test bench turned a 940 stainless steel cylinder (representing the piston) against a rectangular block, with water as the lubricant, a surface velocity of 0.84 m/s, and an applied load of 196 N. The F102 plastic block resulted in lower measured friction torques, and narrower grinding cracks (less wear), leading the authors to recommend it as the better material— what aids this plastic, is its ability to form a transfer film at the surface [36].

Casting the line a little further, in 2009 Yinshui et al. [37] tested seven different piston-cylinder material pairings in a single piston pump test bench over a runtime of 20 hours, and tap water as the hydraulic medium. The first four material pairings comprise a 1Cr18Ni9Ti stainless steel piston: first in combination with a fiber-filled phenol cylinder, then with a 30% carbon fiber reinforced PAI cylinder, next a Torlon 4301 cylinder, and, finally, a T500 bearing. The remaining pairings each feature a Torlon 4301 cylinder, respectively with a TC4 alloy piston, a Monel k500 alloy piston, and a stellite-coated 1Cr18Ni9Ti piston. The pump speed was set to 1,000 rpm, and the operating pressure, to 140 bar— except for the TC4 alloy pairing, which ran at 100 bar. The 1Cr18Ni9Ti piston paired with the fiber-filled phenol cylinder, as well as the TC4 alloy paired with the Torlon 4301 cylinder, failed before the 20 hour test elapsed; one of the leading causes of these failures is the thermal expansion caused by the heat generated due to friction. The best performance (in terms of wear) was delivered by the stellite-coated piston, because of its hardness.

However, the performance of any particular material is very much tied to its exact implementation: the T500 bearing tested by Yinshui et al. developed a visible crack during operation [37], but in 2005, Nie et al. [38] successfully employed this type of self-lubricating material, completing a 50 hour test in a single piston pump of the same displacement, and at the same pressure (140 bar). In that experiment, the T500 was utilized as a *piston sleeve* material, paired with a 17-4PH steel cylinder block sleeve— performance verification in preparation for the construction of an axial piston motor to be run with synthetic seawater. The test differs from that of Lin in its use of T500 for the piston (not the cylinder), its pairing with a different steel, and in the use of seawater as hydraulic medium instead of tap water; the pump speed may also differ (is unclear for this particular test in the work of Nie). In this

new implementation, Nie et al. found the measured wear ratio (μm/h) of the T500 to be an order of magnitude higher than that of the tested steel— but still low enough to construct the desired motor, with a maximum operating pressure of 100 bar.

Heading in a slightly different direction, in 2005 Kim et al. [39] investigated what could be achieved through surface coating. In order to compare the performance of an AISI 4340 steel piston coated in CrSiN to that of a plasma nitrided piston, Kim et al. manufactured cylinders of both materials, and turned them each against a bronze plate under a 196 N load, over a speed range of 0 rpm to 1,600 rpm. The CrSiN coated cylinder produced a significantly lower friction coefficient than the plasma nitrided cylinder, especially above 600 rpm; however, according to the authors, for commercial implementation this coefficent must fall below 0.13, and the tested CrSiN coating produced a coefficient of over 0.15 over most of the 1,600 rpm speed range.

Although many more material combinations and surface coatings are conceivable, today, the piston-cylinder sliding pair for units running with water most commonly consists of a hard material, often Duplex or Super-duplex stainless steel, and a soft material, typically PEEK (polyether ether ketone) or a PEEK composite [40]. Consequentially, variations of this steel-PEEK combination have also been a popular subject of experimental study. For example, Dong. et al [41] tested AISI630 stainless steel sliding against CF/FTFE/graphite-filled PEEK in a water reservoir under loads up to 33.2 bar. The best performance was found to be delivered at a load of 16.6 bar, and a sliding speed of 1 m/s— however, at 33.2 bar, the PEEK cracked, and even delaminated. Similarly, in 2014 Zhang et al. [40] tested a 17-4PH stainless steel/PEEK+CA30 combination in water for use at the slipper-swash plate and cylinder block-valve plate interfaces of APMSPD; they found the wear rate of the PEEK material to be sensitive to a rise in temperature that occurs as sliding speed increases and heat dissipation becomes insufficient. Furthermore, they found that under high load/low speed conditions, the PEEK surface folds/ripples.

For the ambition of climbing the scale in high operating pressures to the top, relying *solely* on the choice of material for a satisfactory performance from the water-lubricated piston-cylinder interface is sub-optimal. In the 300+ bar regime, the loads faced by these materials are significantly higher than those tested in the listed references. Developing a material, (e.g. a type of ceramic), that not only survives such conditions without cracking, rippling, or delaminating, but that also diminishes the high mechanical losses of the mixed and/or solid friction seen under these conditions, to the extent that they can be diminished by bringing the lubricating interfaces into the full film regime, presents a serious challenge. The micro surface shaping approach that constitutes the focus of this work, au contraire, represents a more achievable solution, one that works by alleviating the symptoms of insufficient fluid film load support. That is, instead of choosing materials capable of enduring poor lubrication conditions, surface shaping focuses on improving these conditions, i.e. increasing the load-carrying capacity of the fluid film, thereby diminishing the forces on the piston that must be carried by surface asperities. Benefits include the ability to achieve higher operating pressures, lower wear rates, and a higher mechanical efficiency.

5.3 Surface Shaping as a Solution for Water-Lubricated Journal Bearings

Prior to discussing the surface shapes that have already been developed for APMSPD, it is worth noting that this concept has also been investigated in the context of water-lubricated journal bearings; these exhibit a certain degree of similarity to the piston-cylinder interface in that they build hydrodynamic pressure through the rotational motion of a journal with respect to a sleeve.

One of the cardinal design challenges shared by water-lubricated journal bearings and APM-SPD piston-cylinder interfaces is the trade-off between load support and power loss. This is exemplified by the 2004 study of Majumdar et al. [42]: an analysis of axial grooves in the sleeves of water-lubricated journal bearings via numerical solution of the Reynolds equation. Axial grooves of two different widths are compared, one having an angular extent of 18°, the other an angular extent of 36°. It is shown that narrower grooves offer better load support, because the pressure that is built on the land regions between the grooves is higher than

the groove pressure. However, the bearing with narrower grooves generates more power loss through viscous friction. The gain in load-carrying capacity achieved through the use of narrower grooves is therefore offset a loss in mechanical efficiency.

These axial grooves have also been examined in the context of journal-sleeve misalignment, which, because the journal is tilted in its sleeve, comes a little closer to conditions in the piston-cylinder interface. Mallya et al. [43] models water-lubricated journal bearings with three axial grooves of the same two widths, and using the same modified Reynolds equation, as Majumdar et al. [42] Journal misalignment in two orthogonal planes is found to increase the load-carrying capacity for both groove widths when the eccentricity ratio is high ($\epsilon = e/C = 0.8 - 0.9$, where e is the eccentricity, and C is the radial clearance) [43]. Still, just as in the study by Majumdar et al, the bearing with the narrower grooves (18°) outperforms the bearing with the wider grooves (36°) in terms of load-carrying capacity— and that for all simulated eccentricity ratios ($\epsilon = 0.5 - 0.9$), and for misalignment in either of the two studied planes. Narrower grooves, however, also result in a higher side leakage; this demonstrates again that while a benefit can be drawn from surface shaping, it cannot necessarily be drawn on all fronts. On account of this, developing surface shaping for water-lubricated bearings calls for optimization techniques capable of working out how far a design can be pushed to reap the benefits it offers, before the associated drawbacks become excessive. This is also valid for the piston-cylinder interface, and the need for an optimization scheme will be addressed in later chapters.

5.4 Surface Shaping as a Solution for the Piston-Cylinder Interface

Although the higher viscosity of hydraulic oil lessens the two problems prominent in water-lubricated bearings— low load-carrying capacity and excessive leakage— it does not eliminate them. The hunt for design measures that improve the efficiency and/or load-carrying capacity of the oil-lubricated APMSPD piston-cylinder interface has spawned the invention of a broad repertory of micro surface shapes, forming an important base to draw from in designing for water hydraulics.

For example, in his 1975 analysis of piston-cylinder interfaces in piston-type hydraulic machines, Yamaguchi [44] advocates stabilizing the movement of the pistons by tapering their running surfaces, such as to give the surrounding fluid film a cross-section that diminishes exponentially along the guide length. Nearly a decade later, in 1983, Ivantysynova [45] proposes improving the efficiency of APMSPD through the implementation of a barrel-like micro-surface shape on the pistons, reducing their diameter by 4 μm on either end: see Fig. 5.1 (a). In 2003, Lasaar [46] builds on this by investigating a half-barrel piston shape, shown in Fig. 5.1 (b), for which the diameter reduction at one end of the piston does not equal the reduction at the other.

These barrel- and half-barrel shapes have the advantage that for the piston running surface, the tight machining tolerances required to achieve the intended minimum clearance between that piston and its surrounding bore need only cover the apex of the barrel shape (where the piston takes on the widest diameter). This makes it easier/cheaper to manufacture the interfaces with lower minimum clearances, which reduces the leakage through them. The reduction in leakage attained by this, in combination with any reduction in torque loss achieved by the surface shaping-induced changes in the fluid film's pressure field (especially the hydrodynamic pressure buildup), allow this type of shaping to increase pump efficiency.

Extending this line of thought, a number of other designs can be conceived to reduce the power loss through the piston-cylinder interface. The idea is to design a surface shape such as to decrease torque loss, and to simultaneously enable the use of lower clearances in order to bring down the leakage. Examples of this are shown in Fig. 5.1 (c) and (d). Fig. 5.1 (c) depicts the axial sine wave surface shape invented by Ivantysynova et al. [49], which gives the piston running surface a sine wave profile (lengthwise cross-section). Fig. 5.1 (d) illustrates the waved barrel, a combination of the barrel and axial sine wave shapes described in the works of Wondergem and Ivantysynova [50], [51]: its profile is an axial sine wave that follows the arch of a barrel shape.

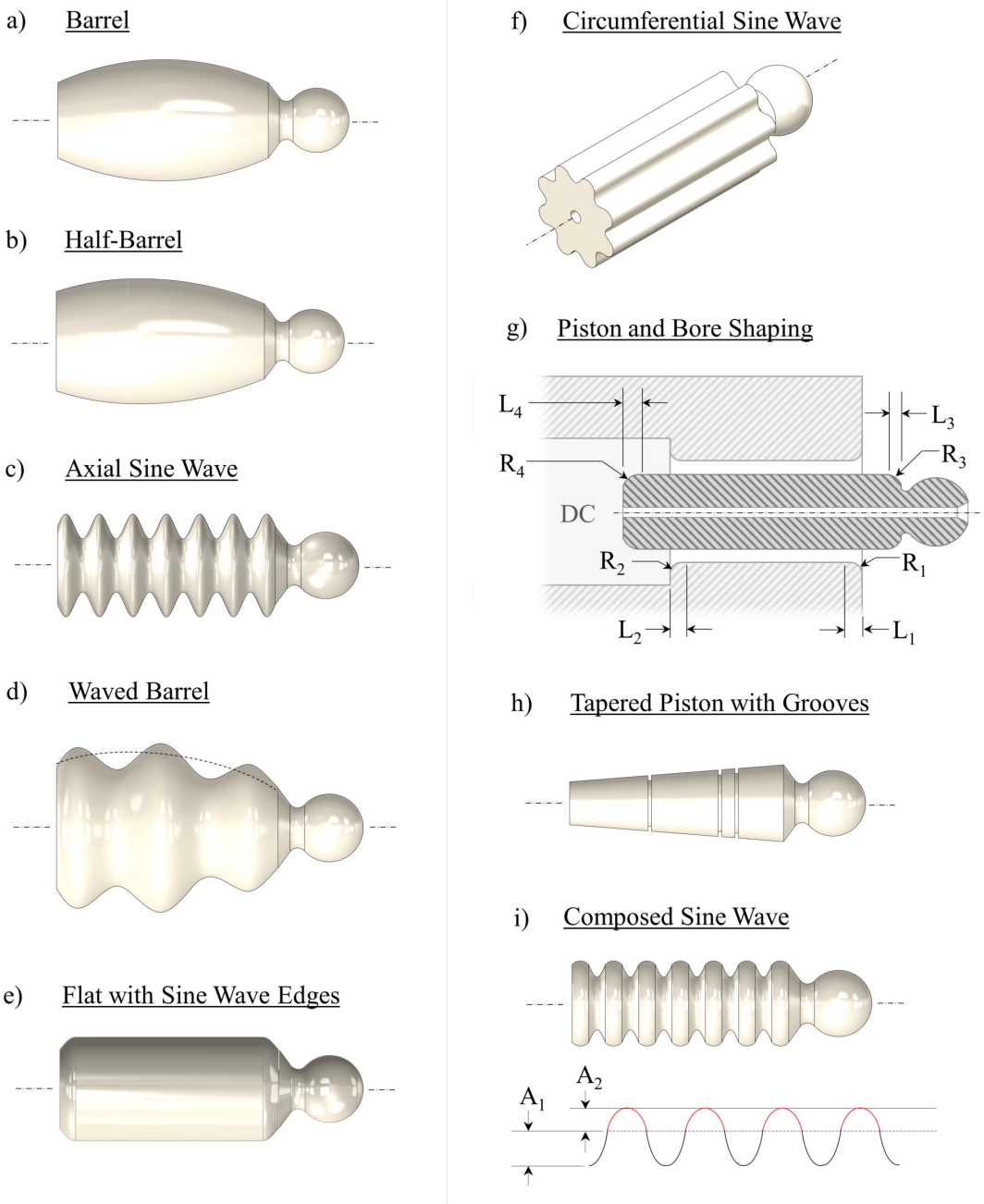

Figure 5.1. State of the art in surface shaping. Images based on [31], [45]–[53].

Wondergem and Ivantysynova also investigate the performance of a flat piston profile that rounds off at either end of the piston running surface, with the roundoff following the curvature of a sine wave segment [50], [51] (see Fig. 5.1 e). The obvious drawback is that for this profile, most of the piston running surface is at the gap's minimum clearance, i.e. under obligation to adhere to correspondingly tight machining tolerances. However, there is also an advantage attached to keeping the piston-bore gap narrow over such a great portion of the guide length: lower leakage rates. This is demonstrated by Wondergem and Ivantysynova [50], in a simulation study conducted with FSTI, using the geometry of a 75 cc stock unit.

In the study, the performance of this surface shape, along with designs b-d from Fig. 5.1, are compared to that of a standard cylindrical piston. The minimum piston-bore clearance for the pistons with surface shaping is reduced to 44% that of the standard piston. Operating conditions simulated comprise full displacement, with a pressure difference across the pump of $\triangle p$=100 bar and 300 bar, each at a pump speed of 1,000 rpm and 2000 rpm, and 20% displacement, with $\triangle p$=100 bar, 1,000 rpm and 2000 rpm, and with $\triangle p$=300 bar, 2,000 rpm. In the study, all simulated surface shapes are able to achieve significant reductions in energy dissipation over the standard piston, albeit not at every operating condition. Unsurprisingly, the greatest reduction in leakage for both, the full and partial displacement, is achieved by the flat piston with rounded edges.

With two further simulation studies, Wondergem and Ivantysynova [52], [54] investigate and compare the power loss reduction achievable through designs b-f from Fig. 5.1, where design f is a shape that gives the piston running surface's circumference a sine wave cross-section. Both studies are conducted using the geometry of a 75 cc stock unit, and both cover pumping, as well as motoring mode for the simulated APMSPD; for pumping mode, the first study covers pressures of $\triangle p$=100 bar, 300 bar, and 400 bar, with pump speeds of 1,000 rpm, 2,000 pm, and 2,800 rpm, whereas the second study covers $\triangle p$=50 bar and 450 bar, with speeds of 500 rpm and 3,600 rpm. It is concluded in both studies that the best overall performance over a standard piston in terms of power loss reduction is delivered by a half-barrel shape.

The total losses at the piston-cylinder interface can also be significantly decreased via the combination of the contoured piston and bore by Gels and Murrenhoff [48] that is shown in Fig. 5.1 (g). Here, the piston and bore are rounded off at the ends of their respective running surfaces, such as to give the formerly sharp edges there the lengthwise cross-section of a circular arc instead of a 90°corner. In order to understand the effect of the dimensions marked in Fig. 5.1 (g)— specifically in terms of the leakage and viscous friction losses of the piston-cylinder interface— Gels and Murrenhoff [48] conducted a study using a Reynolds equation-based simulation tool, and the geometry of a 90 cc unit.

At the studied operating condition of $\triangle p$=250 bar, 2,000 rpm, they found that total losses in the oil-lubricated interface can be decreased by well over 40% for the optimized values of R_1 and L_1. Adjustment of the other dimensions is shown to also lower losses— except for R_3 and L_3, which did not produce a significant effect. The optimized design developed in the study therefore drastically increases the efficiency of the interface. It should be noted that the word "optimized" must be used with caution in this case— not all parameters were optimized simultaneously: rather, one radius-length pair was studied at a time.

Beyond examining the effects of shaping on pump efficiency, the study also observes that the bore contours on either end of the guide length, and the contour on the edge of the piston barrel nearest the DC, aid the interface fluid film in providing load support. Other designs able to increase the piston-cylinder interface's load-carrying capacity include those developed by Berthold [55], Park [47], and Yoshimura et al. [56]. Berthold [55] patented a cooling device that equips the piston-cylinder interface with pressurized circumferential grooves in the bore to guard against piston seizure, while Park [47] studied the effect of a tapered piston with grooves (see Fig. 5.1 h). Simulating this surface shape using a 1-D Reynolds equation, Park found that the grooves help circumferentially even out the pressure around the piston, thereby decreasing the tilting moment imposed on it by the interface's uneven pressure field; the demerit of this design is that the implementation of grooves increases the leakage through the interface. Taking an entirely different approach from Berthold and Park, Yoshimura et al. [56] patented the imposition of a crowning shape on the edges of both ends of the running

surface, and on the edge of the bore at the case end of the interface— this type of shaping will be examined in more detail in a later chapter. All three aforementioned designs can be used with low-viscosity fluids.

Finally, previous work by the author [21], [53] on surface shaping specifically for the water-lubricated piston-cylinder interface of APMSPD includes the study and comparison of circumferential bore grooves, the half-barrel shape, the axial sine wave shape, and the composed sine wave shown in Fig. 5.1 (i), which flattens the upper half of the axial sine wave design (the idea is to generate more hydrodynamic pressure buildup at the flattened peaks than the original axial sine wave profile, and allow the pressure field to even out circumferentially in the deep sine wave valleys). While the studies conducted did find some improvement for the interface in terms of load support, that improvement is accompanied by a heavy compromise in terms of leakage.

The present work pursues the ideal surface shape for the water-lubricated piston-cylinder interface on a much grander scale, not only through vastly more extensive design studies than those previously conducted, but also through the development and implementation of an optimization algorithm tailored for use with FSTI, and through the development of an algorithm able to generate surface shapes specifically adapted to how a piston tilts inside its bore, and to how the surfaces of the piston and its corresponding bore deform during operation. The goal is to push for far higher increases in the load-carrying capacity of the fluid film, and to achieve those increases with a lesser compromise in power loss.

5.5 Summary/Conclusions vis-á-vis the State of the Art

In summary, while a sizable amount of work has been done towards developing and studying the effects of surface shapes for the piston-cylinder interfaces of axial piston machines, a large portion of it is dedicated to units running with hydraulic oil. The investigation of piston-cylinder interface design for water and low-viscosity fluids is limited, focusing largely on the use of grooves, or waves with deep valleys, both of which cause a considerable increase in leakage across the fluid film [21]. The present work aims to provide a systematic investigation

of surface shaping for the water-lubricated piston-cylinder interface that examines, in detail, how contouring on the micron scale can be designed to achieve sufficient load support while keeping leakage across the interface low. Moreover, the present work entails the development of an algorithm that *tailors* the shape of the bore surfaces through which the pistons move to the tilt and deformation of the piston in a given pump at a given operating condition. This moves beyond the traditional trial-and-error approaches to design, and even beyond the approach of choosing a shape of certain dimensions based on trends in pump performance established by design studies or optimization routines with physical or virtual prototypes. It reduces the design space covered by such strategies, allowing for a more effective and efficient design process.

6. BASELINE SETS

In order to give measure to the changes that surface shaping brings about in the behavior of an APMSPD piston-cylinder interface, two sets of baseline simulations are run at the OCs (operating conditions) shown in Table 6.1. These constitute the basis against which simulations run with surface shaping at the interface, and water as a working fluid, can be compared. Both baseline sets utilize the geometry of the stock 75 cc unit introduced in Ch. 4. That, however, is the extent of their commonalities. The most important difference between them is the simulated hydraulic fluid: for the first set, it is water, for the second, hydraulic oil (this set serves mainly to show what magnitude of power loss is reasonable for this unit).

Table 6.1. Baseline operating conditions.

OC #	*OC Abbrev.*	$\triangle p$ *[bar]*	*Pump Speed [rpm]*	*Inlet Temperature [°C]*
1	LP, LS	50	1,000	35
2	LP, HS	50	3,000	35
3	HP, LS	300	1,000	35
4	HP, HS	300	3,000	35

6.1 Baseline Set 1: Water as Hydraulic Fluid

6.1.1 Set 1 Setup

This set of baseline simulations uses pure H_2O as the hydraulic fluid; its purpose is to enable a direct comparison between what happens with, versus without, surface shaping at the water-lubricated piston-cylinder interface. Set 1 is therefore run without any surface shaping, i.e. the surfaces bordering the interface fluid film are perfectly cylindrical. Because the simulated stock unit has bushings set into the cylinder block bores, the outer border of the piston-cylinder interface is the surface of a bushing bore— as opposed to that of a cylinder block bore. The inner border is, of course, a piston running surface.

[0]LP=Low Pressure, HP=High Pressure, LS= Low Speed, HS=High Speed

According to Varandili [57], if water hydraulic components are to have similar leakage flow rates through interfaces (governed by laminar flow) as their oil counterparts, then their clearances must be reduced to a third, or even less, of those found in said counterparts. In aim of constructing a reasonable baseline to compare against, the relative diametrical minimum clearance between the piston and bushing bore surfaces (defined below) is therefore reduced from the 1.64 per mill of the original stock unit being modeled, to 0.58 per mill.

$$\text{Rel. Clearance} = \left(\frac{d_z - d_K}{d_K} \right) \text{ per mill}, \tag{6.1}$$

where d_z is the innermost diameter of the bushing, and d_K, the outermost diameter of the piston.

Three further modifications of the stock unit are made for Set 1. First, in order to render the simulated machine compatible with water as hydraulic fluid, the materials of the stock unit pistons, cylinder block, and bushings are changed to those listed in Table 6.2. Second, the hollow pistons of the original unit have been filled, leaving only the orifice passing through each of them to their respective slipper. This stiffens the piston, thereby lessening its deformation; as will become apparent in the subsequent section, that deformation can increase the severity of load support problems in certain regions of the interface. Stiffening the piston can therefore be a good first step in working towards a higher load-carrying capacity at the water-lubricated piston-cylinder interface. Third, the valve plate of the original unit has been replaced with a plate designed by P. Kalbfleisch specifically for the case of running this unit with water (see [18] for Kalbfleisch's work on valve plate design).

Table 6.2. Materials for Baseline Set 1.

Component	*Material*
Piston	2205 Duplex Stainless Steel
Cylinder Block	2205 Duplex Stainless Steel
Bushings	Brass

6.1.2 Simulation Results for OC4

Because FSTI simulations are computationally expensive, the large design studies to be presented in later chapters cannot cover the full range of designs they span at every OC. Since the focus of this work is high-pressure operation, the approach will be to simulate these large sets of surface shapes at the high pressure, full displacement, high speed operating condition, OC4. Designs that show promising results at this high speed OC, which is conducive to hydrodynamic pressure buildup, can then be simulated at, and adapted to also master, the more challenging, low speed version of this operating condition: OC3. For design studies of considerable computational and temporal cost, starting at OC3 directly is dangerous because at such a difficult OC, the symptoms of failure for the interface may be so pronounced that the origins of load support and power loss problems, as well as the path towards a successful interface, may be obscured. Designs able to handle both OC3 and OC4 will be checked for their performance at OC1-2, and refined as needed.

Since much emphasis will be placed on OC4, the results of the baseline simulation from Set 1 at this OC will be covered in detail in this chapter. Of key interest are load support and power loss; the former will be addressed first. As explained in Ch. 3, FSTI detects failure of the interface to support the imposed load by examining the thickness (height) of the fluid film. Where that height falls below "minimum film thickness," ($h_{\min} < 0.1\mu$m), the model assumes that the fluid film is unable to fully support the load. A good starting point for understanding the simulation results of Set 1 at OC4 in terms of load support is therefore to examine the FSTI-computed interface film thickness.

Fig. 6.1 shows four plots of that film thickness, each corresponding to a different shaft angle: φ=45°, φ=90°, φ=135°, and φ=270°, respectively. In these plots, the fluid film has been "unwrapped" in a manner similar to that illustrated in Fig. 3.3. That is, one axis travels along the length of the interface, while the other travels around its circumference.

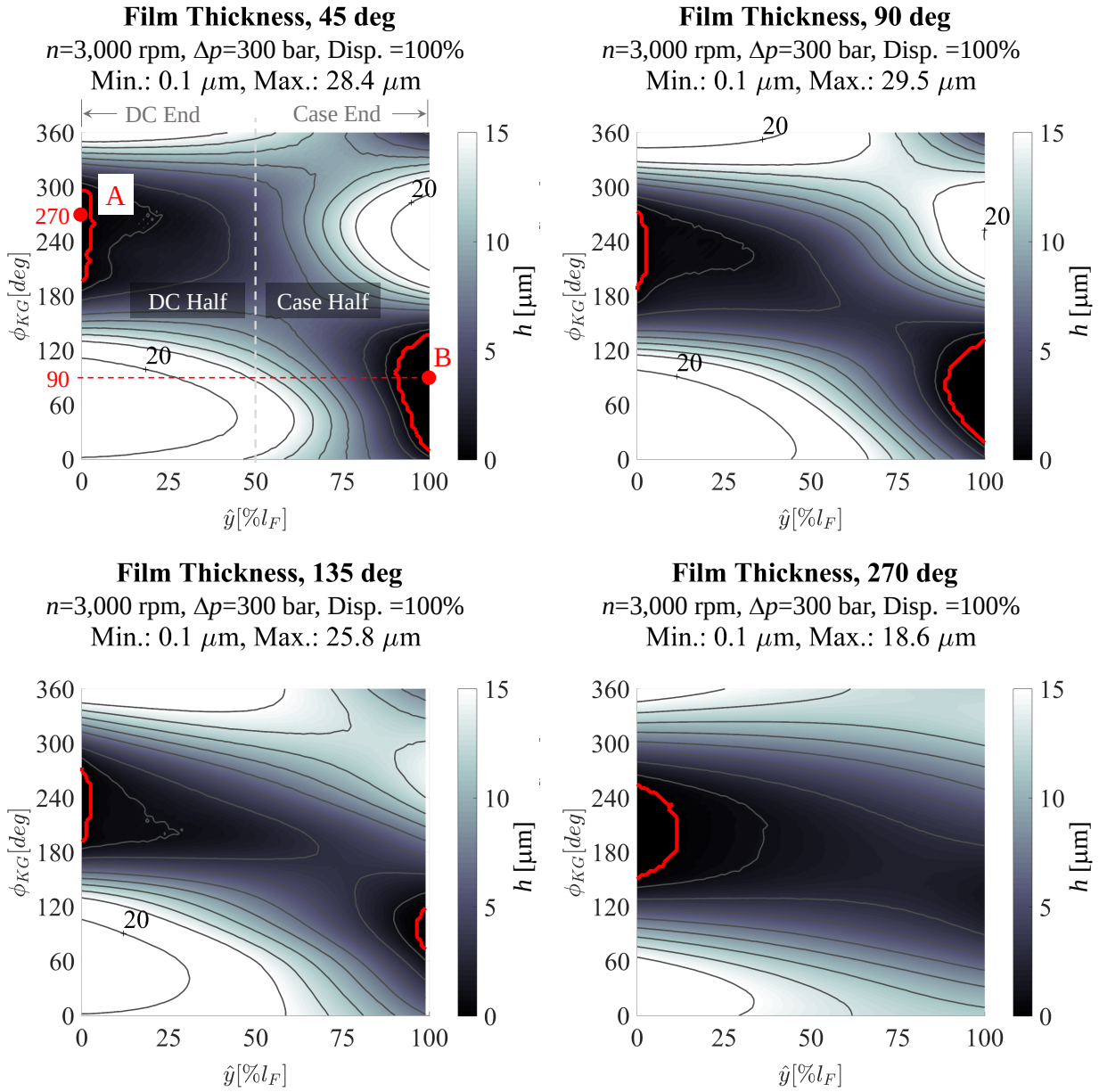

Figure 6.1. Film thickness plots for Baseline Set 1, at OC4.

The axis traveling lengthwise is, in fact, the $\hat{y}$-axis from Fig. 3.3 (shown again in Fig. 6.2 for convenience); the axis traversing the fluid film circumference, however, is not the angular $\hat{\phi}_{\mathrm{K}}$-axis from Fig. 3.3— instead, it is the ϕ_{KG}-axis. This is because the $\hat{\phi}_{\mathrm{K}}$-axis employed by FSTI makes it difficult to discern the orientation of the interface, since its angular starting point changes with the shaft angle; the ϕ_{KG}-axis is designed to make it easier to visualize how exactly the piston sits in its bore (e.g. in which direction it tilts) from this type of

unwrapped fluid film plot. To this end, ϕ_{KG}-axis differs from the $\hat{\phi_K}$-axis *exclusively* in the location of its starting point.

Fig. 6.3 demonstrates for a shaft angle of φ=45°: $\hat{\phi_K}$ is measured starting from the x_K axis, while $\hat{\phi_{KG}}$ is measured starting from a line that is parallel to the global x-axis described in Ch. 3, and that passes directly through the center of the cylinder bore. Consequentially, using the $\hat{\phi_{KG}}$-axis, Pt. A from Fig. 2.5 is always at ϕ_{KG}=90° and $\hat{y}$=100 %l_F, and Pt. B is always at ϕ_{KG}=270° and $\hat{y}$=0 %l_F. For clarity, the two points have been marked ("A" and "B") for the example of ϕ_{KG}=45° in Fig. 6.1.

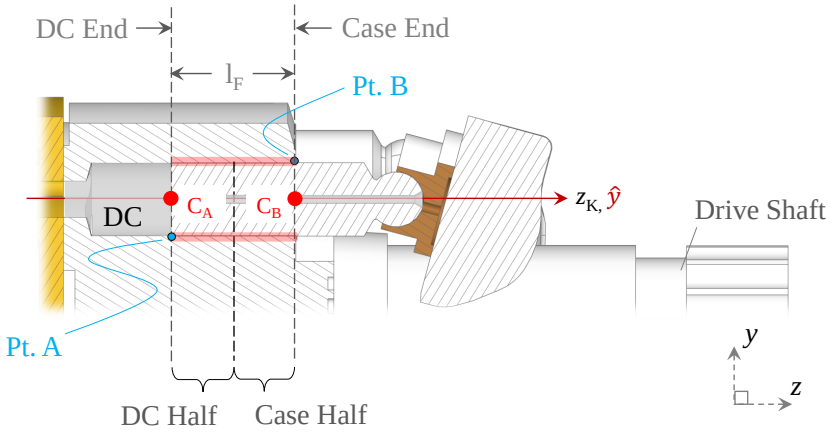

Figure 6.2. The $\hat{y}$ axis.

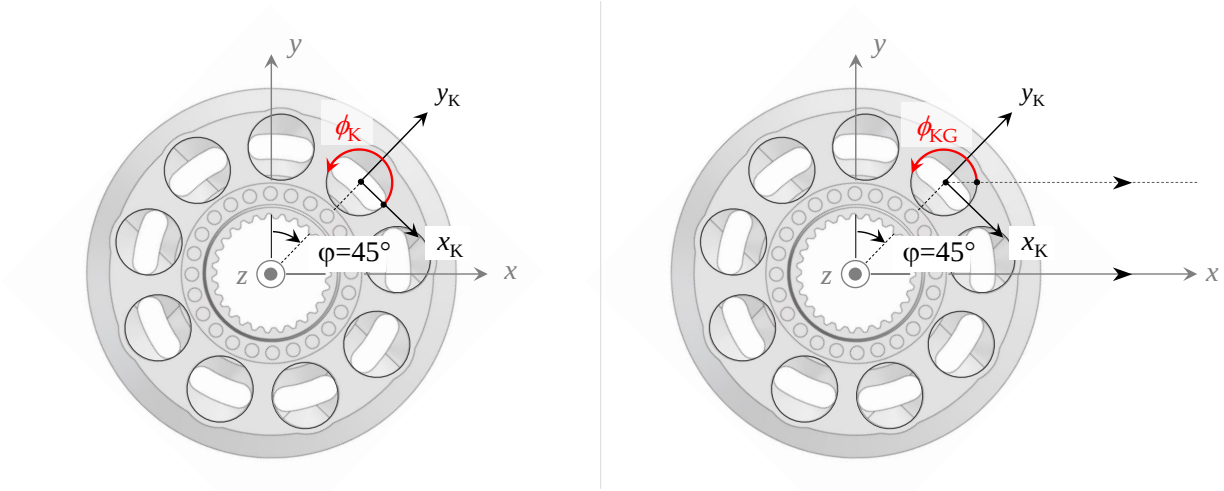

Figure 6.3. ϕ_K (left) versus ϕ_{KG} (right) at φ=45°.

In order to make the film thickness distribution over the interface visible, especially in the regions where that thickness is low, the color bar of these plots has been capped at 15 μm. Low film thickness regions are of special interest because this is where high hydrodynamic pressure buildup is generated. For an easier comparison of these crucial regions between plots, the continuous film thickness plots in Fig. 6.1 have been overlaid with a set of unmarked contour lines, which start at 1 μm, increasing in 2 μm increments up to 15 μm. Lastly, because the color bar is capped, labeled contours are provided for the regions of high film thickness; these contours start at 20 μm, and increase in 20 μm increments.

While the low film thickness regions themselves are of import, the pinnacle of interest in these plots is, of course, the areas where film thickness falls at or below h_{min}: this is where the possibility of solid contact exists. The distinguishing mark of a "good" interface design, sure to not suffer from solid contact, is the absence of such areas; Fig. 6.1 outlines these decisive regions of minimum film thickness in red. For shaft angles of φ=45°, φ=90°, and φ=135°, the Set 1 baseline run at OC4 shows patches of minimum film thickness in both the DC half of the interface (the half of the interface nearest the DC), and the case half of the interface (half of the interface nearest the swash plate). At φ=270°, there is only one patch, in the DC half.

Fig. 6.4 provides an overview of the full shaft revolution by plotting the total area taken up by regions of minimum film thickness within the piston-cylinder interface, as well as the area taken up by the largest individual patch of minimum film thickness— both as a percentage of the total area of the unwrapped fluid film. The latter, i.e. the area of the largest patch, is particularly important to monitor. This is because there may be some small amount of pressure buildup in regions of minimum film thickness that is not captured by FSTI, since the model simply assumes a parallel gap in these areas.

Depending on the severity of the predicted contact in a particular patch of minimum film thickness, the real-life pressure buildup over that patch may suffice to support the piston (prevent solid contact) in that location— *if the patch is small.* If the patch is large, however,

it becomes unlikely that the surfaces abutting the fluid film, with their asperities, thermal and pressure deformations, and surface features produced by nonzero machining tolerances, are of a shape conducive to hydrodynamic pressure buildup to the point of being able to support that entire region. On account of this, the area of the largest patch of minimum film thickness can be a decisive factor in choosing one lubricating interface design over another.

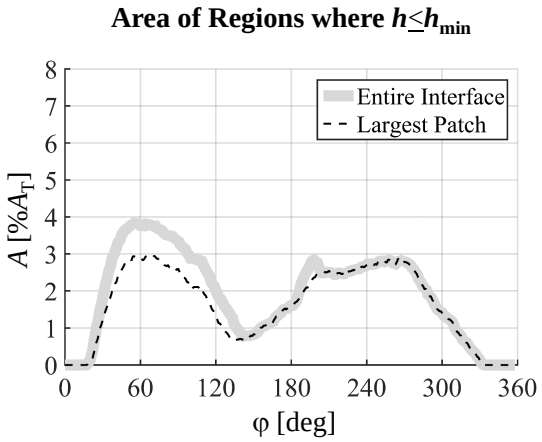

Figure 6.4. Area taken up by minimum film thickness for Baseline Set 1, at OC4.

For the baseline from Set 1 at OC4, the nonzero value of this key parameter indicates potential metal-to-metal contact. That is, the simulated interface may not be able to support the imposed load at OC4. But how severe is the predicted contact? To find out, it is useful to look at the magnitude of the contact stress σ described in Ch. 3, which is ascribed to elements of the 2-D fluid film grid whose film thickness falls below $h_{\min}$. The more severe the penetration, the higher the imposed stress. Fig. 6.5 (a) plots the maximum value of σ against shaft angle— more specifically, it plots the maximum contact stress imposed on any single element in the fluid film grid at a particular shaft angle (in gray), the maximum contact stress imposed on any single element in the case half of the fluid film at a particular shaft angle (in blue), and the maximum contact stress imposed on any single element in the DC half at a particular shaft angle (in red).

The contact stress values are high in both the case and DC halves of the interface. This is an indicator that the predicted contact is at least locally severe. However, depending

on how large an area is spanned by contact stresses of such high magnitudes, the overall effect of the predicted contact on the interface may be small. Much more comprehensive insight into the severity of the predicted contact in terms of that overall effect is given by the correction forces, also described in Ch. 3. These are the forces resulting from the imposition of contact stress, summed to the control points at the case and DC ends of the interface.

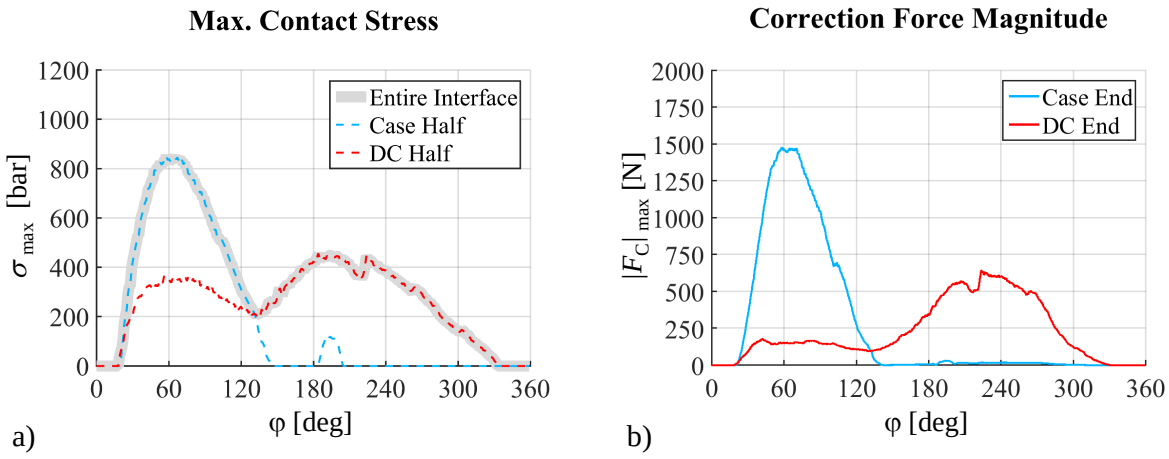

Figure 6.5. a) Max. contact stress and b) correction force magnitude at the two control points C_A and C_A (respectively located at the DC and case ends of the interface) for Baseline Set 1, at OC4.

Fig. 6.5 (b) plots the magnitude of the correction forces at the case and DC end control points, respectively, against shaft angle. As is evident, the magnitudes of these forces are large, i.e. the pressure distribution in the fluid film is predicted to be acutely unable to balance the external forces acting on the piston— but particularly so over the high-pressure stroke. This is because the total contribution of non-ifp (non-interface fluid pressure) forces to the piston side load, i.e. the total contribution of forces that are not interface fluid pressure integrated over area to the side load, is much higher over this first half of the shaft revolution than over the second.

Fig. 6.6 (a) shows this by plotting these non-ifp forces against shaft angle— more specifically, it plots the components of these forces in a particular plane, P_1. This plane passes through the centerline of the bushing bore, and is parallel to the z-y plane in the global coor-

dinate system; it is the plane in which the (typically) largest non-ifp component of the side load acts: F_{SKy}. An example of the location of this plane at φ=45°is provided by Fig. 6.6 (b).

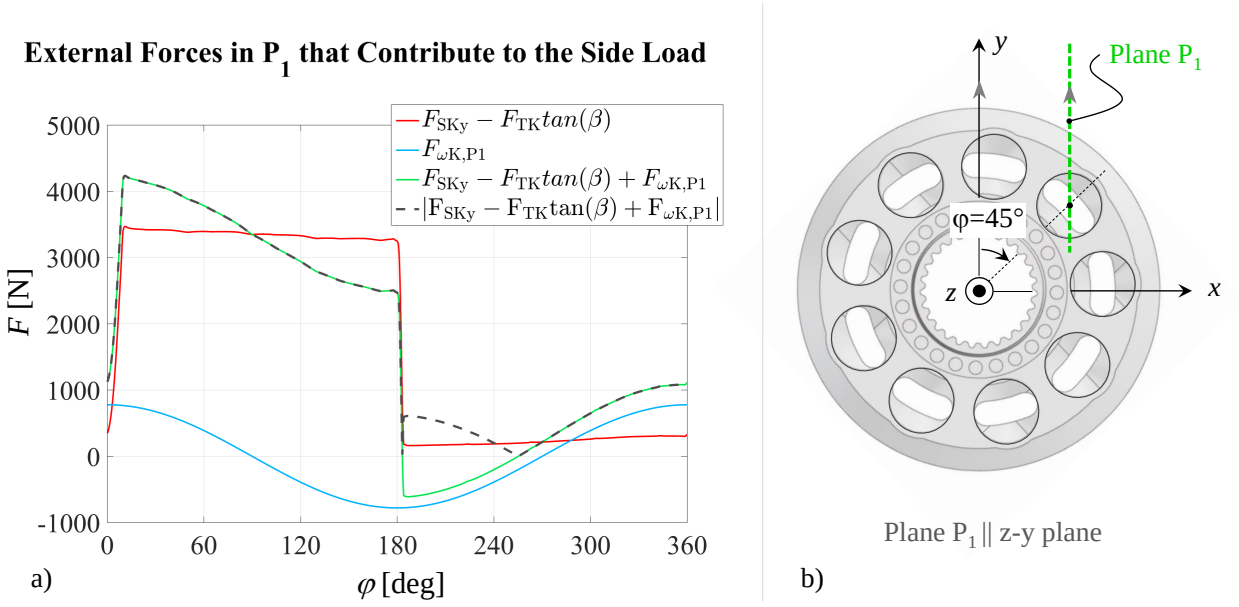

Figure 6.6. External forces in P_1 that contribute to the side load for Baseline Set 1, at OC4.

The forces shown in Fig. 6.6 (a) include $F_{\mathrm{SKy}} - F_{\mathrm{TK}}tan(\beta)$, $F_{\omega\mathrm{K,P1}}$, their sum, and its absolute value. The friction force in the piston-cylinder interface (F_{TK}), as well as any friction contribution from the slipper-swash plate interface, are very small and are thus neglected. $F_{\omega\mathrm{K,P1}}$ is the component of $F_{\omega\mathrm{K}}$ that acts in plane P_1. However, at φ=0°, φ=180°and φ=360°, $|F_{\omega\mathrm{K,P1}}|$=$F_{\omega\mathrm{K}}$, thus allowing the forces in plane P_1 shown to be directly compared against the magnitude of $F_{\omega\mathrm{K}}$ by checking against the value of $|F_{\omega\mathrm{K,P1}}|$ at these shaft angles.

Taking this into consideration, Fig. 6.6 shows that over the high pressure stroke, $F_{\mathrm{SKy}} - F_{\mathrm{TK}}tan(\beta)$ is much larger in magnitude than $F_{\omega\mathrm{K}}$, i.e. dominates the non-ifp forces, but then drops so much in transitioning to the low pressure stroke that $F_{\omega\mathrm{K}}$ takes the lead. This steep difference in the magnitude of $F_{\mathrm{SKy}} - F_{\mathrm{TK}}tan(\beta)$ between the high and low pressure strokes is responsible for the fact that the correction force magnitude from Fig. 6.5 reaches higher magnitudes over the first half of the shaft revolution, versus the second.

The reason behind that difference is the magnitude of the DC pressure, p_{DC}; recall that F_{SKy} is linearly proportional to p_{DC}. Fig. 6.7 shows how p_{DC} changes over the course of a shaft revolution by plotting it, along with the pressure of the low and high pressure ports, against shaft angle. As can be seen, DC pressure is roughly 300 bar higher over the high pressure than over the low pressure stroke. The difference in correction force magnitudes reached over these two strokes is therefore a testament to the impact of DC pressure, and to the challenge that the magnitude of this pressure can pose when operating with a low-viscosity fluid.

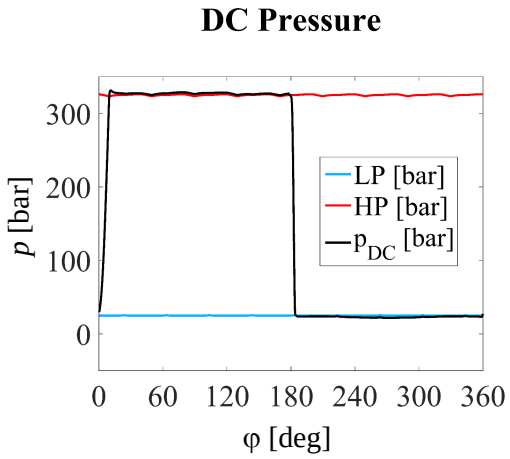

Figure 6.7. DC pressure for Baseline Set 1, at OC4.

Besides the difference in overall correction force magnitudes reached over the high, versus the low pressure strokes, it is also apparent from Fig. 6.5 that the control point at which the larger correction force magnitude is computed switches from the high to the low pressure strokes. That is, the case end correction force dominates the high pressure stroke, and the DC end correction force, the low pressure stroke. Why is this?

As already shown in Fig. 6.6, the non-ifp external forces acting on the piston differ significantly between the high- and low-pressure strokes— consequentially, the fluid pressure distribution of the interface, as well as the deformation, tilt and position of the piston, differ greatly. In order to explore this further, focus will first be given to the high pressure stroke, where the case end correction force magnitude is larger than the DC end magnitude. Fig. 6.6 makes clear that over this stroke, F_{SKy} dominates the non-ifp forces, and is large

in magnitude. Since the case end control point is located closer to the piston head, where F_{SKy} is applied, than the DC end control point, the shorter moment arm mandates a higher counterforce from the case end, which contributes to a higher correction force at the case end control point (than at the DC end control point). Furthermore, F_{SKy} pushes on the piston head, causing the piston to tilt in its bore, and to deform. The tilting, in turn, alters the pressure field of the interface, which then also deforms the piston.

Fig. 6.8 shows what this deformation typically looks like over the high-pressure stroke for a high-pressure OC, e.g. OC4, in plane P_1 (the bushing deformation is not shown). The depicted piston shape is exaggerated in order to make it visible to the naked eye, and of course varies in its exact form with operating condition, materials, pump geometry, and interface design. Furthermore, it is important to note that due to forces on the piston that do not always act in the plane shown— e.g. $F_{\omega\mathrm{K}}$— the maximum piston tilt, as well as the maximum deformation, are not necessarily in the depicted plane. However, when F_{SKy} is large compared to the other non-ifp forces, the maximum tilt and deformation tend to be close to P_1.

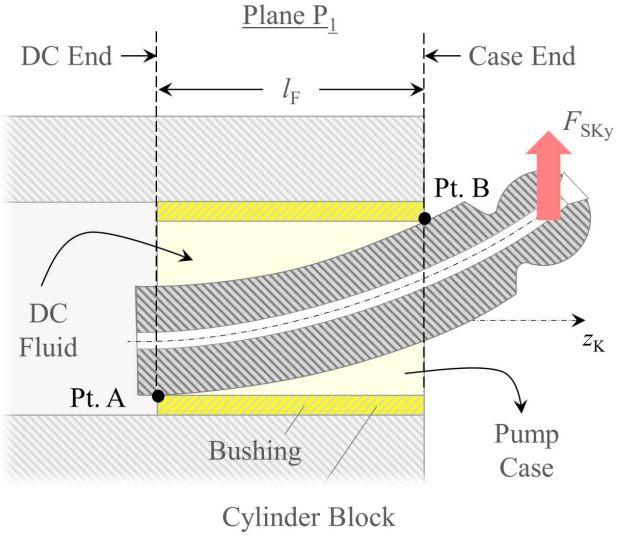

Figure 6.8. Typical high-pressure stroke piston deformation (bushing deformation not shown).

As can be seen from Fig. 6.8, the piston arcs in a manner that increases the conformity of the piston and bore surfaces at the DC end of the interface, and decreases that conformity at the case end. In this way, the piston deformation enables the buildup of high hydrodynamic pressure over a large area near the DC end, where the surfaces come close over a large axial span, but hinders the buildup of such pressure over an area of similar size near the case end. Hydrodynamic pressure buildup is key to preventing contact; lesser buildup near the case end of the interface contributes to higher correction forces at the case end control point.

While Fig. 6.8 is purely conceptual, Fig. 6.9 (a) plots the *simulated* pressure deformation of the piston corresponding to Baseline Set 1, OC4, at a shaft angle of φ=45°. The axes of the plot are identical to those of the film thickness plots in Fig. 6.1— but the color bar for this plot is not capped. Allowing for better direct comparison between deformation plots, the overlaid contour lines mark multiples of 2 μm (-8 μm, -6 μm, -4 μm... 8 μm in this case). As can be seen, in the region stretching left from Pt. B, the piston deforms radially inwards, while circumferentially opposite, it deforms radially outwards. Together, this results in the described arching of the piston.

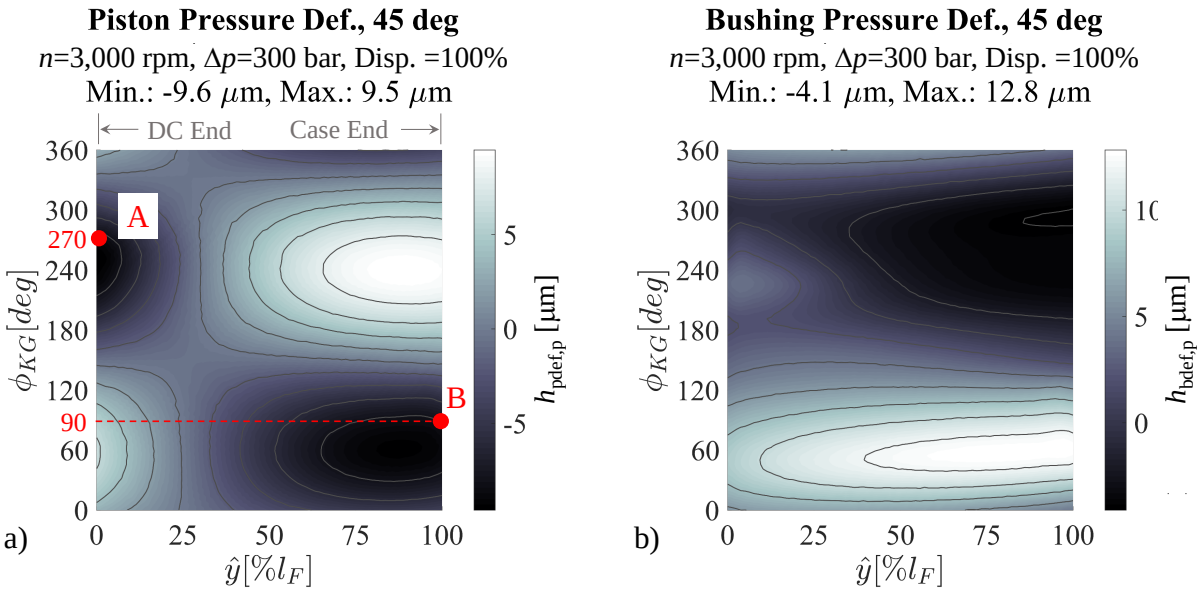

Figure 6.9. a) Piston deformation and b) bushing deformation for Baseline Set 1, at OC4.

Fig. 6.9 (b) shows, in the same format, the deformation of the bushing that was omitted in Fig. 6.8. According to this contour plot, in the region constituting the upper half of the interface sketched in Fig. 6.8, the bore deforms radially outward, and in the lower half, radially inward. In other words, the bushing pressure deformation does not aid the load support predicament in the vicinity of Pt. B.

Having established the effect of piston deformation on the correction forces over the high pressure stroke, two questions remain. First, in what manner does the piston tilt produced by F_{SKy} influence the interface pressure distribution, and second, how does the changed pressure field contribute to not only to the piston deformation, but also directly to the magnitude of the correction forces? In order to answer these questions, the simulated fluid pressure field of the baseline at OC4 must be examined. Fig. 6.10 plots this field over the unwrapped piston-cylinder interface, using the same axes as the film thickness plots of Fig. 6.1, with the color bar capped at the value of the high-pressure port (in this case 325 bar). That pressure value is also marked a thick contour line; the finer contour lines mark pressure increments of 25 bar.

Because of the piston tilt, the contour plots show four distinct pressure regions over the high pressure stroke (φ=45°, φ=90°, and φ=135°). Fig. 6.11 illustrates what these regions typically look like during the high-pressure stroke; it depicts a piston in plane P_1, tilted in its bore as a result of the external forces on it. Regions 1 and 2 are areas near either end of the interface where high hydrodynamic pressure is built as the piston moves and rotates relative to the bore surface; it is where the piston and bore surfaces converge on account of the piston tilt. Region 4 is where the interface opens up to the DC as a result of the piston tilt and deformation, allowing high-pressure fluid from the DC to enter the interface as shown in Fig. 6.8. Lastly, Region 3 is the low-pressure region where the interface opens up to the pump case because of piston tilt. However, region 3 is above case pressure, because fluid from the other regions leaks into it; i.e. from this region, the high pressure in the piston-cylinder interface drains into the low-pressure pump casing.

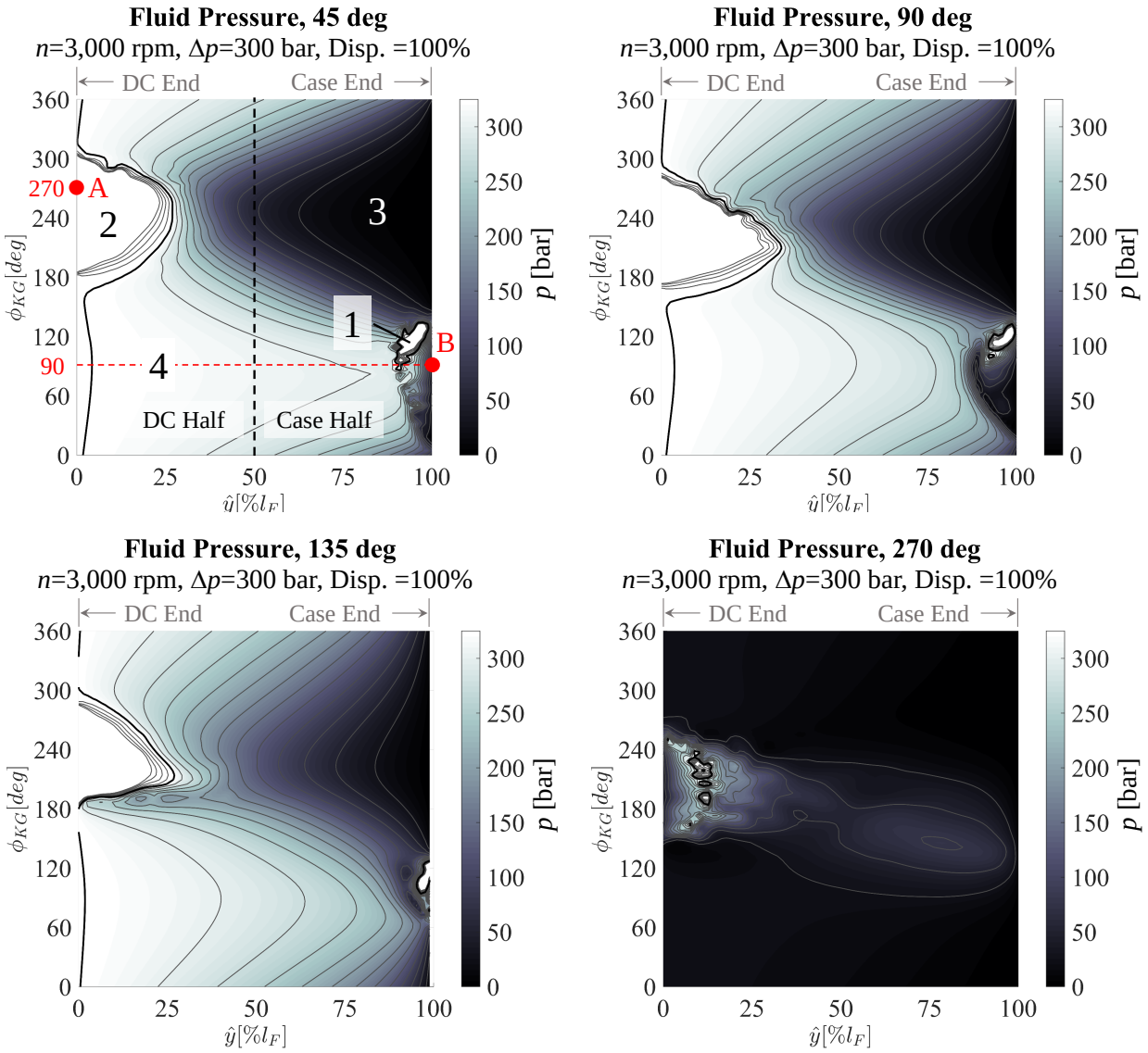

Figure 6.10. Baseline fluid pressure contour plots.

This answers the first question, concerning the effect of piston tilt on the piston-cylinder interface pressure field. In address of the second question, with regards to how that pressure field impacts piston deformation, it can be observed in Fig. 6.11 that the four pressure fields each play a role in molding the piston into the deformed state of Fig. 6.8. The high hydrodynamic pressure buildup of region 1, in conjunction with the incoming DC pressure in region 4, push down on the piston. Simultaneously, the high hydrodynamic pressure buildup in region 2 pushes upwards at the DC end of the interface, as do the external forces near the other end of the interface, namely, the components of $F_{\omega \mathrm{K}}$ and $F_{\omega \mathrm{sKY}}$ that lie in the depicted

plane. The pressure in region 3 is low enough to allow the piston to cave into the shape from Fig. 6.8. Hence, the arched piston.

Finally, as for the direct effect of this pressure field on the correction forces, Fig. 6.11 reveals that fluid pressure can both raise and diminish correction forces. It is the depiction of a balancing act. The hydrodynamic pressure buildup in region 1 helps prevent solid contact near the case end of the interface, therefore (primarily) decreasing the case end correction forces. Furthermore, the pressure buildup in region 1 helps counter the moment on the piston imposed by the external forces acting on the piston head. However, it also pushes down on the piston, which can result in solid contact in Region 2— or increase the severity of any existing contact in that area. Region 2 does the same for the other side of the interface, aiding load support at the DC end, but harming it in region 1. It is therefore critical is to properly balance the forces generated in these two regions.

Region 4, which contains hydrostatic pressure from the DC, pushes down on the piston, driving it toward the bore in region 2, and can therefore contribute to load support problems near the DC end of the interface. Moreover, it contributes to the turning moment M_t of the piston about the center point of the bushing bore; this moment is dangerous in that it forces the piston towards the bore in regions 1 and 2. However, the region 4 pressure does

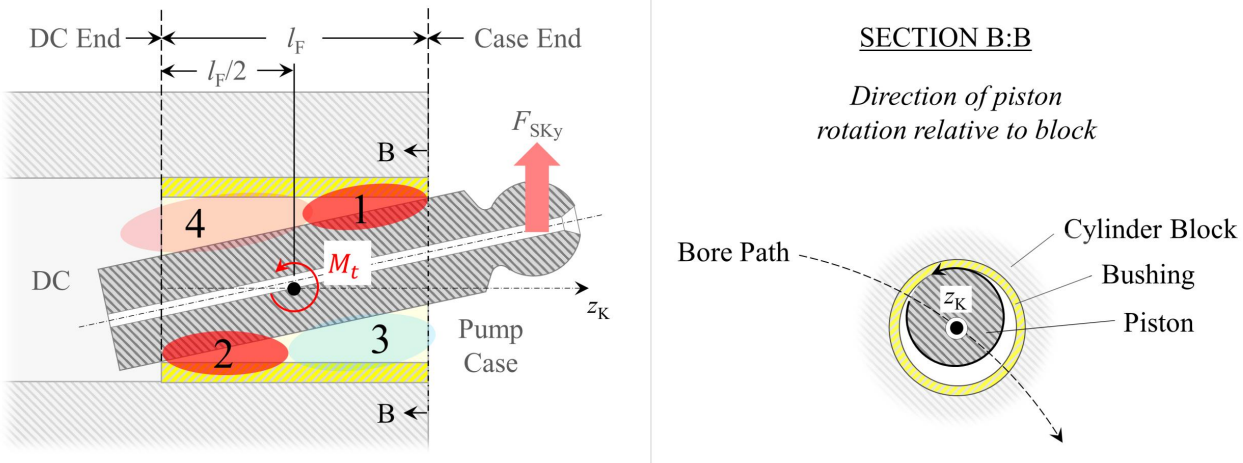

Figure 6.11. Interface during the high-pressure stroke (solid body deformations are not shown).

aid region 1 in countering the forces from regions 2 and 3 that are pushing up on the piston. Region 3 behaves similarly at the case end of the interface, although the magnitude of the pressure it holds is much lower than that of region 4. It pushes the piston up against the bore in region 1, contributes to the turning moment M_t, and aids region 2 in countering the downward force due to the pressure field in regions 1 and 4.

In recognizing the mechanism behind this pressure field, it becomes obvious that the interface is conducting a very delicate balancing act, and that it is not only the magnitude, but also the distribution of the fluid pressure in this interface that decides its load-carrying capacity. According to the correction forces in Fig. 6.5, for Baseline Set 1 at OC4, this balancing act has failed over the high-pressure stroke. The main reason is the insufficient piston-bore surface conformity at either end of the interface, which has led to a deficiency in hydrodynamic buildup, especially in region 1.

The balancing act also fails in the low-pressure stroke. Over this second half of the drive shaft revolution, the DC end correction force is of higher magnitude than the case end force, indicating insufficient hydrodynamic pressure buildup in region 2. Since, as Fig. 6.6 shows, F_{SKy} is much smaller over $\varphi = 180°$-$360°$ than over $\varphi = 0°$-$180°$, over the low-pressure stroke, the piston does not take on the prominent tilt shown in Fig. 6.11. Instead, the fluid forces acting in interface, largely in Regions 2 and 4, pin the piston down at the DC end of the guide length, such as to eliminate need for significant support in the form of solid contact at the case end. This renders the case end correction forces low.

Because $F_{\omega \mathrm{K}}$ is the largest of the non-ifp forces over this stroke, the piston takes on a position predominantly set by the centrifugal effect: pushed close to the bore wall, tilted only slightly by F_{SKy} such as to approach the bore near the DC end of the interface. The low magnitude of F_{SKy}, coupled with the low value of DC pressure, results in a small piston deformation. This means that the piston and bore surfaces come together at a much larger angle, i.e. in a much sharper contact, at the DC end than they would for the high-pressure stroke, over which the deformation aids their convergence. The interface is thus unable to

build sufficient hydrodynamic pressure near the DC end to counter the effect of the moment produced by F_{SKy}, as well as the pressure pushing down on the piston in regions 1 and 4 because of the DC fluid that enters the interface. In consequence, while the case end correction force magnitude is able to remain low, the magnitude at the DC end is considerable.

With the discussion of load support at an end, there are a few things to note on the losses (leakage and viscous friction) through the interface for this baseline. While Set 1 at OC4 fares poorly in load support, the low film thicknesses shown in the film thickness contour plots of Fig. 6.1 indicate low leakage rates. Moreover, since water's viscosity is so much lower than that of traditional hydraulic oil, losses due to viscous friction are generally smaller when using water. This allows for a reasonable power loss at OC4. However, a reasonable power loss is worthless if the interface is not functional on account of solid piston-bore contact.

6.1.3 Summary for All Four OCs

An overview of how the four different operating conditions from Table 6.1 compare in terms of correction forces and power loss is given by Fig. 6.12. As can be seen, OC3 and OC4 constitute the most challenging OCs, with their highest maximum and average correction force magnitudes at the case end control point. This is the challenge that must be addressed by surface shaping: the correction forces should be brought to zero, without excessive compromises in power loss.

6.2 Baseline Set 2: Oil as Hydraulic Fluid

Baseline Set 2 uses hydraulic oil as the working fluid; this set allows the performance of designs tested virtually (in simulation) with water to be assessed in terms of whether they render the APMSPD competitive against a stock unit running on oil. To this end, the Set 2 simulations use the original, unaltered geometry of the 75 cc unit being modeled, which, as in Ch. 4, includes the wear profile on the bushing bores measured by Busquets (see [31]). As a basis to start from, the performance of the simulations from baseline Set 1 can be compared to that of the simulations from Set 2 by comparing Fig. 6.12 to Fig. 6.13.

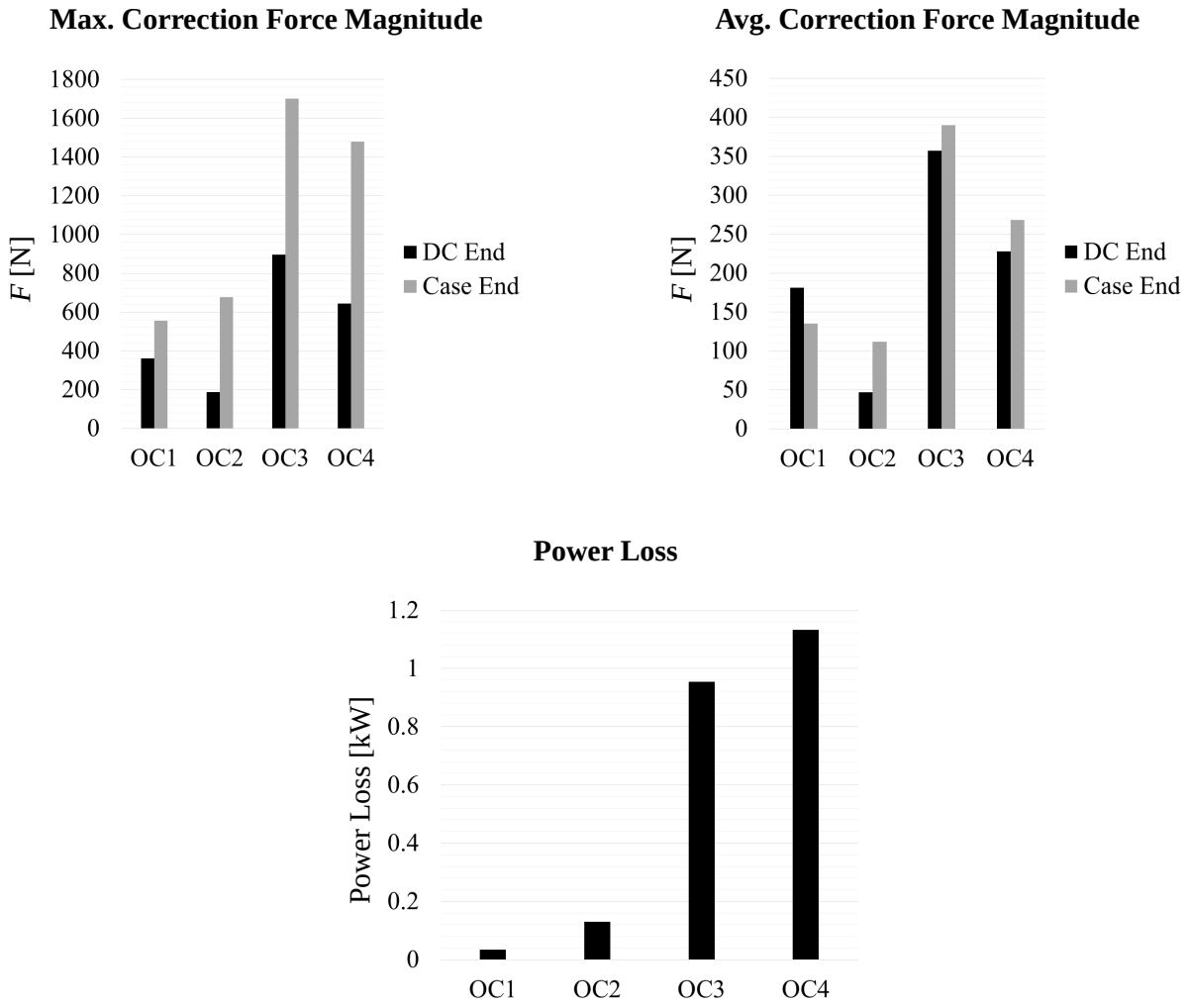

Figure 6.12. Interface performance for Set 1 at OC1-4.

As can be seen, when the working fluid is oil and the unit is run in, the maximum and average correction force magnitudes are practically zero: the simulations predicts no significant metal-to-metal contact, i.e. full-film lubrication. This stands in sharp contrast to Set 1, for which severe contact is predicted. The difference in power loss is not as dramatic, partly on account of the trade-off between torque loss and leakage. Due to water's lower viscosity, the torque loss due to viscous friction is lower for the Set 1 baseline at OC1-4, but the leakage is higher at OC3-4 (at OC1-2, the leakages are similar, indicating that the non-fluid differences between the two sets are mitigating the difference made by fluid viscosity). On account of the lower torque losses associated with Set 1, power loss due to viscous flow is lower for this

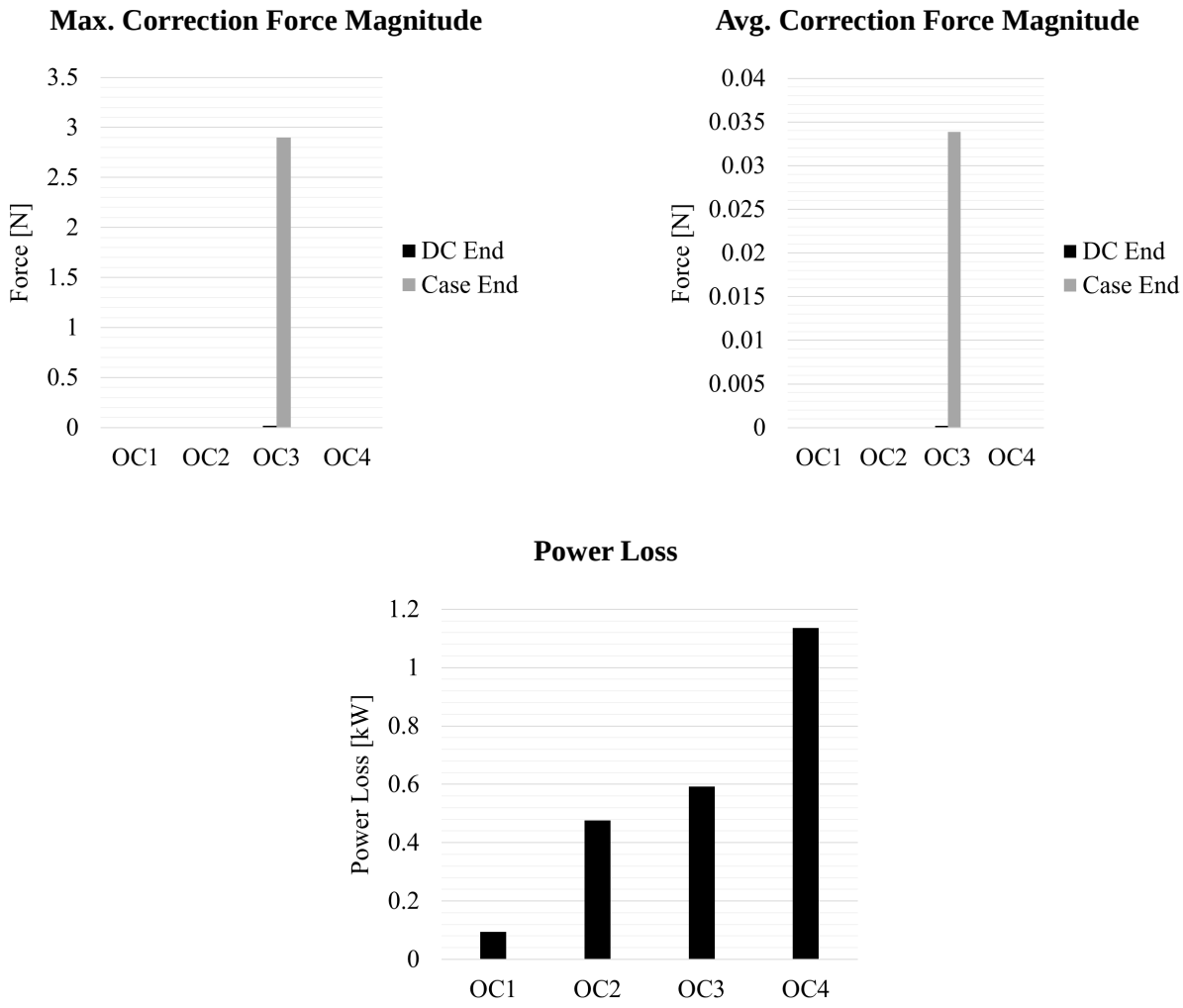

Figure 6.13. Interface performance for Set 2 at OC1-4.

set at OC1-2, but due to the higher leakage rates associated with Set 1 at OC3-4, power loss is lower for Set 2 at OC3, and roughly the same at OC4. It should be noted, however, that losses due to mixed/solid friction are not included in this— according to the plotted correction force magnitudes, however, these will be far higher for Set 1 than Set 2.

6.3 Summary/Conclusions vis-á-vis the Baseline Simulations

Simulation results for piston-cylinder interfaces of a 75 cc unit running at four different operating conditions have been presented, first for the case of water as the working fluid, and second, for the case of hydraulic oil as the working fluid. The results include both the load

support achieved by these interfaces, as well as the power loss they incur. The unit was simulated without any pre-wear surface shaping on the surfaces that form its piston-cylinder interfaces. The results of these simulations therefore represent a baseline, against which later studies conducted with surface shaping at this interface can be compared.

From the simulation results presented, it can be seen that load support at the piston-cylinder interface is a balancing act. It is important to understand that when it comes to preventing metal-to-metal contact, it is the *balance* of the forces acting on the piston, not their magnitude, that is key. Furthermore, it is important to note that, inasmuch as the generation of hydrodynamic pressure can prevent solid contact locally, both hydrodynamic pressure buildup and hydrostatic pressure *can contribute to interface failure*, depending on how they are distributed. That is, in context of the large-scale balancing act of the interface, the pressure in the fluid film is as much part of the problem as it is part of the solution.

For the simulated baseline, the balancing act fails. The surface shapes examined in subsequent chapters aim to address this failure by changing the fluid pressure distribution in the interface, such as to establish a more favorable balance of forces.

7. CONCAVE BORE PROFILE

7.1 Introduction to the Concave Bore Profile

As has been explained, surface shaping is a powerful tool in piston-cylinder interface design, because, as the Reynolds equation described in Ch. 3 states, and as will be demonstrated shortly via FSTI, changing the film thickness— on the order of *microns*— can have a significant effect on the buildup and distribution of pressure within the interface. Although many different surface shapes could be investigated, one of particular interest for water-lubricated piston-cylinder interfaces is the concave bore shape investigated in [31], [58], [59]. This shape is applied to the surface of the bore that the piston traverses; it is radially symmetric about the central axis of that bore, its form arising from the profile (the lengthwise cross-section) shown in Fig. 7.1. The profile consists of a circular arc, defined by a radius R, and a shift l_s— the shaping is on the order of microns in height, but has been exaggerated in this illustration in order to make it visible to the naked eye. The shift is a measure of how far the profile's apex has been moved along the z_K-axis from $z_K = l_{F,max}/2$, where $l_{F,max}$ is the maximum guide length over a shaft revolution: a shift towards the case end of the interface is considered positive, and a shift towards the DC end, negative.

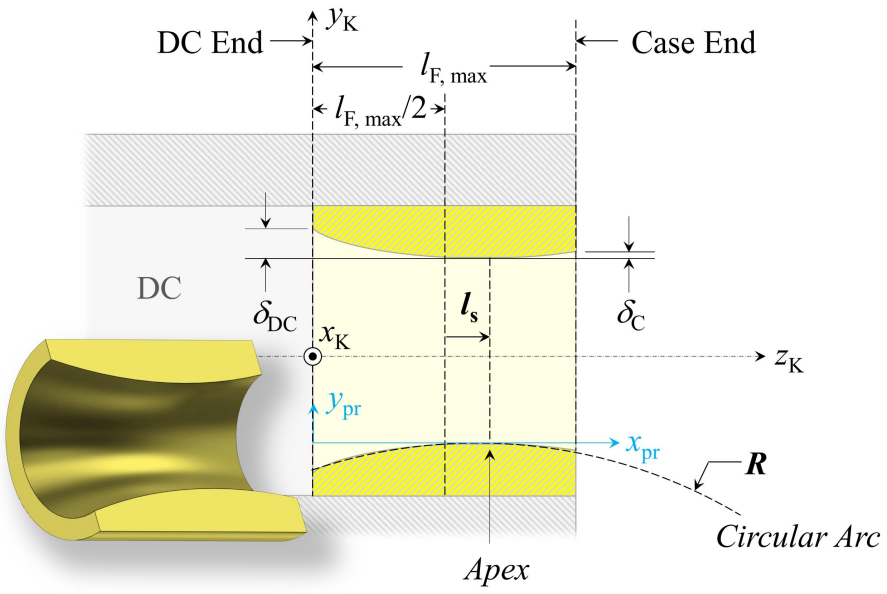

Figure 7.1. Concave bore profile (image based on [59], not to scale).

It should be pointed out that the present work focuses heavily on surface shaping designs made for implementation on a fixed guide length, when the axial extent l_F of the piston-cylinder interface remains constant over the course of the drive shaft revolution. This is because if the guide length is variable, meaning that l_F is not constant (e.g. because the flat end of the piston is inside the bushing), then the piston tilt changes so much with shaft angle that the shape's performance also varies significantly, and can be greatly compromised over parts of the shaft revolution. For the sake of full disclosure, the guide length l_F of the 75 cc unit that will be used for the design studies of the subsequent sections is not completely constant— it shortens when, approaching the conclusion of the high-pressure stroke, the end of the piston running surface nearest the piston head moves into the bushing, and subsequently extends again as, over the beginning of the low-pressure stroke, that end of the running surface moves out of the bushing. While this change takes place from $\varphi = \sim 130°$ to $\varphi = \sim 230°$, i.e. not over the critical first half of the high-pressure stroke, it can have significant effects, which are instructive to see, and which will be included in the discussion of the studies to be presented.

7.2 What Makes this Profile Worth Investigating?

The concave bore shape can, depending on the radius and shift, offer two concrete advantages over a cylindrical bore— specifically during the high-pressure stroke, when load support deficiency tends to be most prominent. First, it can increase the degree of longitudinal conformity between the piston and bore surfaces where they come together, which, in turn, enables the buildup of hydrodynamic pressure over a larger area. That buildup protects the surfaces from engaging in solid contact, and from the solid friction and wear associated therewith. Fig. 7.2 illustrates how this surface conformity compares over the high-pressure stroke for the case when the bore is cylindrical image (a), versus the case when the concave bore surface shape is imposed on it image (b). Due to the manner in which the side load deforms the piston, near the case end of the interface, the cylindrical bore results in sharp contact (see the region near Pt. A); near the DC end (in the vicinity of Pt. B), the piston deformation aids in providing surface conformity, though not necessarily to a degree sufficient for full load support. In either case, the concave bore profile, shown in image (b), allows the

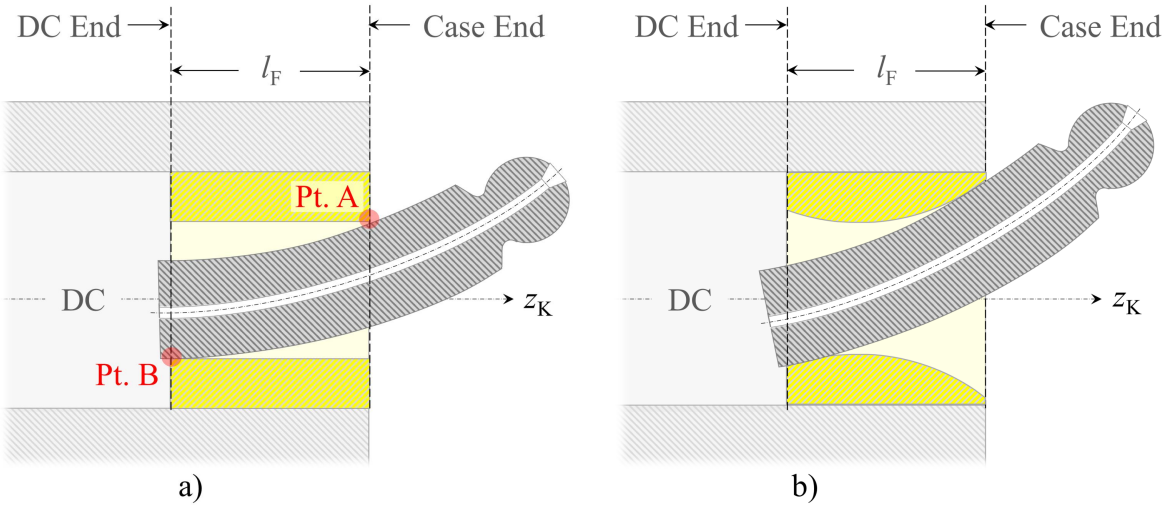

Figure 7.2. a) Cylindrical bore, b) bore with concave bore surface shape imposed on it (bushing deformation not shown).

piston and bore surfaces to converge more smoothly, and remain close over a longer stretch, in a manner conducive to hydrodynamic pressure buildup.

It is important to note that the surfaces should not conform to the point of being nearly, or even completely, parallel, as this eliminates the wedge effect (the effect captured by the wedge term in the Reynolds equation) that is so critical to generating hydrodynamic pressure. Rather, the conformity produced via surface shaping should promote this effect: firstly, by bringing the surfaces close enough together, and secondly, by providing a surface convergence shape favorable to this type of pressure buildup in both the axial and radial directions. Furthermore, it should be noted that although designing for longitudinal surface conformity provides more area for hydrodynamic pressure buildup, a surface shaping that promotes a high degree of surface conformity does not necessarily produce more total hydrodynamic pressure than a shaping that promotes a lower degree of conformity.

This is because, beyond changing the pressure buildup in the area(s) whose surface conformity it is designed to increase, the shaping may also change other parts of the pressure field, thereby altering the forces due to fluid pressure acting on the piston in those regions. Changing these forces, i.e. changing the overall balance of forces acting on the piston, in

turn, can change how the piston and bore surfaces deform and converge, and thus how much hydrodynamic pressure is ultimately built in the region(s) of interest. This can lead the shaping conducive to a high degree of surface conformity to ultimately produce a lower total pressure buildup than its low-conformity counterpart.

However, this does not mean that the high-conformity shape provides a lesser degree of load support. On the contrary: depending on how it affects the overall pressure field and force balance on the piston, the high-conformity shape can lower the pressure buildup that is required to prevent solid piston-bore contact. In short, a shape conducive to a greater surface conformity is better able to supply the *needed* hydrodynamic pressure buildup for the piston-cylinder interface, but the measure of that needed pressure buildup can differ significantly from that of a shape not conducive to surface conformity.

In fact, the second merit of the concave bore profile is that it can reduce said needed measure. More specifically, during the high-pressure stroke, this type of surface shape helps to drain away some of the pressure in the region of the fluid film located circumferentially opposite Pt. A, marked as region 3 in Fig. 7.3. In doing so, it lowers the contribution made by the pressure in that region to the side-load-induced turning moment on the piston (about the fluid film's center point), which drives it toward collision with the bore at either end of the guide length. The concave bore profile is able to aid in draining away region 3 pressure because its implementation increases the film thickness of that region from what it would be for a cylindrical (unshaped) bore, thereby widening the passage into the pump case.

As a result of the enlarged connection, the fluid pressure within region 3, which builds above pump case pressure through the influx of fluid from the DC, as well as from regions within the interface undergoing hydrodynamic pressure buildup, is able to dissipate to a greater degree. Less pressure in region 3 is advantageous, because any pressure in this region that is in the half of the interface nearest the case end increases the aforementioned turning moment on the piston, and, moreover, pressure anywhere in region 3 pushes the piston towards the circumferentially opposite side of the interface— into the bore in region 1. Lower pressure in

region 3 therefore means that preventing piston-bore contact, especially in region 1, requires less hydrodynamic pressure buildup.

Besides providing these two advantages on the load support front, the concave bore surface shape also lends itself to reducing power loss in APMSPD running on hydraulic oil; its effectiveness in this context is investigated by Busquets [31], who finds it to deliver a significant performance improvement. Furthermore, as stated in Ch. 5, a similar shape has been studied by Gels and Murrenhoff [48]— in the interest of both, increasing efficiency, and enabling the use of harder materials at the interface (by introducing surface contouring that eliminates the need for the interface-forming components to wear in). However, that bore shaping is defined by four parameters— two radii, and two lengths— with the design study varying one radius-length parameter pair at a time.

Because the design handled in this work is defined by only two parameters, a more complete study of the available design space can be undertaken. Beyond this, the present work distinguishes itself from both of the aforementioned two in that it strives to examine, in detail, how and why load support changes across the design space (i.e. as the radius and shift of the concave bore profile are varied). Lastly, the present work focuses on assessing the

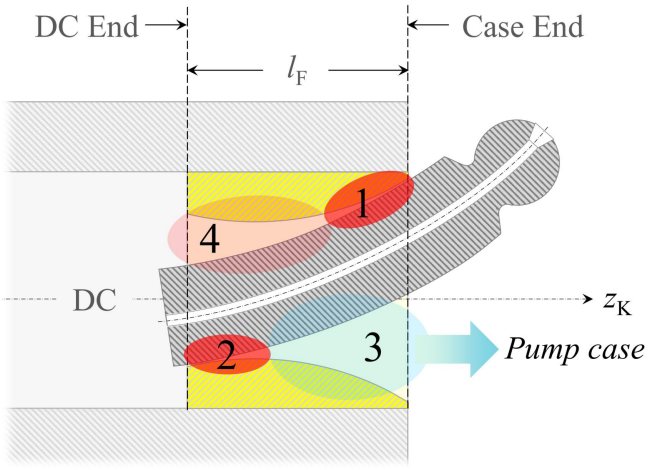

Figure 7.3. Fluid regions in the piston-cylinder interface (with concave bore profile) during the high-pressure stroke.

performance of these dimensional variations in an APMSPD with the working fluid *water*, which, as the baseline simulations have already shown, produces very different power loss values than oil— because its low viscosity begets less viscous friction, and more leakage.

7.3 Design Studies

Delivering on these points, two design studies will be presented in this section. The first focuses exclusively on the concave bore profile: it maps out the relationship between the dimensions of its two defining parameters (R and l_s), and the behavior of the interface in terms of load support and power loss; two similar studies conducted by the author and Ivantysynova can be found in [58], [59]. The study is split into two parts, the first examining profiles with a negative shift ($l_s \leq 0\%\ l_{F,max}$), and the second, profiles with a positive shift ($l_s \geq 0\%\ l_{F,max}$). The second study addresses the point that it can be less expensive to machine the piston running surface than the bore surface. Comparing the performance of the concave bore profile to that of a barrel piston profile— i.e. comparing the performance that results from imposing the circular arc profile on the bore, versus on the piston— this study demonstrates why the concave bore profile can be worth the extra expense.

To render the simulations of both studies comparable to the Ch. 6 baselines, they are set up using the same 75 cc pump geometry and materials as baseline Set 1, and their minimum nominal diametrical piston-bore clearance (the clearance at the surface shape apex) is the same as the nominal diametrical clearance of that baseline. Furthermore, both studies are run at OC 4 from Ch. 6: 100% displacement, $\triangle P$=300 bar, 3,000 rpm. The hydraulic fluid used is, of course, water.

7.3.1 Study 1: Concave Bore Profile

Profile with Negative Shift ($l_s \leq 0\%\ l_{F,max}$)

The design space for this first part of the concave bore profile study is set up such that $l_s \leq 0\%\ l_{F,max}$, and, such that the dimensions δ_C and δ_{DC} marked in Fig. 7.1, i.e. the

deviation of the shaping from a cylindrical bore at the DC and case ends of the maximum guide length, respectively, are restricted to the domain:

$$0.09660\mu\text{m/mm} \leq \{\delta_{DC}/d_{\text{K}}, \delta_C/d_{\text{K}}\} \leq 1.449\mu\text{m/mm}$$

Why this domain? As the radius increases in value, the concave bore profile becomes flatter—and as the deviation of the profile from the flat line that would correspond to a cylindrical bore diminishes, it becomes more and more difficult to manufacture. Hence, some lower limit has to be imposed on δ_C and δ_{DC}. 0.09660μm/mm was chosen as a starting point for that limit, and as will be seen from the simulation results, the opposing trends of power loss and load support eliminate the need to explore lower values. Furthermore, the use of FSTI necessitates the imposition of an upper bound that prevents the interface film thickness from becoming so high as to call into question the validity of FSTI's laminar flow assumption.

The design space described by these limits is shown in Fig. 7.4(a). On the x-axis is the concave bore profile radius, expressed as a percentage of the guide length (divided by 1000 in order to render the scale more readable). On the y-axis is the profile shift, also expressed as a percentage of the guide length. Since the region shown is relatively simple in shape, the

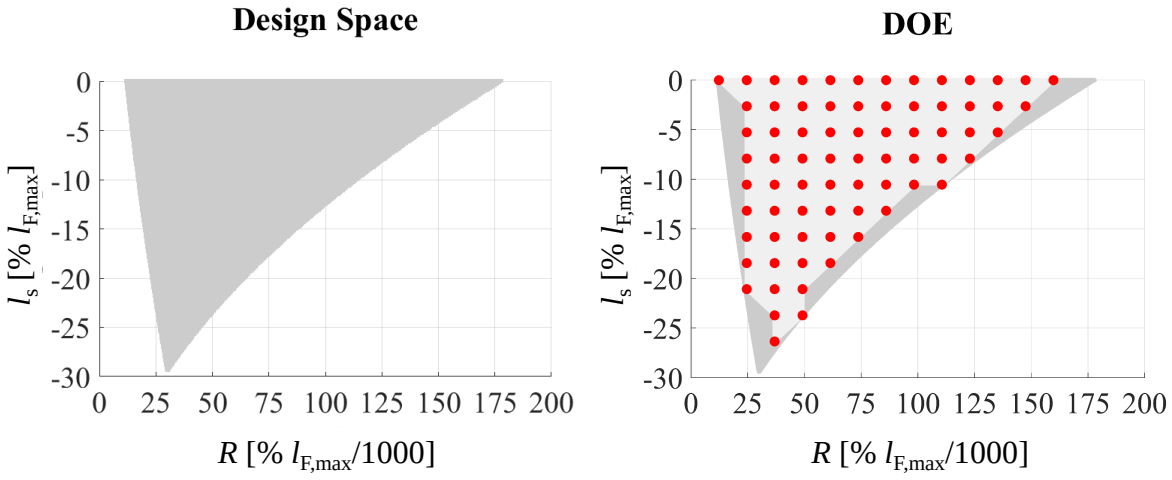

Figure 7.4. a) Design space, and b) DOE, for $l_s \leq 0\%\ l_{F,max}$.

DOE (design of experiments) for this study— i.e. the choice of which points in the design space should be simulated— is a uniform grid: see Fig. 7.4(b). The most critical simulation results for the points in this grid are presented in Fig. 7.5 and Fig. 7.6; the former speaks toward the impact of the concave bore profile on pump efficiency, and the latter, toward its impact on the load support capacity of the piston-cylinder interface fluid film. These will now be addressed in detail, starting with Fig. 7.5.

Fig. 7.5(a) plots (in red), for each DOE grid point, the total power loss incurred by the piston-cylinder interfaces in the APMSPD being simulated— when the bore profile design corresponding to that grid point is implemented on all of them. Since FSTI simulates only one, single piston-cylinder interface, this total power loss is obtained by multiplying the loss computed for that single interface by the number of these interfaces in the unit (nine), under the assumption that they all behave the same. It should be noted that losses due to mixed and solid friction are excluded from the power loss values shown. This is because FSTI, being made to analyze units operating in— and to design units for operating in— the full-film lubrication regime, does not model either of these effects. Furthermore, it should be

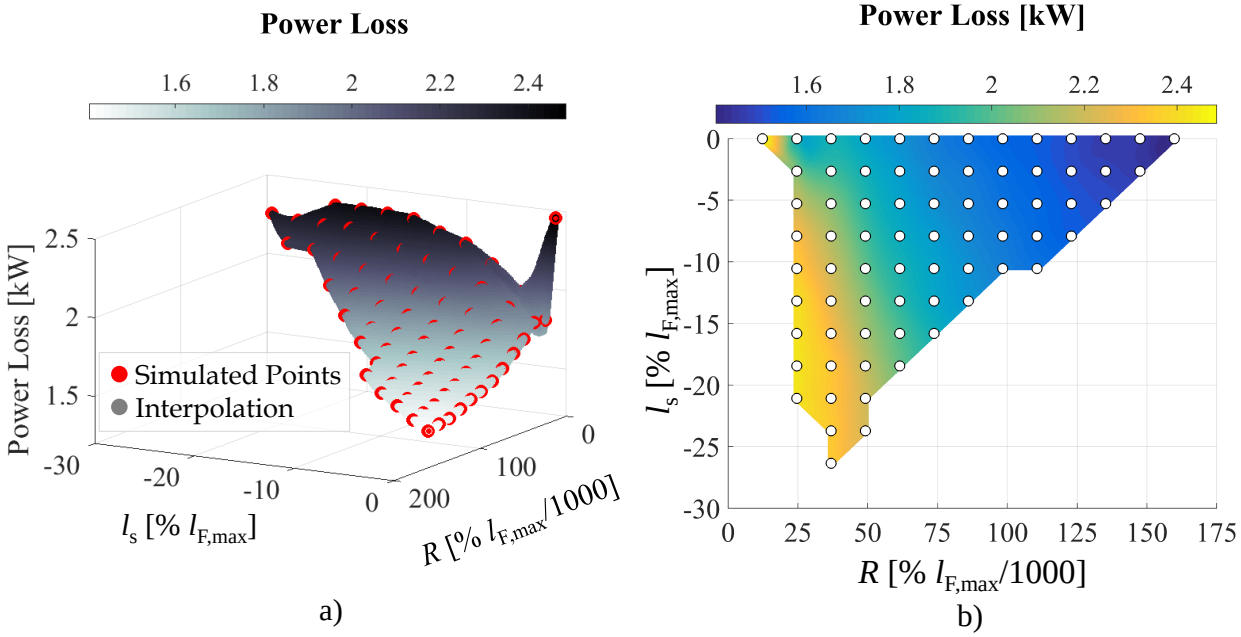

Figure 7.5. For the DOE grid over which $l_s \leq 0\% l_{F,max}$: power loss at OC4.

noted that since the energy dissipation of the interface fluid film changes with shaft angle, the power loss values shown are a time-based average over the simulated revolution.

In addition to the power loss values corresponding to the simulated DOE grid points, Fig. 7.5(a) also shows a radial basis function interpolation of these values, covering the region within the design space that they encompass (i.e. the light gray area in Fig. 7.4b). Fig. 7.5(b) plots this interpolation in color, with the locations of the simulated points marked in; it provides a clearer view of trends across the design space. From this plot it can be seen that, within the span of the simulated grid, the power loss tends to decrease as the radius, R, increases. Over the majority of the design space under study, one of the main contributors to this trend is the decrease in leakage with increasing radius. As the radius grows, i.e. as the profile flattens, the bore diameter on either side of the profile apex decreases. This helps narrow decisive sections of leakage path, which, at least over part of the high-pressure stroke, suffices to lessen the rate of flow through the interface. However, it should be noted that, for $(l_s = 0\% l_{F,max}) \cap (R \leq 49.17\% l_{F,max}/1000)$, and for $(l_s < 0\% l_{F,max}) \cap (R \leq 36.88\% l_{F,max}/1000)$, a reduction in torque loss dominates— and the leakage rate actually increases with radius.

Most likely, this effect on the leakage largely comes about because profiles of lower radius (higher curvature) allow for a more pronounced piston tilt. A greater tilt can aid in slowing the leakage flow by blocking off, for a portion of the streamlines, the straight path through the interface that runs parallel to the bore centerline, and by narrowing key parts of the leakage path. This is especially important because the centrifugal effect can move the piston to one side of the bore, opening a wide leakage path on the circumferentially opposite side; if, instead of sitting straight against the wall, the piston is allowed to tilt, then at least part of that path can be blocked. As the radius increases, and the extent to which the piston can tilt becomes more and more limited, less and less flow can be blocked in this manner, causing an increase in leakage with radius. Once the radius reaches a certain magnitude, however, the described effect of tilt is overshadowed by the impact of the profile's flattening on bore diameter, giving way to the trend of decreasing leakage with increasing radius.

The shift, l_s, also plays a decisive role: especially at the lower of the simulated radii, Fig. 7.5(b) clearly shows a rise in power loss as the magnitude of the negative shift increases. This trend is driven almost exclusively by a rise in leakage with shift magnitude. The larger $|l_s|$, i.e. the further the profile apex is moved towards the DC end of the guide length, the more region 3 (refer back to Fig. 7.3) opens up, axially extending further and further towards the DC. Consequentially, the path of DC fluid into a region of high film thickness that is wide open to the pump case becomes shorter. Simultaneously, the constriction in the leakage passage created by the centrifugal effect opens up, its film thickness increasing with $|l_s|$. The result is a higher leakage rate for profiles with larger $|l_s|$. However, towards the right end of the plotted design space, where the radius R becomes very large, and the profile extremely flat, this shift-driven trend fades away; that is, the l_s is of import mainly for profiles with pronounced curvature.

With the radius- and shift-driven power loss trends established, the effect of R and l_s on the load support capacity of the fluid film will now be examined— first, in the context of correction force magnitudes. These are plotted in Fig. 7.6; more specifically, Fig. 7.6 shows the maximum, and the average, of the DC end correction force magnitude (the correction force magnitude at control point C_A), and of the case end correction force magnitude (magnitude at control point C_B), over the course of a full simulated drive shaft revolution. The four parameters are graphed over the DOE-enclosed design space, in the same format as Fig. 7.5(b).

If FSTI does not predict any piston-bore contact, then the value of those four parameters is zero. As can be seen from Fig. 7.6, within the plotted design space, the desired zero is not quite achieved— however, a significant reduction in the maximum and average correction force magnitude from those of the Ch. 6 baseline (no surface shaping) *is*. Fig. 7.7 shows this, providing a direct comparison of the DC and case end maximum and average correction force magnitudes of the baseline, versus those of two concave bore designs: Design A and Design B. Design A is the profile design, out of those simulated, that is most able to reduce the maximum correction force magnitude at the DC end control point, while Design B is the design most able to reduce it at the case end control point.

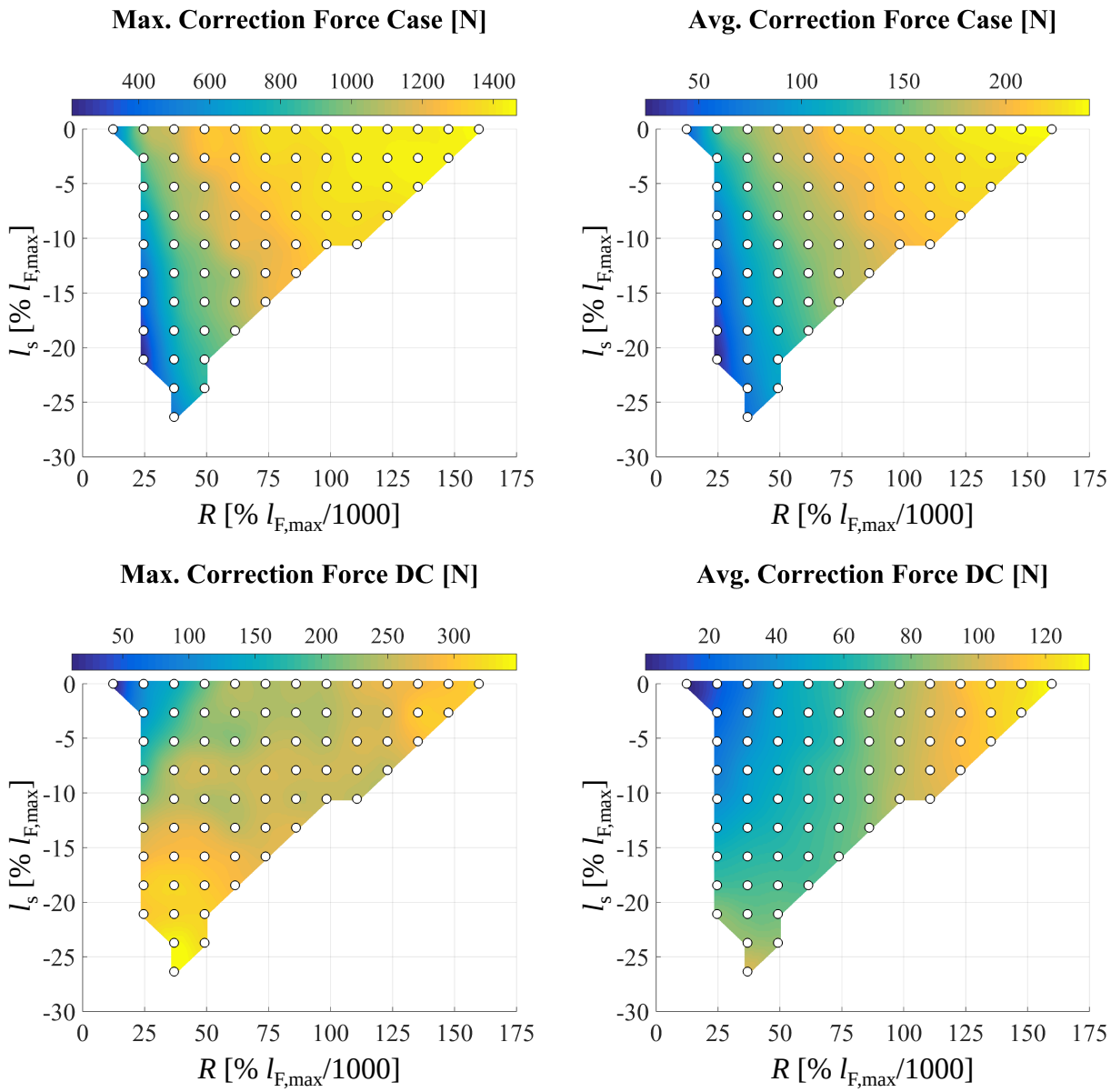

Figure 7.6. For the DOE grid over which $l_s \leq 0\% l_{F,max}$: max. and avg. correction force magnitudes of the simulated shaft revolution at the DC and case end control points (C_A and C_B, respectively), at OC4.

The locations of these two within the design space are marked in Fig. 7.7(a)— and the comparisons of their maximum, and average, correction force magnitudes to those of the baseline are shown in Fig. 7.7(b) and (c), respectively. From these plots, it can be seen why the concave bore profile, and the trends associated with it, are worth investigating: this type of profile has the potential to drastically reduce the severity of piston-bore contact. At the DC

end control point, Design A nearly brings both the maximum and average correction force magnitudes to zero, while Design B more than cuts the baseline values in half. At the case end control point, Design A achieves an improvement of more than 60% over the baseline for the maximum correction force magnitude, and an improvement of roughly 80% for the average correction force magnitude; Design B achieves more than an 80% improvement for the former, and more than a 90% improvement for the latter.

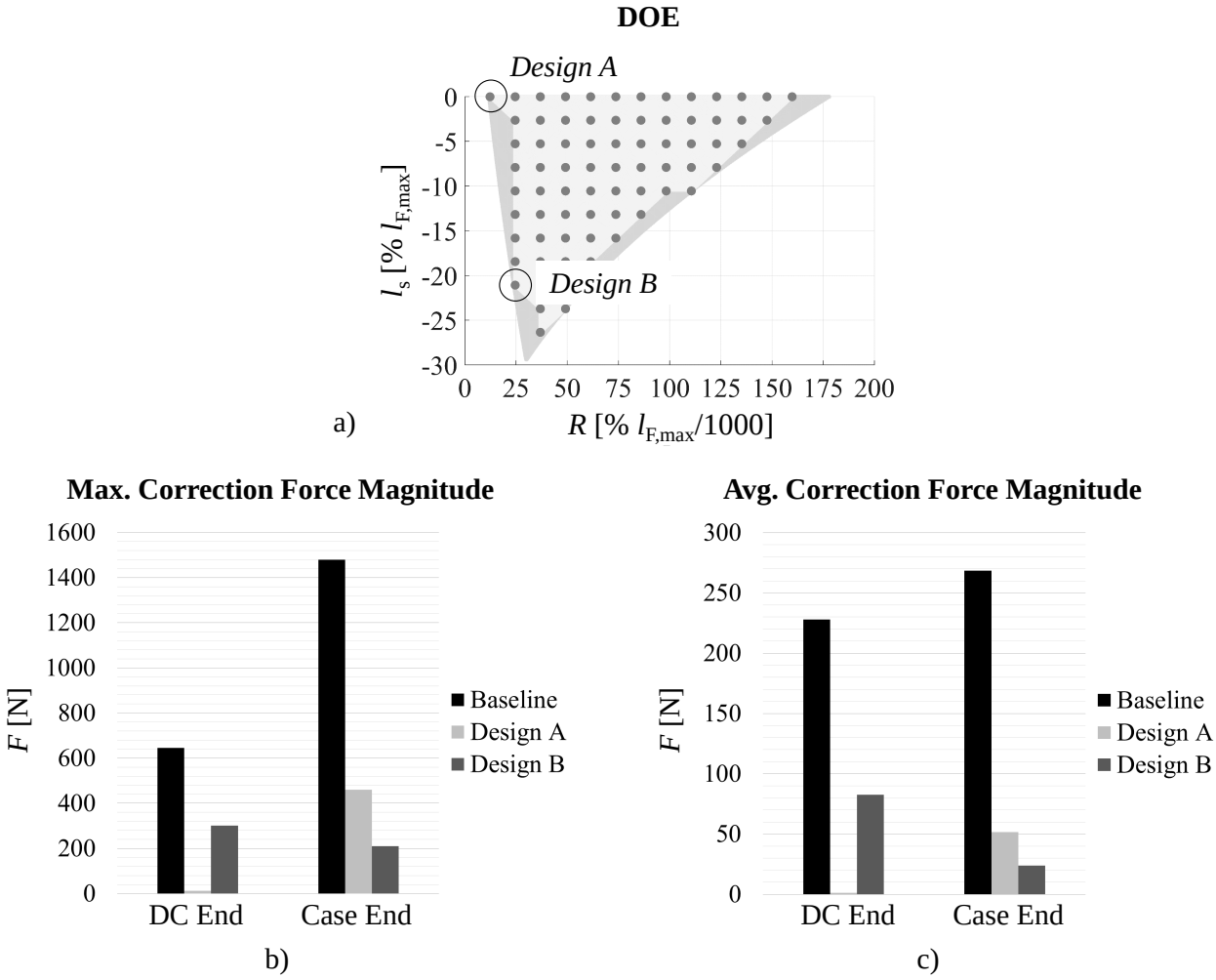

Figure 7.7. Load support comparison of Design A ($R = 12.29\% l_{\mathrm{F,max}}/1000$, $l_{\mathrm{s}} = 0.000\% l_{\mathrm{F,max}}$) and Design B ($R = 24.59\% l_{\mathrm{F,max}}/1000$, $l_{\mathrm{s}} = -21.07\% l_{\mathrm{F,max}}$) to the baseline at OC4.

How are these improvements achieved, and, why do Designs A and B rank among the most successful of those simulated? An understanding of the trends in correction force magnitude across the design space spanned by profile radius and shift provides answers for these, and many other important questions regarding this type of surface shaping. From Fig. 7.7(a), it can be seen that Designs A and B have two of the smallest radius values in the DOE grid, while their shift values fall towards either end of the range covered by that grid. The correction force trends that drive designs A and B towards these positions within the design space clearly show in Fig. 7.6.

From these plots it can be observed that, at both control points, the maximum and average correction force magnitudes tend to increase with radius— i.e. they increase in moving towards the right end of the DOE grid. Because of this, both Design A and Design B fall towards the left end, where the radii are small. Furthermore, it can be seen that at the case end control point, the plotted parameters decrease in value as the magnitude of the negative shift increases, while at the DC end control point, the opposite trend emerges. Hence, Design A, the design with the lowest maximum correction force magnitude at the DC end control point, has a shift magnitude of zero, whereas Design B, with the lowest maximum correction force magnitude at the case end control point, has one of the largest shift magnitudes in the simulated grid.

Where do these trends come from? The increase in maximum and average correction force magnitude with radius will be examined first. This trend is largely related to the two advantages of the concave bore profile that were described in section 7.2, both of them pertaining mainly to the high-pressure stroke. First, this type of profile can increase the longitudinal piston-bore surface conformity at either end of a fixed guide length, thereby increasing the area over which significant hydrodynamic pressure buildup can take place, and second, it can open the interface up more to the low-pressure fluid in the pump case, thus lessening the pressure (in region 3) that contributes to the turning moment on the piston. Within the limits of the DOE grid used in this study, these advantages become more pronounced as the radius becomes smaller.

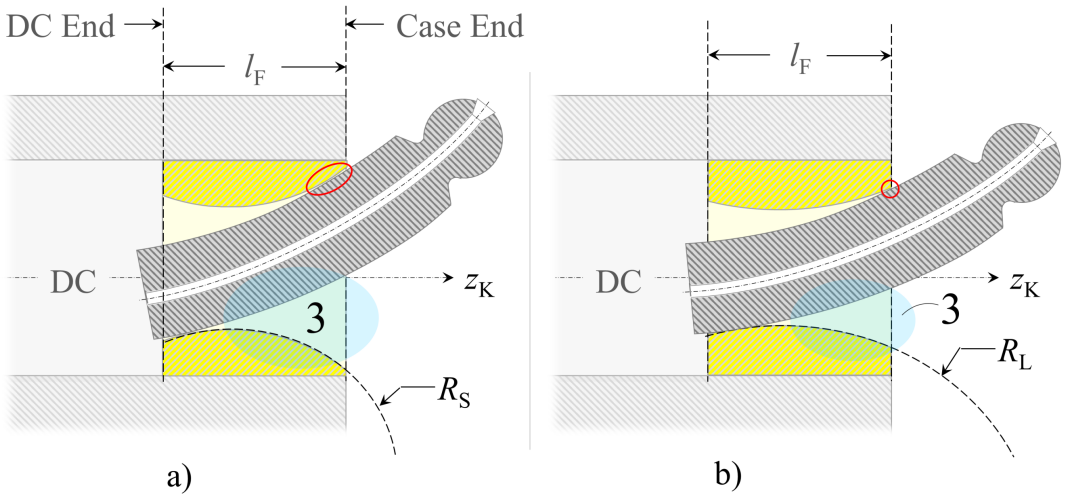

Figure 7.8. Comparison of concave bore profiles with a) a small radius, versus b) a large radius, during the high-pressure stroke.

Fig. 7.8 illustrates, depicting a cross-section of the piston-cylinder interface during the high-pressure stroke when two different concave bore profiles are implemented: one with a small radius R_S (image a), and one with a large radius R_L (image b). As can be seen, near the case end of the interface, the region of piston-bore surface conformity (circled in red) is significantly longer for the profile with R_S, than for the one with R_L. Near the DC end, the effect of radius with regards to this appears small; the concave bore profile *can* elongate the region of conformity there, but whether it does so, and to what extent, depends heavily on the profile shift l_s. For either end, it should be kept in mind that, as already explained in Section 7.2, a larger area of high surface conformity does not necessarily translate into more pressure buildup— rather, it means that more area is available to build the *required* amount of pressure (for preventing solid component contact), which the effects of the profile on the fluid pressure field, piston eccentricity and/or deformation, may lower. In addition to its effect on piston-bore conformity, the radius also changes the degree to which region 3 opens up to the pump case: as can be seen from the illustration, the profile with R_S causes this region to open wider than that with R_L; hence, R_S allows more of the pressure in that region to dissipate into the pump case.

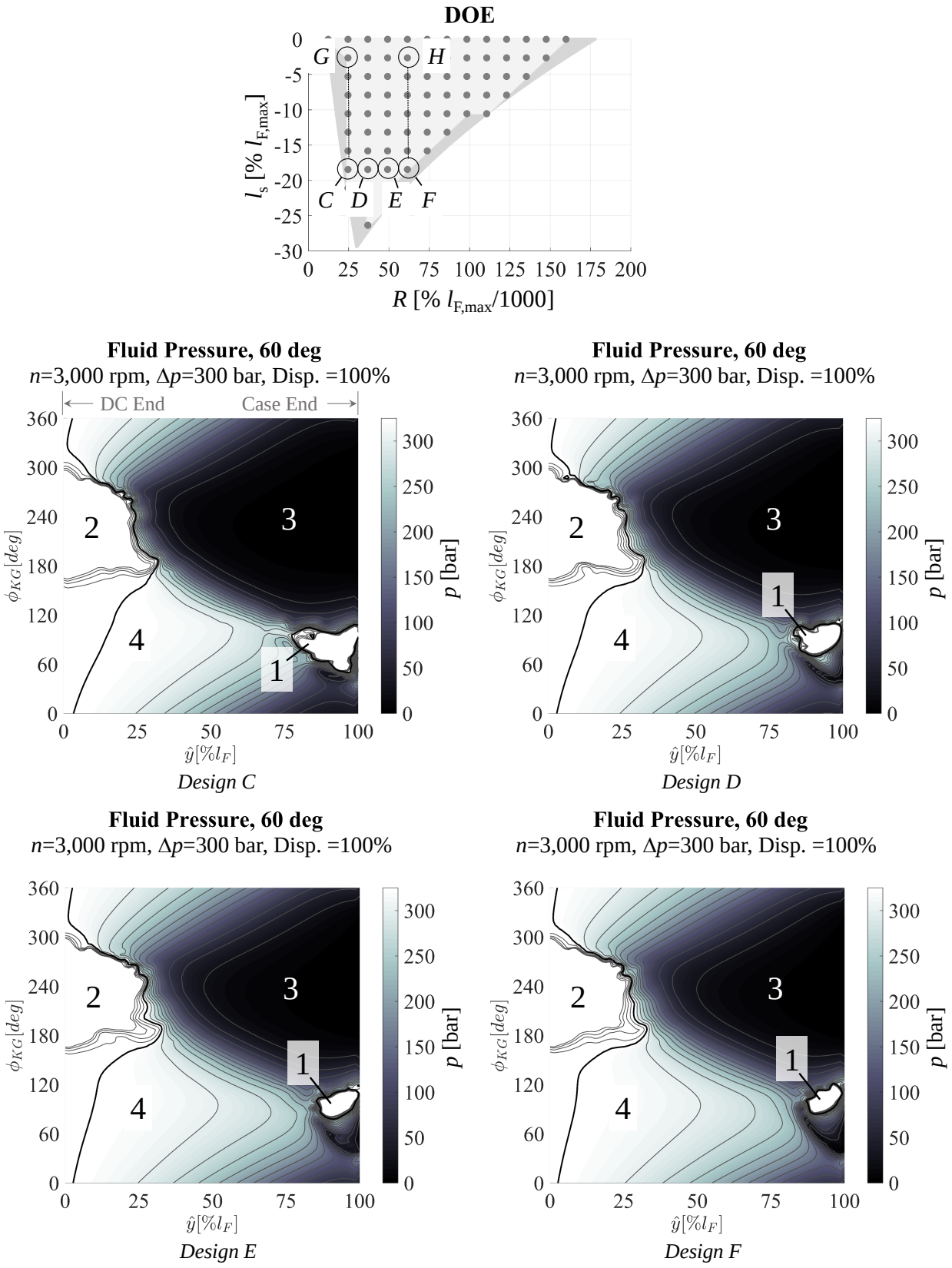

Figure 7.9. Fluid pressure fields of Design C-F ($l_s = -18.44\%l_{F,max}$, and $R = 24.59\%l_{F,max}/1000$, $36.88\%l_{F,max}/1000$, $49.17\%l_{F,max}/1000$, and $61.47\%l_{F,max}/1000$, respectively), at OC4, $\varphi = 60°$.

Fig. 7.9 demonstrates these two effects, using the four simulated profile designs from the DOE grid that have a shift of $l_s = -18.44\% l_{F,max}$. Shown are the locations of these designs— designs C-F— within the design space, and the corresponding interface fluid pressure fields at OC4, at a shaft angle of $\varphi = 60°$. The plots are in same format as the fluid field contour plots of the baseline in Ch. 6. Since the color bar is cut off at the nominal HP port pressure, the white regions near the case end (right end) of the interface indicate hydrodynamic pressure buildup in region 1. From these plots, it is apparent that the most longitudinally extensive region 1 footprint belongs to Design C, the profile design with the smallest radius, and the least longitudinally extensive region 1 footprint, to Design F, the design with the largest radius. The area over which region 1 extends, i.e. the area over which significant hydrodynamic pressure builds near the case end of the interface, shrinks as the radius grows. Furthermore, as the radius increases, the darkest section of region 3, indicating its lowest pressure, shrinks. This indicates that, as explained, when the radius becomes larger, less of the pressure in region 3 is able to dissipate into the pump case.

These effects drive the trends that render designs A and B successful; their prominence for these two designs can be observed in Fig. 7.10, which provides a direct comparison of their fluid pressure fields with that of the baseline, at OC4 and $\varphi = 60°$. The baseline, which has no surface shaping, is essentially a concave bore profile of infinite radius— as such, it exhibits a smaller region 1, and a smaller low-pressure section of region 3, than designs A and B.

While the pressures in regions 1 and 3 that are impacted by the described effects of radius both influence the magnitude of the moment on the piston that drives it to collide with the bore, these regions are closer to the case end of the interface; hence, the described effects exert themselves more prominently on the correction force at the case end control point than on that at the DC end control point. Moreover, although the pressure in region 3 contributes to the aforementioned piston moment, it also pushes the piston towards the circumferentially opposite side of the bore: away from region 2, and towards region 1 (see Fig .7.3). That is, a lower pressure in region 3 holds more benefit for preventing solid contact near the case end of the interface (preventing collision in region 1) than near the DC end (preventing collision

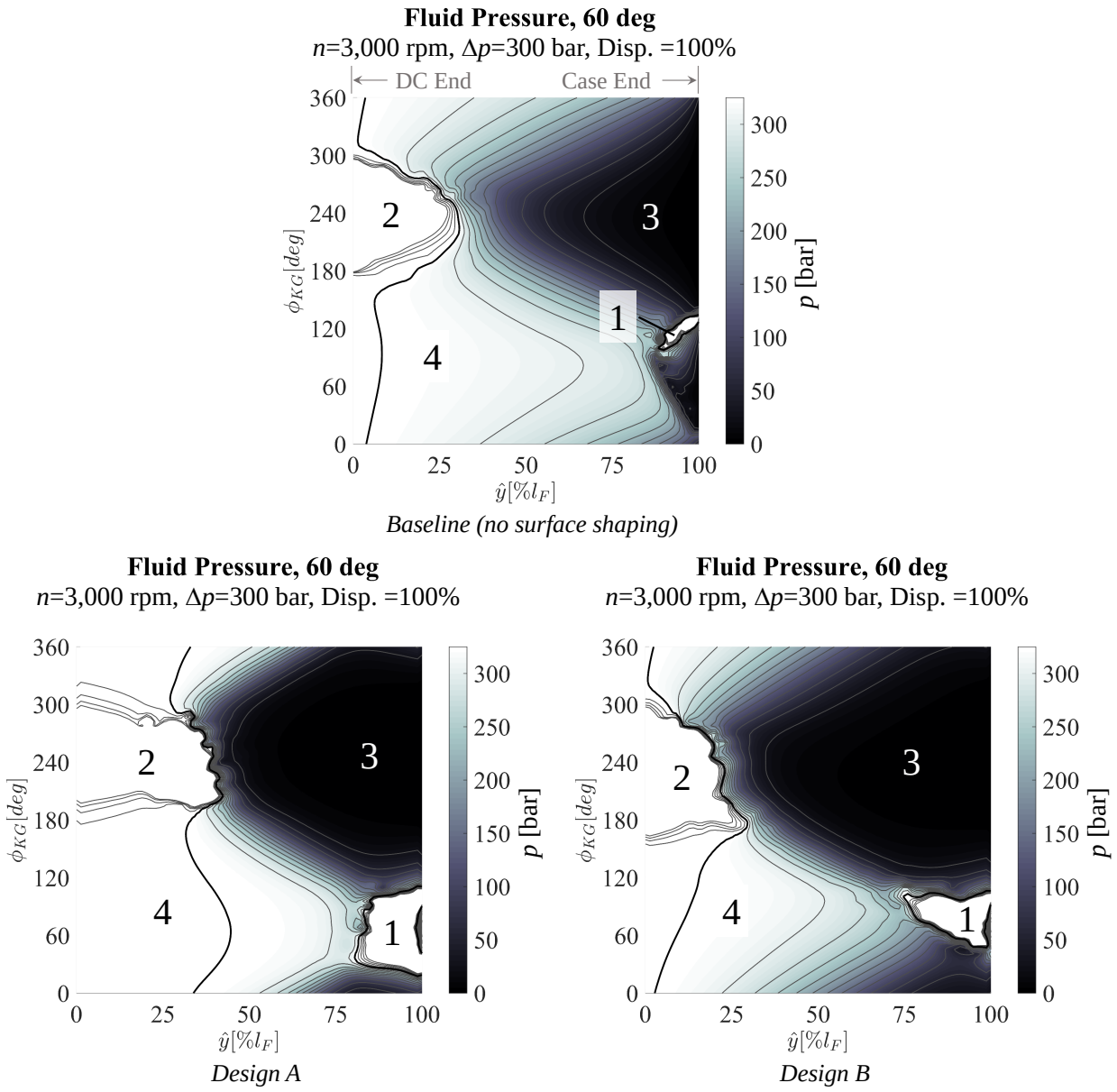

Figure 7.10. Fluid pressure fields of the baseline, and designs A and B, at OC4, $\varphi = 60°$.

in region 2). Taking all of this into consideration, it should come as no surprise that as the profile radius becomes smaller, the reduction in maximum correction force magnitude at the DC end control point tends to be lower than that at the case end.

This can be seen in Fig. 7.11: plotted are the DC and case end correction force magnitudes for Designs C, F, G, and H, against shaft angle, at OC4. In referring back to the top image of Fig. 7.9, which shows the position each of these designs within the DOE grid, it can be seen

that designs C and G have the same radius, as do designs F and H. Furthermore, designs C and F both have the same shift— the second lowest in the grid— and designs G and H both have the same, significantly larger, shift. In comparing the pairs of designs with the same shift (C to F, and G to H), a much greater change in maximum correction force magnitude can be observed for the case end control point (blue line) than for the DC end control point (red line). Reworded, in moving from the right to the left column of plots, i.e. from a large to a small radius, the reduction in maximum correction force magnitude is lower for the DC end control point than for the case end control point.

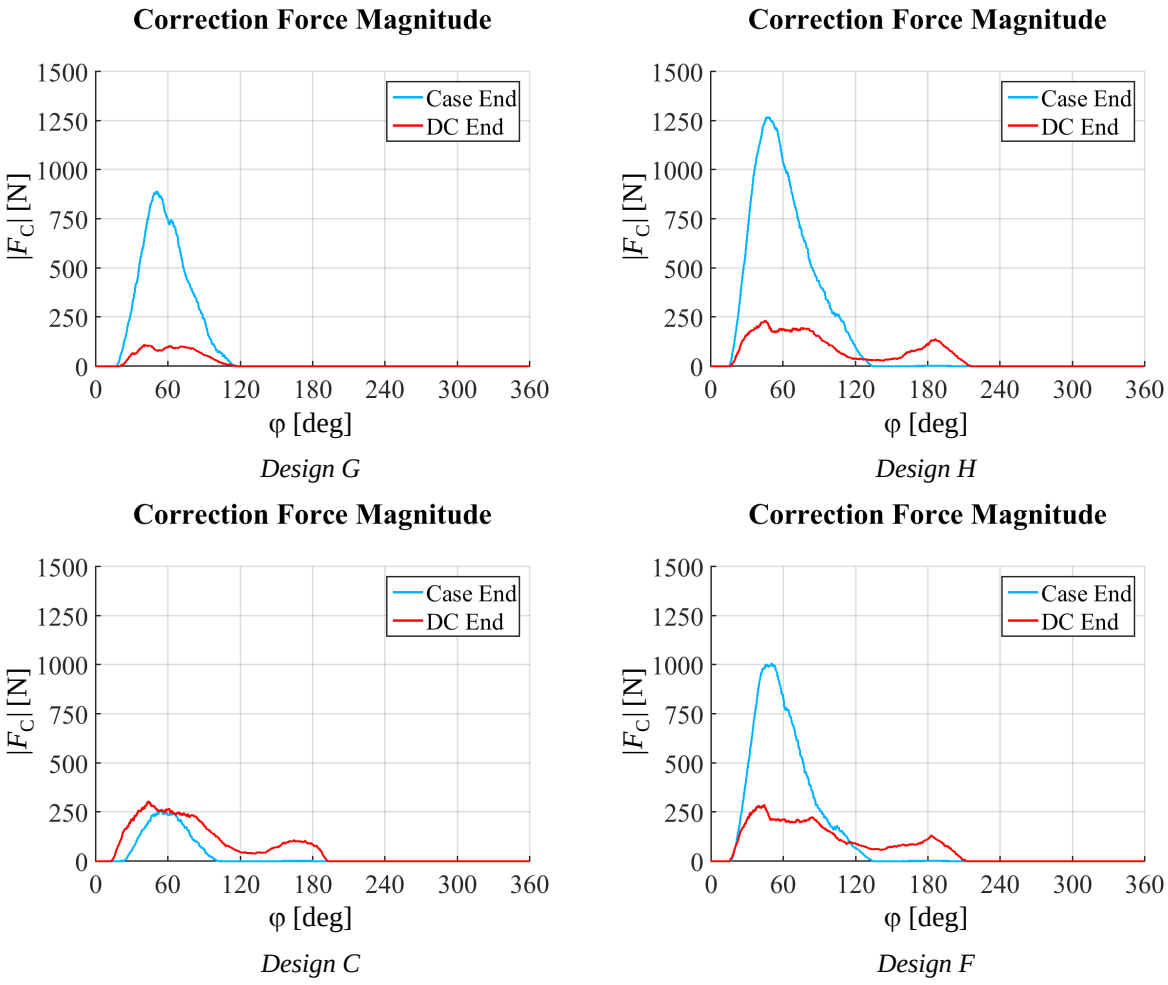

Figure 7.11. Correction force magnitudes at C_A and C_B for Design C, Design F, Design G ($R = 24.59\% l_{F,max}/1000$, $l_s = -2.634\% l_{F,max}$), and Design H ($R = 61.47\% l_{F,max}/1000$, $l_s = -2.634\% l_{F,max}$), at OC4.

Fig. 7.11 also shows that, at the DC end control point, there can be two main peaks in correction force magnitude: one at around $\varphi = 60°$, and one near $\varphi = 180°$. The first responds to the effects described. The presence of the second arises from the shortening of the guide length near IDC (shortening the guide length increases piston tilt, thereby decreasing piston-bore surface conformity); this peak grows higher as the profile radius becomes larger, and hydrodynamic pressure buildup near the DC end of the interface lessens over the bulk of the shaft angle span during which the guide length is changing ($\varphi = \sim$130°-230°). It does eventually becomes large enough to dictate the maximum correction force magnitude at the DC end control point— within the simulated grid, this takes place at radii $\geq \sim 100\% l_{\mathrm{F,max}}/1000$.

There is one more important observation to be made from the inspection of Fig. 7.11: in moving from Design C to Design F, the maximum DC end correction force magnitude changes very little, whereas, in going from Design G to Design H, it nearly doubles. This is the effect of profile shift. As already stated, and as Fig. 7.6 clearly shows, for the case end control point, the maximum and average correction force magnitudes decrease as the magnitude of the shift increases— for the DC end control point, the opposite is true. Fig. 7.12 illustrates the primary origins of these effects.

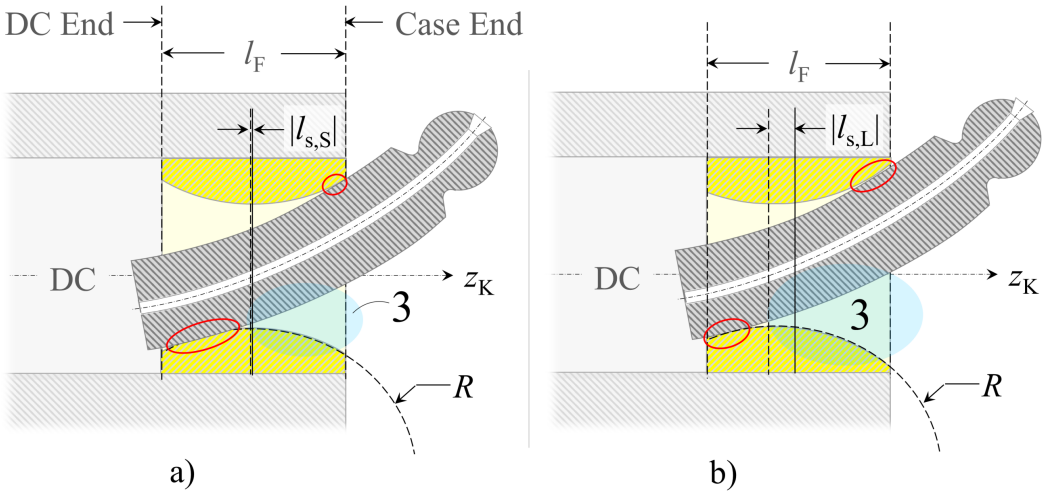

Figure 7.12. Comparison of concave bore profiles with a negative shift that is a) small in magnitude, versus b) large in magnitude, during the high-pressure stroke.

Depicted is a cross-section of the piston-cylinder interface during the high-pressure stroke, with two different concave bore profiles. One has a shift of small magnitude, denoted $l_{s,S}$ (image a), and the other, a shift of large magnitude, denoted $l_{s,L}$ (image b). In comparing the two, it becomes apparent that, during the high-pressure stroke, with the piston tilting and deforming as shown, an increase in the magnitude of the negative shift lengthens the region of piston-bore surface conformity near the case end of the interface (region 1), but shortens it near the DC end of the interface (region 2). Additionally, shifting the profile apex towards the DC opens region 3 wider to the pump case, which, as explained, is more advantageous for preventing contact near the case end of the interface than near the DC end.

As a result, at the DC end control point (the control point whose correction force is most heavily affected by load support in region 2), both the correction force peak near $\varphi = 60°$, and the part of the peak near $\varphi = 180°$) that falls within the high-pressure stroke, rise as the shift grows longer, while at the case end control point (the control point whose correction force is most heavily affected by load support in region 1), the single major correction force peak becomes lower. Consequentially, the maximum and average correction force magnitudes at the DC end control point are lowest when there is barely any negative shift, whereas those at the case end control point are lowest when there is a substantial negative shift.

In order to demonstrate the described changes in surface conformity, and in region 3, Fig. 7.13 shows the simulated fluid pressure fields of four designs from the DOE grid, at OC4, at a shaft angle of $\varphi = 60°$. Designs I-L are marked in the DOE grid map in the top image of the figure: they all have the same profile radius, but different shift values. Examining their fluid pressure fields, in moving from Design I to Design L, i.e. in going from a profile with a small $|l_s|$ to one with a large $|l_s|$, region 2 is receding, while region 1 is expanding. This shows that, as stated, increasing the shift magnitude diminishes piston-bore conformity near the DC end of the interface, and grows it near the case end. In moving from Design I to Design J, it can also be seen that the darkest section of region 3, marking the lowest pressure of that region, is expanding (i.e. designs with a larger shift allow more pressure in that region to dissipate into the pump case).

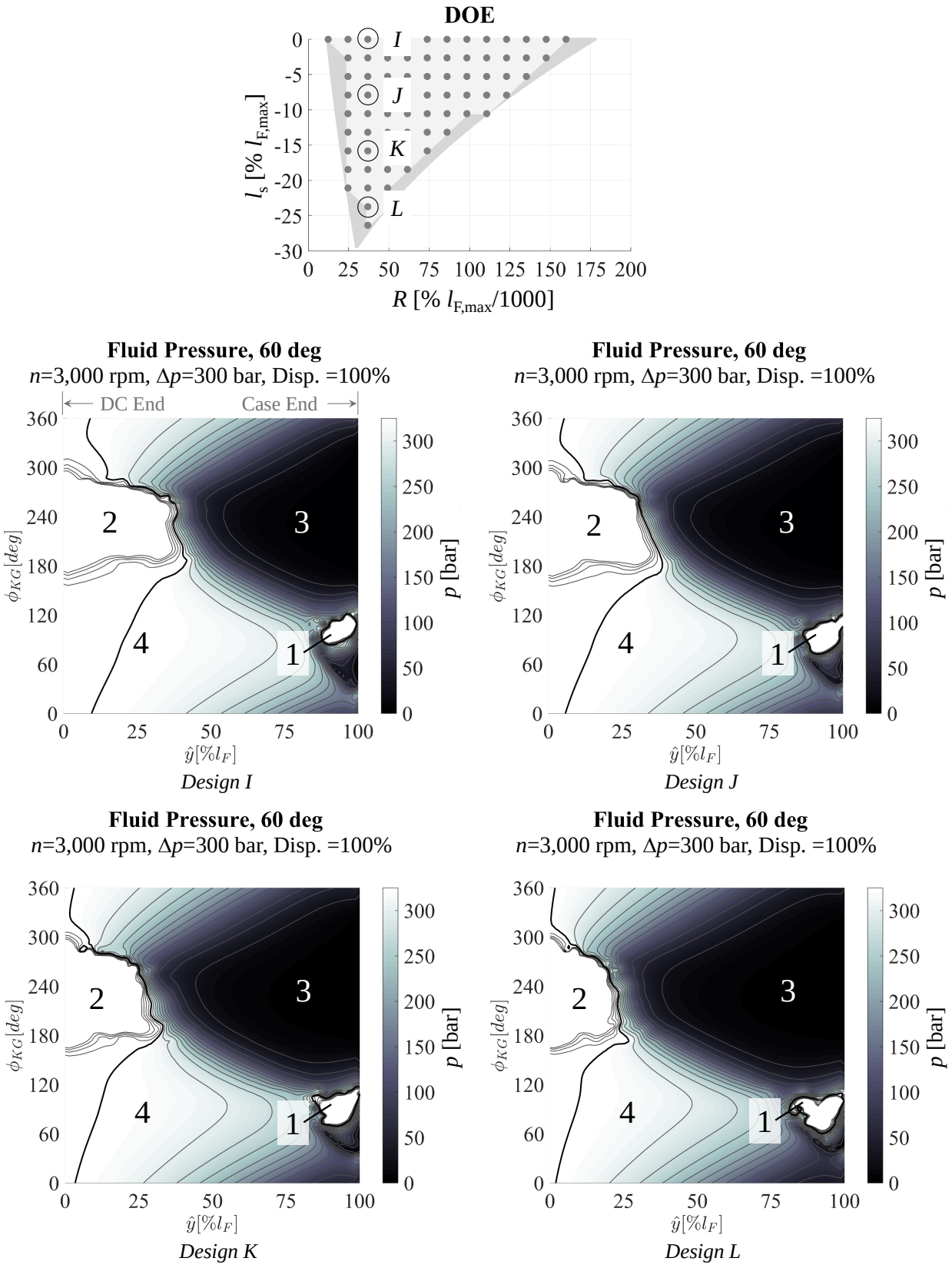

Figure 7.13. Fluid pressure fields of Design I-L ($R = 36.88\%l_{\mathrm{F,max}}/1000$, and $l_{\mathrm{s}} = 0.000\%l_{\mathrm{F,max}}$, $-7.903\%l_{\mathrm{F,max}}$, $-15.81\%l_{\mathrm{F,max}}$, and $23.71\%l_{\mathrm{F,max}}$, respectively), at OC4, $\varphi = 60°$.

Of the two opposing trends reflected in these pressure field plots— the change in correction force magnitude with shift at the case end control point, versus at the DC end control point— the former is of greater import. This is because, over most of the DOE grid, the maximum and average correction force magnitudes at the case end control point are higher than those at the DC end control point. As explained in Ch. 6, the more severe predicted contact near the case end of the interface that drives this difference is a consequence of the piston deformation, and of the case end being closer to the center of piston head where F_{SKy} acts. That difference in severity of predicted contact at either end of the interface not only asserts itself in terms of higher correction forces at the case end control point, but also in terms of the magnitude of the contact stress, σ, that is imposed by the interface model when the gap height falls below h_{min}.

Fig. 7.14 plots, over the DOE grid-spanned space, the value of the maximum contact stress imposed on any one element in the fluid film grid over the course of a full shaft revolution. Its trends are very close to those of the maximum case end correction force shown in Fig. 7.6,

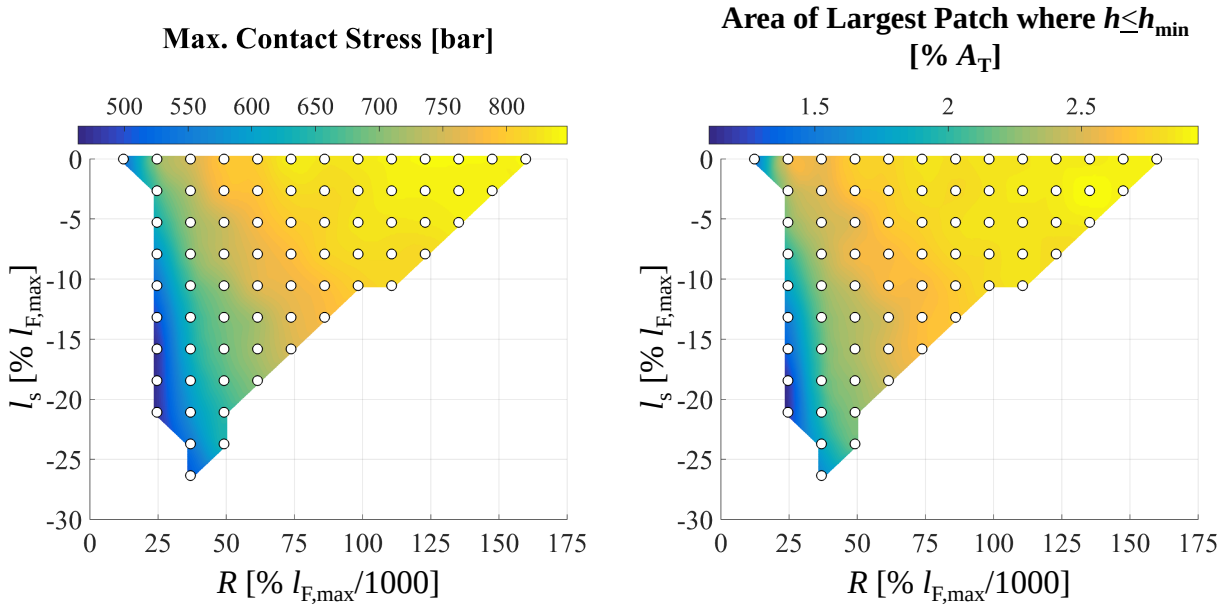

Figure 7.14. For the DOE grid over which $l_{\mathrm{s}} \leq 0\% l_{\mathrm{F,max}}$: max. contact stress over the simulated shaft turn, and max. area occupied by a single patch of $h \leq h_{\mathrm{min}}$ at any simulated shaft angle (expressed as a percentage of the area occupied by the whole interface at that angle), at OC4.

while the trends of the DC end correction force are not strongly represented. The same holds for the maximum total area taken up by the largest single patch of $h \leq h_{\min}$ at any one point in time over the simulated shaft revolution, which is also plotted in Fig. 7.14. On account of this, for a given radius, a profile will perform better in terms of load support with a greater shift towards the DC. However, as was shown in Fig. 7.5, both decreasing the radius, and increasing the shift magnitude, increases power loss. Although that increase can be offset by lowering of the piston-bore clearance, when designing a concave bore profile, its radius should be made as large, and the magnitude of its shift as small, as possible without compromising the interface's ability to carry the load imposed on it.

Profile with Positive Shift ($l_s \geq 0\%\ l_{F,max}$)

The design space for this part of the study is set up such that $l_s \geq 0\%\ l_{F,max}$, with d_{DC} and d_C subject to the same constraints as in the previous part. The simulated designs again form a uniform grid across the design space, as shown in Fig. 7.15.

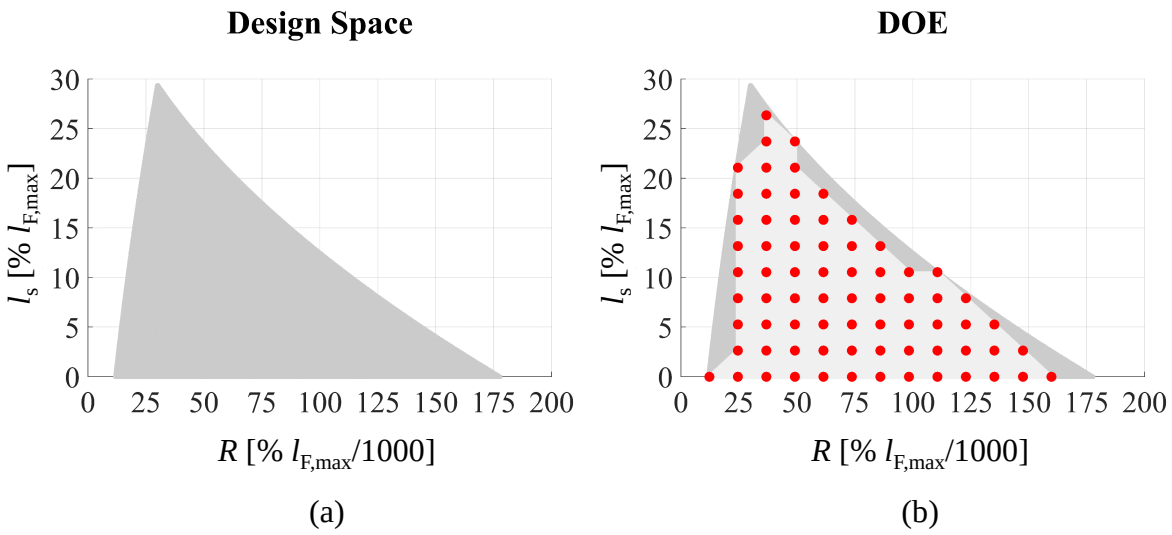

Figure 7.15. a) Design space, and b) DOE, for $l_s \geq 0\%\ l_{F,max}$.

The simulation results can be seen in Fig. 7.16. Specifically, these plots show the maximum correction force magnitude brought about by profiles with a positive shift, and compare them to the forces incurred by profiles with a negative shift. The left-hand column of the figure

pertains to profiles with a shift less than or equal to zero, and the right-hand column, to profiles with a shift greater than or equal to zero. For each case ($l_s \leq 0$ and $l_s \geq 0$), the bottom plot graphs the maximum correction force magnitude (over a full shaft revolution) at the case end control point against that at the DC end control point for each design in the corresponding DOE grid. The non-dominated designs, i.e. those that for which no other design can be found in the plot with a lower maximum correction force magnitude at *both*

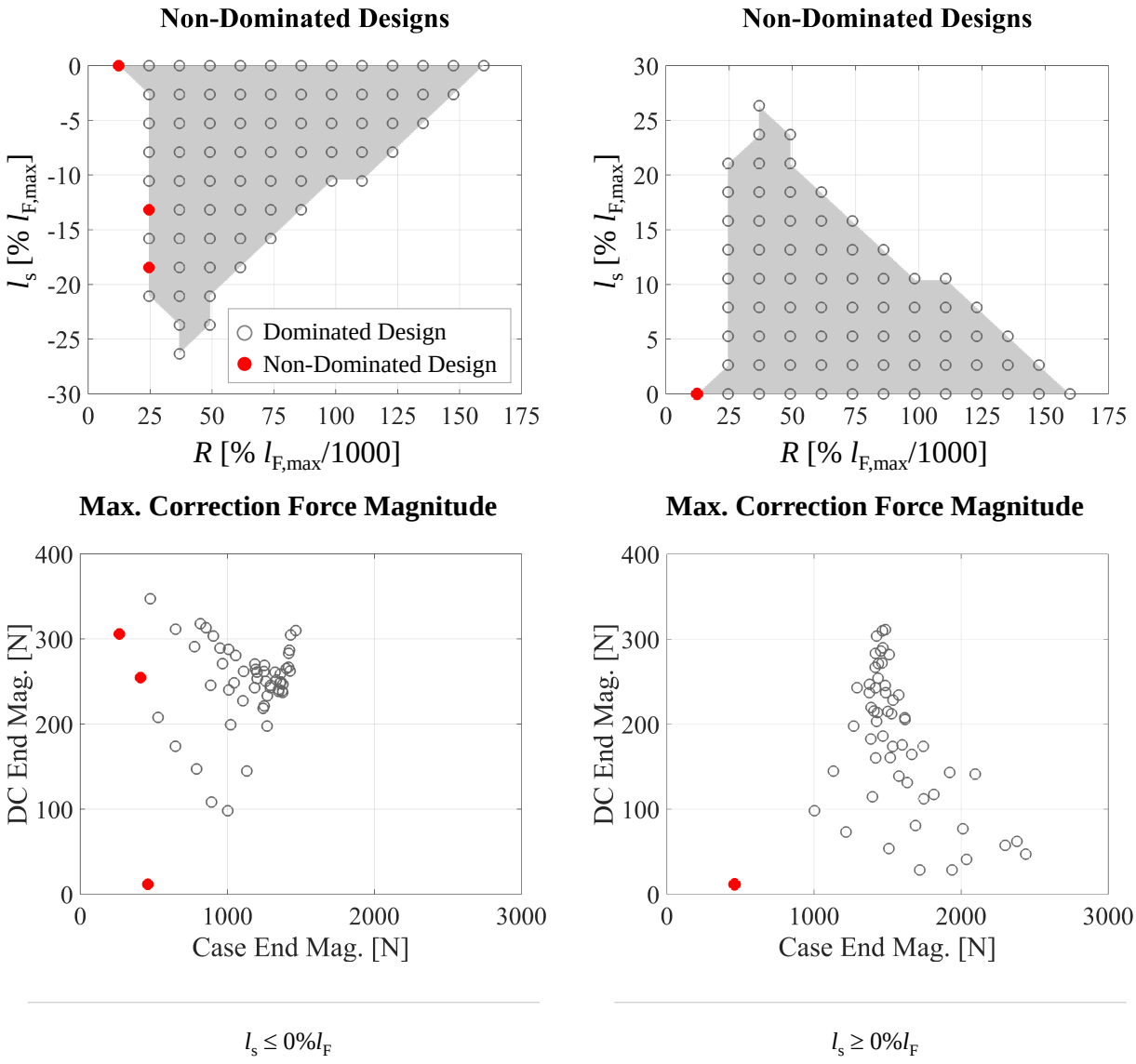

Figure 7.16. Non-dominated designs for profiles with negative shift (left) vs. positive shift (right).

control points, are marked in red. Their location in the corresponding DOE grid is shown in the top row of plots.

Comparing the bottom two plots, it can be seen that while more of the designs with a positive shift can achieve a maximum correction force magnitude of under 100 N at the DC end control point, more designs with a negative shift can achieve a maximum correction force magnitude of under 1,000 N at the case end control point. This is because the negative shift, as previously explained, increases piston-bore surface conformity near the case end of the interface, but decreases it near the DC end, while a positive shift does the opposite. Furthermore, a negative shift opens region 3 of the fluid film from Fig. 7.3 up further to the pump case, thus allowing the pressure in this region, which contributes to the force and moment that causes metal-to-metal contact at the case end of the interface, to drain away to a greater degree, while a positive shift narrows this region, causing more of its pressure to be retained.

Consequentially, for the case of $l_s \leq 0$, two of the non-dominated designs are able to achieve a lower maximum case end correction force magnitude than the single non-dominated design for the case of $l_s \geq 0$. The lowest maximum correction force magnitude at the DC end among non-dominated designs is the same for both cases, indicating that this is a design with zero shift. Examining the top row of plots in Fig. 7.16, it becomes clear that while for the case of $l_s \leq 0$, two of the non-dominated designs have a negative shift, for the case of $l_s \geq 0$, *the entire DOE grid is dominated by a design with zero shift*. This demonstrates that, when it comes to their overall performance in terms of load support, concave bore profile designs with a positive shift are not worth pursuing.

7.3.2 Study 2: Comparing the Concave Bore Profile to the Barrel Piston Profile

The third, and final study of this chapter, presents a comparison between shaping the bore, versus shaping the piston. Specifically, it compares giving the bore surface a lengthwise cross-section in the shape of a circular arc, i.e. a concave bore profile, to giving the piston running surface a lengthwise cross-section of in the shape of a circular arc: a barrel piston profile. This piston profile is depicted in Fig. 7.17: the circular arc in this case spans the length of the piston running surface, whose extent is denoted l_{KG}. As can be seen, just as the concave bore profile, this arc, too, is defined by a radius and a shift. In order to distinguish these from their concave bore profile counterparts, they are denoted R_{P} and $l_{\mathrm{s,P}}$, respectively. $l_{\mathrm{s,P}}$ is measured from the midpoint of the running surface; for the sake of consistency with the sign convention of the bore profile, a shift towards the piston head is considered positive, while a shift towards the flat end of the piston is considered negative.

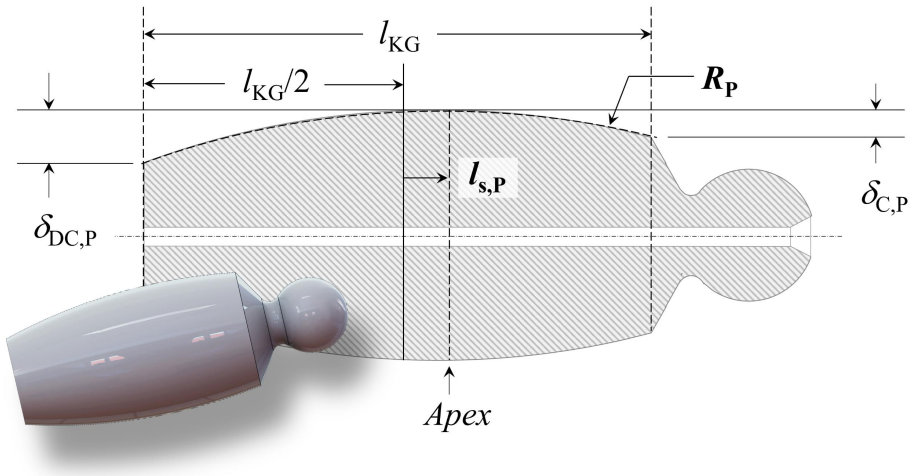

Figure 7.17. Half-barrel profile (figure not to scale).

Since the previous section showed concave bore profiles with a shift less than or equal to zero to outperform those with a positive shift, the present comparison study only includes concave bore profiles for which $l_{\mathrm{s}} \leq 0\% l_{\mathrm{F,max}}$. That is, the present study compares the performance of the barrel piston profile to that of the concave bore profiles simulated in the first study. Furthermore, it includes only barrel piston profiles with a shift of $l_{\mathrm{s,P}} \leq 0\% l_{\mathrm{KG}}$ (the reason

behind this becomes clear from the study results). In addition to these constraints on shift values, the domains of radius-shift value pairs (the design spaces) for the concave bore and barrel piston profiles are each subject to two additional limits. For the concave bore profiles, since the results from the first study will be used for the present comparison to the barrel piston profile, these limits are simply the upper and lower bounds on δ_{DC} and δ_{C} that were already specified in Section 7.3.1. For the barrel piston profiles, these additional limits are imposed on the dimensions $\delta_{\mathrm{DC,P}}$ and $\delta_{\mathrm{C,P}}$ shown in Fig. 7.17: they are the deviations of a profile from the flat line describing a cylindrical piston (without shaping) at either end of the running surface. The values of the upper and lower bounds on these dimensions are the same as those on δ_{DC} and δ_{C}:

$$0.09660\mu\mathrm{m/mm} \leq \{\delta_{DC,P}/d_{\mathrm{K}}, \delta_{C,P}/d_{\mathrm{K}}\} \leq 1.449\mu\mathrm{m/mm}$$

The upper limit on δ_{DC} and δ_{C} is actually the same as the upper limit on the maximum deviation of the piston shape from that of a cylindrical piston *within the axial limits of the interface*, i.e. the constraint is exactly the same as for the concave bore profiles. This is because all of the shift values being considered are zero or negative, i.e. $\delta_{\mathrm{DC,P}} \leq \delta_{\mathrm{C,P}}$. The greatest deviation of the piston shape from cylindrical inside the interface therefore takes place when the edge of the running surface nearest the piston head enters the bushing. That is, the maximum $\delta_{\mathrm{C,P}}$ is the maximum deviation of the shaping from cylindrical at the case end of the guide length. Since $\delta_{\mathrm{DC,P}} \leq \delta_{\mathrm{C,P}}$, the deviation at the DC end is automatically under the same upper limit (this is also true for the concave bore profiles with negative shift).

The lower bound on $\delta_{\mathrm{DC,P}}$ and $\delta_{\mathrm{C,P}}$, on the other hand, being set, for the sake of simplicity, to the same value as that of δ_{DC} and δ_{C}, causes the constraints on the concave bore and barrel piston profiles to differ. Because the piston running surface is longer than the maximum guide length, setting the lower limit of these deviations equal permits the barrel piston profile to take on larger radius and shift values than those in the design space of the concave bore profile. However, as will be seen, even this more expansive design space, shown in Fig. 7.18, does not suffice for the barrel piston profile to outperform the concave bore profile.

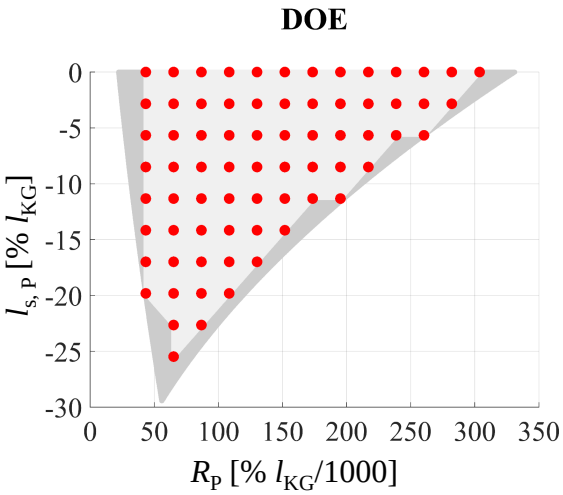

Figure 7.18. Design space for $l_s \leq 0\%\ l_{KG}$ (gray), and DOE (red).

The difference in the performance of these two surface shaping types can be most clearly seen if the maximum and average correction force magnitudes at the case end control point (over a full shaft revolution) are examined first. Fig. 7.19 shows these two parameters, plotted in the same format as for the previous two studies. The FSTI simulation results for the concave bore profile (from the first study) are in the left-hand column, and the simulation results for the barrel piston profile— corresponding to the designs specified by the uniform DOE grid in Fig. 7.18— are in the right-hand column. In order to make the results of the two different types of surface shaping directly comparable, the color scale is kept the same within each row of plots.

In examining Fig. 7.19, three observations can be made. First, the trends of the plotted parameters with respect to radius and shift are the same for the concave bore profile as for the barrel piston profile; that is, for both, the maximum and average case end correction force magnitudes increase as the radius becomes larger, and as the absolute value of the shift becomes smaller. Second, because of those trends, both surface shape types achieve the lowest values for the plotted parameters at the smallest of the radii in the DOE grid, specifically at the largest shift magnitudes that the grid covers for those radii. Third, over the grid covered, the barrel piston profile does not reduce the maximum or average correction force magnitudes at the case end control point as much as the concave bore profile.

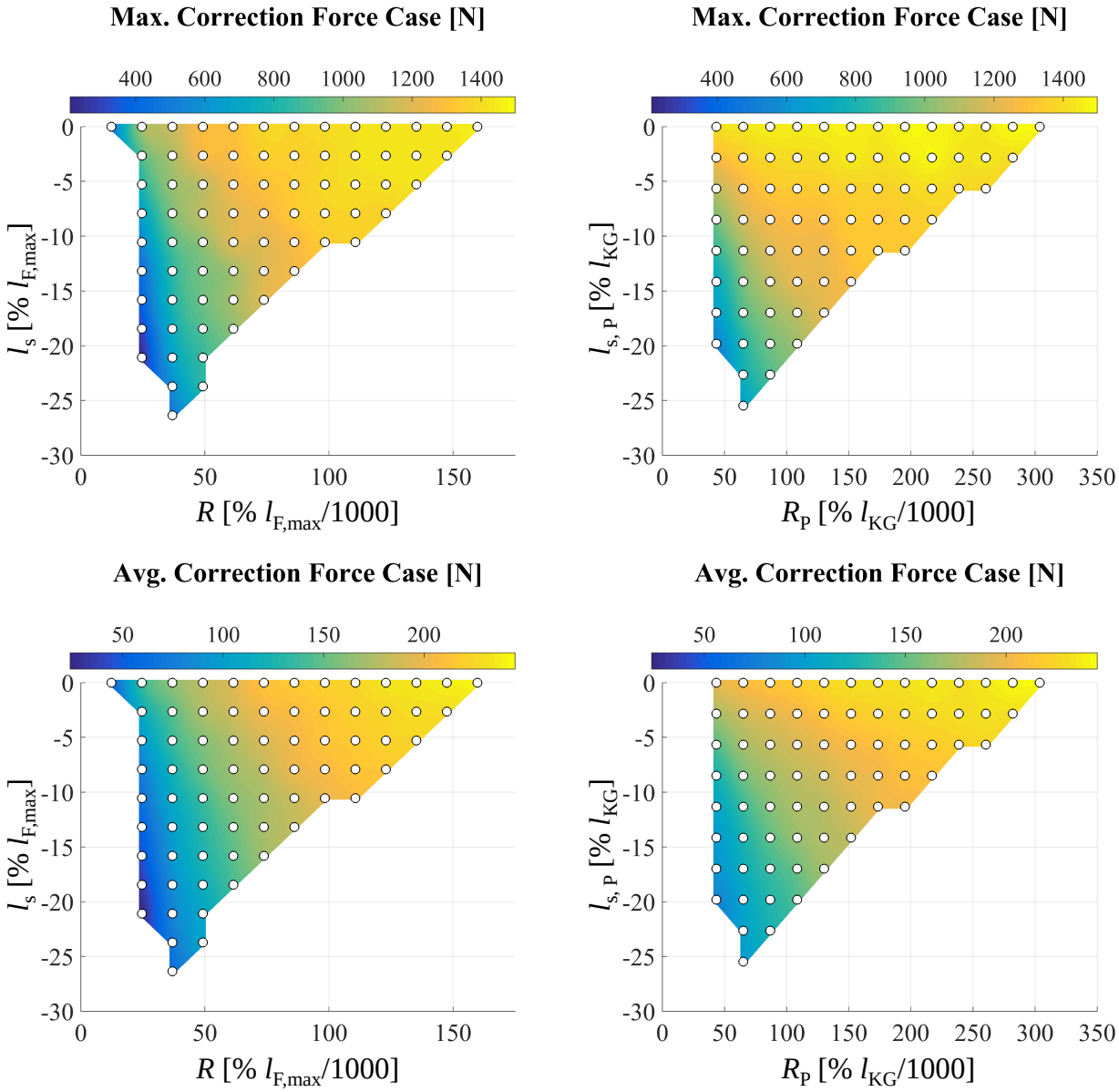

Figure 7.19. Comparison of the concave bore profile (left) vs. the barrel piston profile (right): max. and avg. correction force magnitudes of the simulated shaft revolution at the case end control point (C_B), at OC4.

In order to understand where the described correction force trends of the barrel profile come from, it is useful to examine Fig. 7.20. The illustration depicts a cross-section of the piston-cylinder interface over the high-pressure stroke, with the barrel profile implemented on the piston, deforming roughly as shown. Image (a) depicts the interface in the beginning of the high-pressure stroke, and image (b), towards the end of the high-pressure stroke. From either image, it can be seen that increasing the radius, which would flatten the profile and increase the piston diameter on either side of its apex, would cause region 3 to become narrower. The pressure of that region would then dissipate less easily/quickly into the pump case, resulting in more pressure being held there. This pressure contributes to the turning moment on the piston, and to the force pushing it towards the circumferentially opposite side of the bore, into region 1. Hydrodynamic pressure buildup in region 1 is unable to compensate for this effect, since the axial extent of said region is being kept extremely short by the piston deformation, which diminishes piston-bore conformity near the case end of the interface. As a result, the difference between the required and the supplied load support near the case end of the interface grows as the profile radius increases, causing the maximum and average correction force magnitudes at the case end control point to increase with radius.

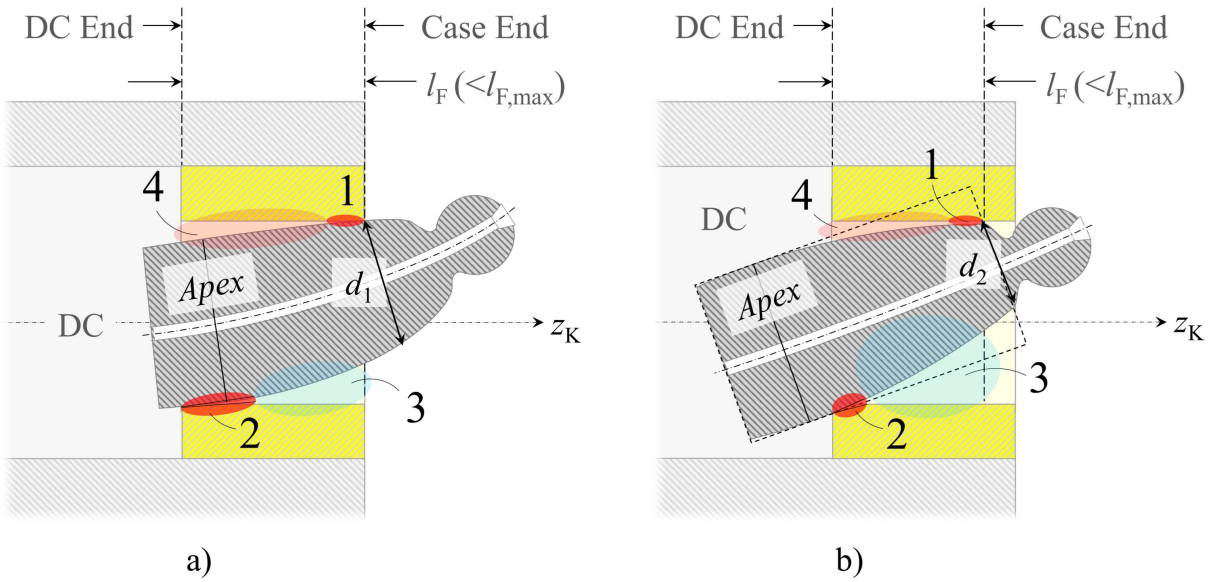

Figure 7.20. Fluid regions in the piston-cylinder interface (with barrel piston profile) at a) the beginning of the high-pressure stroke, and b) near the end of the high-pressure stroke.

As the magnitude of the shift grows, however, these parameters decrease. Referring once more to Fig. 7.20, it can be seen that because the piston diameter decreases on either side of the barrel profile apex, increasing the magnitude of the negative shift, i.e. moving the barrel profile apex towards the DC, opens region 3 up wider to the pump case. This allows the pressure of that region to dissipate into the pump case to a slightly greater degree, and contribute less to the turning moment on the piston, and to the force driving it towards collision with the bore in region 1. Consequentially, the amount of hydrodynamic pressure buildup required for full load support in region 1 diminishes, causing the maximum and average correction forces at the case end control point to decrease as $|l_{s,P}|$ grows. Towards the right edge of the DOE grid, where the radius becomes so large (the profile so flat) that the location of the apex no longer has a significant impact, this effect of course fades away.

The described changes in the fluid film over the high-pressure stroke with piston profile radius and shift can be seen in Fig. 7.21, which shows the fluid pressure fields of four profile designs at OC4, and $\varphi = 60°$. The locations of designs Q-T in the DOE grid are shown in Fig. 7.21: designs Q and S have the same (small) radius, designs R and T have the same (large) radius, and designs S and T have the same (small) shift magnitude, while designs Q and R have the same (large) shift magnitude. From Fig. 7.21, it can be seen that when increasing the radius (moving from the left to the right column of plots), the darkest section of region 3, denoting the lowest pressure, shrinks. This corresponds to the described increase in this region's retention of pressure as the radius becomes larger. The described widening of region 3 with increasing $|l_{s,P}|$ can also be seen in moving from the plot of Design S to that of Design Q: the dark low-pressure region expands.

In addition to these trends, all four plots show that the footprint of region 1 is very small, indicating that the piston and bore do not conform well in this area. As seen in the previous section, designs A and B of the concave bore profile exhibit much larger footprints for region 1. One of the differences between the two profile types that contribute to this is that, when the barrel piston profile is implemented, the deformation of the piston over the high-pressure stroke takes away from that shaping, which diminishes piston-bore conformity

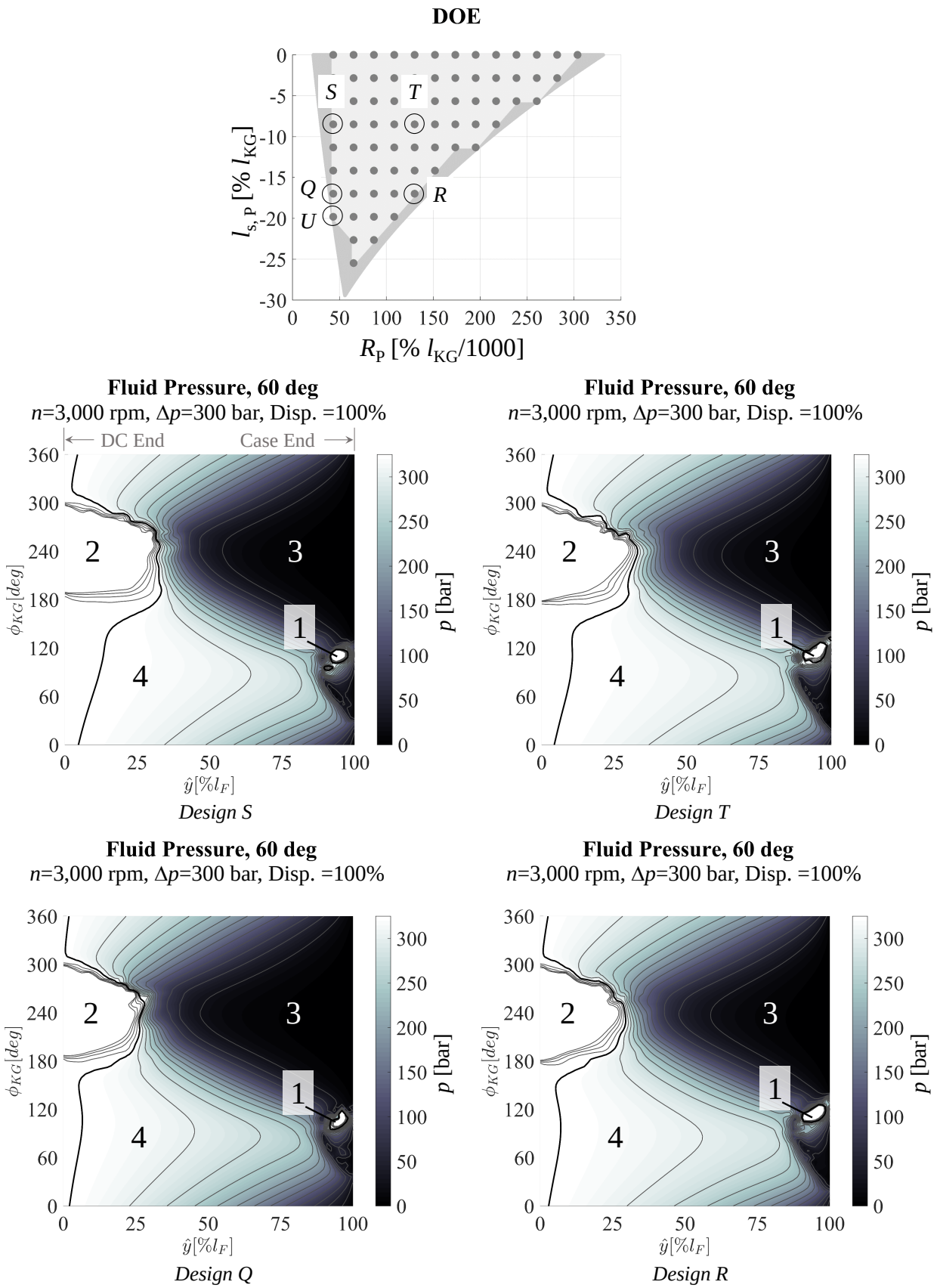

Figure 7.21. Fluid pressure fields of Design Q-T, at OC4.

near the case end of the interface— whereas for the concave bore profile, the deformation of the piston does not detract from the shaping, and the deformation of the bushing aids surface conformity. Although the smaller region 1 footprint produced by the barrel piston profile, i.e. the smaller available area suitable to hydrodynamic pressure buildup, does not necessarily lead to a lesser fluid-pressure-generated force in comparison to that of the concave bore profile, it does detract from the ability of this piston shaping type to compensate for a second disadvantage inherent to it.

The demerit in question stems from the fact that while the concave bore profile is stationary relative to the piston-cylinder interface, the barrel piston profile moves (with the piston). As a result, the piston diameter at a particular location along the z_{K}-axis within the guide length changes with shaft angle. For a profile of shift $|l_{\mathrm{s,P}}| < 0$, the smallest piston diameter is located at the end of the piston running surface nearest the piston head. For the unit being modeled in the present study, this end only enters the interface near the end of the high-pressure stroke, when the guide length begins to reduce— for a unit with fixed guide length, it would only enter the interface at the very end of the high-pressure stroke, or not at all. This limits the time over which the fluid film thickness in region 3 is at its maximum. For the concave bore profile, by contrast, the largest bore diameter is part of the interface until the guide length reduces. Thus, given a barrel piston and a concave bore profile with a non-positive shift, and with the deviations $\delta_{\mathrm{C}} = \delta_{\mathrm{C,P}}$, the bore profile will exhibit a larger film thickness in region 3 over the critical first half of the high-pressure stroke than the barrel profile.

This helps the concave bore profile drain away more pressure from region 3, which, in turn, lowers the region 1 pressure buildup required to prevent contact, and allows the concave bore profile to achieve lower average and maximum correction force values than the barrel piston profile when, as is done in the present study, the upper bound on the values of δ_{C} and $\delta_{\mathrm{C,P}}$ is the same. Fig. 7.22 shows the difference between the two profile types using the examples of concave bore profile Design B— the design with the lowest maximum case end correction force magnitude in the first study of this chapter— and barrel piston profile U— the design

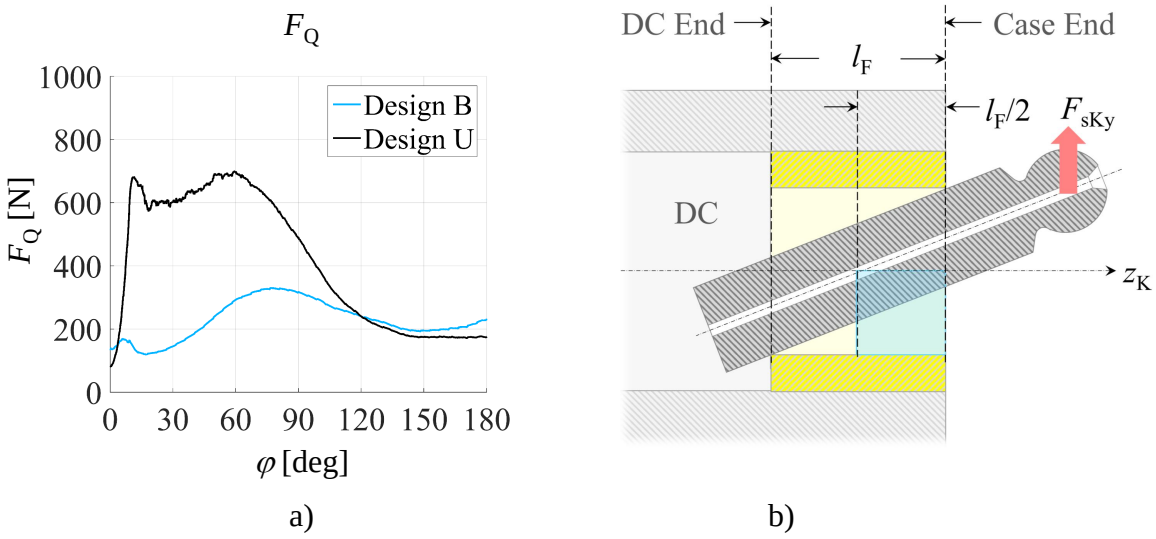

Figure 7.22. a) F_Q over the high-pressure stroke, and b) a cross-section of the interface at plane P_1 with the direction of F_{SKy} marked in (other forces on piston not shown).

with the lowest maximum case end correction force magnitude in the present study. The location of Design U within said grid is marked in Fig. **??**. Fig. 7.22 (a) plots, for both designs, a force F_Q against shaft angle over the high-pressure stroke. F_Q is the component of the force generated by the fluid pressure in the quarter of the interface marked in Fig. 7.22 (b) that acts in the same direction as the prominent side load component F_{SKy}. The quarter of the interface in question covers the part of region 3 that adds to both, the force pushing on the piston in roughly the same direction as the hydrodynamic pressure buildup of region 2, and to the moment about the center of the interface exerted on the piston by F_{SKy}. Fig. 7.22 (b) depicts this quarter by illustrating a cross-section of the interface at the plane P_1 that was introduced in Ch. 6. Within this cross-section, the highlighted quarter of the fluid film is located below the z_K-axis, and within the half of the interface that terminates at the case end.

Comparing the plots of F_Q for concave bore Design B and barrel piston Design U in Fig. 7.22 (a), it can be seen that contribution to the force and moment introduced by F_{SKy} is higher for the latter (Design U) over the critical first half of the high-pressure stroke. This

demonstrates that, as explained, the barrel piston profile is retaining more pressure in the crucial part of region 3 nearest the case end of the interface, over shaft angles when the external load on the piston is particularly high. Of course, this effect lessens as the piston diameter near the case end of the interface becomes smaller, vanishing when the region 3 film thickness near the case end of the interface becomes sufficiently similar for the two profile types— as can be seen in Fig. 7.22 (b), the two lines converge about two thirds of the way through the high-pressure stroke.

The described effect, in conjunction with the trends shown in Fig. 7.19, indicates that the barrel piston profile would be able to achieve lower correction force magnitudes at the case end control point if the upper bound on the deviations $\delta_{\mathrm{DC,P}}$ and $\delta_{\mathrm{C,P}}$ were to be raised, allowing for smaller radii and larger shift magnitudes. It prompts the question: if the deviations from flat at either end of the barrel piston profile are allowed to be larger than those of the concave bore profile, will the former be able to outperform the latter? This line of thought, however, fails to take into account the trends associated with the correction forces at the other control point, and with the power loss incurred across the interface.

The first of these can be observed in examining Fig. 7.23, which compares the maximum and average correction force magnitudes of the concave bore and barrel piston profiles at the DC end control point. As can be seen from the plots corresponding to the barrel piston profile, at the largest shift magnitudes corresponding to the smallest radii in the grid, precisely where the maximum and average correction force magnitudes at the case end control point are lowest, those at the DC end control point are the highest. The dramatic increase in these parameters with decreasing radius and increasing shift magnitude is tied to the rise of a large DC end correction force peak over the end of the high-pressure stroke, when the guide length is becoming shorter for the simulated unit.

The peak can be seen in Fig. 7.24, showing the correction forces of designs Q-T, at OC4, plotted against shaft angle. In moving from the two profiles with a large radius to those with a small radius, i.e. from the right-hand column of plots over to the left, the correction force

peak centered at around $\varphi = 180°$ shoots up. The same is true when moving from Design S, with a small shift magnitude, to Design Q, with a large shift magnitude (for designs R and T, the radius is so large, i.e. the profile so flat, that shift makes very little difference). The rise of this correction force peak near the end of the high pressure stroke mainly derives from a drastic decrease in the hydrodynamic pressure buildup of region 2 as the radius decreases, and/or the shift magnitude increases (provided the radius is small enough for shift to make a significant impact). This effect is so exaggerated over the end of the high-pressure stroke because as the guide length shortens (piston tilt increases, piston-bore surface conformity lessens), region 2 becomes more sensitive to changes in radius and shift.

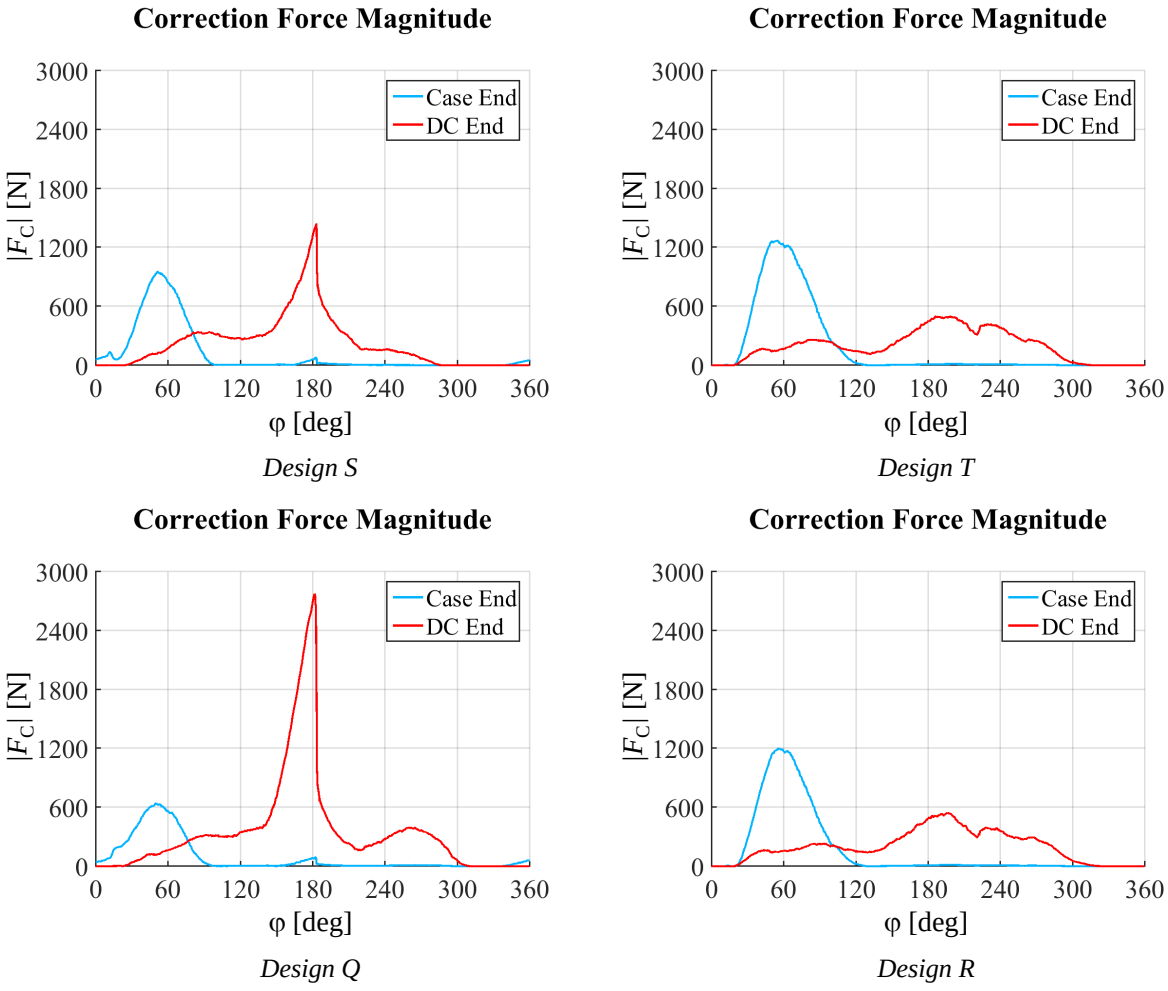

Figure 7.24. Correction force magnitudes at C_A and C_B for design Q-T, at OC4.

Why do the two profile-defining parameters affect hydrodynamic pressure buildup near the DC end of the interface as described? Decreasing the radius, as well as increasing the magnitude of the negative shift (moving the profile apex closer to the DC), both decrease

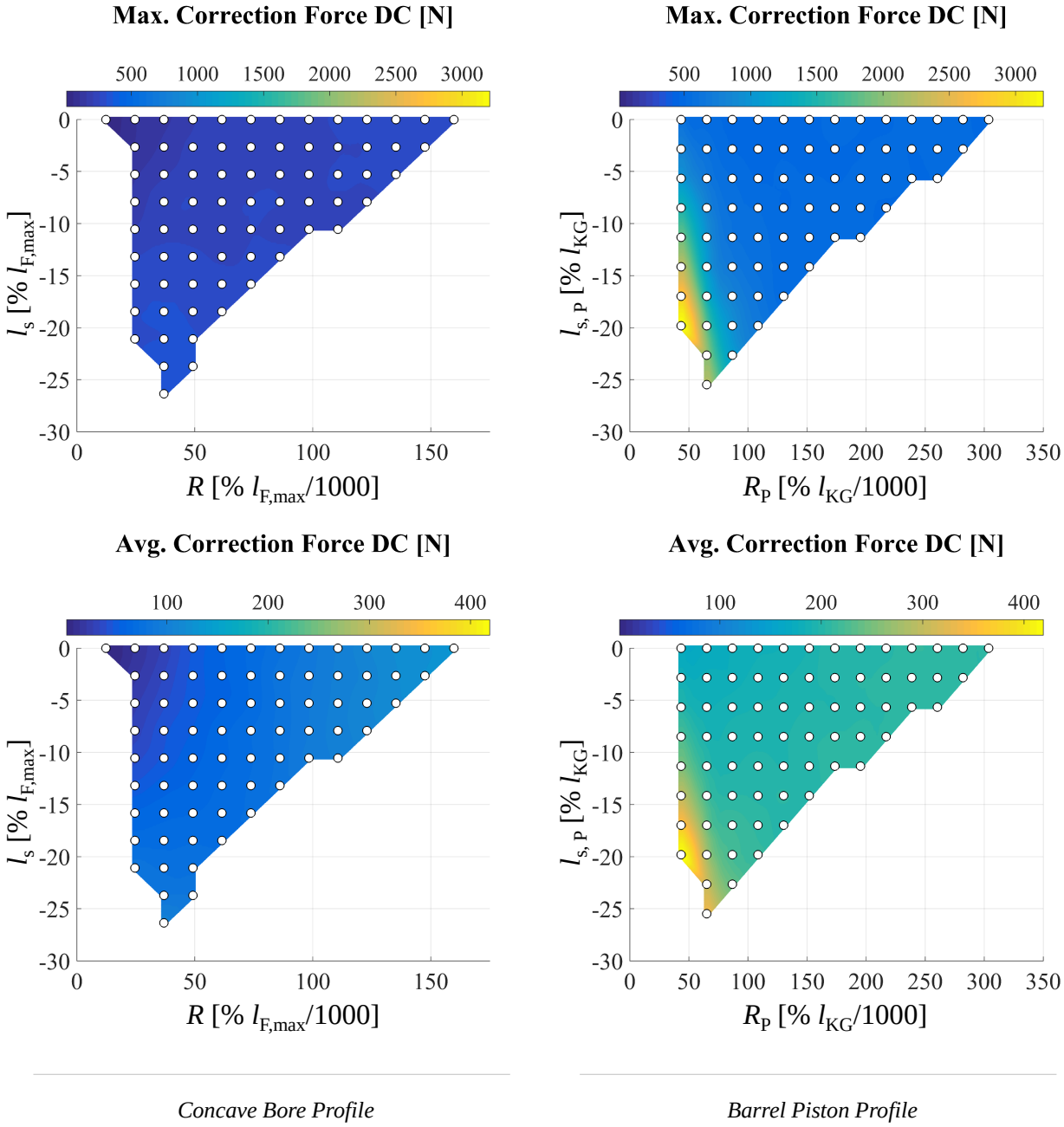

Figure 7.23. Comparison of the concave bore profile (left) vs. the barrel piston profile (right): max. and avg. correction force magnitudes of the simulated shaft revolution at the DC end control point (C_A), at OC4.

piston-bore surface conformity near the DC end of the interface, in two ways. First, these changes in radius and shift decrease the piston diameter at the end of the running surface closest to the piston head. Consequentially, the piston diameter at the case end of the interface near the end of the high-pressure stroke also becomes smaller.

In examining Fig. 7.20 once more, specifically image (b) portraying the end of the high-pressure stroke, it can be seen that once the barrel profile apex has exited the interface, and moved into the DC (for the unit being studied this takes place at $\varphi = \sim 150°$), decreasing the piston diameter near the case end of the interface will increase piston tilt. This lessens piston-bore conformity near the DC end of the interface, and, depending on the deformation of the bore surface, may shorten the extent of region 2 along the z_K-axis. Secondly, in comparing the barrel shape to the dashed box representing the outline of an unshaped piston, it can be seen that the barrel shape itself causes the piston and bore surfaces to diverge more in the bottom half of the interface shown than they would in the absence of shaping; decreasing the radius and increasing the shift magnitude amplify this effect.

In addition to the diminishing pressure buildup in region 2, making the radius smaller and the shift magnitude larger also brings down the pressure held by region 3, which pushes in roughly the same direction as the pressure in region 2 (aiding load support at the DC end). As described earlier, region 3 opens up to the pump case more as the radius becomes smaller and the apex is shifted further towards the DC, allowing more pressure to dissipate into the pump case. This effect also contributes to the DC end correction force peak near the end of the high-pressure stroke, though it should be noted that said contribution shrinks as the region 3 pressure becomes so low that further decreases in radius, or increases in shift magnitude, have little to no effect on it.

The described changes of regions 2 and 3 with radius and shift are demonstrated by Fig. 7.25, which shows the fluid pressure fields of designs Q-T at $\varphi = 170°$. Moving from the profiles of large radius (the right column of plots) to those of a smaller radius (left column), it can be seen that the section of region 3 with lowest pressure (the darkest section of the

plot) expands: region 3 holds less pressure for the profile of smaller radius. Furthermore, in moving from Design T to Design S, the extent of region 2 along the $\hat{y}$-axis reduces. For designs R and Q, there is little change in this because the area of conformity is so small that its extent is largely dictated by bushing deformation.

The same is true when moving from Design S, with a small shift magnitude, to Design Q, with a larger shift magnitude: the extent of region 2 hardly changes. In moving from Design T (small shift magnitude) to Design R (larger shift magnitude), the effects described earlier become more visible, though they remain subtle. The extent of region 2 along the $\hat{y}$-axis becomes shorter, and the section of region 3 with the lowest pressure expands slightly. In order to make this change in region 3 easier to see, the 25 bar contour is highlighted in white. A vertical line segment of the same length l is marked at the same location along the $\hat{y}$-axis for both designs and as can be seen, for Design T, this segment spans the extent of the 25 bar contour at that location, but falls short of covering the extent of that contour for Design R, indicating that region 3 is wider for Design R.

While this explains the trends seen in the right half of Fig. 7.19, it does not explain the difference between the barrel piston and concave bore profiles with regard to the DC end correction force magnitude. What distinguishes these two profile types is piston-bore surface conformity. Specifically, in order to enhance surface conformity near the DC end of the interface over what it would be in the absence of shaping, the apex of either profile with negative shift (barrel piston or concave bore) must have a positive z_{K}-coordinate. This is illustrated in Fig. 7.26.

From the interface cross-sections depicted in images (a) and (b), it can be seen that the concave bore shape only contributes to surface conformity where the components converge at the DC end of the interface if it gives the bore surface in that region a slope that is positive, like that of the piston. This is the case when the apex of the concave bore profile is located to the right of the DC end of the interface (has a positive z_{K}-coordinate), as in image (a): the slope of the bore surface in the described region (green line) is greater than

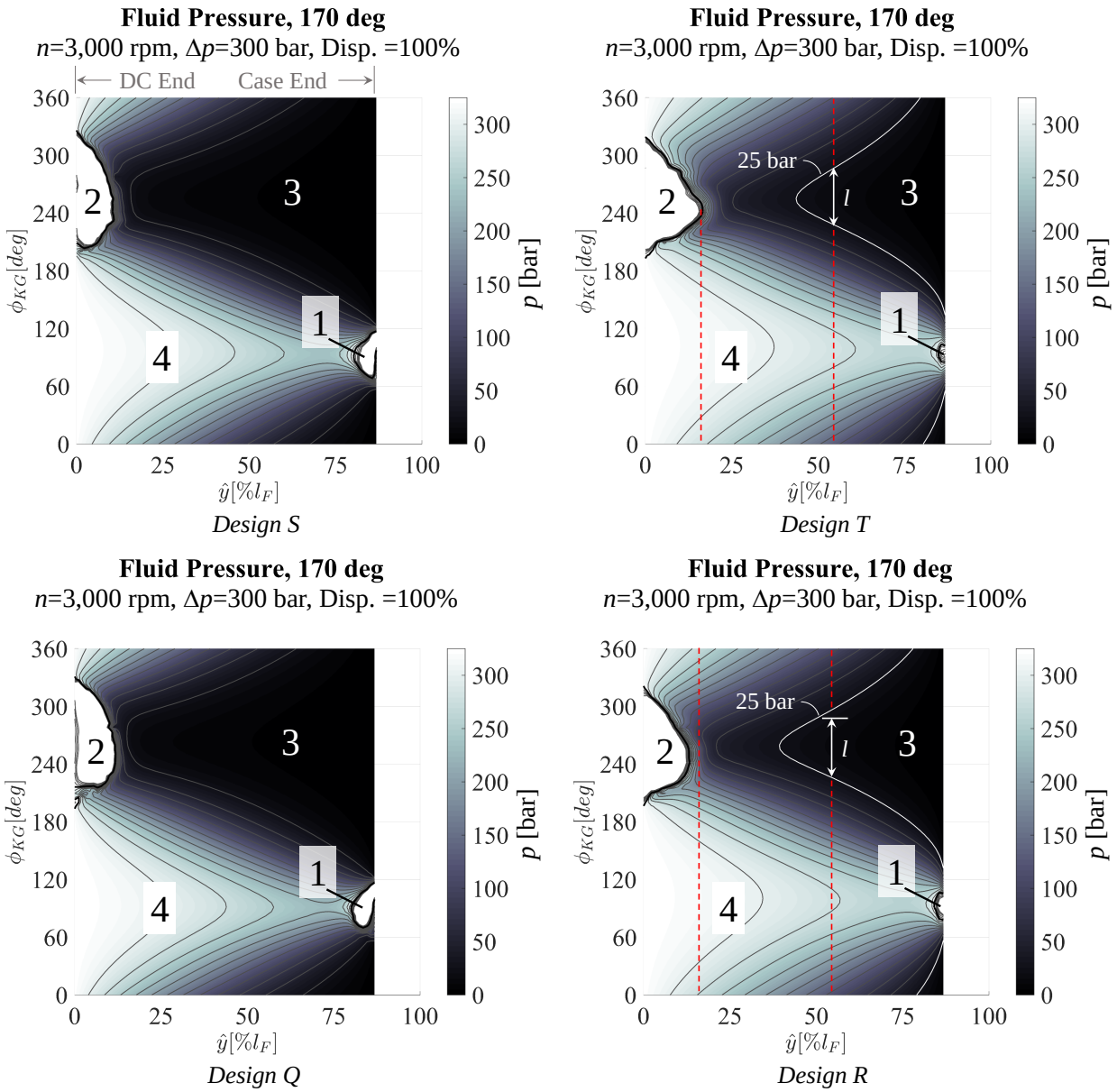

Figure 7.25. Fluid pressure fields of Design Q-T, at OC4.

zero. Without shaping, the slope of the bore surface (red line) is equal to zero. Comparing these two slopes (green line to red line) in image (a) shows that when the apex is located within the interface, the concave bore shape can improve surface conformity over what it would be without surface shaping.

If, however, the apex is located in the DC (has a negative z_K-coordinate), as in image (b), then slope of the bore surface in the region of interest is negative. In this case, comparing

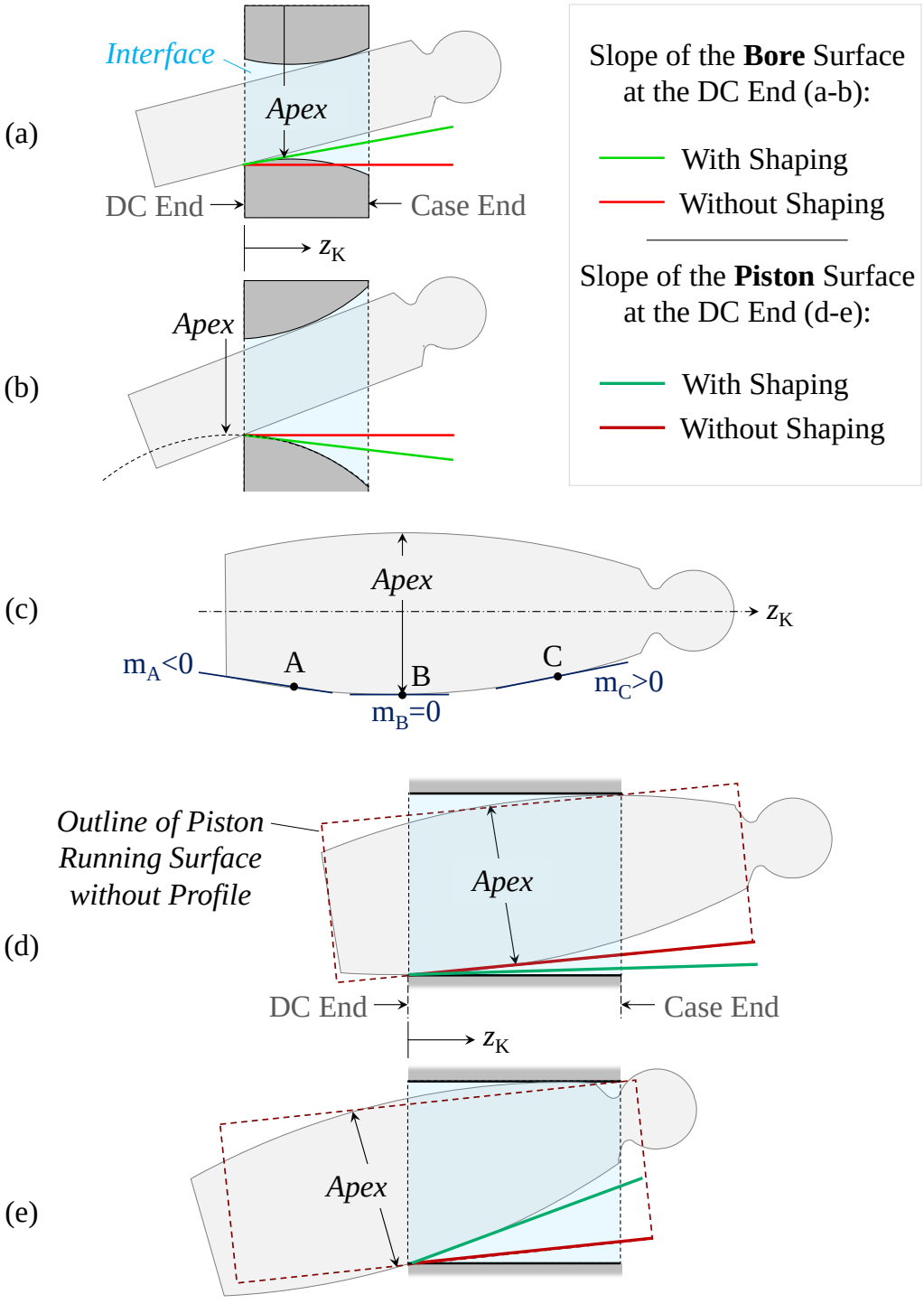

Figure 7.26. The impact of apex location over the high-pressure stroke.

the slopes with and without the concave bore profile shows that the shaping is detracting from conformity near the DC end of the interface. That is, the slope of zero corresponding to no surface shaping (red line) comes closer to the positive slope of the piston than the negative slope of the bore with surface shaping (green line). Piston and bore deformation do provide some compensation to this effect by forcing a patch of conformity— how much depends on the magnitude of the side load, and on the properties of the piston, bushing, and cylinder block materials.

Fig. 7.26 (c)-(e) pertain to the barrel piston profile. This shape increases piston-bore surface conformity when, moving in the negative z_{K} direction towards the point where the two surfaces converge near the DC end of the interface, it gently brings the slope of the piston to zero. If the piston is not tilting, i.e. if its centerline aligns with the bore axis as in image (c), then the piston surface conforms with the unshaped bore at its apex, where the slope is zero (at Point B). To the left of the apex, the slopes are negative (e.g. at Point A); to the right of the apex, they are positive (e.g. at Point C). If the piston now tilts, as shown in images (c) and (d), the negative slopes to the left of the apex increase, coming closer to zero, which enables greater surface conformity at the DC end. It should be noted that there is a limit to this advantage: if the tilt is large enough, these slopes become positive, and if the tilt is then increased further, the surface conformity at the DC end begins to suffer.

The slopes to the right of the apex are positive even when the tilt is zero, as shown in image (c). When the piston tilt increases, so do these positive slopes. Because they are already higher than the slope of the piston centerline in the absence of tilt, they will also be higher in the presence of tilt— and therefore higher than the slope of an unshaped piston surface. For this reason, the part of the piston to the right of the apex cannot contribute to piston-bore surface conformity at the DC end of the interface.

Consequentially, surface conformity can only be increased through this type of piston shaping if the DC end of the interface is located to the left of the barrel piston profile apex: if the apex has a positive z_{K}-coordinate. This case is illustrated in image (d). Comparing the

slopes of the piston surface at the DC end of the interface with and without the barrel piston profile (green to red line), it can be seen that the surface shaping contributes to surface conformity in the region of interest. In image (e), however, the piston profile apex has a negative z_K-coordinate. As a result, the slope corresponding to the implemented profile is higher than that of the unshaped piston, and thus further from the zero slope of the bore surface. Moreover, because the apex is in the DC, the maximum piston diameter within the interface is smaller than it would be if the apex were located within the fluid film. As a result, the minimum piston-bore clearance is larger, and the piston tilt is higher (making for worse surface conformity), than it would be if the apex had a positive z_K-coordinate.

Having established that the apex needs to have a positive z_K-coordinate for the concave bore and barrel piston profiles in order to increase surface conformity at the DC end of the interface, it can now be understood why the load support performance of the two profiles differs for this region. Fig. 7.27 plots the concave bore profile, and barrel piston profile, with the lowest maximum case end correction force in the simulation sets run for their respective shapes. Both profile designs have already been introduced: Design B for the concave bore shape, and Design U for the barrel piston shape. The solid (light blue line) indicates the section of the profile that is inside the interface at $\varphi = 170°$, i.e. near the end of the high-pressure stroke. As can be seen, for Design B, the z_K-coordinate is positive, while for Design U, it is negative. This means that Design B is able to contribute to conformity at the DC end of the interface, but not Design U.

This can also be observed in the film thickness contour plots corresponding to these designs, shown in Fig. 7.27 for the same shaft angle, at OC4 (same plot format as in Ch. 6). Moving from the DC towards the case end of these plots at $\phi_{KG} = 270°$, it can be seen that near the DC end of the interface, the film thickness does not increase as rapidly for Design B as for Design U, and remains lower over a longer stretch. Furthermore, the patch of minimum film thickness near the DC end of the interface (outlined in red), signaling potential metal-to-metal contact in that region, is significantly larger for Design U than for Design B.

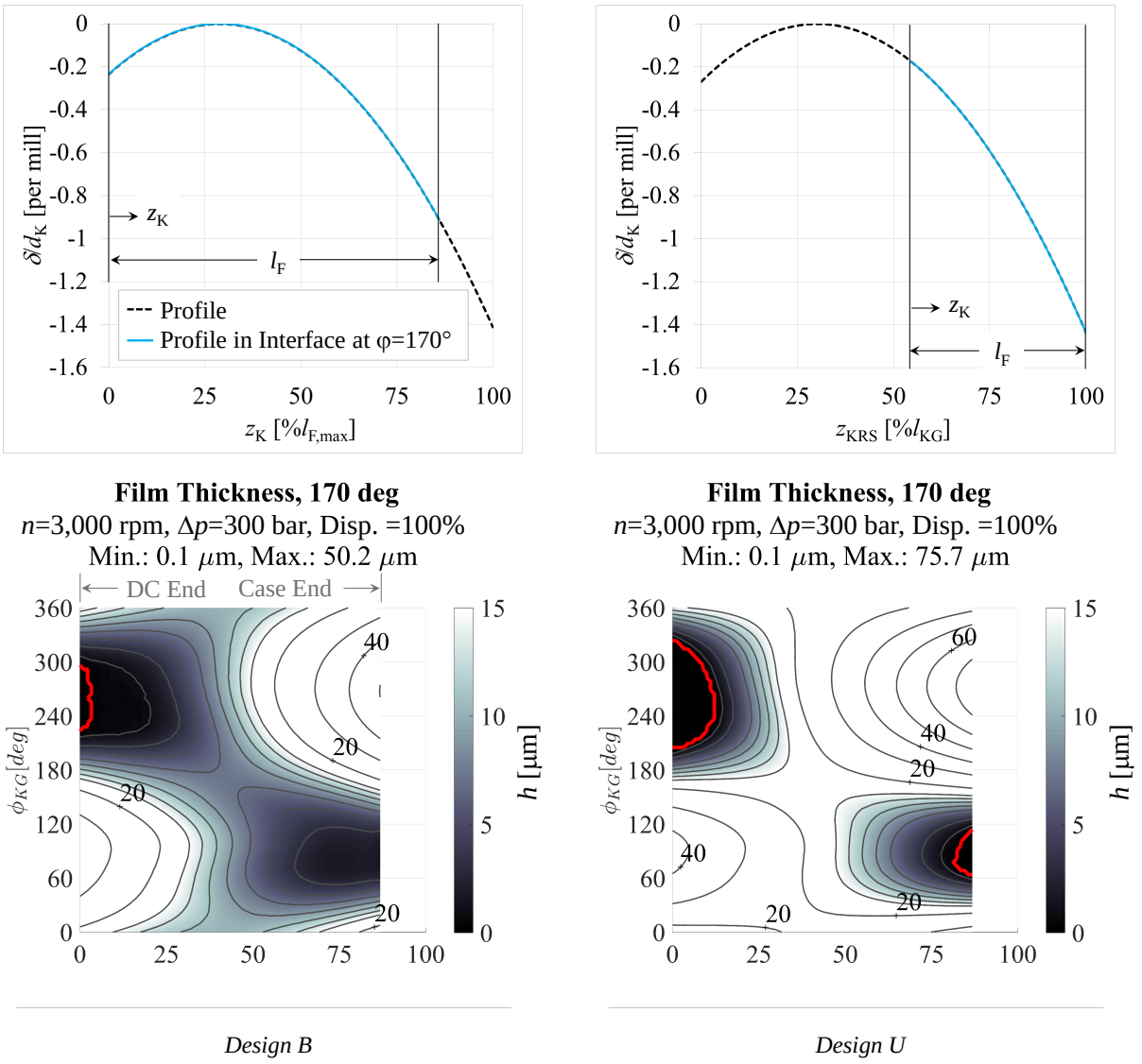

Figure 7.27. Design B (concave bore profile) and Design U (barrel piston profile), as well as their film thickness fields at OC4.

The location of its apex is a disadvantage for Design U. Examining its profile plot in Fig. 7.27 once more, it can be seen that even if the shift of the profile were to be zero, the apex would still have a negative z_{K}-coordinate. In other words, all piston profiles with negative shift that can be constructed for this unit have their apex at a negative z_{K}-coordinate at $\phi_{\mathrm{KG}} = 170°$. One might argue that this can be remedied by using a positive shift instead; however, as already explained, moving the apex towards the piston head increases the correction forces at the case end control point.

One might also argue that the guide length could be extended to include the apex. The difficulty in keeping the apex of the barrel piston profile at a positive z_K-coordinate is that the piston moves: its apex travels the length of the piston stroke. This is a disadvantage inherent to the barrel piston profile. While a variable guide length reduces the problem, it can add manufacturing expense because a longer bore must be machined to hold extremely tight machining tolerances [4]. For Design B, the apex is located at a z_K-coordinate of over $25\% l_{F,max}$— to achieve the same for Design U, whose apex is at $z_K < 0\% l_{F,max}$, the guide length would need to be extended by more than 25%: a drastic increase in length. For the concave bore profile, by contrast, keeping the z_K-coordinate of the apex positive is a simple matter of choosing the right shift value, and can be achieved without any change in the guide length.

The effect of this difference between the two surface shaping types can, as shown in the plots of maximum and average correction force at the DC end control point, be drastic. While for the concave bore profile, the trends in how the maximum contact stress and maximum area taken up by a single patch of $h \leq h_{min}$ vary with profile radius and shift are largely dictated by the case end correction force, for the barrel piston profile, they mimic the trends of the DC end correction force. This can be seen in Fig. 7.28, which compares the mentioned parameters for the two types of surface shaping. These plots express the overall load support performance of the piston-cylinder interface across the DOE grids of the concave bore and barrel piston profile studies— and they show the piston-barrel shaping to perform worse.

A clearer view of the difference in performance can be attained from Fig. 7.29, plotting the maximum correction force magnitude of the DC end control point against that of the case end control point for the designs from the concave bore profile DOE grid (left), and for those from the barrel piston profile grid (right). The designs that are non-dominated with respect to the plotted parameters are highlighted in red. Comparing the locations of these non-dominated designs in the plots for the two surface shaping types being studied, it can be seen that those of the concave bore profile are closer to zero than those of the barrel piston profile. In fact, the non-dominated designs of the barrel piston profile form a front that

indicates a trade-off between the maximum DC and case end correction force magnitudes: the smaller the one, the larger the other. This is the result of the opposing trends in the maximum correction force magnitudes at the two control points, and leads the barrel piston profile to perform poorly compared to the concave bore profile.

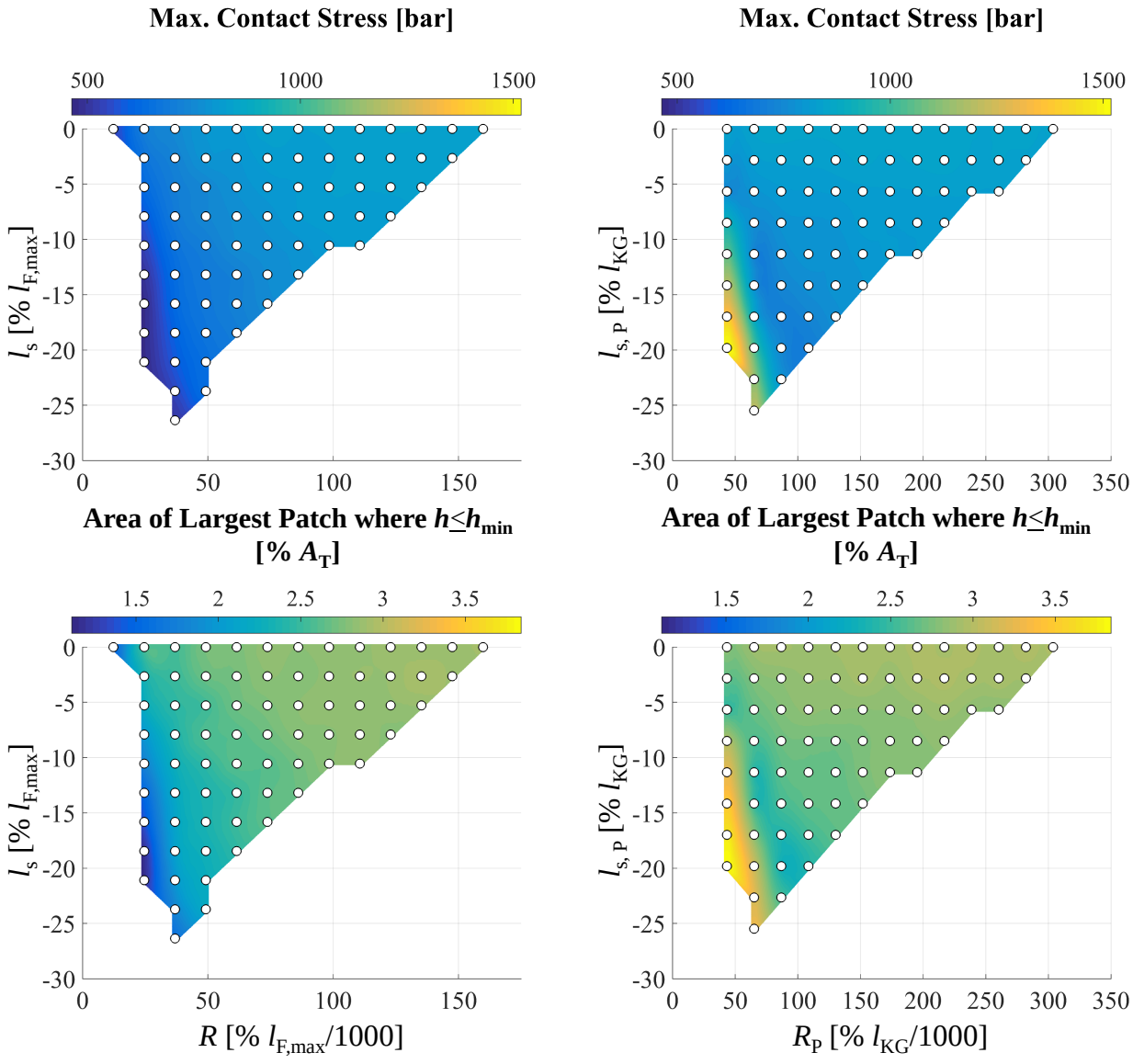

Figure 7.28. Comparison of the concave bore profile (left) vs. the barrel piston profile (right): max. contact stress, and max. area occupied by a single patch of $h \leq h_{\min}$, at OC4.

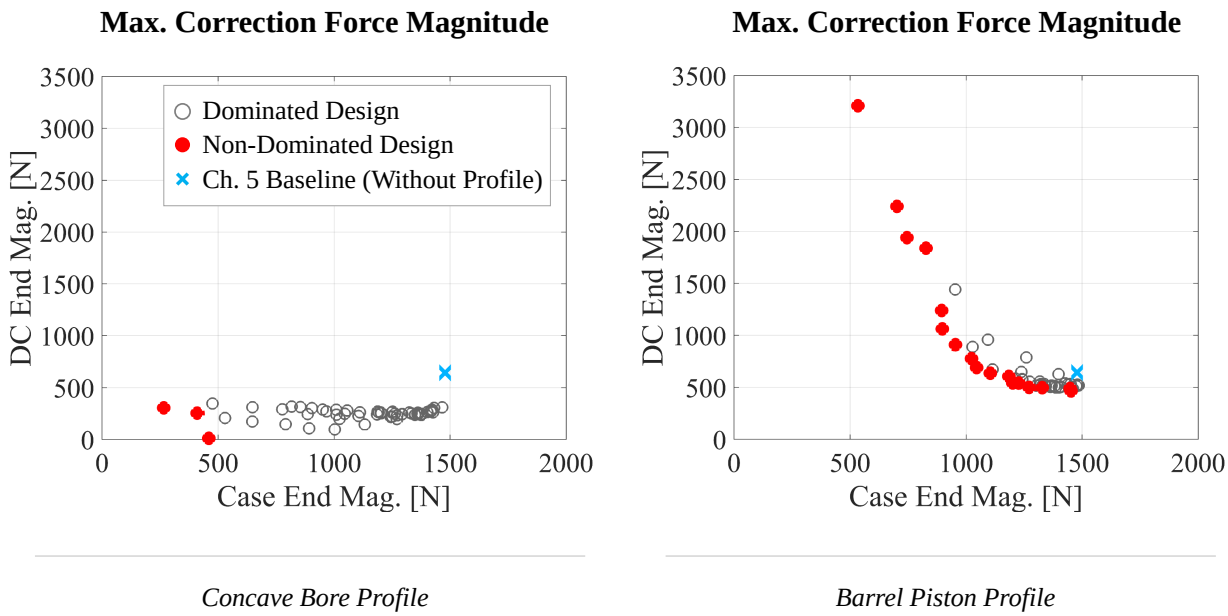

Figure 7.29. Non-dominated designs for the concave bore profile with negative shift (left) vs. the barrel profile with negative shift (right).

However, as pointed out earlier, for barrel piston profiles of small radius and large shift magnitude in the simulated DOE grid, the highest DC end correction forces are seen at the end of the high-pressure stroke, when the guide length is reducing. If the section of the drive shaft revolution over which the guide length changes were removed when computing the maximum and average DC end correction force magnitude, how would the barrel piston and concave bore profiles compare? Fig. 7.30 shows the results: the DC end correction force of the barrel piston profile still increases drastically in moving towards the designs with the smallest radius and largest shift magnitude in the DOE grid, and the concave bore profile still excels.

What has changed is that the increase in the maximum DC end correction force magnitude when approaching the largest shift magnitudes of the smallest two radii in the DOE grid now corresponds to the rise of a peak in the DC end correction force centered at $\varphi = \sim 270°$, i.e. in the low-pressure stroke. An example of this peak can be seen in the plot of the DC end correction force for Design Q, in Fig. 7.24. While a number of effects play into when this peak begins to rise and fall over the low-pressure stroke, the increase of its maximum

value with increasing shift magnitude for profiles of small radii is related to the location of the profile's apex. At $\varphi = 270°$, even the apex of the fifth largest shift magnitude in the DOE grid has a z_K-coordinate of only $\sim 10\% l_{F,max}$. For profiles with either of the smallest two simulated radii, whose curvature is highly pronounced, the apex being so near (or even

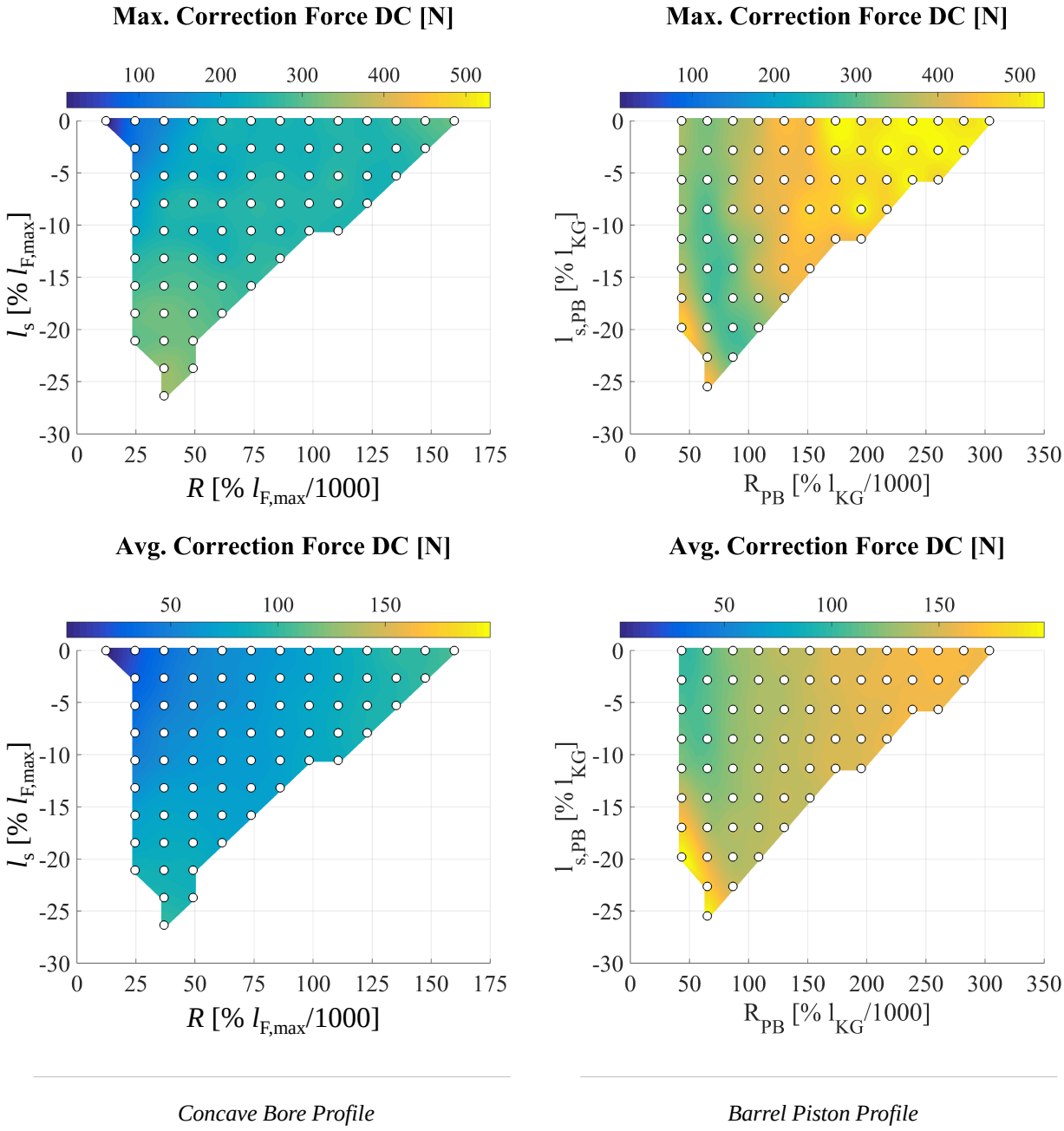

Figure 7.30. Comparison of the max. and avg. correction force magnitudes at the DC end control point (C_A) for the concave bore and piston barrel profiles, when the degrees over which the guide length reduces are omitted, at OC4.

inside) the DC causes the piston and bore surfaces to diverge further over the decisive circumferential span of the fluid film than other profiles in the DOE grid. That decisive span is the span of ϕ_K angles over which pressure buildup contributes to load support at the DC end of the interface.

Fig. 7.31 shows the described surface divergence by comparing the film thicknesses of two barrel piston designs with the same radius, but different shift values: Design S, with a small shift magnitude, and Design U, with a large shift magnitude. Design U has the higher DC end correction force peak of the two over the low-pressure stroke, which rises to its apex

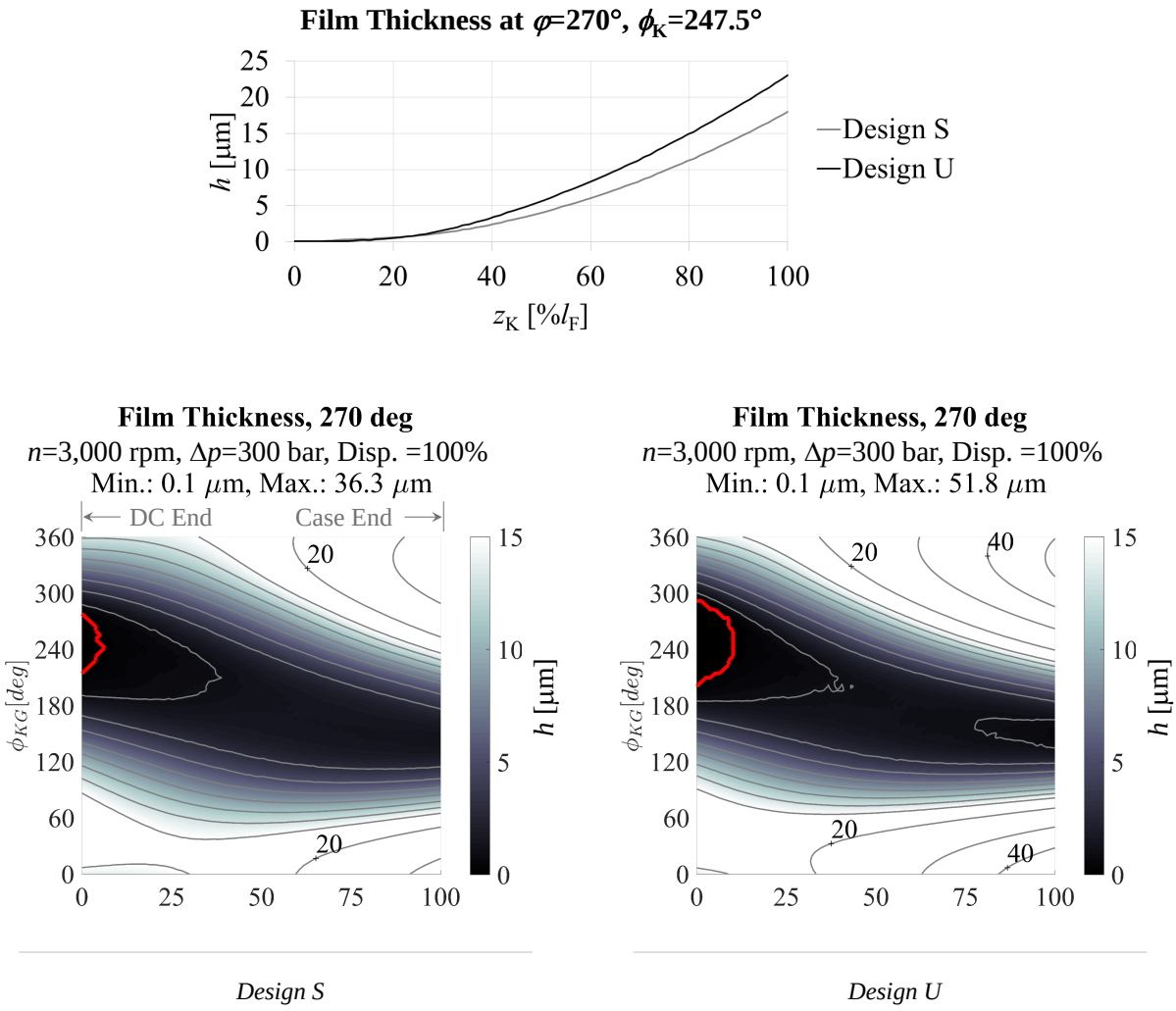

Figure 7.31. Film thickness of Design B vs. Design U at OC4.

in the vicinity of $\varphi = \sim 270°$— the comparison in Fig. 7.31 is therefore conducted at this shaft angle (at OC4). The top plot compares the film thickness of designs B and U at the fluid film's circumferential location ϕ_K=247.5° , which, as can be seen from the film thickness fields of the two designs at $\varphi = \sim 270°$ in the two lower plots, is the circumferential location that falls roughly at the center of the patches of minimum film thickness at the DC end of the interface (outlined in red). From the top plot, it can be seen that, over most of the length of the interface, the film thickness is higher for Design U than for Design S. That is, for Design U, the piston and bore surfaces diverge more rapidly. This rapid divergence takes away from the hydrodynamic buildup of Design U at and in the vicinity of the plotted circumferential location— buildup that is essential to pushing the piston towards the circumferentially opposite side, and preventing contact at the DC end of the interface.

The result is a higher DC end correction force peak over the low-pressure stroke for Design U than for Design S, and a higher maximum DC end correction force over the full drive shaft revolution— when the shaft angles over which the guide length changes are omitted. Having now seen the change that this omission of the shaft angle range $\varphi = \sim 130°$-$\varphi = \sim 230$ makes in the DC end correction force, the question becomes: how does it change the overall load support performance that was shown in Fig. 7.29? Fig. 7.32 answers this question. Its top two plots are the same as those of Fig. 7.29, except that the maximum correction force magnitude at either control point is not the maximum over the entire shaft revolution, but over the entire revolution *with the exception of the aforementioned range of shaft angles.*

In order to provide a more holistic view of the results, the bottom two plots repeat this for the average correction force magnitude. The designs that are non-dominated in terms of the plotted parameters are highlighted in red for all four plots. As can be seen from this figure, even without the shaft angles entailing a change in guide length, the concave bore is still able to outperform the barrel piston profile— even if by a smaller margin.

This is because for the non-dominated piston profiles, a decrease in maximum or average correction force magnitude at the case end control point is met with an increase of these

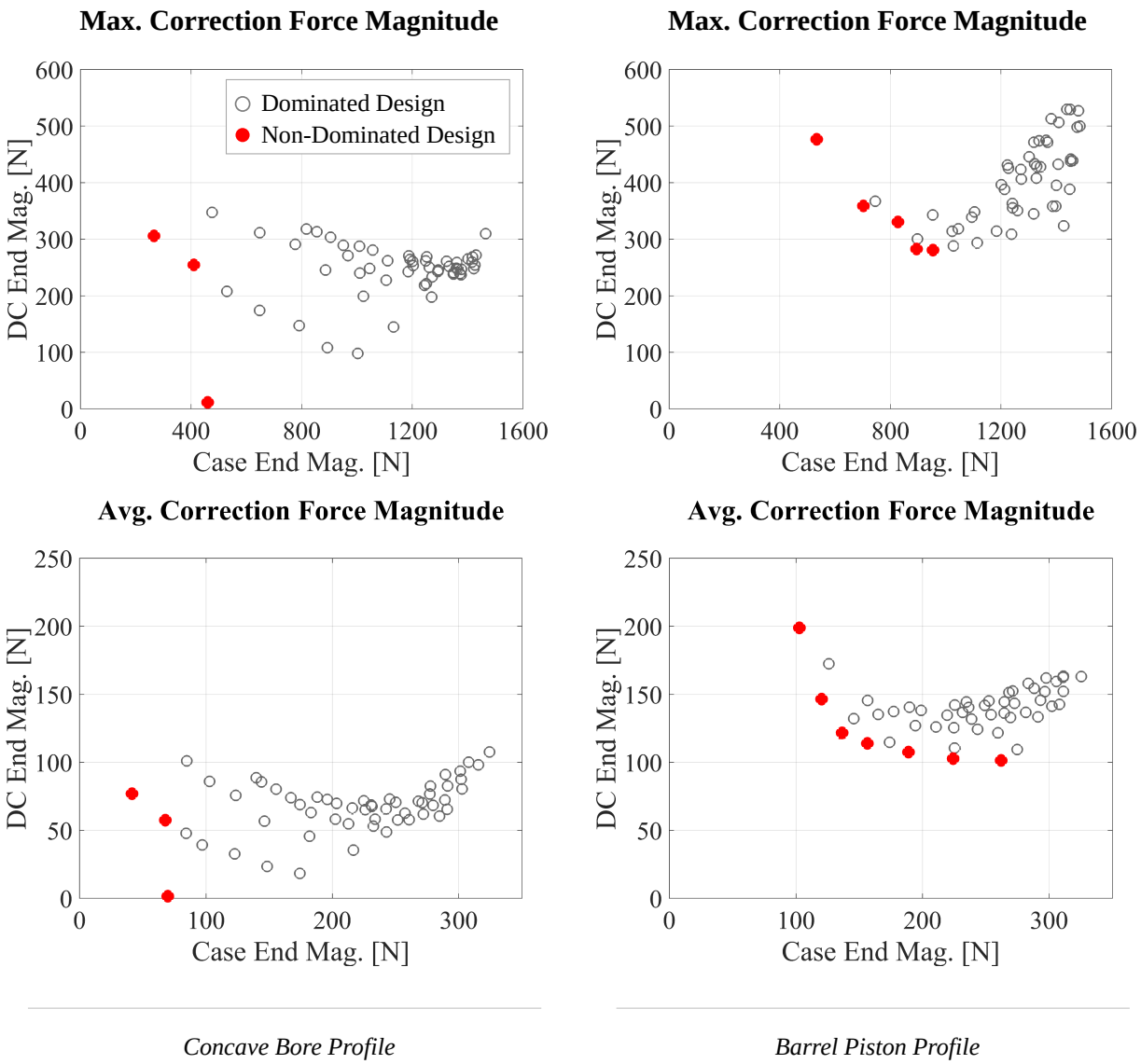

Figure 7.32. Non-dominated designs for the concave bore profile with negative shift (left) vs. the barrel profile with negative shift (right).

parameters at the DC end control point. Similarly, the designs in the studied barrel piston profile DOE that exhibit the lowest maximum case end correction force magnitudes also result in the highest power loss values. Fig. 7.33 compares the power loss incurred by all nine piston-cylinder interfaces of the simulated APMSPD for both profile types (the time-average power loss values shown pertain to the whole shaft revolution). For comparison purposes, the range of the color bar is set to be the same for both plots. As can be seen, for the barrel piston profile, the power loss rises as the profile radius becomes smaller, and the shift

magnitude larger. While the concave bore profile exhibits a similar trend, the maximum power loss values it reaches over the simulated DOE grid are lower than those of the barrel piston profile.

The key difference is again the profile apex location: for a barrel piston shape with a given shift value, the moving apex reaches much lower z_{K}-coordinates than the fixed apex of a concave bore profile with the exact same shift. Since the piston diameter reduces on either side of the apex, moving the apex towards the DC progressively opens up the leakage path on the side of said apex nearest the piston head. Once the apex exits into the DC, the minimum piston-bore clearance increases, which also drives up the leakage. These effects are most pronounced when the shift magnitude of the barrel piston profile is large (the apex is already near $z_{\mathrm{K}} = 0\% l_{\mathrm{F,max}}$ at the beginning of the high-pressure stroke), and the radius is small (the reduction in piston diameter on either side of the apex is large enough to significantly open the leakage path through the interface).

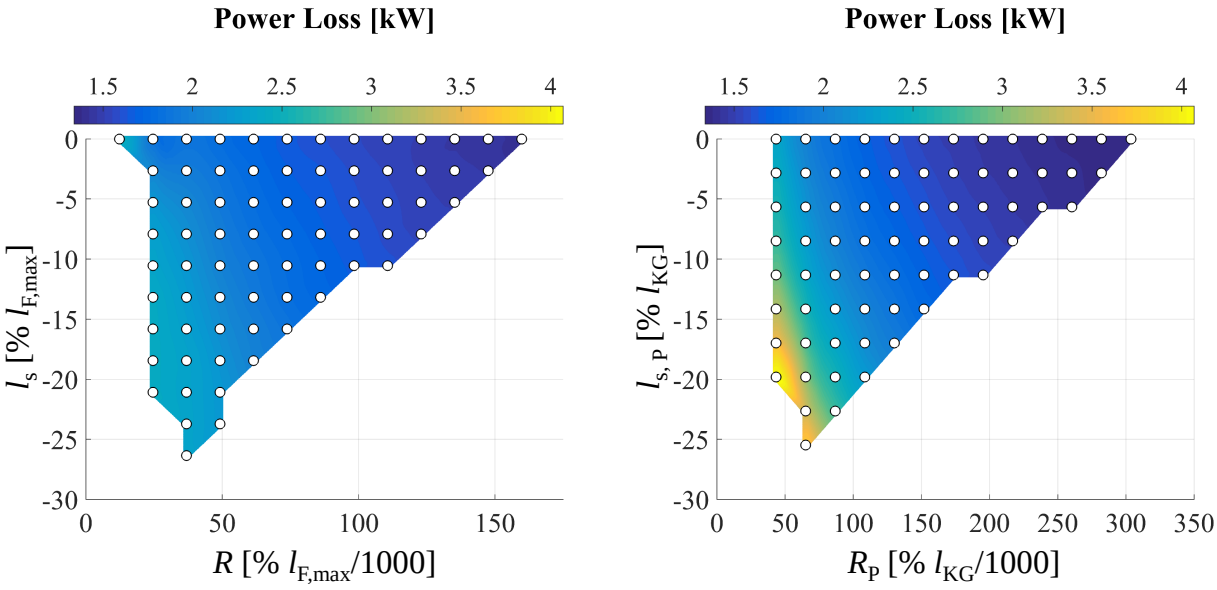

Figure 7.33. Comparison of the concave bore profile (left) vs. the barrel piston profile (right): power loss at OC4.

For the concave bore profile, the apex does not travel towards the DC end of the interface, let alone exit into the DC. On account of this difference between the two profile types, the barrel piston shaping fails to outperform the concave bore profile in terms of power loss, just as is the case for load support.

7.4 Summary/Conclusions vis-á-vis the Concave Bore Profile

In this chapter, two types of surface shaping have been examined with respect to load support and power loss at the piston-cylinder lubricating interface: the concave bore profile, which gives the bore surface the lengthwise cross-section of a circular arc, and the barrel piston profile, which gives the piston running surface the lengthwise cross-section of a circular arc. The simulation study conducted at OC4 for the first of these two, with the same pump setup as the baseline simulations in Ch. 6, showed that the concave bore profile can significantly reduce the maximum and average correction forces at both control points. The case end correction force is most reduced for profiles whose apex is closer to the DC end of the maximum guide length than the case end, or halfway between the two. The DC end correction force, on the other hand, is most reduced for profiles whose apex is either closer to the case end, or halfway between the two ends. On account of the way in which the piston deforms over the high-pressure stroke, the case end correction force is higher, causing the profiles with negative shift to be more effective in mitigating the most severe metal-to-metal contact. For these profiles, it is found that over the design space studied, the greater the magnitude of the negative shift, and the smaller the radius, the higher the power loss due to viscous flow incurred at the piston-cylinder interface. That is, the profile apex should not be shifted more towards the DC than the need for full load support demands.

Comparing the performance of the concave bore shaping to that of the barrel piston at OC4, it is found that when the apex of the corresponding profiles is either at the profile midpoint, or shifted towards the DC, the former is able to outperform the latter. This is largely because as the piston moves, the apex of the barrel piston profile travels towards the DC, compromising surface conformity at the DC end of the interface (increasing the maximum DC end correction force magnitude), and opening up the leakage path through

the fluid film (increasing power loss). In short, even if the manufacture of the concave bore shape is more difficult, it can offer a significant advantage over the piston barrel shape in terms of both load support and power loss.

However, this, and all other information gained via the studies presented in the present chapter, arises from large-scale trends across the design space spanned by the radius and shift values that define the profiles examined. These trends are, in the studies presented, drawn from a simple uniform grid, which is not guaranteed to capture all significant features, nor the global optimum, of the key interface performance parameters within the design space of interest. The coming chapter addresses this issue: the concave bore profile is re-examined—this time through the lens of an optimization algorithm.

8. A RESPONSE SURFACE ALGORITHM FOR PISTON-CYLINDER INTERFACE DESIGN

8.1 Introduction to Response Surface Algorithms

A response surface algorithm has been developed, specifically for piston-cylinder interface design based on a multi-physics model of the fluid film that requires extensive computational time, e.g. FSTI. RSA (response surface algorithms) can be employed as a tool for solving optimization problems; the underlying concept is simple: in order to obtain, for instance, the minimum of the function f(x,y) shown in image 1 of Fig. 8.1, this function is evaluated at a small set of points within the design space (image 2). From the results, a surrogate model— an interpolation or regression fit— is constructed to represent the original function (image 3) [60]. This typically constitutes one iteration of the algorithm. In subsequent iterations, the function is evaluated at more points, and the surrogate model is improved, until evaluating the function at more points no longer significantly changes it. The minimum of the function is then taken to be the minimum of the surrogate. Since it is much less computationally expensive to run function evaluations with the surrogate than with the original function, that minimum can be obtained quickly— usually via a second optimization method consisting of a direct search, gradient-based, or meta-heuristic technique [60].

It is this reduction in function evaluation time that makes the described RSA method so suitable to optimization problems involving the piston-cylinder module of FSTI, which can

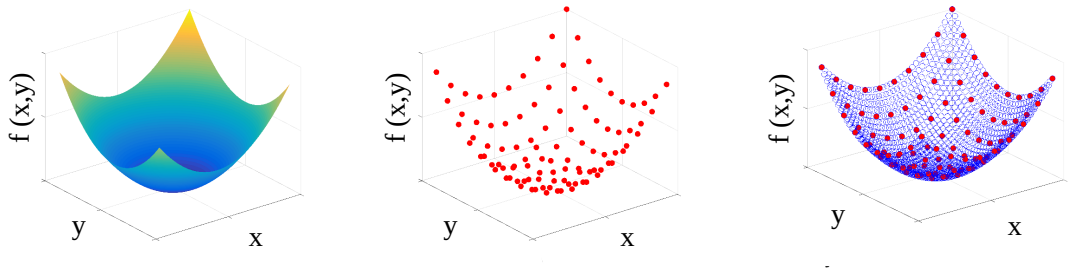

Figure 8.1. Response surface generation.

take on the order of days to run, or to any comparable model of the fluid film with similar run time. Use of an RSA can allow exploration of a design space within a reasonable time frame without making compromising simplifications to the fluid film model. Moreover, the method can be extended to finding the point(s) that minimize multiple objective functions (f_1, f_2, f_3, ... f_n); in this case, the RSA generates a surrogate model for each function, and the most favorable points within the design space can then be located based on those surrogates. In either case (single or multi-objective optimization), constraints can be placed on both the input variables, and on the permissible objective function values of the optimized design(s); this simply entails shaping the design space spanned by the surrogate model(s) such as to exclude regions where the input variables, and/or the objective functions, take on unacceptable values. RSA are versatile— tailorable to the problem of piston-cylinder interface design, in the many different forms that it can take on (perfecting micro surface shaping, piston-bore clearance, guide length, etc.).

While RSA can and will be used as an optimization tool in this work, interest in the RSA vis-à-vis the research objectives in Ch.1 also derives heavily from its modeling capabilities: in particular its ability to capture significant function features within a given design space. As stated at the end of the previous chapter, a simple design study may miss some of these features— a well-designed RSA can lower the chances of that. Furthermore, the RSA is able to concentrate simulation efforts on the regions in the design space that require the most function evaluations in order to fully capture the sought design trends. The result is a more computationally economical and accurate representation of the function/parameter being modeled.

8.2 PCID (Piston-Cylinder Interface Design) RSA Overview

The basic structure of the algorithm developed for piston-cylinder interface design via a high-fidelity multi-physics model such as FSTI is shown in Fig. 8.2; it is set up in three stages, denoted S1, S2, and S3. The starting point is S1 of Iteration 0. As explained earlier, RSA construct surrogate models from the design space locations, and corresponding objective function values, of a set of points. This means that a set of points within the

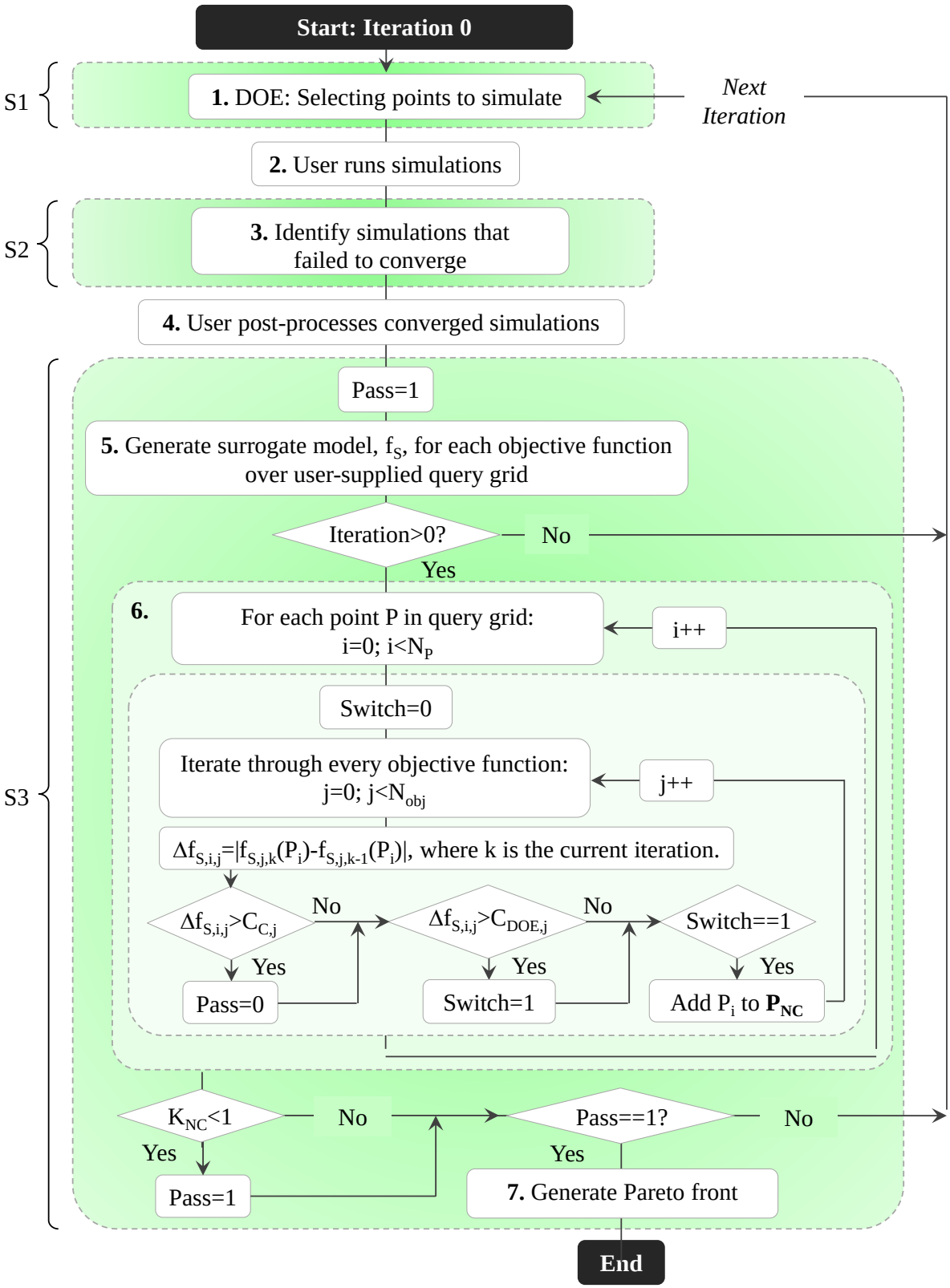

Figure 8.2. PCID RSA overview.

design space must be chosen, and the objective functions must be evaluated at those points, so that the surrogate models can then be built using that data. Step one of the PCID is therefore DOE (Design of Experiments): the methodological selection of these points within the design space. The algorithm developed for this selection process will be discussed in detail in the next section. For now, it suffices to know that said algorithm chooses points from a user-supplied query grid, i.e. from a set of points defining the shape and extent of the design space, and that it aims to maximize the space between each chosen point and its neighbors, such that none will be wasted representing the same design space region twice.

When the selection process is finished, the RSA has a full list of the chosen points' locations within the design space. Now, the objective functions should each be evaluated at those design space locations. That is, FSTI simulations corresponding these chosen points must be set up and run (step 2 in Fig. 8.2). This is done outside the RSA (is not part of the RSA code) in order to avoid chaining the algorithm to a particular simulation input structure, or a particular setup for communicating with a computer cluster, as these may evolve with future users.

Due to the complexity of the numerical simulations being run (especially in terms of the effects the model's simplifying assumptions can have on its stability), and the fact that prior to running FSTI, it is not necessarily foreseeable whether a design is nonfunctional to the point of making the interface behavior incomputable, there may be simulations that fail to converge— or that fail to converge within the user-set maximum number of iterations. Data from non-converged simulations is not reliable, and should not be included in the RSA surrogate model. The S2 (step 3) RSA code identifies these simulations, using information from a log that FSTI outputs for each run; their names are written to a text file. S2 then goes into the RSA's list of design space locations detailing which simulations have been run, and removes the locations pertaining to non-converged simulations, so that their objective function values will not become part of the surrogate model. However, S2 does store these locations in a separate file, so that the points within the design space where convergence failed can be marked in the final surrogate model, making it clear where that model may be less reliable.

Once S2 completes, it is up to the user to post-process the outputs of the converged FSTI simulations in order to obtain the required objection function values from them (step 4). This, too, is excluded from the RSA code in order to give future users flexibility in the approach— the RSA simply requires the obtained objective function values to be delivered in text files of a specific format. With this in hand, the user can launch S3.

This stage commences by constructing surrogate models from the provided simulation data: one model per objective function. These models are generated via a radial basis interpolation. Specifically, for each objective function, the simulation data is used to compute the coefficients of a radial basis function— a type of function that generates outputs based on the distance of a given input to an origin point, or a set of origin points (in this case, the locations of the simulated points within the design space). The radial basis function defined by these coefficients is then evaluated over the same user-supplied query grid from which sampling sites were selected in step 1, yielding a surrogate model. Ergo, the query grid not only defines the design space, but also sets the resolution of all surrogate models— this should be taken into consideration by the user when setting up that grid.

Once step 5 finishes, Iteration 0 is complete. The surrogate models have been generated and stored, and the algorithm moves on to Iteration 1. It begins exactly where the previous iteration did (S1), and runs through steps 1-5 again. A new set of design space points is evaluated, and the corresponding surrogate models are generated based on the results of *both*, this set of points, and the set from Iteration 0. That is, when step 5 finishes, two sets of surrogate models have been generated: the first, constructed using only the function evaluations of the design space points from Iteration 0, and the second, constructed using the function evaluations of the points from Iteration 0 *and* Iteration 1.

In Iteration 1, the algorithm proceeds to step 6, which checks for convergence by comparing the described sets of surrogate models from the current and previous iterations at every query grid point. Fig. 8.2 shows a simplified overview of how this step is structured. For every point P_i in the query grid, the algorithm iterates through each objective function,

calculating the change in the corresponding surrogate model value between the current and previous iterations:

$$\triangle f_{S,i,j} = |f_{S,j,k}(P_i) - f_{S,j,k-1}(P_i)| \tag{8.1}$$

i: Subscript indicating the query grid point being handled

j: Subscript indicating the objective function being handled

k: Subscript indicating the iteration being handled (k=current, k-1=previous)

Based on this computed change, the algorithm then assesses whether the algorithm has achieved convergence. This is determined by comparing the value of $\triangle f_{S,i}$ obtained for each objective function to the corresponding value in a user-supplied vector, denoted $\mathbf{C_C}$. If $\triangle f_{S,i,j} > C_{C,j}$ for one or more objective functions at the query grid point P_i being examined, the variable "Pass" is set to zero— the algorithm is not converged. Convergence is only achieved ("Pass=1") if $\triangle f_{S,i,j} \leq C_{C,j}$ for every objective function, at every query grid point.

In addition to checking for convergence, the PCID algorithm also examines the change in the objective function value at P_i in order to determine whether this point should be considered for selection in step 1, S1 of the next iteration. That is, in the subsequent iteration, the algorithm chooses points for function evaluations not from the entire query grid, but only from the set of points within that query grid where the surrogate models have not achieved convergence. This allows the algorithm to refine the surrogate in regions where large changes from one iteration to the next indicate that significant objective function features may have been missed, or are not yet fully defined.

Whether P_i will be considered by the next execution of step 1 is determined by comparing the value of $\triangle f_{S,i}$ to the values of a second user-supplied vector, $\mathbf{C_{DOE}}$, for every objective function. If $\triangle f_{S,i,j} > C_{DOE,j}$, i.e. if the change in the surrogate model of any objective function exceeds the corresponding user-supplied limit, then the point P_i is added to the vector P_{NC}, and will be considered by the next iteration of step 1. This does not mean that it will be selected, but does mean that it is in the pool of design space locations from which the algorithm will choose.

When all points in the query grid have been assessed by step 6, if the percentage of query grid points at which at least one objective function has failed to converged is less than 1%— i.e. if the fraction of the surrogate models being updated has become negligible— the "Pass" variable is set to 1. At this point, if Pass has a value of 1, indicating convergence, the algorithm generates a Pareto front and terminates. Otherwise, a new iteration begins, starting at step 1, S1, and repeating the process described for Iteration 1. The cycle continues until convergence is achieved. With every pass, the radial basis interpolation for each objective function is constructed with simulation data from more and more points: the points chosen by the algorithm for that iteration, and the points chosen in previous iterations. With each cycle of steps 1-6, more details on the surrogate models are filled in, fleshing out the features of the objective functions on the surrogate models until further FSTI simulations no longer add significant information.

This concludes the overview of the PCID algorithm. The next two sections will address, in detail, step 1 (DOE), and step 5 (the construction of the surrogate models).

8.3 DOE (Design of Experiments)

In each iteration, the PCID algorithm selects points in the design space at which the objective functions will be evaluated. As should be clear from the algorithm overview, the PCID RSA requires the DOE method employed for this to be capable of handling two cases. First, in iterations 0 and 1, it must be able to choose points representative of the entire design space within the user-set constraints, regardless of what shape they may cause that space to take on. Second, in all further iterations, the chosen DOE technique must be able to choose points representative of the odd-shaped regions composed of the query grid points at which one or more of the surrogate models underwent a change from the previous iteration that exceeds the user-specified limit(s).

Uniform sampling is not easily employed here, because it would entail fitting a regular lattice of points to the highly irregular design space shapes that the PCID algorithm is likely to produce. Especially in the second of the two aforementioned cases, the algorithm may

be assigned to sample a space consisting of small islands, and/or narrow corridors. These are not covered well by a uniform grid, unless the lattice spacing is made sufficiently small. However, decreasing the spacing drives up the number of sample points, and, consequentially, the number of function evaluations. This should be avoided, as function evaluations are of particularly high computational expense.

Moreover, the PCID RSA receives description of the design space only in form of a query grid, submitted by the user as a set of coordinates. The grid is not required to be structured, and the coordinates of its points are not required to be submitted in any particular order. While this gives the user great latitude in terms of what type of design spaces can be handled, and simplifies the task of specifying constraints, it means that fitting any type of DOE grid requires first processing the submitted set of unordered query grid coordinates, such as to determine where the design space boundaries are located. Even irregular or adaptive grids, which can cover an intricate design space shape without forcing as many function evaluations as a uniform grid, require this pre-processing— no grid can be fit to a design space without knowing where its border runs. However, such pre-processing adds considerable computational time.

The described problems can be circumvented by choosing the pseudo-Monte Carlo sampling method, which selects points from the design space— whatever its shape— at "random," via a pseudo-random number generator [61]. This suits the PCID RSA, because it entails nothing more than randomly choosing from the user-supplied list of query grid coordinates. There are, however, two caveats. First, a standard random number generator will rarely choose points in the corners and crevices of the design space (instead, the chosen points will mostly fall into large open regions). Secondly, the "randomly" chosen points tend to clump, as illustrated in Fig. 8.3.

Stratified Monte Carlo sampling handles both caveats by dividing the design space into a grid, and forcing the algorithm to place one point at a "random" location inside each grid space [61]. This concept can even be taken a step further: LHS (Latin hypercube sampling)

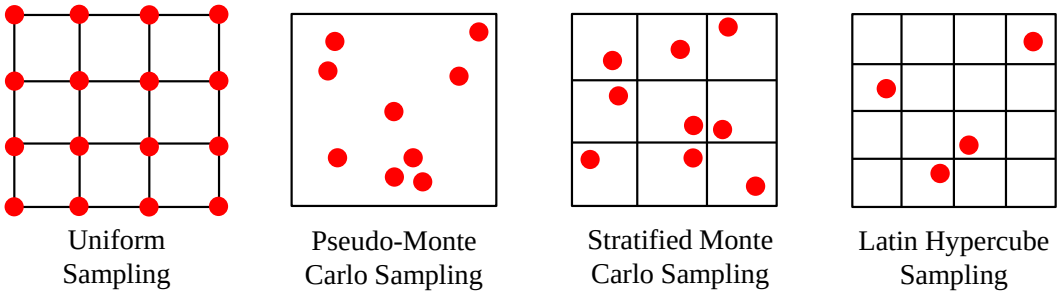

Figure 8.3. DOE methodology state of the art (images based on [61]).

employs the same basic approach, but only places a point into grid spaces that do not share variable values with any other point-containing grid space. That is, if the design space is spanned by two variables, LHS will *not* place a point into grid spaces that share a row or column with any other point-containing grid space. Although this strategic and frugal placement of sampling points is a popular approach, and solves the some of the problems associated with simple pseudo-Monte Carlo method, it involves fitting a grid to the sampling space, which, as discussed, is not ideal for the PCID algorithm.

As can be seen from this example, the PCID algorithm demands great versatility from its sampling method, as designing the piston-cylinder interface can pose numerous challenges of vastly different nature. While the focus of this work remains on micro surface shaping, the algorithm is intended to permit as large a range of studies as possible. The sampling algorithm written for the PCID RSA therefore strives to minimize the described drawbacks associated with other methods— without unnecessarily limiting the scope of what information the user can pursue via the RSA. Moreover, this algorithm limits the user's effort in specifying the design space to the submission of the described set of unordered coordinates.

It does share, with the others mentioned, the Achilles' heel of not being as quick to execute as pseudo-Monte Carlo sampling; however, it drastically reduces the sample site clumping typical for the pseudo-Monte Carlo approach. This is critical, because it helps lower the number of RSA iterations required to capture all significant features of the objective func-

tions. Simulating the piston-cylinder interface is slow, causing each iteration to take on the order of days to complete— wasting sampling sites is not an option. Although an increased concentration of sites may be needed for regions in the design space where one or more objective functions take on a more complex shape, that concentration should not be achieved by allowing clumping throughout the entire space. The PCID RSA handles this case, starting in Iteration 2, by restricting the regions from which sampling sites may be chosen to those where one or more surrogate models have failed to converge, i.e. where the number of sampling sites has been insufficient to capture all significant objective function features. This increases the concentration of sampling sites only where needed.

A clear overview of which part(s) of the design space are sampled from during which iteration is provided in Fig. 8.4: a simplified diagram of the PCID RSA DOE algorithm. As can be seen from step 1, for iterations 0 and 1, the full set of query grid points, denoted Set A, is used as the pool of sampling sites to choose from. Starting at Iteration 2, only the query grid points at which at least one of the surrogate models failed to converge are used— this is denoted Set C.

The DOE algorithm reads in the relevant pool of sampling sites for the iteration being handled (Set A or C), as well as all sampling sites already selected in any previous iterations, which should not be chosen by the DOE a second time (Set B if It.=1, Set D if It.¿1). From the pool of sites (Set A or C), a set of random sites is selected, denoted Set E (step 2). For every site in Set E, $l_{\mathrm{min,i}}$, the distance to its nearest neighbor (out of sets B, D, and E) is calculated (step 3). The algorithm then iterates once more through all sites in Set E. This time, for each point $\mathrm{P_{E,i}}$ in this set, it selects a second set of random points: Set $\mathrm{F_i}$ (step 4). Next, it determines which site in Set $\mathrm{F_i}$, if any, the point $\mathrm{P_{E,i}}$ should be replaced with in order to maximize $l_{\mathrm{min,i}}$ (step 5). Once this has been done for every point $\mathrm{P_{E,i}}$ in Set E, the entire loop consisting of steps 4-5 is repeated, until all the points from the new $\mathrm{F_i}$ sets fail to replace $\mathrm{P_{E,i}}$, i.e. fail to increase $l_{\mathrm{min,i}}$, for 5,000 consecutive iterations. At that point, convergence is achieved, and Set E constitutes the chosen set of sampling sites.

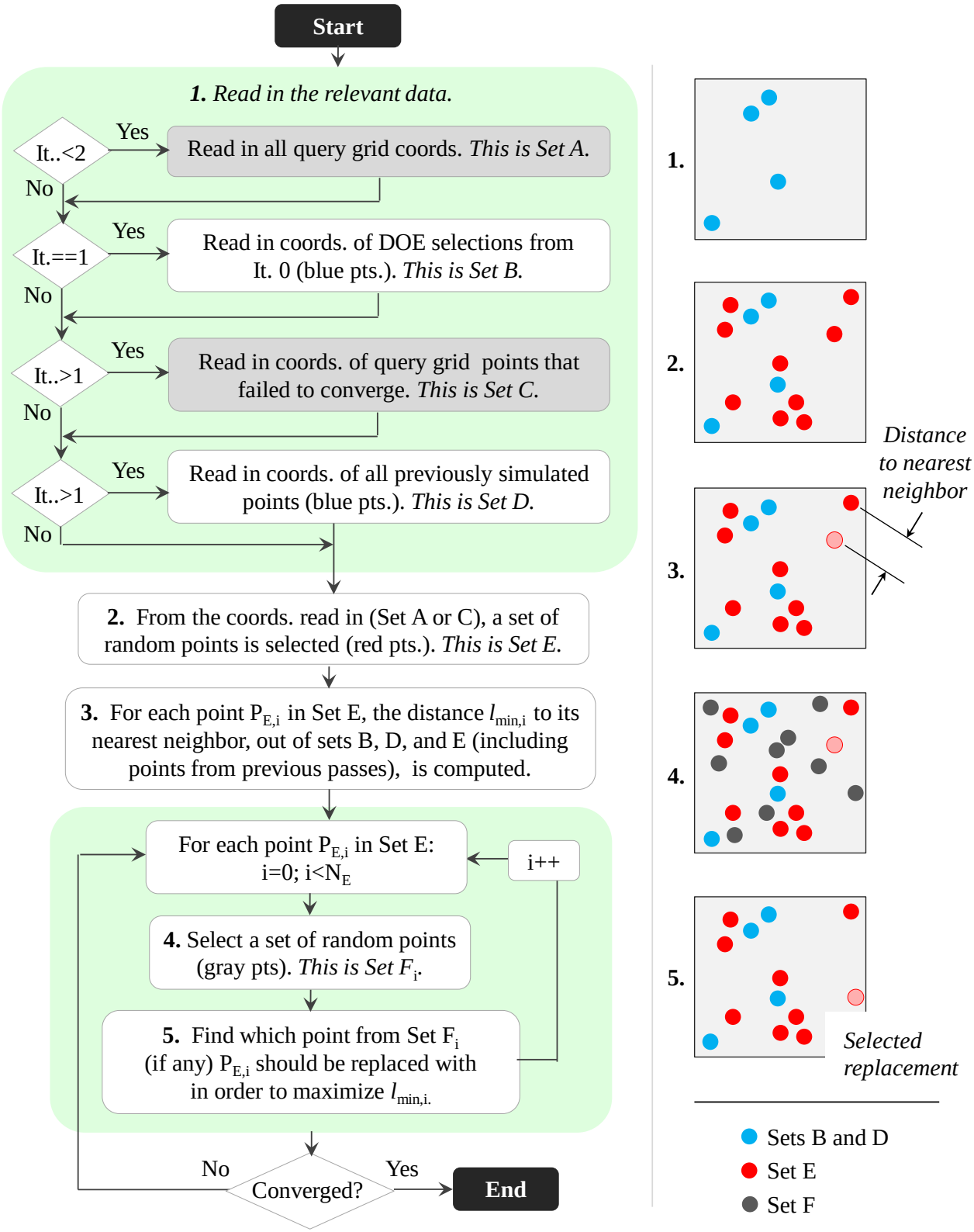

Figure 8.4. PCID RSA DOE Algorithm.

Two examples of the output that can be achieved via the PCID RSA DOE algorithm, specifically in comparison to pseudo-Monte Carlo sampling, are shown in Fig. 8.5. In the two plots at the top, sixty sampling sites are selected by the two DOE methods in order to cover a triangular design space. As can be seen, the recommended sampling sites generated by the pseudo-Monte Carlo method exhibit clumping, and large regions of the design space are left un-sampled. In contrast, the recommended sites generated by the PCID RSA DOE algorithm do not exhibit significant clumping, and cover the design space more evenly.

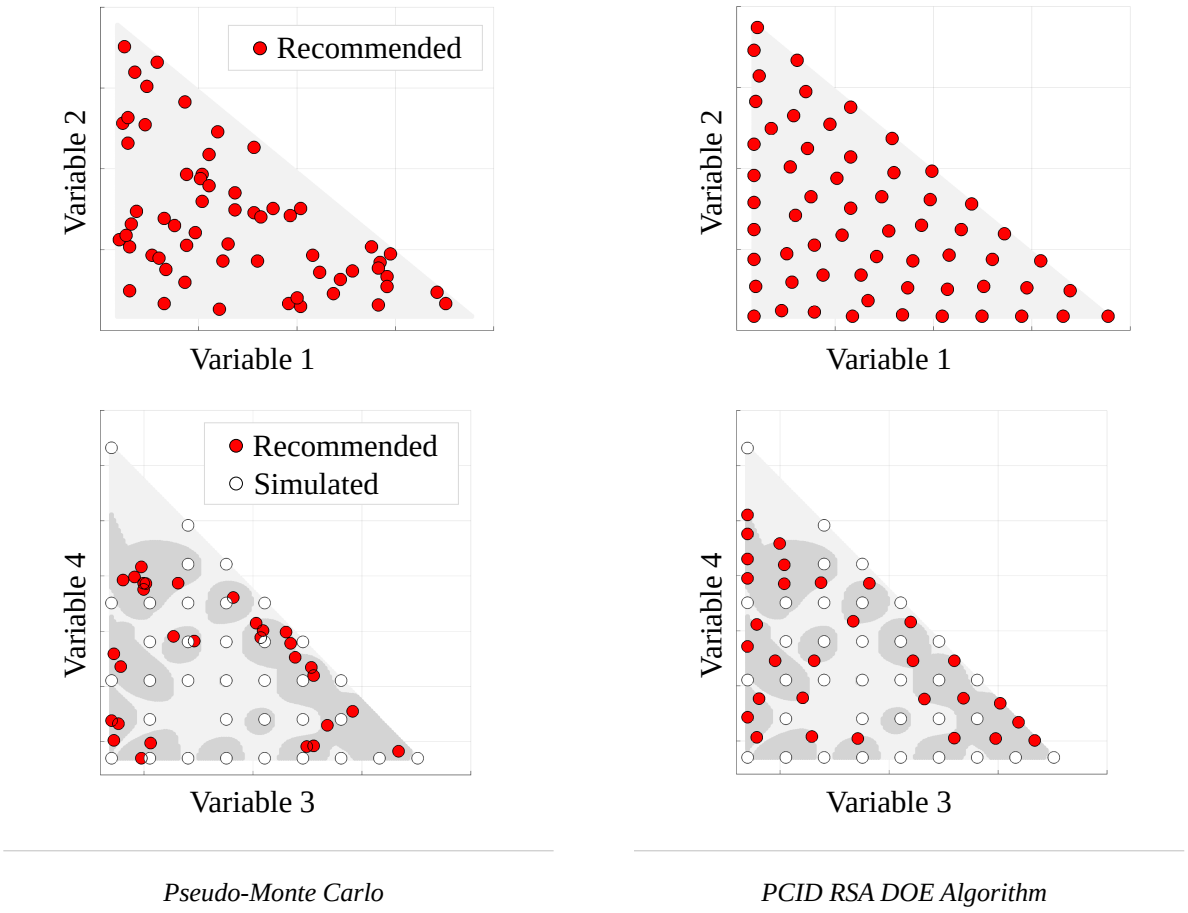

Figure 8.5. Pseudo-Monte Carlo sampling (left) vs. the PCID RSA DOE algorithm (right).

The second example (bottom plots) compares the two DOE methods for the case of the type of the design space to be covered when PCID RSA It.>1. The light gray region represents the full design space to be covered; the dark gray areas mark query grid points at which

one or more surrogate models have failed to converge. The objective in this case is selecting sampling sites that fall only within those dark gray areas, but avoid the sampling sites that have already been selected in previous simulations (white points). The pseudo-Monte Carlo method again exhibits clumping, and misses two of the "islands" in the space to be sampled. The PCID RSA DOE algorithm again covers the space more evenly, and only misses one of the islands.

However, even this algorithm is sometimes challenged by sampling spaces in island form. The PCID RSA DOE algorithm will spread most of the sampling sites over the island(s) of largest area, which, depending on the shape and size of the islands, and the number of sampling sites to be set, may cause islands of smaller, yet considerable area, to not be assigned any sites. This problem can be overcome by running multiple passes of the DOE algorithm. That is, the entire algorithm outlined in Fig. 8.4 can be run repeatedly, generating a new Set E every time. Each new set strives to maximize not only the distance between its own sites, as well as between its sites and those from previous iterations, but also between its sites and those of the previous passes in the current iteration. As a result, large islands are less likely to be able to fit as many sampling sites as they would be able to in the absence of passes, i.e. when the algorithm is spreading out all the sites at once. What cannot fit onto the large islands will be delegated to the smaller ones, granting them the desired representation.

The number of passes made is left up to the user. The same is true of the number of sampling sites to be selected by the DOE. The more sites are chosen, the more information will be available to construct the surrogate models. However, the more sites, the more computationally expensive it is to complete the corresponding function evaluations. Furthermore, an excessive number of sites could, for objective functions that are not well-behaved, cause the interpolation process to generate unwanted spikes in the surrogate models. For iteration 2 and above, it is therefore advisable to decrease the number of sites in proportion to the amount of design space area that those sites will cover— i.e. as the area spanned by non-converged query grid points shrinks, the number of sites to be chosen for the next iteration should be smaller than that used for the current iteration.

8.4 The Radial Basis Interpolation Scheme

As explained in Section 8.2, the RSA sets up one radial basis function per objective function. Each such radial basis function is then evaluated over the query grid, thereby creating a surrogate model of the respective objective function. The radial basis function, to be evaluated at a point $(x_1, x_2, x_3, ...)$ in the design space, takes on the following form [62]:

$$g(x_1, x_2, x_3, ...) = \sum_{\mathrm{k=1}}^{\mathrm{M}} W_{\mathrm{K}} f(r_{\mathrm{K}}) \tag{8.2}$$

This function is a summation from k=1 to k=M, where M is the total number of objective function evaluations that will be used to construct the surrogate model. That is, the product $W_{\mathrm{K}} f(r_{\mathrm{K}})$ is computed for each objective function evaluation— where $\mathrm{W_K}$ is a weight, and r_{K}, a distance. Let the location of the $\mathrm{k^{th}}$ objective function evaluation within the design space be denoted $(x_{\mathrm{k},1}, x_{\mathrm{k},2}, x_{\mathrm{k},3}, ...)$. Then, r_{K} is the distance from $(x_1, x_2, x_3, ...)$ to $(x_{\mathrm{k},1}, x_{\mathrm{k},2}, x_{\mathrm{k},3}, ...)$, i.e. from the point at which the radial basis function is being evaluated, to the location of the $\mathrm{k^{th}}$ objective function evaluation.

f is a function that determines the type of interpolation created by the radial basis function (linear, cubic, etc.). The chosen type is known as the multiquadratic function [63]:

$$f(r_{\mathrm{K}}) = \sqrt{(r_{\mathrm{K}})^2 + \sigma^2} \tag{8.3}$$

Inserting this into Eq. 8.2, the radial basis function becomes:

$$g(x_1, x_2, x_3, ...) = \sum_{\mathrm{k=1}}^{\mathrm{M}} W_{\mathrm{K}} \sqrt{(r_{\mathrm{K}})^2 + \sigma^2} \tag{8.4}$$

Modeling an objective function with a radial basis function of this form entails determining the distances r_{K}, the value of σ, and the weights W_{K}. The distances are trivial; σ is not— this parameter affects how far the influence of a function evaluation extends within the radial basis interpolation [64]. Fig. 8.6 gives a very simple example: an interpolation runs through three points, two of which are on the x-axis, and one of which has a positive

y-value. The point with the positive y-value will create a peak in the interpolation. If the influence of this point extends far, that peak is wide– e.g. image (a). If the influence of this point does not extend as far, the peak is narrower: see image (b). σ is significant because the surrogate model may have difficulty converging if the influence of the points at which the objective functions are evaluated extends too far, or not far enough, to accurately model those functions.

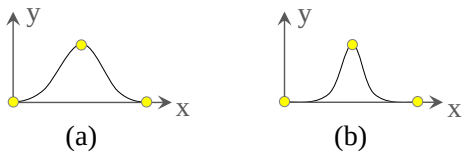

Figure 8.6. Effect of σ.

Though typically a constant, for the PCID RSA this parameter was found to perform well when set to half the minimum of the computed r_{K} values:

$$g(x_1, x_2, x_3, ...) = \sum_{\mathrm{k}=1}^{\mathrm{M}} W_{\mathrm{K}} \sqrt{{r_{\mathrm{K}}}^2 + {\sigma_{\mathrm{K}}}^2}, \text{ where : } \sigma_{\mathrm{K}} = \frac{r_{\mathrm{K,min}}}{2} \tag{8.5}$$

Finally, the weights, W_{K}, are determined based on the constraint that the interpolation must pass though each of the M points generated by evaluating the objective function being modeled. Ergo, at these M points, both $g(x_1, x_2, x_3, ...)$ and $f(r_{\mathrm{K}})$ are known— and W_{K} can be solved for.

With the resulting W_{K} values in hand, the radial basis function is evaluated over the query grid, generating the desired surrogate model. An example of these models will be shown in the next section, which presents an optimization study of the concave bore profile using the PCID RSA.

8.5 Concave Bore Profile Optimization Study

The study to be presented in this section uses the PCID RSA to optimize the defining dimensions of the concave bore profile for use in the same 75 cc unit that was simulated in the previous chapter, and at the same operating condition (OC4). The hydraulic fluid is water, and the materials and nominal minimum clearance are those of the corresponding Ch. 6 baseline. The maximum guide length, however, has been extended from that of the baseline by 11%, in aim of investigating whether with this extension, the concave bore profile can achieve full load support.

8.6 Variables to be Optimized

The values of the following variables will be optimized:

1. *R, the concave bore profile radius*
2. l_s, *the concave bore profile shift*

As described in the previous chapter, the surrogate model for each objective function is generated via a radial basis function of the form:

$$g(x_1, x_2, x_3, ...) = \sum_{k=1}^{M} W_K f(r_K) \tag{8.6}$$

For this study, the function becomes:

$$g(R, l_s) = \sum_{k=1}^{M} W_K f(r_K) \tag{8.7}$$

One difficulty in generating a suitable radial basis function with R and l_s is that the concave bore profile radius is on up to four times the order of magnitude of the shift— if not properly handled, such a considerable difference in magnitude can result in a poor interpolation. To guard against this, the RSA reads in a set of user-specified scaling factors, one per variable being optimized, and multiplies the variable values of all the simulated and query grid points by their respective factors from that set prior to computing the distance r_K from them. Upon completion of the surrogate models, the variables are multiplied by the inverse

of those scaling factors, returning them to their proper magnitudes. The implementation of these scaling factors is nothing more than a temporary unit conversion that aids the interpolation scheme. For this study, the concave bore profile radii are multiplied by a factor of 0.0005, and the shifts by a factor of 1, thereby bringing both onto roughly the same scale.

8.7 Objective Functions

Optimization algorithms seek to find the minimum point of "objective functions" (e.g. f(x,y) in the example from Fig. 8.1). As explained, in the process of obtaining this minimum, the RSA constructs a surrogate model of the objective function— a model that can convey much information about how the objective function changes over a given design space. This merits choosing the objective functions carefully. Designing a functional, efficient piston-cylinder interface calls for objective functions that serve as clear metrics of load support and power loss— especially when the hydraulic fluid is water. For the study to be presented in the next chapter, the following objective functions have been selected:

1. $f_1 = P_L$: *The time average of the power loss due to viscous flow, incurred, in total, by all piston-cylinder interfaces in the simulated unit, over the shaft revolution being modeled.* In order to obtain the value of this parameter, the value corresponding to the single piston-cylinder interface being simulated is multiplied by the number of such interfaces in the unit.

2. $f_2 = \sigma_{\text{max,rev}}$: *the maximum contact stress magnitude at any fluid grid element over the simulated shaft revolution (σ is the stress that FSTI applies when $h < h_{\text{min}}$).* $\sigma_{\text{max,rev}}$ is an important metric because, if the stress is excessive, it could cause plastic deformation of the piston and cylinder bore (or bushing) material.

3. $f_3 = |F_{\text{C,DC}}|_{\text{max,rev}}$: *the maximum magnitude of the DC end correction force (the correction force at control point C_{A}) over the simulated shaft revolution.*

4. $f_4 = |F_{\text{C,DC}}|_{\text{avg,rev}}$: *the average magnitude of the DC end correction force over the simulated shaft revolution.* Examining the average DC correction force in addition to the maximum guards against being misled by any numerical spikes in the correction forces.

5. $f_5 = |F_{C,C}|_{max,rev}$: *the maximum magnitude of the case end correction force (the correction force at control point C_B) over the simulated shaft revolution.*

6. $f_6 = |F_{C,C}|_{avg,rev}$: *the average magnitude of the case end correction force over the simulated shaft revolution.*

7. $f_7 = A_{p,max}$: *Area of the largest patch of min. film thickness ($h \leq h_{min}$) over the simulated shaft revolution.* This is important because, while some load support may exist in small patches of minimum film thicknesses, in very large patches, it is likely that there are dry regions of solid contact. Thus, a smaller area is more favorable— provided the contact stress remains small.

8.8 Constraints

1. *As in the studies of the previous chapter, so for this study:* $0.09660\mu m/mm \leq \{\delta_{DC}/d_K, \delta_C/d_K\} \leq 1.449\mu m/mm$.

2. $l_s \leq 0\%\ l_{F,max}$. This constraint is set because the simple design studies covered in Ch. 7 show that a profile with a positive shift is unlikely to constitute an optimum.

The design space described by these constraints is shown in Fig. 8.7, along with the 35 sampling sites selected by the PCID RSA DOE algorithm for Iteration 0, and the 35 selected for Iteration 1.

8.9 Results

The surrogate models generated by the PCID RSA algorithm for the seven objective functions listed in Section 8.7 are shown in Fig. 8.10-8.8, with the sites of all objective function evaluations completed in the process marked in. Sites at which the FSTI simulation conducted converged within 15 simulated shaft revolutions are shown as circles, while sites at which convergence was not achieved are shown as diamonds. The latter are not used in the construction of the surrogate model; most likely, non-convergence of the designs with low radius and shift seen in the aforementioned figures results from instabilities due to the simple modeling of regions in the piston-cylinder interface with film thickness at/below h_{min}.

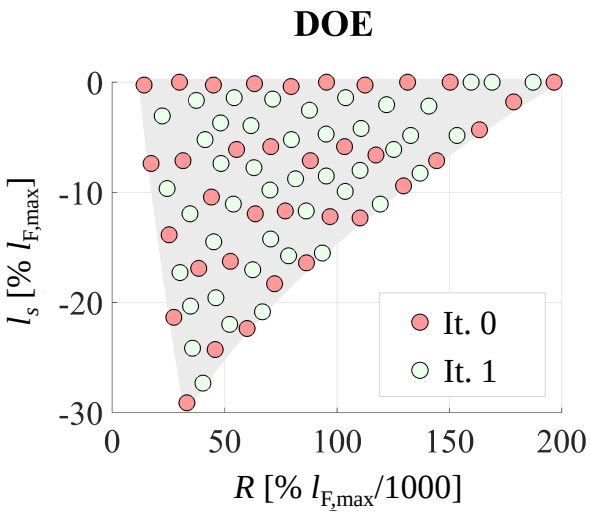

Figure 8.7. DOE for Iteration 0 and 1 over the design space spanned by the study (in grey).

However, a more complex model will be more computationally expensive, and the surrogate models generated by the PCID RSA for the maximum and average case end correction force magnitudes using converged sites indicate that this corner of the design space is unlikely to yield profiles conducive to full-film lubrication in the interface.

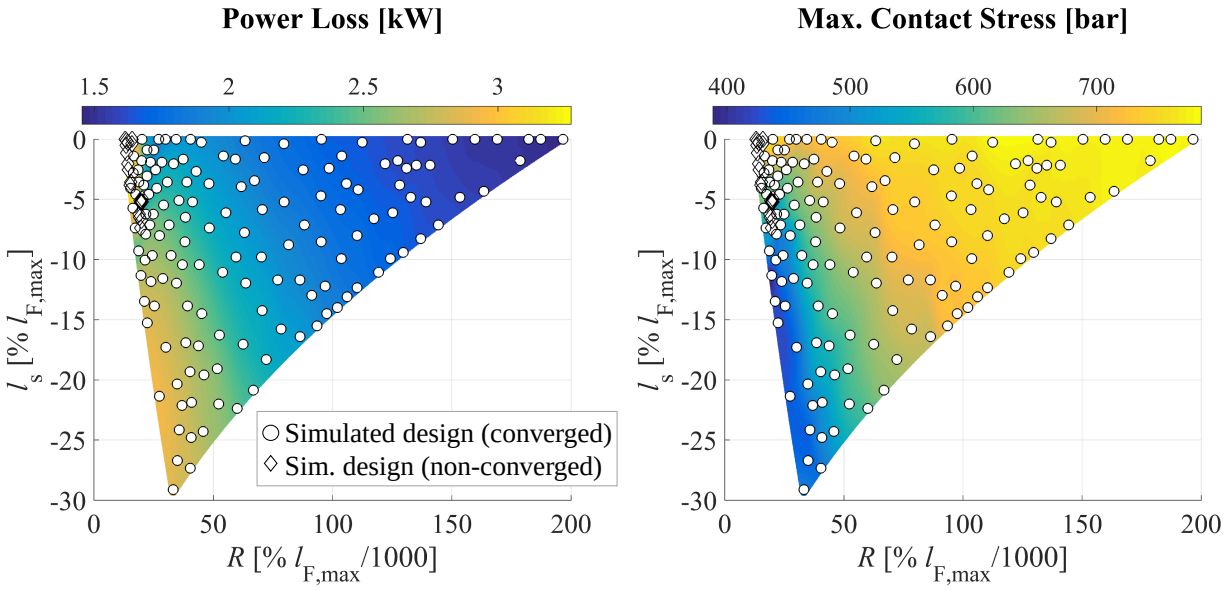

Figure 8.8. Models of f_1 and f_2 developed by PCID RSA.

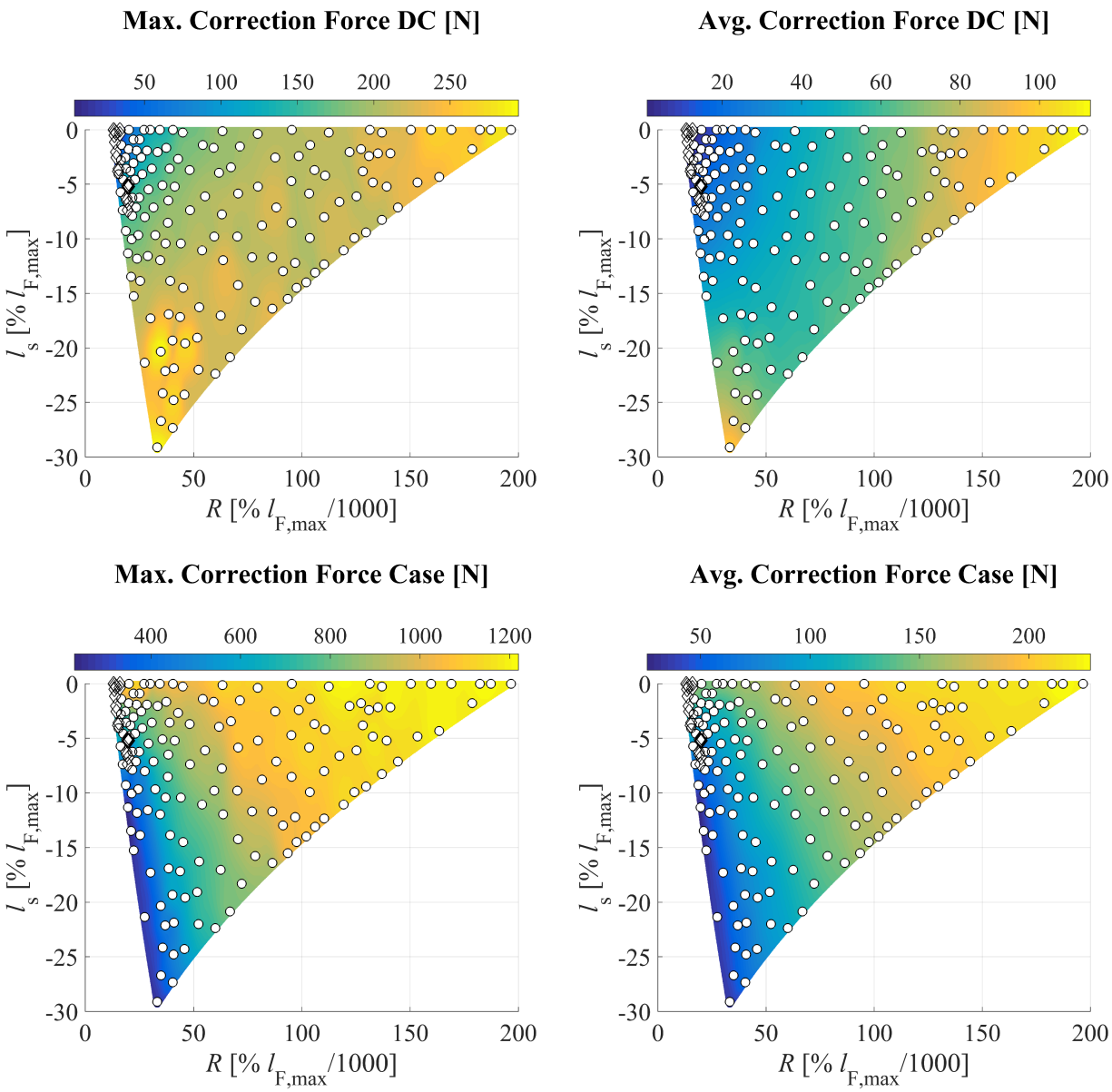

Figure 8.9. Models of f_3-f_6 developed by PCID RSA.

Examining the surrogate models in Fig. 8.10-8.8, it can be seen that the overall design trends largely mimic those seen in Study 1 of Ch. 7. That is, the lowest power loss corresponds to designs of large radius, the lowest maximum DC end correction force magnitude to designs of small radius and low shift magnitude, and the lowest maximum case end correction force, to designs of small radius, and large shift magnitude. Use of the PCID RSA has enabled a more reliable representation of the objective functions than the simple study of the previous chapter, allowing the described trends to be confirmed (for the case of an extended guide

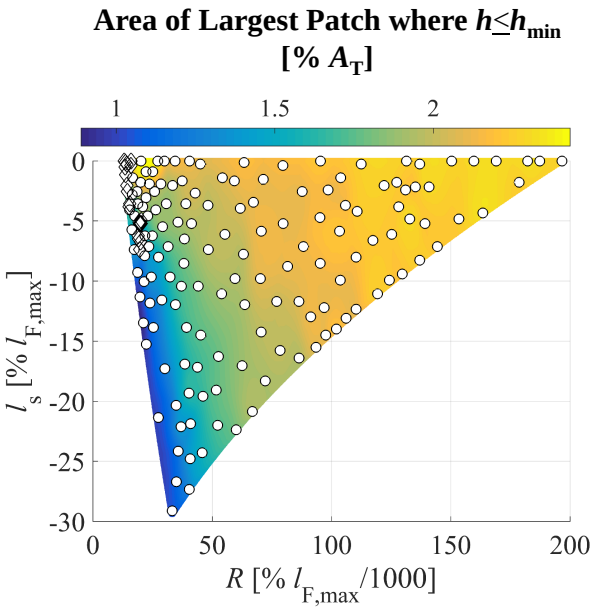

Figure 8.10. Model of f_7 developed by PCID RSA.

length). In addition to these trends, the RSA-generated objective function models show that the concave bore profile has the potential to significantly improve load support— but indicate that, despite the extended guide length, it cannot provide full film lubrication (the correction forces cannot be brought to zero) for the simulated unit over the extent of the design space examined. Furthermore, they indicate that attempts to provide full load support via expansion of the design space will come at the cost of an unacceptable increase in power loss.

These observations are confirmed by, and can be expanded upon in viewing the PCID RSA-generated pareto front; as this is a seven-dimensional front (because there are seven objective functions), only a few key views of this front will be provided here. Fig. 8.11 shows three views, plotting f_3 against f_5, f_4 against f_6, and f_1 against f_2. Designs on the pareto front are shown in red, all others in gray. The Ch. 6 baseline values are indicated as well, allowing for direct comparison.

From this, it can be seen that all profiles in the design space, even those of large radius, whose curvature is insignificant, exhibit significantly lower maximum and average correction force magnitudes than the baseline— a consequence of the extended bushing length used in this

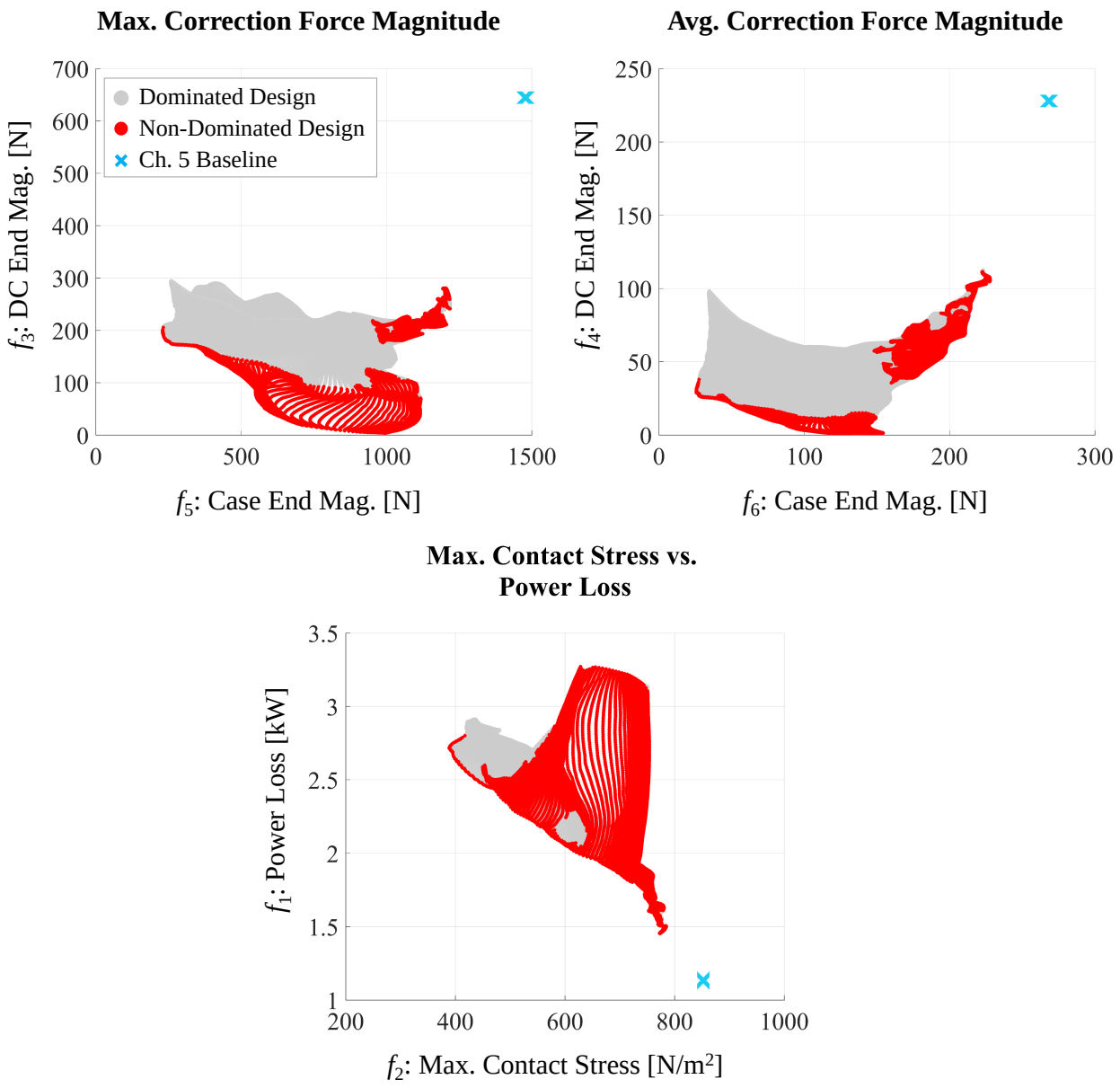

Figure 8.11. Pareto front for concave bore profile optimization study at OC4.

study (11% longer than that of the baseline). More importantly, the distance between those designs on the pareto front, versus those not on it, makes clear that significant improvement in these parameters is also achievable through the choice of profile. The bottom plot shows that the design space examined does not yield any profiles able to match or outperform the baseline in terms of power loss *due to viscous flow*, and that lowering the maximum contact stress increases the minimum achievable power loss; however, this power loss value does not

include losses due to mixed/solid friction, which will be lowered by profiles that improve load support at the interface.

Thus, for some APMSPD, depending on their size, materials, and geometric setup, this profile type may already constitute a satisfactory solution— but as it does not suffice to provide full load support for the unit simulated in this study, the next chapter explores a more powerful approach to bore surface shaping.

8.10 Summary/Conclusions vis-á-vis Concave Bore Profile Design via the PCID RSA

A RSA has been developed, specifically for use in piston-cylinder interface design based on a multi-physics model of the fluid film, such as FSTI, that requires extensive computational time. Implementing this algorithm, an optimization study was conducted in order to design concave bore profiles for the 75 cc unit from the previous chapter, with water as the working fluid, and the bushing length extended by 11%. The results comprise models for seven objective functions: the power loss due to viscous flow, maximum contact stress, maximum and average correction force magnitudes at both control points, and the area taken up by the largest patch of $h_{\min}$. Since these models are the product of an optimization algorithm that corrects their shape until it converges, they are more reliable than the results of a simple design study with a set DOE grid. From them, it can be seen that a significant improvement in load support is achievable via the implementation of a concave bore profile on the extended bushing— but that over the design space examined, this type of profile is not able to achieve full-film lubrication at the piston-cylinder interface for the simulated unit. The next chapter presents an algorithm capable of generating bore profiles that solve this problem.

9. ALGORITHM FOR GENERATING BORE PROFILES TAILORED TO PISTON TILT AND DEFORMATION

A version of this chapter has been previously published in [2].

9.1 Concept Introduction

While the simulation results of the previous two chapters show the concave bore profile to be capable of great improvements in load support, the degree of piston-bore surface conformity that can be achieved with such a profile is limited. Bringing the surfaces close enough over a sufficiently large area to allow for high hydrodynamic pressure buildup is key to protecting the piston and bore surfaces from direct, metal-to-metal contact. Hence, pushing the concept of that shape a step further, this chapter is dedicated to an algorithm that generates bore profiles *tailored* to achieve, for a given pump geometry, piston-bore conformity at either end of a fixed guide length. Specifically, through these profiles, the bore is tailored to both: the piston's tilt, and its deformation. It has already been shown how absolutely critical the eccentricity and deformed shape of the piston are with respect to generating a fluid pressure field that can hold the imposed load; a computationally efficient approach that adapts the shape of the bore to both *while keeping power loss due to leakage and viscous friction as low as possible* is needed.

Fig. 9.1 illustrates how piston tilt lessens piston-bore surface conformity. That is, Fig. 9.1 (a) shows a piston tilting as a result of the external forces (side load) acting on its head— and the nature of the piston-bore overlap that would be seen if the piston could move through the bushing material. As the findings of this chapter are also applicable to pumps with an undercut in the cylinder block bore instead of a bushing, Fig. 9.1 (b) repeats the illustration for that case. For either construction, the surface of the bushing/cylinder bore can be adapted to piston tilt through the imposition of a profile in the form shown in Fig. 9.2.

Essentially, this profile is some type of curve that follows, very closely, the piston surface at either end of the guide length— and then gently diverges from it in moving towards

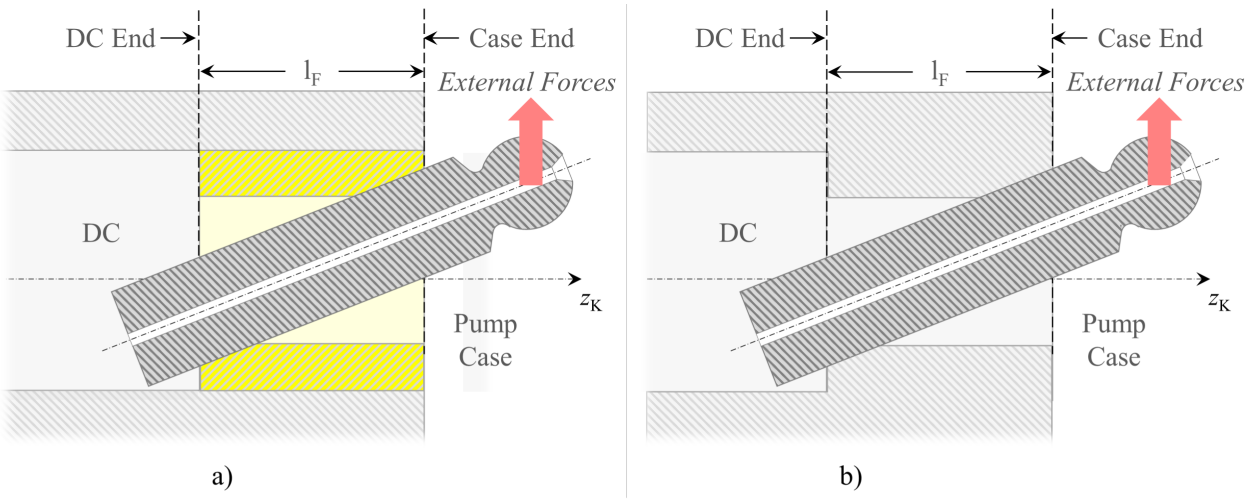

Figure 9.1. Piston tilt for the case of a cylinder block a) bushing, b) undercut.

the (guide length) midpoint. As will be shown, this shape can significantly improve the load-carrying capacity of the piston-cylinder interface [2]— but not as much as a shape accounting also for piston deformation. Fig. 9.3 shows how that deformation changes the conforming bore profile relative to the previous example. To that end, Fig. 9.3 (a) marks, on the image of a deformed piston, lines approximating the slope of its surface at either end of the guide length— and Fig. 9.3 (b) gives an example of how these slopes may differ from those of a rigid (undeformed) piston, whose running surface is depicted as a red box. In

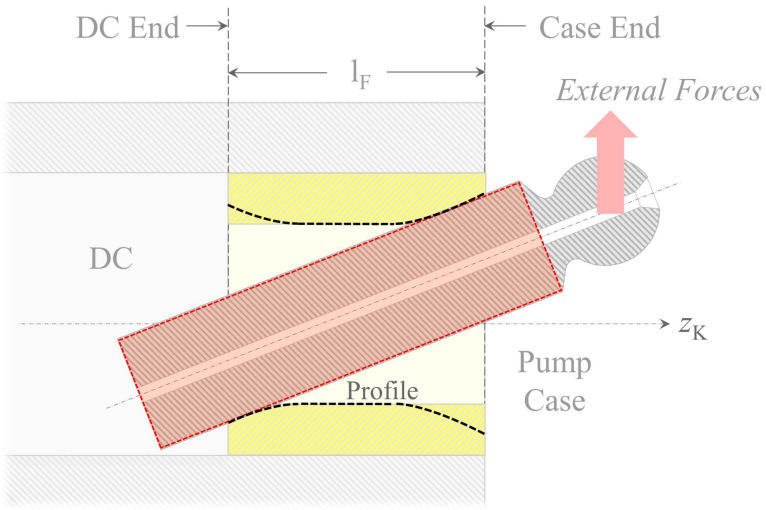

Figure 9.2. Profile conforming to piston tilt (image based on [2].

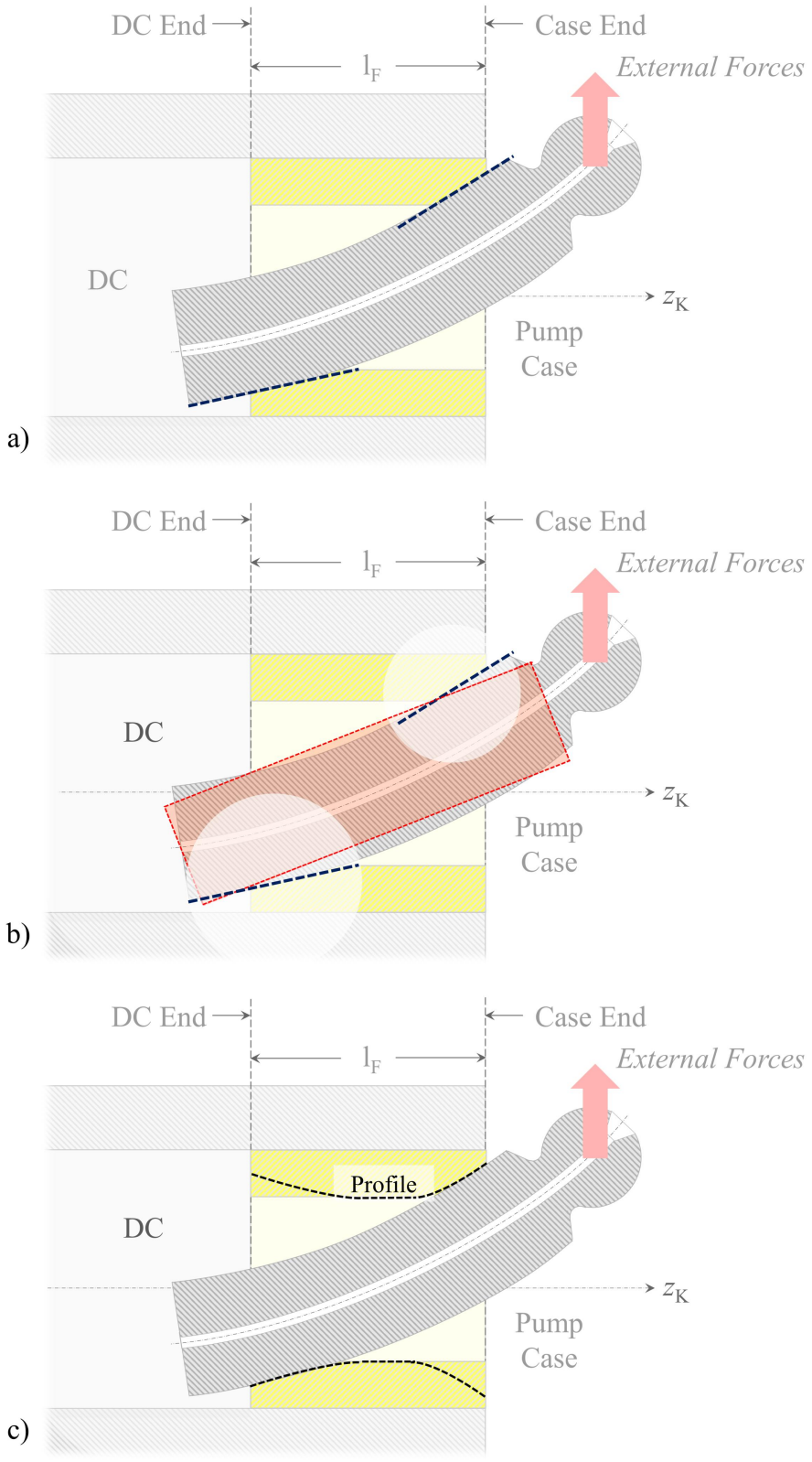

Figure 9.3. a) Slopes of a deformed piston, b) slopes of the deformed piston vs. a non-deformed piston, c) profile conforming to piston tilt and deformation.

conclusion, Fig. 9.3 (c) shows a profile suitable for the deformed piston. It is this profile that has tremendous potential to increase the load support of the lubricating interface, and with relatively low power loss.

Previous researchers have explored similar shapes, opening up the bore through which the piston moves at its edges. As already mentioned in Ch. 5, Gels and Murrenhoff [48] proposed rounding off those edges, as well as those of the piston running surface, in the shape of a circular arc. However, much like the concave bore profile, the piston-bore conformity achievable through these circular arcs is limited. Yoshimura et. al [56] came closer, proposing a "crowning" curve of the bore at the case end of the guide length, in conjunction with a similar crowning of the piston at either end of the guide length, neither of which is restricted to the shape of a circular arc.

However, their patent does not include shaping at the DC end of the guide length— most likely because it focuses on the case of a variable guide length. For a fixed guide length, as will be examined here, shaping the DC end is essential. Furthermore, as the design studies of piston and bore surfaces in previous chapters have made clear, it is difficult to get piston shaping to perform as well as bore shaping, because the piston moves, forcing the piston-bore conformity to vary. Shaping the piston in addition to the surrounding bore material also adds to manufacturing expense. If possible, it is therefore more cost-effective to only shape the bore surface. For this reason, the present work examines a bore shaping intended to be implemented without additional machining on the piston running surface.

Most critically, the present work distinguishes itself from previous attempts in that it replaces the trial-and-error approach to designing suitable profiles (whether experimental or virtual), and the design studies that first experimentally/virtually try out a number of profiles, then compare their performance, with an approach that tailors the bore to piston tilt and deformation based on the geometry and simulated behavior of the interface, thus strategically excluding much of the design space; this saves a tremendous amount of time/computational power. It is also important to note that while the type of profile to be generated emulates,

to a certain extent, the shaping a bushing/cylinder bore takes on as a result of wear-in, it is *not* the intent to achieve a desirable profile by modeling surface wear [2]. There are several reasons for this.

Firstly, an accurate wear prediction tool requires experimental data to model solid friction between the piston and bore; for example, the model developed by Brinkschulte et. al [65] requires an experimentally determined solid friction coefficient [2]. Acquiring experimental data adds not only to the monetary expenditures required for developing a suitable profile (especially when considering multiple novel material sets), but also to the time expenditure. Secondly, the bore shape created by wear-in does not necessarily represent an ideal shape for the interface; it may, for example, generate more power loss than another profile that is able to achieve a similar degree of load support. Thirdly, when the pump geometry is challenging (not conducive to load support at the piston-cylinder interface), the viscosity of the hydraulic fluid being used is low, and/or the materials don't make a good pairing for a smooth run-in process, wear-in simulations that start with a cylindrical (unshaped) bore may experience numerical instabilities, and may not arrive at a solution.

The present work proposes an algorithm for generating high-performance bore profiles that oversteps these obstacles [2]:

1. It requires no experimental data.
2. It seeks the *set* of solutions to the load support problem that is attainable by the profile form it studies, and then allows the user to select the profile delivering the best overall performance (beyond only load support).
3. The starting set of profiles simulated with FSTI in this algorithm is pre-shaped such as to aid the bore surface in conforming to the piston, thus providing a more robust starting point for challenging conditions at the interface than the cylindrical (unshaped) bore.

The proposed algorithm draws on the capabilities of FSTI to serve as a tool that can generate, in a time- and cost-effective manner, bore profiles aimed at supporting the high-pressure operation of the pistons in APMSPD for low-viscosity fluids like water.

9.2 The Tailored Profile Generator Algorithm

9.2.1 Overview

The TPGA (Tailored Profile Generator Algorithm) produces bore profiles of the form shown in Fig. 9.4 [2]. A number of parameters define the shape of such a profile— but three are critical: δ_1, δ_2, and δ_3. These parameters are given to the algorithm as inputs by the user, and play a vital role in determining the locations of the skeleton points that are used to construct such a profile. δ_1 and δ_2 are especially decisive, in that they dictate the axial extent of piston-bore conformity at either end of the guide length. Because these parameters can significantly change the behavior of the piston-cylinder interface, multiple combinations of different values for them should be explored, such as not to overlook profiles with good performance.

The algorithm is designed to take (as inputs) any number of value combinations for these, as well as four other parameters that also modify the shape of the profile [2]. For each combination of values of those seven parameters, the algorithm generates one profile. That is, the TPGA does not create a single profile: it creates a set of profiles— as many as the number of value combinations supplied by the user. The best profile among the set can be chosen at the end.

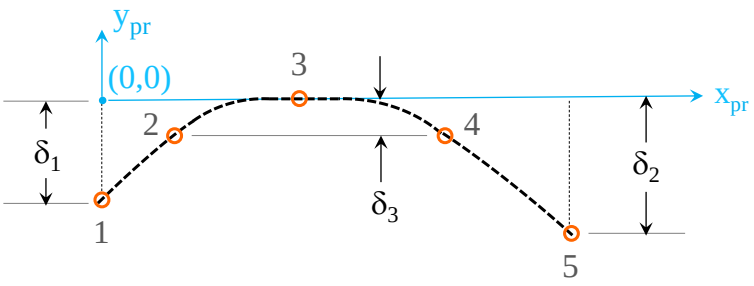

Figure 9.4. Form of the profiles generated by the TPGA (image based on [2]).

Fig. 9.5 gives a high-level overview of how the TPGA generates the described set of profiles. The algorithm is comprised of two stages: in Stage 1, it uses value sets of the aforementioned seven parameters, in conjunction with other geometric inputs, to create a set of bore profiles that conform only to piston tilt, under the assumption of a rigid piston (as in Fig. 9.2) [2]. In Stage 2, the performance of the piston-cylinder interface with those initial profiles is simulated via FSTI; the results, in particular those relating to piston deformation, are then utilized to refine the profiles such as to allow for higher piston-bore conformity (as in Fig. 9.3 c). In overview, the bore shape is first adapted to piston tilt, then to piston tilt *and* deformation.

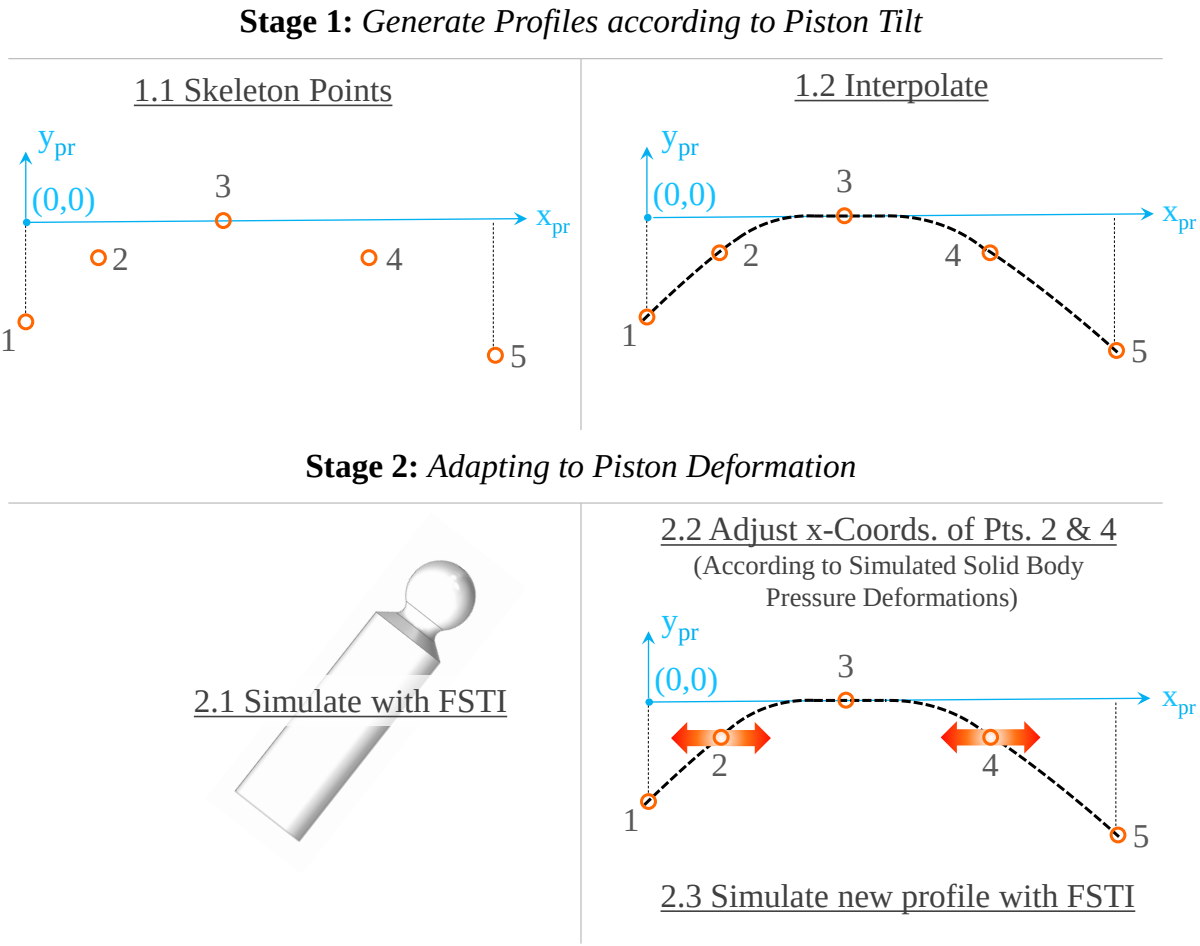

Figure 9.5. TPGA Overview (image based on [2]).

The algorithm constructs each bore profile as an interpolation that passes through a set of skeleton points [2]. In step 1.1 of Stage 1 (see Fig. 9.5), the locations these skeleton points are computed for every user-supplied value set. Step 1.2 then employs an interpolation scheme to convert each set of skeleton points into a complete bore profile, adapted to conform exclusively with piston tilt. This marks the end of Stage 1. Stage 2 begins with the user simulating the behavior of the piston-cylinder interface for each of the generated bore profiles with FSTI (step 2.1). Step 2.2 of the algorithm adapts the shape of the bore profile to the shape, position, and tilt of the simulated piston, with the aim of achieving higher piston-bore conformity when piston deformation is factored in. Specifically, the profile shape is adapted by changing the x_{pr}-coordinates of skeleton points 2 and 4, and then re-interpolating over the entire guide length. Finally, in step 2.3, the new profiles are simulated with FSTI to verify their performance.

If necessary, steps 2.2-2.3 can be repeated to achieve a better outcome. However, additional iterations in Stage 2 of course add to the computational cost. This is actually the reason for having Stage 1. The idea behind Stage 1 is to get the piston shape simulated in step 2.1 for each value set to come close to the form it will take on when simulated in conjunction with the corresponding final bore profile generated by the algorithm [2]. This is done to reduce the number of iterations through steps 2.2-2.3 required for the interplay between the bore shape and the piston position/deformation/eccentricity to reach a successful finish. Preferably, only one iteration of steps 2.2-2.3 should be required. Because Stage 1 does not involve FSTI, the computational time required for it is significantly lower than that of Stage 2; if Stage 1 can reduce the number of required Stage 2 iterations, it is a worthy investment of computational power.

Fig. 9.6 shows a basic code diagram summarizing the TPGA, and the described loop in Stage 2 [2]. The diagram also lists the user inputs required by the algorithm, which are divided into three sets: IS1 (Input Set 1), IS2, and IS3. How these sets are employed by the algorithm will be explained later, but it is nevertheless important to have an overview. IS1 (see Table 9.1) is the input set whose values are common to all profiles the TPGA generates.

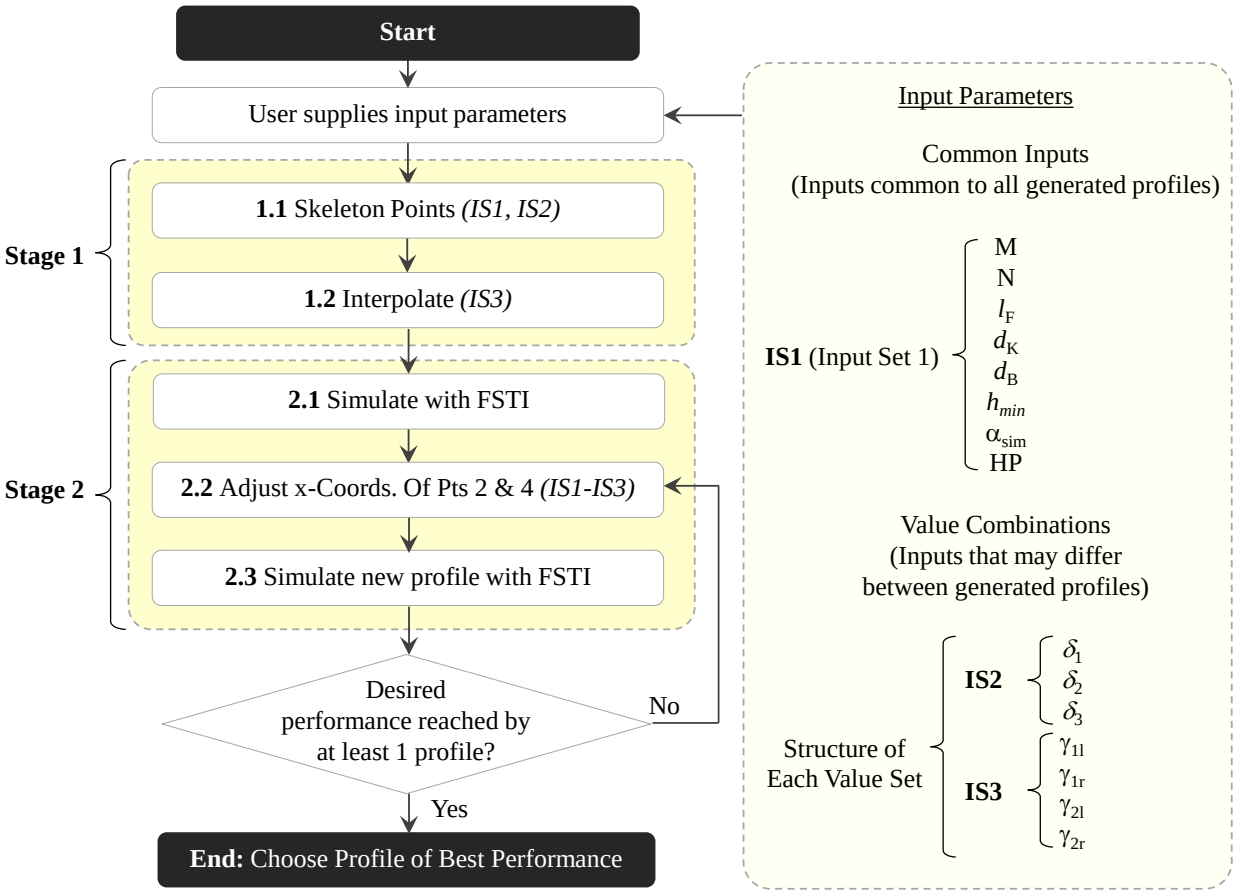

Figure 9.6. TPGA code diagram (image based on [2])).

Table 9.1. Input parameters.

Input	*Definition*
M[1]	Number of fluid grid elements along the interface length
N[1]	Number of fluid grid elements around the interface circumference
l_F	Guide length
d_K	Piston diameter
d_B	Minimum bore surface diameter over the guide length
h_{min}	Minimum film thickness
α_{sim}[1]	Shaft angle degree steps in which FSTI outputs film thickness, contact stress, and deformation values over the whole fluid grid
HP	Pressure of high-pressure port

[1] These inputs are primarily used in extracting data corresponding to a certain shaft angle from FSTI output files for step 2.2. M is also used as the number of points constituting a profile.

In addition to these common inputs, there are also inputs that may differ between one generated profile and another— these correspond to the seven parameters for which the user is to supply value sets. They are subdivided into two input sets, IS2, and IS3. IS2 is comprised of the three critical dimensions from Fig. 9.4 that help define the locations of a profile's skeleton points, and IS3 contains the remaining four parameters, which are used by the profile interpolation scheme in step 1.2 (more details on this later).

9.2.2 The Skeleton Points

All three input sets are employed by Stage 1 of the TPGA [2]. As previously stated, this stage generates a set of bore profiles conforming to the tilt of a rigid piston. Each bore profile is generated in two steps: first, the location of a set of skeleton points is calculated using IS1 and IS2, then, an interpolation scheme constructs a profile passing through those skeleton points using IS3. Since the intent is to achieve conformity of the bore surface with a rigid, tilted piston, the skeleton points should align with that piston at either end of the guide length.

Fig. 9.7 (a) shows the cross-section of such a rigid piston, taken lengthwise at a plane passing through the bore's center axis. The piston is depicted as tilting to the full possible extent due to the external forces acting on its head, with Line 1 and Line 2 marking the outline of its running surface at that eccentricity. Line 3 is simply the reflection of Line 1 about the bore center axis. These lines determine the profile of Stage 1— that is, profiles generated in Stage 1 should conform with Line 2 at the DC end of the guide length, and with Line 3 at the case end.

The coordinate system in which said profiles are to be generated is shown in Fig. 9.7 (b) [2]. The y_{pr}-axis of that system is perpendicular to the bore center axis, and intersects it at the end of the guide length abutting the DC; the x_{pr}-axis is parallel to the bore center axis, and passes through the apex of the profile to be generated. Therefore, the highest point of that profile has a y-coordinate of zero. Within the context of this coordinate system, the structure of the profile skeleton step 1.1 sets up for each user-supplied value set can be examined.

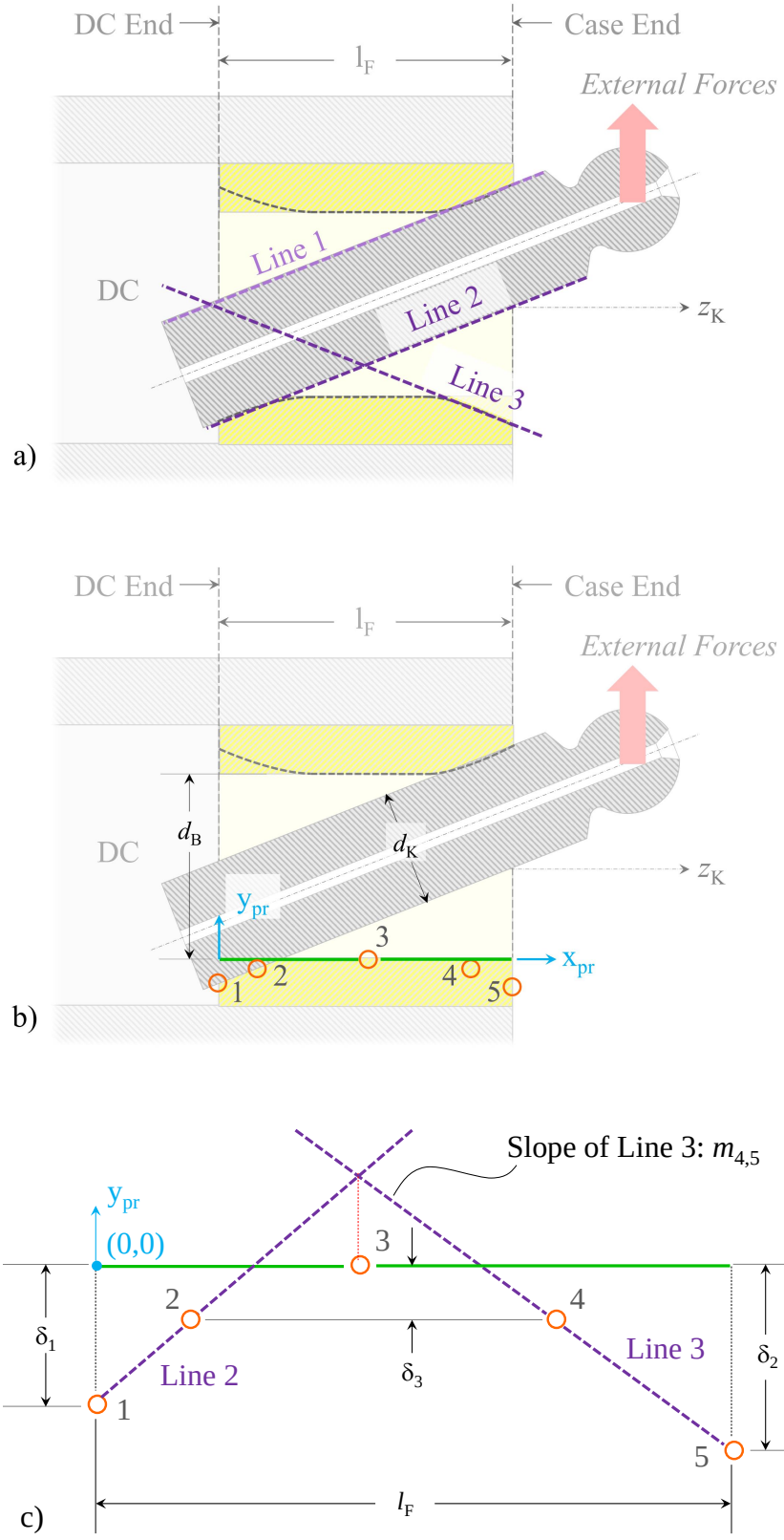

Figure 9.7. a) Lines 1-3, b) skeleton points, c) skeleton points close-up. (images based on [2])

Fig. 9.7 (c) lays out this underframe, comprised of five skeleton points [2]. The basic idea behind the arrangement shown is that the piston will conform with the bore between Pts. 1 and 2, and between Pts. 4 and 5. In moving from Pt. 2 to Pt. 3, and from Pt. 4 to Pt. 3, there should be a gentle transition to a flat profile. This is done so that if the piston tilt lessens from its maximum (e.g. during the low-pressure stroke), and the piston surface "sits" against those regions, it will not encounter any sharp corners.

Implementing this idea for the profile's skeletal frame, the location of its points are as follows [2]:

1. Pt. 1 is located at the DC end of the guide length (at $x_{\text{pr}} = 0$), and at $y_{\text{pr}} = -\delta_1$, where δ_1 is a user input.

2. Similarly, Pt. 5 is located at the case end of the guide length (at $x_{\text{pr}} = l_{\text{F}}$), and at $y_{\text{pr}} = -\delta_2$, where δ_2 is a user input.

3. In order to keep the profile simple, Pts. 2 and 4 have the same y_{pr}-coordinate: $y_{\text{pr}} = -\delta_3$, where δ_3 is a user input. Their x_{pr}-coordinates are computed such that Line 2 from Fig. 9.7 (a) passes through Pt.2, and Line 3 through Pt. 4.

4. Point 3 is the apex (highest point) of the profile; its y_{pr}-coordinate is zero. Again for simplicity, the x_{pr} coordinate of this point is taken to be the x_{pr} coordinate of the point at which Line 2 and Line 3 intersect.

From this, the values of the x_{pr}- and y_{pr}-coordinates of skeleton Pts. 1 and 5 are clear, as are the values of the y_{pr}-coordinates of Pts. 2-4. What remains unknown is how to compute the x_{pr}-coordinates of Pts. 2-4.

9.2.3 Step 1.1: Calculating the Location of the Skeleton Points

The values of these x_{pr}-coordinates can be obtained using the slopes of Line 2 and Line 3. Let the slope of Line 3 be denoted $m_{4,5}$. Then, since Line 3 is the reflection of Line 1 about the bore center axis, the slope of Line 1 is -$m_{4,5}$. Furthermore, since Line 1 is parallel to

Line 2, the slope of Line 2 is also -$m_{4,5}$. From this slope (of Line 2), the x_{pr}-coordinate of Pt. 2 can be determined:

$$-m_{4,5} = \frac{-\delta_3 - (-\delta_1)}{x_{\text{pr},2}} \tag{9.1}$$

$$=> x_{\text{pr},2} = \frac{\delta_3 - \delta_1}{m_{4,5}} \tag{9.2}$$

Similarly, from the slope of Line 3, the x_{pr}-coordinate of Pt. 4 becomes:

$$m_{4,5} = \frac{-\delta_2 - (-\delta_3)}{l_{\text{F}} - x_{\text{pr},4}} \tag{9.3}$$

$$=> x_{\text{pr},4} = \frac{\delta_2 - \delta_3}{m_{4,5}} + l_{\text{F}} \tag{9.4}$$

Finally, the x_{pr}-coordinate of Pt. 3 is the x_{pr}-coordinate at which Line 2 intersects Line 3. The equation of Line 2 in the x_{pr}-y_{pr} coordinate system is:

$$y_{\text{pr}} = -m_{4,5}x_{\text{pr}} - \delta_1 \tag{9.5}$$

The equation of Line 3 is:

$$y_{\text{pr}} = m_{4,5}(x_{\text{pr}} - l_{\text{F}}) + \delta_2 \tag{9.6}$$

Setting the right-hand sides of these equations equal to each other and solving for the x_{pr}-coordinate of the point of intersection:

$$-m_{4,5}x_{\text{pr}} - \delta_1 = m_{4,5}(x_{\text{pr}} - l_{\text{F}}) - \delta_2 \tag{9.7}$$

$$=> x_{\text{pr}} = \frac{\left(\frac{\delta_2 - \delta_1}{m_{4,5}}\right) + l_{\text{F}}}{2} \tag{9.8}$$

Table 9.2 summarizes the x_{pr}- and y_{pr}-coordinates of all five skeleton points. However, there remains one unknown: $m_{4,5}$. To determine its value as a function of the user inputs, the geometry of the tilting piston must be re-examined. In order for the piston to align with the profile for a bore of given diameter d_{B}, the piston running surface must penetrate the traditional cylindrical bore by the user-specified values of δ_1 at the case end, and δ_2 at the

Table 9.2. x_{pr} and y_{pr} coordinates of the skeleton points [2].

Skeleton Pt.	x_{pr}	y_{pr}
1	0	-δ_1
2	$\frac{\delta_3-\delta_1}{m_{4,5}}$	-δ_3
3	$\frac{\left(\frac{\delta_2-\delta_1}{m_{4,5}}\right)+l_{\mathrm{F}}}{2}$	0
4	$\frac{\delta_2-\delta_3}{m_{4,5}}+l_{\mathrm{F}}$	-δ_3
5	l_{F}	-δ_2

DC end. This is shown in Fig. 9.8 (a), which depicts the lengthwise cross-section of a such a piston on a plane passing through the bore's center axis, just as in Fig. 9.7.

In order to obtain $m_{4,5}$, a new coordinate system is set up: the x_{sK}-y_{sK} system. The origin of that system is located where Line 1 intersects the case end of the interface. From there, the y_{sK}-axis moves radially outward, perpendicular to the bore's center axis— and the x_{sK}-axis moves towards the DC end of the interface, parallel to the bore's center axis. Within this coordinate system, the slope $m_{4,5}$ is the negative tangent of α_{sk}, the (positive) angle between the x_{sk}-axis and Line 1 that is marked in Fig. 9.8 (b) [2]:

$$m_{4,5} = -tan(\alpha_{\mathrm{sk}}) \tag{9.9}$$

This angle, in turn, can be expressed as the difference between two further angles [2]:

$$\alpha_{\mathrm{sk}} = \beta_{\mathrm{sk}} - \xi_{\mathrm{sk}} \tag{9.10}$$

Here, β_{sk} is the angle between the x_{sk}-axis and Line 4, and ξ_{sk} is the angle between Line 1 and Line 4. As can be seen from Fig. 9.8 (a), Line 4 is the line passing through Pt. P1 and Pt. P3. The former (Pt. P1), is simply the origin of the x_{sk}-y_{sk} coordinate system, whereas Pt. P3 is where Line 2 intersects the DC end of the interface.

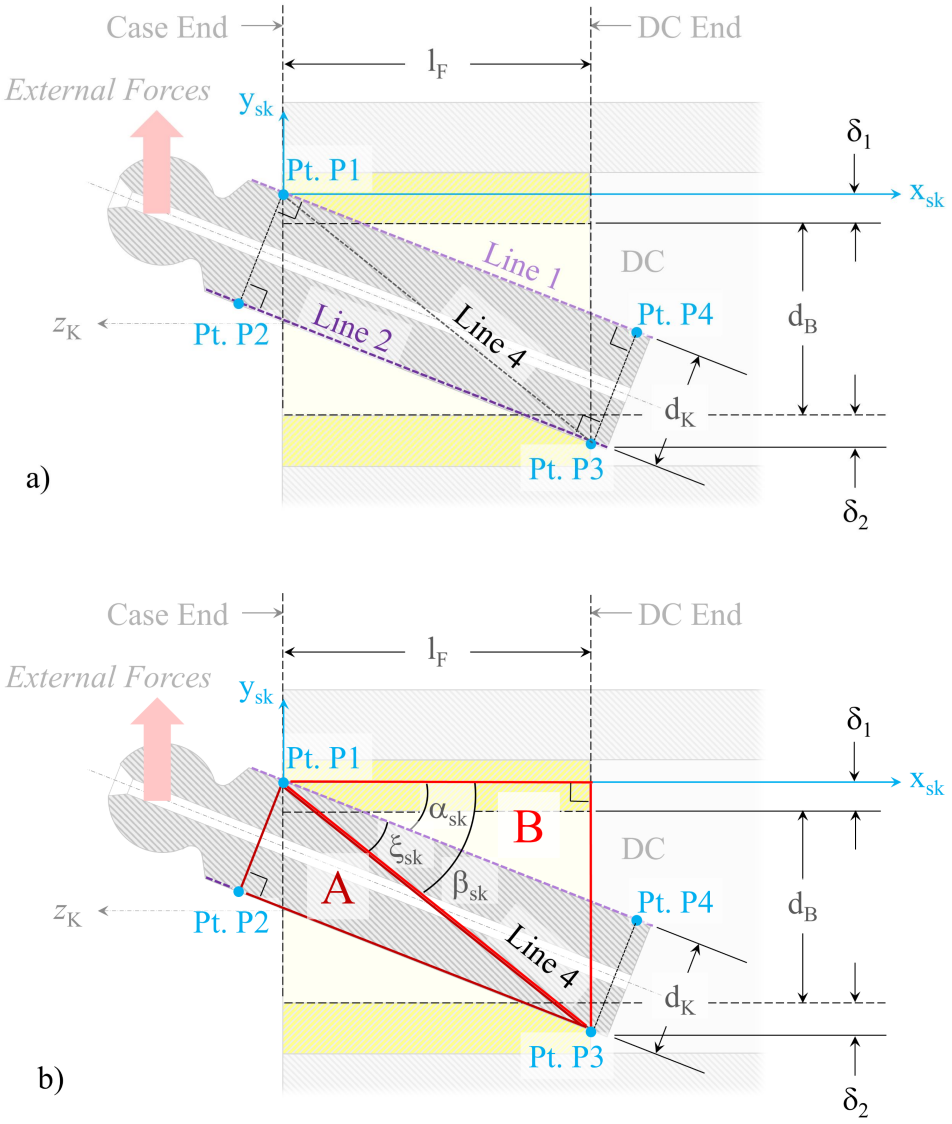

Figure 9.8. Deriving the slope $m_{4,5}$ of Line 1.

The angle β_{sk} is calculated by the TPGA from the coordinates of Pt. P3 [2]:

$$tan(\beta_{\text{sk}}) = \frac{y_{\text{sk,P3}}}{x_{\text{sk,P3}}} \tag{9.11}$$

$$=> \beta_{\text{sk}} = tan^{-1}\left(\frac{y_{\text{sk,P3}}}{x_{\text{sk,P3}}}\right), \text{ where : } \begin{cases} x_{\text{sk,P3}} = l_{\text{F}} \\ y_{\text{sk,P3}} = -y_{\text{tot}} \\ y_{\text{tot}} = \delta_1 + d_{\text{B}} + \delta_2 \end{cases} \tag{9.12}$$

$$\therefore \beta_{\text{sk}} = tan^{-1}\left(\frac{-y_{\text{tot}}}{l_{\text{F}}}\right) \tag{9.13}$$

The angle ξ_{sk} is determined from the nominal piston diameter, d_{K}, and the distance from Pt. P2 to Pt. P3, denoted l_2 [2]:

$$tan(\xi_{\text{sk}}) = \frac{d_{\text{K}}}{l_2} \tag{9.14}$$

$$=> \xi_{\text{sk}} = tan^{-1}\left(\frac{d_{\text{K}}}{l_2}\right) \tag{9.15}$$

The length l_2 can be obtained from two triangles, A and B, shown in Fig. 9.8 (b). Each triangle can be used to write and expression for the distance l_3 from Pt. P1 to Pt. P3, and in setting these two expressions equal to each other, l_2 can be solved for in terms of user inputs. Expressing l_3 in terms of the sides of triangle A [2]:

$$(l_3)^2 = (l_2)^2 + (d_{\text{K}})^2 \tag{9.16}$$

Expressing l_3 in terms of the sides of triangle B [2]:

$$(l_3)^2 = (l_{\text{F}})^2 + (y_{\text{tot}})^2 \tag{9.17}$$

Setting the right-hand sides of the previous two equations equal to each other and solving for l_2:

$$(l_2)^2 + (d_{\text{K}})^2 = (l_{\text{F}})^2 + (y_{\text{tot}})^2 \tag{9.18}$$

$$=> l_2 = \sqrt{\left((l_{\text{F}})^2 + (y_{\text{tot}})^2 - (d_{\text{K}})^2\right)} \tag{9.19}$$

Finally, combining Eqs. 9.9, 9.10, 9.13, 9.15, and 9.19, the slope $m_{4,5}$ is expressed in terms of user inputs as follows [2]:

$$m_{4,5} = -tan\left(\left|tan^{-1}\left(\tfrac{-y_{\text{tot}}}{l_{\text{F}}}\right)\right| - \left|tan^{-1}\left(\tfrac{d_{\text{K}}}{l_2}\right)\right|\right)$$

$$\text{where}: \begin{cases} l_2 = \sqrt{\left((l_{\text{F}})^2 + (y_{\text{tot}})^2 - (d_{\text{K}})^2\right)} \\ y_{\text{tot}} = \delta_1 + d_{\text{B}} + \delta_2 \end{cases} \tag{9.20}$$

In summary, Step 1.1 of the TPGA computes $m_{4,5}$ as indicated in Eq. 9.20, and then the coordinates of the skeleton points according to the equations in Table 9.2.

9.2.4 Step 1.2: Interpolating Between the Skeleton Points

With the locations of the skeleton points known, a full bore profile can be generated. For this conversion from skeleton point framework to profile, step 1.2 of the TPGA employs an interpolation scheme that splits the profile into four sections. These are shown in Fig. 9.9: each pair of adjacent skeleton points spans one section, and each profile section is tangent to its neighbor [2]. As can be seen, the interpolation in section 1 is formed using a circle, while the interpolation in section 2 is formed using an ellipse and two tangent lines (Line A and Line B).

The interpolation scheme for sections 1 and 4 is the same, as is the scheme for sections 2 and 3 [2]. For this reason, the interpolation over each pair of sections is completed via the same TPGA function: sections 1 and 4 are handled by the *SolveSubset1* function, and sections 2 and 3 by the *SolveSubset2* function. That is, the *SolveSubset1* function has been set up to interpolate section 1, and the *SolveSubset2* function has been set up to interpolate section 2— the interpolation of sections 3 and 4 is achieved by taking the reflection of their skeleton points about the horizontal location of skeleton point 3 ($y_{\text{pr}} = x_3$), and then moving them to the appropriate location so that they can be fed into the respective functions in the same

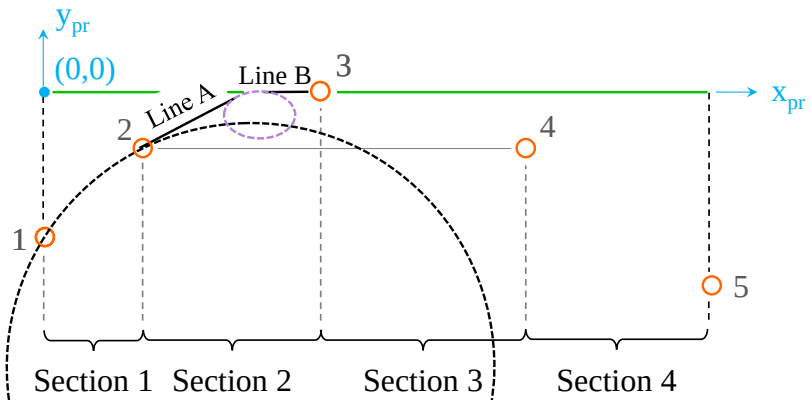

Figure 9.9. Interpolation sections (image based on [2]).

format as sections 1 and 2. Upon completion, the interpolation of these sections is flipped back and moved to its proper place in the profile.

An overview of the TPGA's implementation of its two interpolation functions is provided in Fig. 9.10— because the TPGA starts with *SolveSubset1*, this function will be covered first.

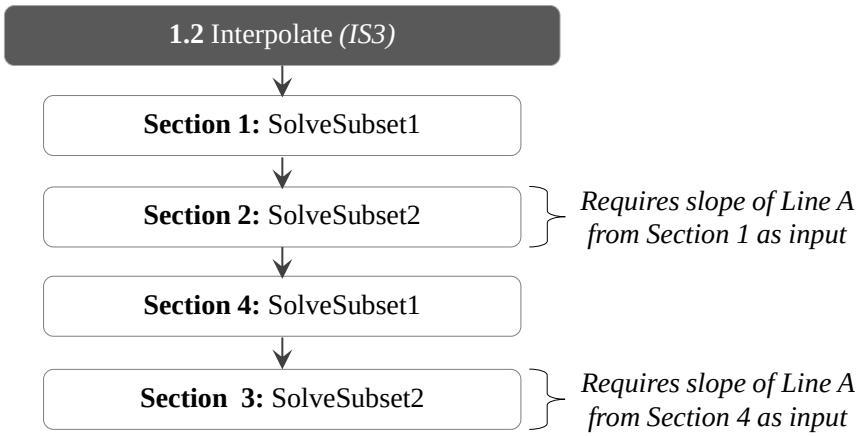

Figure 9.10. Step 1.2 overview.

The *SolveSubset1* Function: Interpolating Sections 1 and 4

As mentioned, the interpolations over sections 1 and 4 are respectively constructed from a single shape: a circular arc [2]. The intent is to introduce a slight curvature to these crucial sections, which can aid in fitting the shapes of the piston and bore surfaces by providing a small range of slopes on the bore surface for the piston to "sit" against, rather than the single slope of a line between skeleton points 1 and 2 (or between points 4 and 5). Due to a variety of factors, e.g. the fact that the TPGA adapts the bore surface to the piston deformation only at a single shaft angle, the slope of the line between those skeleton points may be slightly sub-optimal in how closely it brings the surfaces together, and over how large a section of the interface. Curvature in sections 1 and 4 of the profile can help to compensate for this, as well as for the fact that at the case end of the interface, the piston surface facing the bore may be slightly concave, i.e. would not converge smoothly with a linear bore profile in that region.

The degree of curvature in profile sections 1 and 4 is (indirectly) set by the user input γ_1 (denoted γ_{1l} for section 1, and γ_{1r} for section 4) [2]. This input pertains to the maximum distance between the circular arc interpolation over the section being handled, and the line defined by the two skeleton points bordering that section. That is, it pertains to the maximum of the circular arc in the $x_r - y_r$ coordinate system shown by Fig. 9.11. The pinpoints defining this coordinate system are the two skeleton points at either end of profile section 1 (or 4): its origin is located at the point in this pair that also constitutes an endpoint of the whole profile, and its positive x_r-axis passes through the other point. For the example of section 1, the origin is located at Pt. $s_1 1$ (skeleton point 1 in the section 1 subsystem), and the positive x_r-axis passes through Pt. $s_1 3$ (skeleton point 3).

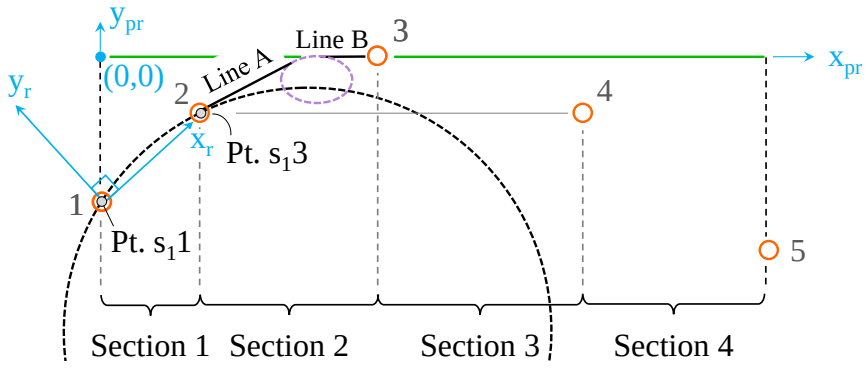

Figure 9.11. Section 1 shape overview (image based on [2]).

In order to make the section 1 and 4 subsystems easier to work with, the TPGA generates the interpolation in this $x_r - y_r$ coordinate system— and then converts the finished profile segment back into the $x_{pr} - y_{pr}$ system [2]. The interpolation shape for section 1 in the $x_r - y_r$ system is shown in Fig. 9.12: the circular arc passes through Pt. $s_1 1$, located at (0,0), and through Pt. $s_1 3$, located at (2L,0), where L is the horizontal distance from the origin to the midpoint of the profile section. Let the circle whose arc will form the interpolation be defined by the following equation:

$$(R_c)^2 = (x_r - a_c)^2 + (y_r - b_c)^2 \tag{9.21}$$

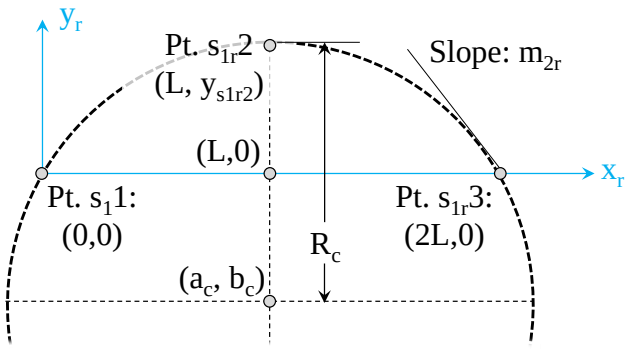

Figure 9.12. Section 1 subsystem (image based on [2]).

The geometric constraints imposed on that circle are given in Table 9.3, along with the corresponding equations. Solving for its radius, and the coordinates of its center point, yields the equations given in Table 9.4: these represent the basic solution that allows for the interpolation in sections 1 and 4.

However, these equations are not only functions of the value of L, which is known as it can easily be calculated from the known positions of Pt. $s_1 1$ and Pt. $s_1 3$, but also of the parameter y_{s1r2}. This is the y_{r}-coordinate of the circle's maximum. Its values is set by determining its highest allowable value (according to geometric constraints to be described shortly), and then multiplying that value by the user-supplied γ_1.

Table 9.3. Circle constraints [2].

#	*Constraint*	*Equation*	
1	The circle center lies on the line y=L.	$a_{\mathrm{c}} = L$	(9.22)
2	(0,0) is on the circle.	$(R_{\mathrm{c}})^2 = (a_{\mathrm{c}})^2 + (b_{\mathrm{c}})^2$	(9.23)
3	The point (L, y_{s1r2}) is on the circle.	$(R_{\mathrm{c}})^2 = (L - a_{\mathrm{c}})^2 + (y_{\mathrm{s1r2}} - b_{\mathrm{c}})^2$	(9.24)

Table 9.4. Defining parameters of the circle [2].

#	*Constraint*	*Equation*	
1	a_c	$a_c = L$	(9.25)
2	b_c	$b_c = \frac{(y_{s1r2})^2 - (a_c)^2}{2y_{s1r2}}$	(9.26)
3	R_c	$R_c = \lvert y_{s1r2} - b_c \rvert$	(9.27)

The highest allowable value this y_r-coordinate can take on is determined by checking three constraints: these are outlined in the code diagram of the *SolveSubset1* function in Fig. 9.13 (steps 1.2.1.3.-1.2.1.7) [2]. The first of these conditions pertains to ensuring that the slope of the profile at the skeleton point bordering on the adjacent section is not too flat for the profile segment in that adjacent section to be able to successfully reach skeleton point 3 at the correct y_{pr}. For section 1, this means ensuring that the slope at skeleton point 2 is not too low for section 2, because section 2 is tangent to section 1 at that (skeleton) point. The TPGA enforces this constraint by limiting the maximum y_{s1r2}-value such that this slope is at least twice the slope of the line between skeleton points 2 and 3, i.e. high enough to also eliminate designs with an extremely short Line B (the flat section at the top of the profile marked out by Line B can be useful in limiting leakage).

Let the acceptable slope for section 2 in the $x_{pr} - y_{pr}$ coordinate system be denoted m_2. As can be seen from Fig. 9.13, the TPGA converts this to m_{2r}, the equivalent slope in the $x_r - y_r$ coordinate system (step 1.2.1.3) [2]. m_{2r}, along with the distance L, are then passed to the *Maxh* sub-function (step 1.2.1.4), which determines the corresponding maximum allowable y_{s1r2} of the circular arc. From Fig. 9.12, it can be seen that:

$$y_{s1r2} = b_c + R_c \quad (\text{where } b_c < 0) \tag{9.28}$$

Setting the slope of the circular arc to m_{2r} yields b_c. The slope of that arc is given by:

$$\frac{dy_r}{dx_r} = -\left(\frac{x_r - a_c}{y_r - b_c}\right) \tag{9.29}$$

Knowing that $a_c = L$ (see Table 9.4), the slope at Pt. $s_1 3$ becomes:

$$m_{2r} = -\left(\frac{2L - L}{0 - b_c}\right) \tag{9.30}$$

$$=> b_c = \frac{L}{m_{2r}} \tag{9.31}$$

With b_c known, R_c can be obtained by evaluating the equation of the circular arc at (0,0):

$$(R_c)^2 = (0 - a_c)^2 + (0 - b_c)^2 = (L)^2 + (b_c)^2 \tag{9.32}$$

$$\therefore R_c = \sqrt{\left(L^2 + {b_c}^2\right)} \tag{9.33}$$

Because the *Maxh* sub-function enforces both this and the next constraint on y_{s1r2} (steps 1.2.1.4 and 1.2.1.6), and was initially set up for the latter, the slope passed to it in step 1.2.1.4 is $-m_{2r}$ (rather than m_{2r}). Let the slope and length passed to this sub-function be denoted m_{maxh} and L_{maxh}; then, the maximum allowable y_{s1r2} is calculated by the TPGA in the following form:

$$\begin{cases} b_{c,maxh} = -\left(\frac{L}{m_{maxh}}\right) \\ R_{c,maxh} = \sqrt{\left({L_{maxh}}^2 + {b_{c,maxh}}^2\right)} \\ \\ y_{s1r2} = b_{c,maxh} + R_{c,maxh} \end{cases} \tag{9.34}$$

The next constraint imposed on y_{s1r2} by the TPGA (steps 1.2.1.5-1.2.1.6) is that this value may not force the slope of the profile at Pt. $s_1 1$ to become vertical in the $x_{pr} - y_{pr}$ coordinate system [2]. To determine the maximum allowable y_{s1r2} under this condition, the TPGA converts the slope of a vertical line in the $x_{pr} - y_{pr}$ system into the slope that vertical line has in the $x_r - y_r$ system, and then feeds this value, along with the distance L, into the *Maxh* sub-function.

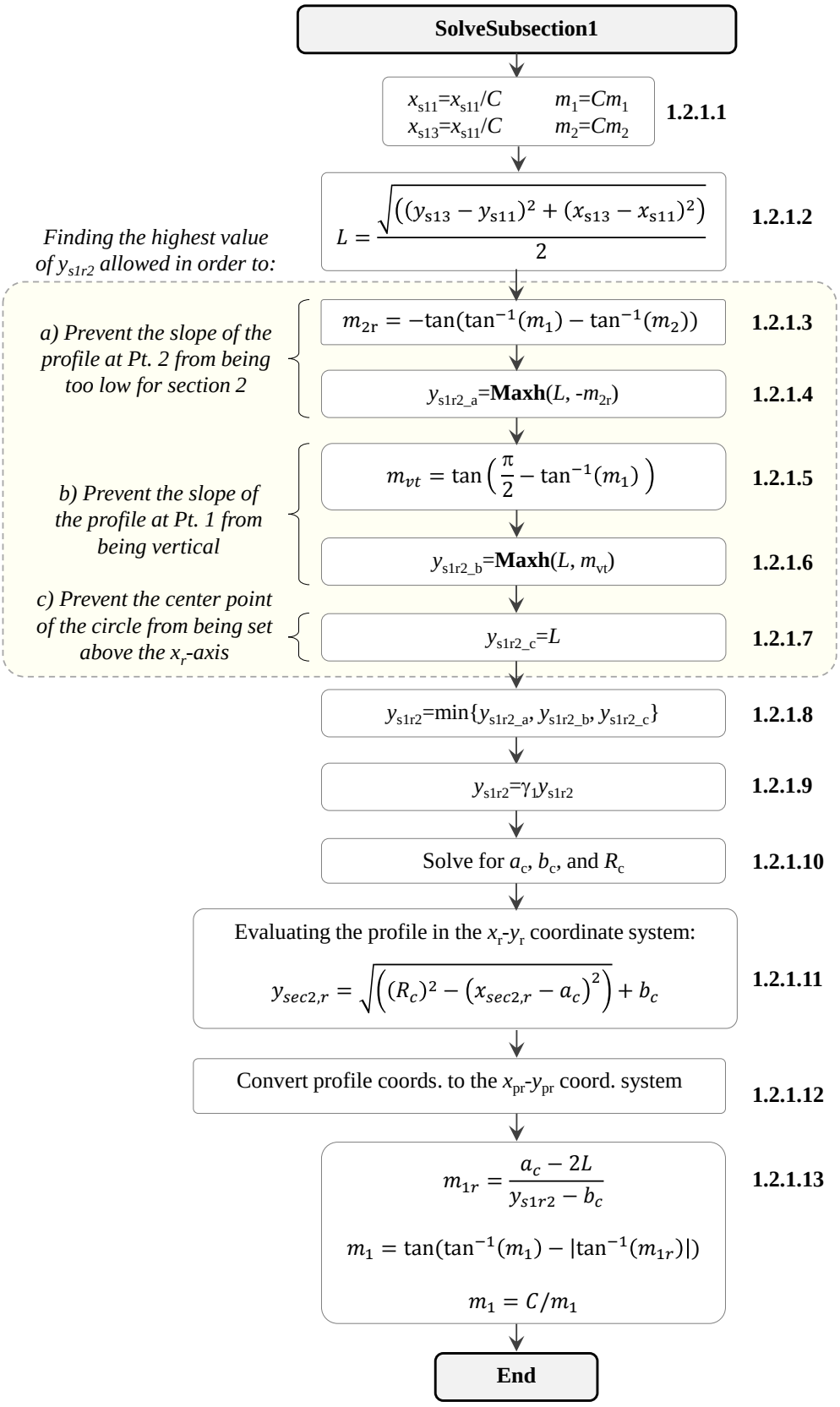

Figure 9.13. Subsection 1 code diagram.

The third and final constraint imposed on the magnitude of y_{s1r2} (step 1.2.1.7) is that it may not force the slope of the profile at Pt. $s_1 1$ to become negative, i.e. the center point of the circle used to construct the interpolation cannot be located above the x_r axis [2]. The maximum y_{s1r2} value satisfying this constraint is L.

Once the maximum value of y_{s1r2} permissible under each of the three geometric constraints is known, the TPGA takes the minimum of these to be the highest value allowed (step 1.2.1.8) [2]. The actual value of y_{s1r2} used to construct the interpolation is then taken to be this maximum value allowed, multiplied by the user-supplied value of γ_1 (step 1.2.1.9). With this value in hand, the TPGA evaluates the coefficients of the circular arc (a_c, b_c) according to the equations in Table 9.4 (step 1.2.1.10). Then, the algorithm constructs the interpolation corresponding to the shape of that circular arc, and converts the resulting coordinates to the $x_{pr} - y_{pr}$ coordinate system (steps 1.2.1.11 and 1.2.1.12, respectively). Similarly, it evaluates the slope of the circular arc at Pt. $s_1 3$ in the $x_r - y_r$ coordinate system, and then converts it to its value in the $x_{pr} - y_{pr}$ system so that it can be utilized as an input to the *SolveSubset2* function (step 1.2.1.13).

With that, the interpolation of section 1 (or section 4) is complete— but there are a couple of extra steps that have been added to the *SolveSubset1* function. Due to the concern that the machining tool used to create such a profile may not be as accurate in its position along its horizontal axis as it is along its vertical axis, the algorithm allows the interpolation to be generated on a scaled version of the x_{pr}-axis, thereby creating a horizontally stretched version of the circular arc whose features may then be easier for the machining mechanism to capture. This is achieved through the user-supplied constant, C, which is employed in step 1.2.1.1 to compress the x_{pr}-axis by scaling the horizontal coordinates of Pt. $s_1 1$ and Pt. $s_1 3$, as well as the horizontal component of the slopes m_1 and m_2. In step 1.2.1.13, the horizontal component of the slope m_1 is then stretched back onto the original x_{pr}-axis, and the y_{pr}-coordinates of the profile interpolation are used in conjunction with the uncompressed version of their x_{pr}-coordinates, thereby stretching the circular arc.

The *SolveSubset2* Function: Interpolating Sections 2 and 3

Unlike the interpolations for sections 1 and 4, the sections interpolated by *SolveSubset2* are constructed using three shapes: an ellipse and two tangent lines [2]. Fig. 9.14 gives an example of how these shapes form an interpolation over section 2 for an actual profile generated by the TPGA. Zooming in, Fig. 9.15 (a) depicts the subsystem comprised of the section 2 interpolation shapes. The points of this subsystem are given the subscript "s2;" the skeleton points 2 and 3 marking the endpoints of section 2 become Pt. $s_2$1 and Pt. $s_2$3, respectively. The point of tangency for Line A and the ellipse is denoted Pt. $s_2$1, and the point of tangency for Line B and the ellipse is denoted Pt. $s_2$3. Lastly, the point that modulates how much of the section being interpolated will be taken up by the ellipse, versus the two lines, is denoted Pt. $s_2$2. Basically, the position of this point sets how "sharp" a corner section 2 will form when the interpolation is complete. For example, the interpolation in Fig. 9.14 shows a much sharper corner in section 2 than in the adjacent section 3: the location of Pt. $s_2$2 differs for the two sections.

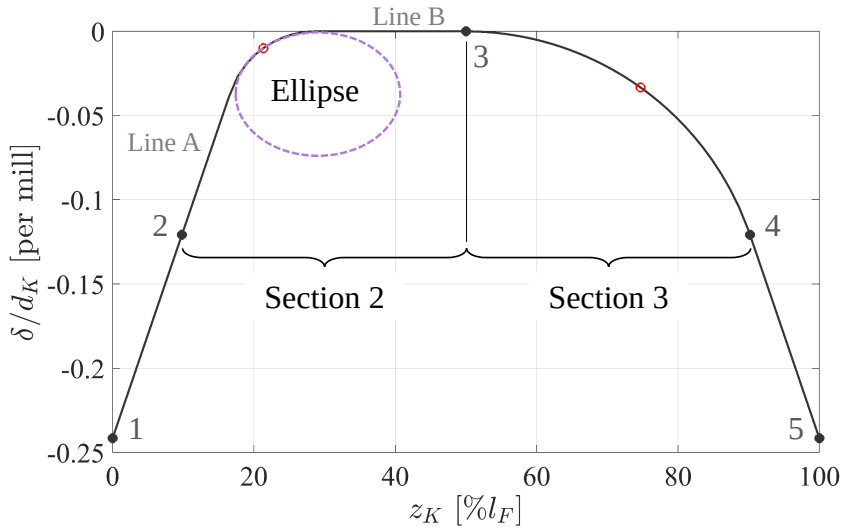

Figure 9.14. Section 2 shape overview (image based on [2]).

Table 9.5 lists the geometric constraints that define the two lines and the ellipse of this interpolation scheme, based on the coordinates of Pt. $s_2$1-Pt. $s_2$3 [2]. They dictate tangency of Line A and Line B to the ellipse, and that Pt. $s_2$2 is the highest point in the $x_e - y_e$ coordinate system shown in Fig. 9.15 (a) (origin at Pt. $s_2$1, x_e-axis passing through Pt. $s_2$3). They also specify the slopes of lines A and B. In order to keep the profile smooth and the sections tangent, the slope m_1 of Line A for sections 2 and 3 is set to be the same as the slopes at the borders to sections 1 and 4, respectively. This slope is received as an input by the *SolveSubset2* function, generated from the outputs of *SolveSubset1*. As for Line B, it constitutes the flat top of the profile, and therefore has a slope of zero. Since the slopes of lines A and B are known, and the coordinates of Pt. $s_2$1 and Pt. $s_2$3 (i.e. skeleton points 2 and 3) are known, the only question that remains is: where is Pt. $s_2$2 located?

In order to allow the user to choose how sharp a corner to construct in sections 2 and 3, the location of Pt. $s_2$2 is determined by a user input:"γ_2" (denoted γ_{2l} for section 2, and γ_{2r} for section 3) [2]. When $\gamma_2 = 0$, the interpolation in these sections consists only of an ellipse, as shown in Fig. 9.16. When $\gamma_2 = 1$, the interpolation consists only of Line A and Line B. For the former case, Pt. $s_2$2 is located at Pt. P (see Fig. 9.15 b). Pt. P, in the $x_e - y_e$ coordinate system, is the maximum point of an ellipse that is both tangent to lines A and B, and passes through Pt. $s_2$1 and Pt. $s_2$3. For the latter case, Pt. $s_2$2 is located at Pt. Q, the intersection point of lines A and B. For values of γ_2 between zero and 1, the location of Pt. $s_2$2 falls between points P and Q, onto the line they define (shown in red in Fig. 9.15 b). Let this line be denoted Line D, and let its equation be written as specified in Fig. 9.15 (c): $y = m_p x + b_p$.

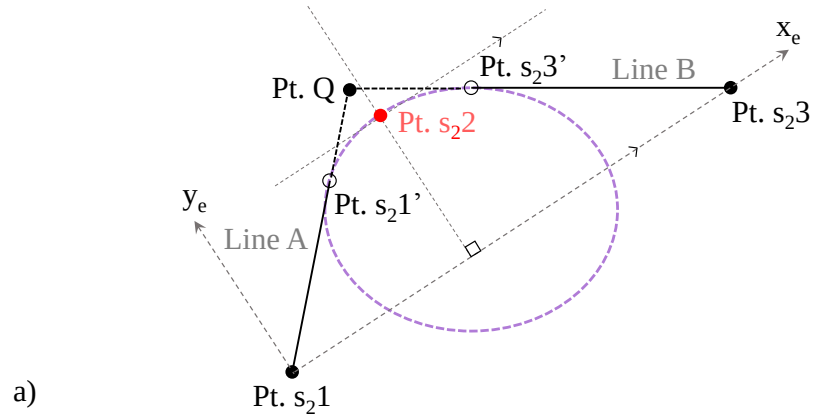

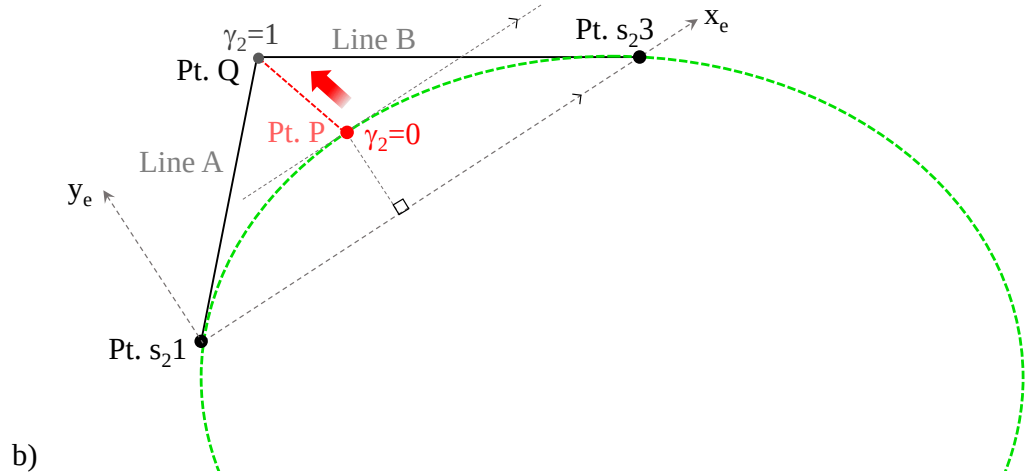

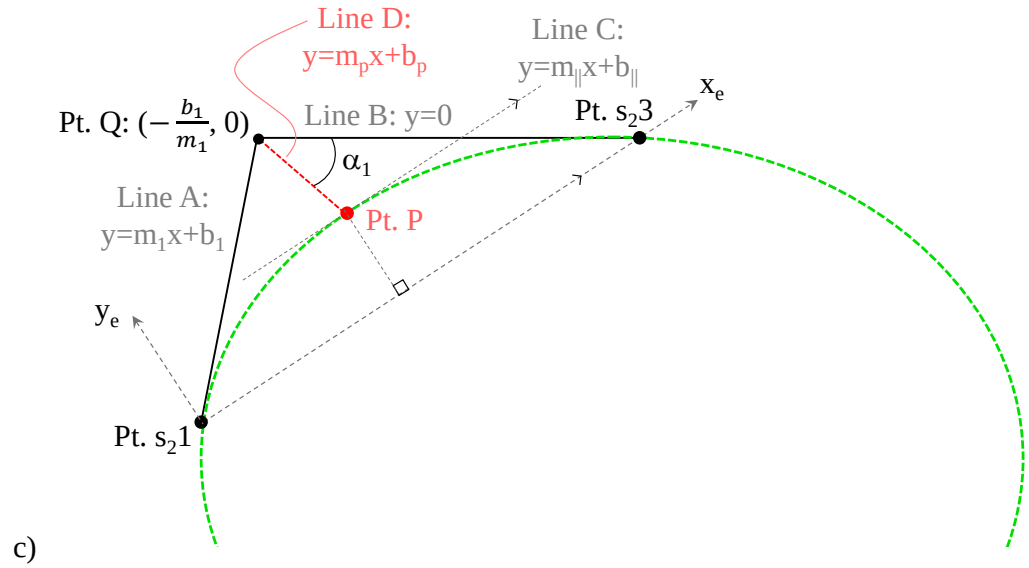

Figure 9.15. Geometry of section 2. Note that although the $x_e - y_e$ coordinate system is shown here, all geometrical entities are defined in the $x_{pr} - y_{pr}$ system (image based on [2]).

Table 9.5. Constraints on Line A, Line B, and the ellipse [2].

Shape	#	*Constraint*
Line A	1	Tangent to the profile in Section 1 at Pt. $s_2 1$.
	2	Passes through Pt. $s_2 1$.
Line B	1	Slope is zero.
	2	Passes through Pt. $s_2 3$.
Ellipse	1	Same slope as Line A at Pt. $s_2 1$.
	2	Same slope as Line B at Pt. $s_2 3$.
	3	Pt. $s_2 1$ is on the ellipse.
	4	Pt. $s_2 1$ is on Line A.
	5	Pt. $s_2 3$ is on the ellipse.
	6	Pt. $s_2 3$ is on Line B.
	7	Pt. $s_2 2$ is on the ellipse.
	8	Pt. $s_2 2$ is the highest point on the ellipse in the $x_e - y_e$ coordinate system, and a line tangent to the ellipse at this point is parallel to the x_e-axis.

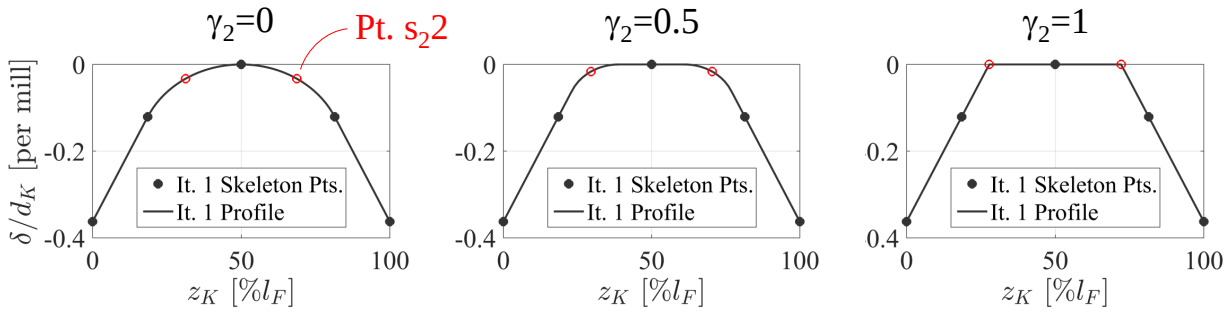

Figure 9.16. Interpolation in sections 2 and 3 for different values of γ_2 (image based on [2]).

The coordinates of Pt. $s_2 2$ can be calculated from the slope of this line, the coordinates of Pt. P, and the user-specified value of γ_2, as shown in Eqs. 8.35 and 8.36 of Table 9.6. In these two equations, the angle α_1 is the inverse tangent of the slope m_p. The other unintroduced parameter, H_e, is the distance from Pt. P to Pt. $s_2 2$, which is calculated by the TPGA as the product of γ_2 with H_T: the distance from Pt. P to Pt. Q. H_T, in turn, can be calculated from the coordinates of points P and Q. Since the slope and intercept of Line A are determined by the interpolation in the adjacent outer section of the profile, i.e. received by the *SolveSubset2* function as inputs, and since Line B is simply y=0, the coordinates of Pt. Q are easily obtained (see Fig. 9.15 c). The resulting equation for H_T is specified at the bottom of Table 9.6.

Table 9.6. Evaluating α_1, H_T, H_e, $x_{\mathrm{s}2}$, and $y_{\mathrm{s}2}$ [2].

Parameter	*Equation*	
$x_{\mathrm{s}2}$	$x_{\mathrm{s}2} = x_\mathrm{p} - H_\mathrm{e} cos(\alpha_1)$	(9.35)
$y_{\mathrm{s}2}$	$y_{\mathrm{s}2} = y_\mathrm{p} + H_\mathrm{e} sin(\alpha_1)$	(9.36)
α_1	$\alpha_1 = tan^{-1}\lvert m_\mathrm{p}\rvert$	(9.37)
H_e	$H_\mathrm{e} = \gamma_2 H_\mathrm{T}$	(9.38)
H_T	$H_\mathrm{T} = \sqrt{\left(\left(x_\mathrm{p} + \frac{b_1}{m_1}\right)^2 + {y_\mathrm{p}}^2\right)}$	(9.39)

What is still missing, however, are the coordinates of Pt. P— and the slope m_p. For these, the equation of the ellipse for the case $\gamma_2 = 0$ needs to be determined as a function of known values. The equation of this ellipse takes the following form:

$$\frac{(x_\mathrm{pr} - a_{\gamma 0})^2}{{h_{\gamma 0}}^2} + \frac{(y_\mathrm{pr} - b_{\gamma 0})^2}{{k_{\gamma 0}}^2} = 1 \tag{9.40}$$

The unknowns are the four constants, $a_{\gamma 0}$, $b_{\gamma 0}$, $k_{\gamma 0}$, and $h_{\gamma 0}$. Fittingly, four geometric constraints describe the ellipse, all listed in Table 9.7, along with the equations that describe them. These can be used to solve for the four unknowns— the result is in Table 9.8. Since

Pt. P is the maximum point on the ellipse in the $x_e - y_e$ coordinate system, the slope of the ellipse at that point, in that system, must be zero. Hence, in the $x_{pr} - y_{pr}$ coordinate system, the slope of the ellipse at Pt. P must be the same as the slope of the x_e axis. Let this slope be denoted $m_{||}$. As the coordinates of Pt. $s_2 1$ and Pt. $s_2 3$ are known, this slope is also known. Setting $m_{||}$ equal to the slope of the ellipse at Pt. P:

$$m_{||} = \left(\frac{k_{\gamma 0}}{h_{\gamma 0}}\right) \frac{(a_{\gamma 0} - x_p)}{\sqrt{\left({h_{\gamma 0}}^2 - (x_p - a_{\gamma 0})^2\right)}} \tag{9.41}$$

The x_{pr} coordinate of Pt. P can be obtained by solving the equation above for it. The y_{pr} coordinate of Pt. P can then be found by plugging that x_{pr} coordinate into the equation of the ellipse and solving. Lastly, since Pt. P is also on Line D (refer to Fig. 9.15 c), the slope m_p can be determined by plugging the coordinates of Pt. P into the equation of Line D and solving for it. The resulting equations for the coordinates of Pt. P (x_p, y_p) and the slope m_p are listed in Table 9.9.

Table 9.7. Constraints on the ellipse when $\gamma_2 = 0$.

#	*Constraint*	*Equation*	
1	Same slope as Line A at Pt. $s_2 1$.	$m_1 = \left(\frac{k_{\gamma 0}}{h_{\gamma 0}}\right)^2 \left(\frac{a_{\gamma 0} - x_{s21}}{y_{s21} - b_{\gamma 0}}\right)$	(9.42)
2	Same slope as Line B at Pt. $s_2 3$.	$a_{\gamma 0} = x_{s23}$	(9.43)
3	Passes through Pt. $s_2 1$.	$\frac{(x_{s21} - a_{\gamma 0})^2}{(h_{\gamma 0})^2} + \frac{(y_{s21} - b_{\gamma 0})^2}{(k_{\gamma 0})^2} = 1$	(9.44)
4	Passes through Pt. $s_2 3$.	$\frac{(x_{s23} - a_{\gamma 0})^2}{(h_{\gamma 0})^2} + \left(\frac{b_{\gamma 0}}{k_{\gamma 0}}\right)^2 = 1$	(9.45)

Table 9.8. Defining parameters of the ellipse when $\gamma_2 = 0$.

Parameter	*Equation*	
$a_{\gamma 0}$	$a_{\gamma 0} = x_{\text{s}23}$	(9.46)
$b_{\gamma 0}$	$b_{\gamma 0} = y_{\text{s}21}\left(\dfrac{y_{\text{s}21} + m_1\left(a_{\gamma 0} - x_{\text{s}21}\right)}{2y_{\text{s}21} + m_1\left(a_{\gamma 0} - x_{\text{s}21}\right)}\right)$	(9.47)
$k_{\gamma 0}$	$k_{\gamma 0} = b_{\gamma 0}$	(9.48)
$h_{\gamma 0}$	$h_{\gamma 0} = \sqrt{\left(\dfrac{\left(b_{\gamma 0}\right)^2\left(a_{\gamma 0} - x_{\text{s}21}\right)}{m_1\left(y_{\text{s}21} - b_{\gamma 0}\right)}\right)}$	(9.49)

Table 9.9. Evaluating the coordinates of Pt. P, and the slope of Line D.

Parameter	*Equation*	
x_{p}	$x_{\text{p}} = a_{\gamma 0} - \sqrt{\left(\dfrac{{h_{\gamma 0}}^2}{\left(\frac{k_{\gamma 0}}{h_{\gamma 0} m_{\|\|}}\right)^2 + 1}\right)}$	(9.50)
y_{p}	$y_{\text{p}} = \left(\dfrac{k_{\gamma 0}}{h_{\gamma 0}}\right)\sqrt{\left({h_{\gamma 0}}^2 - (x_{\text{p}} - a_{\gamma 0})^2\right)}$	(9.51)
m_{p}	$m_{\text{p}} = -\dfrac{y_{\text{p}}}{\left(-\frac{b_1}{m_1} - x_{\text{p}}\right)}$	(9.52)

Having established the equations required to calculate the location of Pt. $s_2 2$, it is possible to solve for the shape of the ellipse for the case of $0 < \gamma_2 < 1$. Let that ellipse be described by the following equation:

$$\frac{\left(x_{\text{pr}} - a\right)^2}{h^2} + \frac{\left(y_{\text{pr}} - b\right)^2}{k^2} = 1 \tag{9.53}$$

The unknowns a, b, k, and h must be solved for— as well as the coordinates of the points at which lines A and B are tangent to the ellipse, namely: Pt. $s_2 1$ and Pt. $s_2 3$. To this end, Table 9.10 lists the equations corresponding to the geometric constraints that define the three interpolation shapes, whose verbal description was provided earlier, in Table 9.5.

Solving this system yields the values of the seven unknowns (a, b, h, k, x_{s21}, y_{s21}, x_{s23}, and y_{s23}) that define the interpolation over section 2 (or section 3).

The TPGA solves the system for five of these unknowns (a, b, h, k, x_{s21}, and y_{s21}) using a simple linear search method. The method is based on two key facts. First, as can be observed from Fig. 9.17, the greatest negative value b can take on (in the $x_{pr} - y_{pr}$ coordinate system) is $b_{\gamma 0}$, i.e. its value for the case when $\gamma_2 = 0$. Second, Pt. $s_2 2$ is defined such that it is the maximum point on the ellipse in the $x_e - y_e$ coordinate system, and such that a line tangent to the ellipse at this point is parallel to the x_e-axis. If $b \geq y_{s22}$, this is impossible. Thus, $b_{\gamma 0} \leq b < y_{s22}$.

Table 9.10. Constraints on Line A, Line B, and the ellipse.

Shape	*Constraint #*	Equation	
Line A	1-2	$y = m_1 x + b_1$	(9.54)
Line B	1-2	$y = 0$	(9.55)
Ellipse	1	$m_1 = \left(\frac{k}{h}\right)\left(\frac{a - x_{s21}}{y_{s21} - b}\right)$	(9.56)
	2	$0 = \left(\frac{k}{h}\right)\left(\frac{a - x_{s23}}{y_{s23} - b}\right) \Rightarrow x_{s23} = a$	(9.57)
	3	$\frac{(x_{s21} - a)^2}{h^2} + \frac{(y_{s21} - b)^2}{k^2} = 1$	(9.58)
	4	$y_{s21} = m_1 x_{s21} + b_1$	(9.59)
	5	$\frac{(x_{s23} - a)^2}{h^2} + \frac{(y_{s23} - b)^2}{k^2} = 1$	(9.60)
	6	$y_{s23} = 0$	(9.61)
	7	$\frac{(x_{s22} - a)^2}{h^2} + \frac{(y_{s22} - b)^2}{k^2} = 1$	(9.62)
	8	$m_{\|\|} = \left(\frac{k}{h}\right)\left(\frac{a - x_{s22}}{y_{s22} - b}\right)$	(9.63)

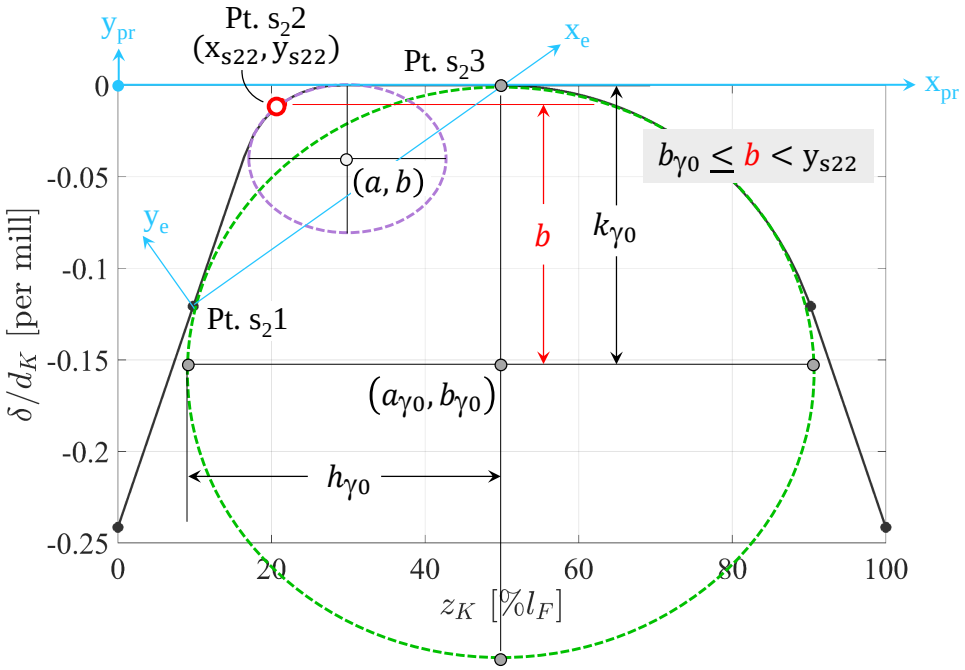

Figure 9.17. The limits of b.

The TPGA line search method seeks a solution for b within that range; the other variables can then easily be solved for. An overview of the SolveSection2 function, including the linear search method, is provided in Fig. 9.18. As can be seen, the search method starts by setting the value of b to the value of y_{s22} (step 1.2.2.5), and then subtracting δb, which is the user-set step size of the line search (1.2.2.6). The algorithm then evaluates the unknowns a, h, k, x_{s21}, and y_{s21} based on the assumed value of b, according to the equations in Table 9.11 (1.2.2.7).

In order to assess whether the resulting set of values constitutes a valid solution set, the algorithm evaluates $E_1 - E_4$. These four expressions are the magnitude of the difference between the left and right-hand sides of the Table 9.10 equations that were not used to evaluate a, h, k, x_{s21}, and y_{s21} in step 1.2.2.7. Hence, if $E_1 - E_4$ each evaluates to less than E, the user-provided allowed error, then a solution has been found (1.2.2.8). If not, the algorithm returns to step 1.2.2.6, decreases the assumed value of b, and assesses whether this new value solves the system of equations that describe the ellipse. The loop repeats until either a solution is found, or $|b|$ becomes larger than $|b_{\gamma 0}|$, in which case the step size is cut in half, b is set back to $y_{s22} - \delta b$, and the search starts over.

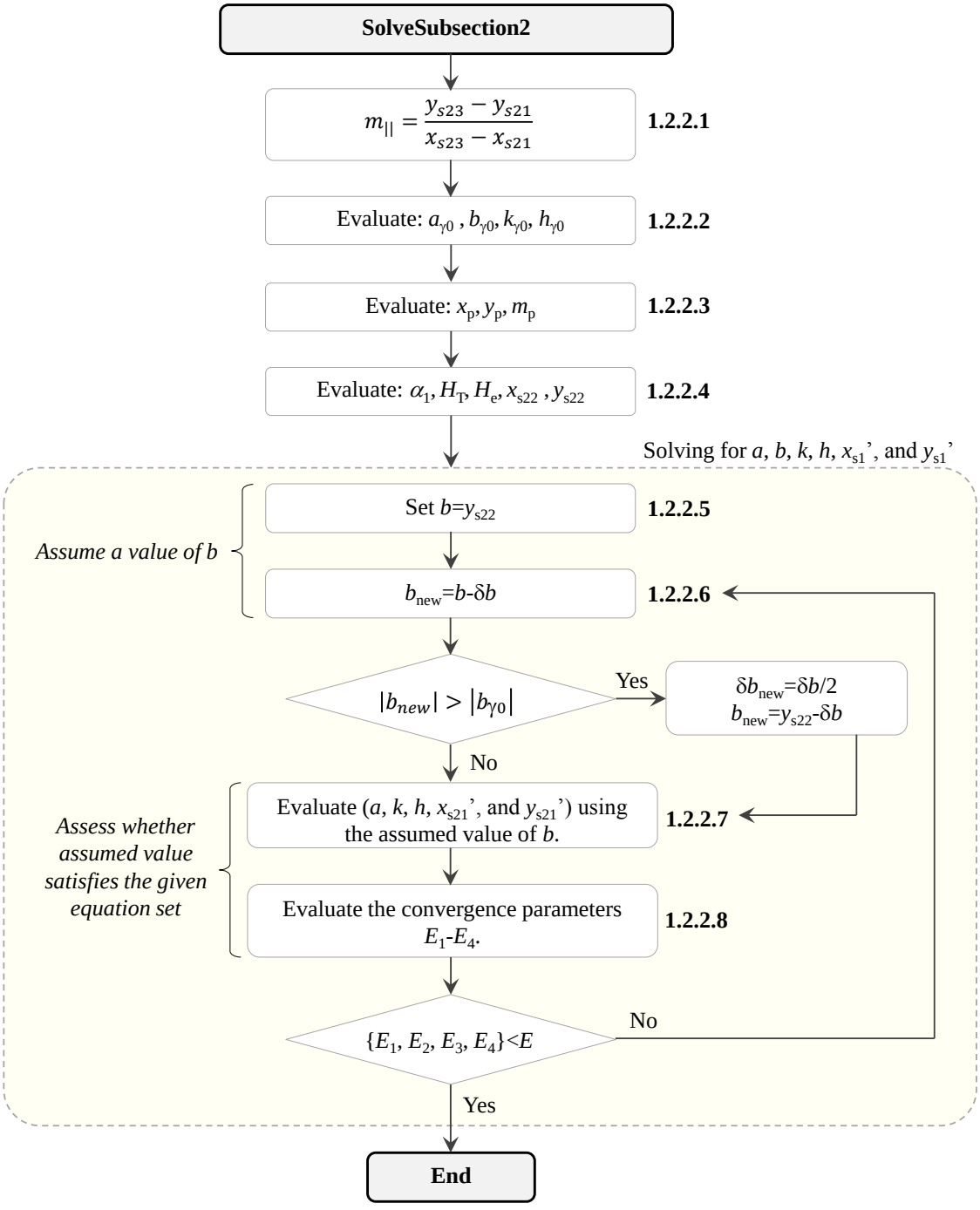

Figure 9.18. Subsection 2 code diagram.

Once a solution is found for a, b, h, k, x_{s21}, and y_{s21}, the only unknowns remaining are x_{s23}, and y_{s23}. From Table 9.10:

$$x_{s23} = a \quad \text{and} \quad y_{s23} = 0 \tag{9.64}$$

Since a has been solved for, x_{s23} can be evaluated. Finally, the interpolation over section 2 (or section 3) can be generated according to the equations:

$$\begin{cases} \text{Equation of Line A:} & y_{pr} = m_1 x_{pr} + b_1 \\ \text{Equation of Line B:} & y_{pr} = 0 \\ \text{Equation of the ellipse:} & y_{pr} = \sqrt{k^2 - \left(\frac{k}{h}\right)^2 (x_{pr} - a)^2} + b \end{cases} \tag{9.65}$$

There is a single exception to the described interpolation procedure: when $\gamma_2 = 1$, i.e. when the interpolation consists only of lines A and B, the *SolveSubset2* function is not run— instead, the equations of the two lines are evaluated directly, with their point of intersection located at $x_{pr} = -b_1 m_1$.

Table 9.11. Solving for a, h, k, x_{s21}, and y_{s21} based on the value of b.

Unknown	*Equation*	
1	$k = -b$	(9.66)
2	$h = \sqrt{\left(\left(\frac{b}{m_{\|\|}}\right)^2 \left(\frac{b^2}{(y_{s22} - b)^2} - 1\right)\right)}$	(9.67)
3	$y_{s21} = b + \sqrt{\left(\frac{b^2}{\left(\frac{m_1 h}{b}\right)^2} + 1\right)}$	(9.68)
4	$x_{s21} = \frac{y_{s21} - b_1}{m_1}$	(9.69)
5	$a = m_{\|\|} \left(\frac{h}{b}\right)^2 (y_{s22} - b) + x_{s22}$	(9.70)

Table 9.12. Verifying conditions 1, 3, 7, and 8 with convergence parameters $E_1 - E_4$.

#	*Equation*	
1	$E_1 = \left\lvert \frac{(x_{s21} - a)^2}{h^2} + \frac{(y_{s21} - b)^2}{k^2} - 1 \right\rvert$	(9.71)
2	$E_2 = \left\lvert \left(\frac{b}{h}\right)\left(\frac{a - x_{s21}}{y_{s21} - b}\right) - m_1 \right\rvert$	(9.72)
3	$E_3 = \left\lvert \frac{(x_{s22} - a)^2}{h^2} + \frac{(y_{s22} - b)^2}{k^2} - 1 \right\rvert$	(9.73)
4	$E_4 = \left\lvert \left(\frac{b}{h}\right)\left(\frac{a - x_{s22}}{y_{s22} - b}\right) - m_{\|\|} \right\rvert$	(9.74)

9.2.5 Stage 2: Adapting to Piston Deformation

The interpolation of the skeleton points from step 1.1 completes Stage 1. As described in the algorithm overview, Stage 2 begins with the user simulating, via FSTI, the behavior of the piston-cylinder interface that is elicited by each of the bore profiles developed in Stage 1— this constitutes step 2.1 [2]. Then, in step 2.2, the information from the outputs of these simulations is employed in adapting the profiles to the corresponding simulated piston deformation; this adaptation is implemented by changing the x_{pr}-coordinates of skeleton points 2 and 4. The procedure of step 2.2 will now be described in detail, guided by the code overview diagram provided in Fig. 9.19.

As a pre-step to this part of Stage 2, the current version of the code actually re-calculates the skeleton point coordinates from Stage 1, as opposed to reading them in— because this is quick and relieves the user of having to find the data from the previous stage. However, the code can be easily modified to read in these coordinates instead for a small speedup. With the required Stage 1 information in hand, step 2.2 runs through a loop that addresses each profile in turn (see steps 2.2.1-2.2.6 in Fig. 9.19).

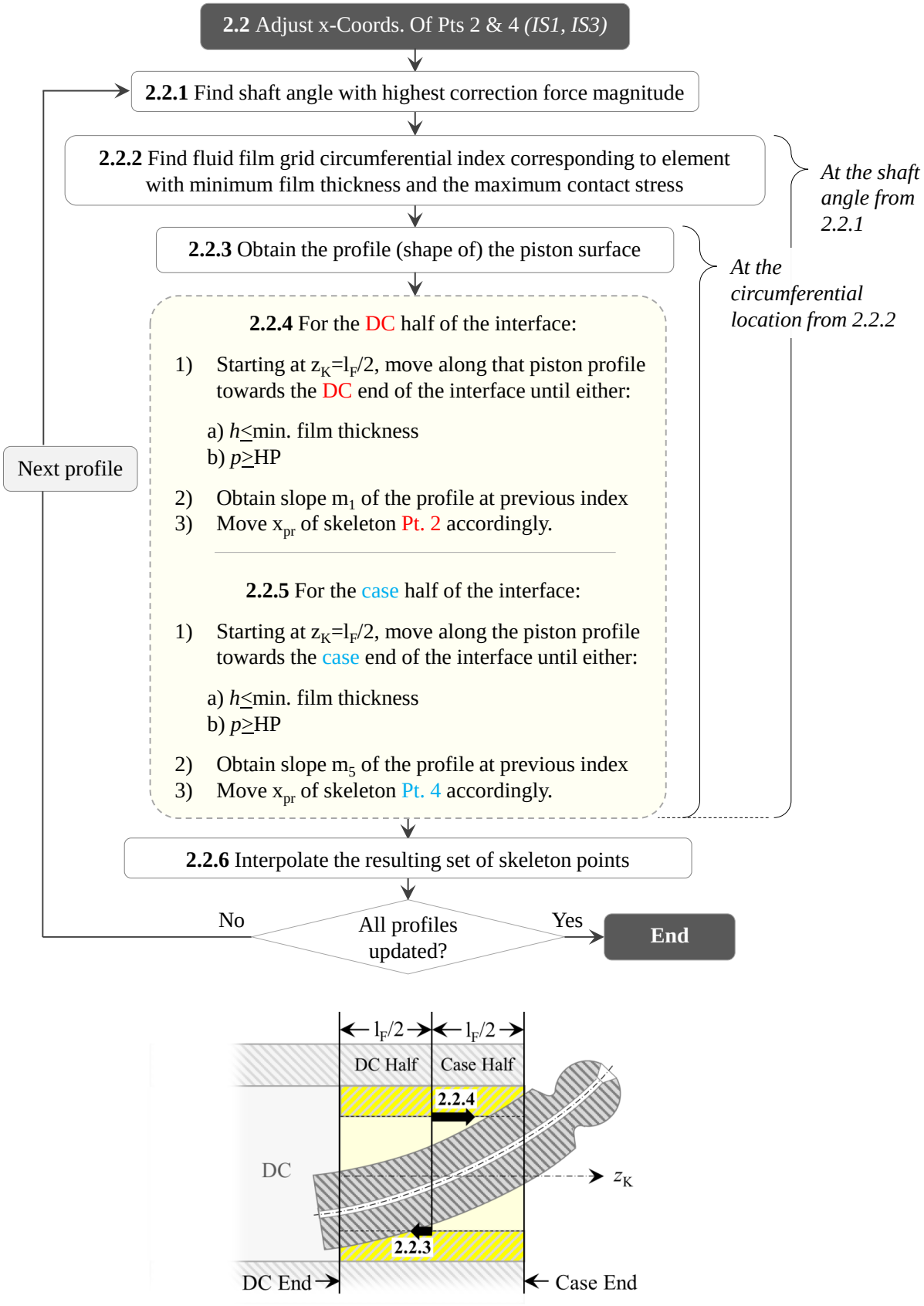

Figure 9.19. Step 2.2 overview and illustration of steps 2.2.3-2.2.4 (image based on [2]).

When trying to match the bore profile to the shape of the deformed piston surface, the first question that needs to be addressed by the algorithm is: match at which shaft angle? While the piston deformation due to thermal effects is only updated by FSTI once every full shaft revolution, the deformation due to pressure is updated at every simulated time step, and can change drastically over the course of a shaft turn. For which shaft angle, then, should the bore be shaped? As can be seen from Fig. 9.19, sub-step 2.2.1 of the TPGA handles this by obtaining the shaft angle corresponding to the highest correction force magnitude at either the DC or case end control point [2]. That is, a single "worst-case scenario" shaft angle is chosen, and not one for either end of the guide length. This is done because the manner in which the piston conforms to the bore at one end will impact how it conforms to the bore at the other, i.e. designing for two different shaft angles may produce unacceptable results for both.

Having determined the shaft angle to work with, the algorithm must proceed to decide at which location on the interface circumference the bore profile should be adapted to the deformed piston shape. This is because, although the surface shape the TPGA generates will be symmetric about the bore's center axis, the piston deformation is not. Again taking the worst-case approach, sub-step 2.2.2 computes, at the shaft angle from sub-step 2.2.1, the circumferential location on the fluid film grid with minimum film thickness, and the highest contact stress value [2]. Specifically, the circumferential location is determined in form of the corresponding index for the matrices extracted from the FSTI simulation outputs that describe the fluid film thickness, contact stress, fluid pressure, piston and bushing deformations, etc.

At this point, it is possible to obtain the shape of the deformed piston for the chosen shaft angle, and at the chosen circumferential location (sub-step 2.2.3). Fig. 9.20 illustrates how the algorithm approaches that step. Shown in the upper right-hand corner is the lengthwise cross-section of a cylinder bore, its bushing holding a piston at full tilt; the cross-section is taken on a plane that cuts through the center axis of said bore, and is oriented such as to show the chosen circumferential location (at which the bore shape will be matched to that of the piston). The center image zooms in on the indicated area from the upper half of that

cross-section, showing a deformed bushing, a deformed piston, and the fluid in between. A dashed line marks the shape of the corresponding bore profile from Stage 1 of the algorithm.

The piston contour (the shape of the deformed piston within the depicted plane) is calculated by the TPGA from FSTI simulation outputs as the height, h_{pc}, for each fluid grid point along the guide length (at the chosen circumferential location on the interface) [2]. In order to define this height, it is convenient to set up the y_{pc}-axis: this axis will be perpendicular to the z_K-axis, and will lie in the depicted plane. Its zero point is set to be the vertical coordinate of the bore profile at the end of the guide length where it deviates furthest from flat. For the example illustrated in Fig. 9.20, the bore profile deviates most from flat, i.e. from a cylindrical bore surface, at the case end of the guide length. Hence, y_{pc}=0 for the point on the bore profile at its case end. h_{pc} can now be defined at any given point along the z_K axis as the distance spanning vertically from the zero point of the y_{pc}-axis to the piston surface.

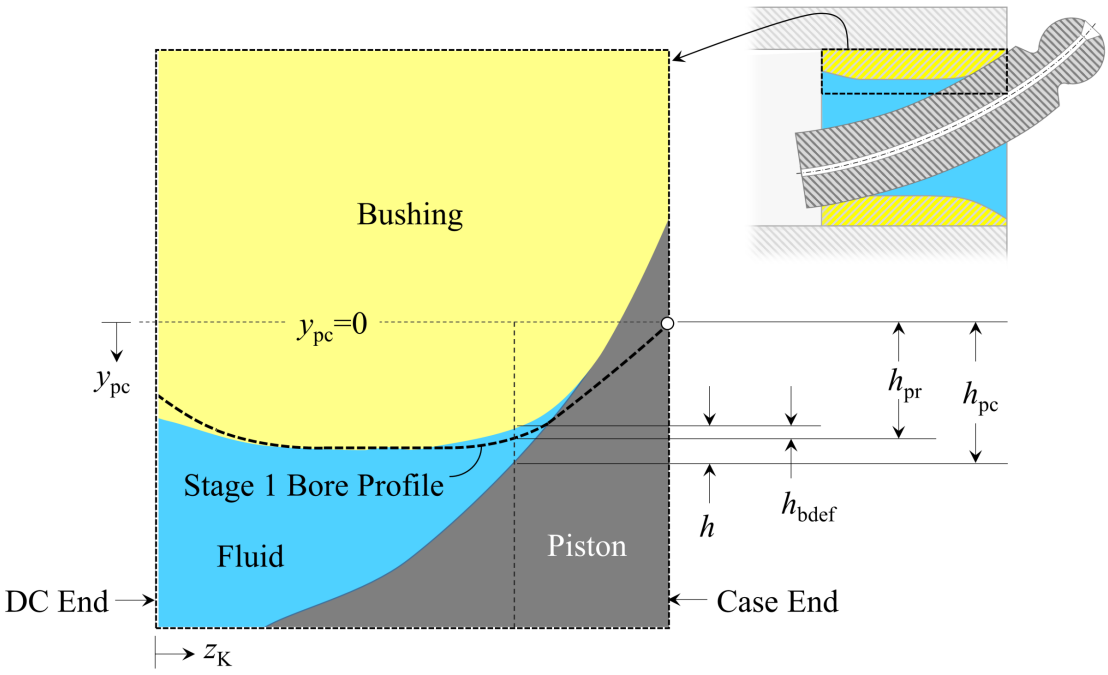

Figure 9.20. Determining the piston contour (image based on [2]).

As Fig. 9.20 shows, h_{pc} can be determined from the fluid film thickness, the Stage 1 shape of the bore profile, and the (bushing) bore surface deformation, as follows [2]:

$$h_{\mathrm{pc}} = h + h_{\mathrm{pr}} \underbrace{-h_{\mathrm{bdef,p}} - h_{\mathrm{bdef,t}}}_{\text{Bore Deformation}} \tag{9.75}$$

Here, h is the fluid film thickness calculated by FSTI, and h_{pr} is the height of the Stage 1 bore profile, measured relative to the zero point of the y_{pc}-axis [2]. Lastly, $h_{\mathrm{bdef,p}}$ and $h_{\mathrm{bdef,t}}$ are the bore surface deformations due to pressure and thermal loads, respectively.

Once the piston contour has been calculated as $h_{\mathrm{pc}}(z_{\mathrm{k}})$, the TPGA determines the slope of that contour in the regions where the piston and bore surfaces come together (are about to converge) near either end of the guide length; those two slopes will then be used to shift skeleton Pts. 2 and 4 [2]. More exactly, the code runs a loop consisting of three steps, its first iteration culminating in the shifting of Pt. 2, and its second in the shifting of Pt. 4. In essence, the three steps entail finding the point at which the piston contour slope should be determined, calculating that slope, and moving the respective skeleton point. Taking the first iteration of the loop (sub-step 2.2.4) as an example to explain all three steps in detail, the location for obtaining the piston contour slope is found by starting in the middle of the guide length, and then moving towards the DC end of the interface until either [2]:

1. The film thickness h falls at or below the minimum film thickness.
2. The fluid pressure p reaches or exceeds HP (the pressure in the high-pressure port).

The latter condition is imposed to avoid designing towards a deformation caused by fluid pressure spikes that may drastically change when the bore profile is adjusted at the end of step 2.2 [2].

When at least one of the two aforesaid conditions is met, the algorithm calculates the slope, m_1, of the piston contour [2]— at the previous grid point (just before the film thickness hits the 0.1 μm minimum film thickness saturation point of FSTI, or the pressure reaches HP).

m_1 is taken as the slope of a line between this point, whose fluid grid index will be denoted $\mathrm{i_{DC}}$, and a second point, with a fluid grid index of $\mathrm{i_{DC}} + \triangle_{\mathrm{i}}$:

$$m_1 = \frac{h_{pc}(\mathrm{i_{DC}}) - h_{pc}(\mathrm{i_{DC}} + \triangle_{\mathrm{i}})}{z_{\mathrm{K}}(\mathrm{i_{DC}}) - z_{\mathrm{K}}(\mathrm{i_{DC}} + \triangle_{\mathrm{i}})} \tag{9.76}$$

For the simulations to be presented in the results section of this chapter, $\triangle_{\mathrm{i}}$ has been set to five; setting this value greater than one helps to avoid local fluctuations in the slope of the piston surface that only span from one grid point to the next.

With the piston contour slope in hand, the new position of skeleton Pt. 2 on the x_{pr}-axis is calculated as follows:

$$x_{\mathrm{pr},2} = \frac{y_{\mathrm{pr},2} - y_{\mathrm{pr},1}}{m_1} + x_{\mathrm{pr},1} \tag{9.77}$$

Having shifted skeleton Pt. 2, the TPGA moves on to repeating the process for skeleton Pt. 4, as specified in sub-step 2.2.5 of Fig. 9.19. The slope of the piston contour is obtained as follows:

$$m_5 = \frac{h_{pc}(\mathrm{i_{case}}) - h_{pc}(\mathrm{i_{case}} - \triangle_{\mathrm{i}})}{z_{\mathrm{K}}(\mathrm{i_{case}}) - z_{\mathrm{K}}(\mathrm{i_{case}} - \triangle_{\mathrm{i}})} \tag{9.78}$$

Finally, skeleton Pt. 4 is moved horizontally as follows:

$$x_{\mathrm{pr},4} = \frac{y_{\mathrm{pr},4} - y_{\mathrm{pr},5}}{m_5} + x_{\mathrm{pr},5} \tag{9.79}$$

When the horizontal positions of the two skeleton points, Pt. 2 and Pt. 4, have been adjusted according to the simulated piston shape, the interpolation scheme from step 1.2 of the TPGA turns the resulting set of new skeleton points into a full profile [2]. The last part of Stage 2 (step 2.3) consists of the user simulating the new set of profiles using FSTI. Steps 2.2 and 2.3 can be repeated until a profile of desired performance is found— however, for the simulation studies conducted, a single iteration proved sufficient.

9.3 Results

This section presents the results of two studies, each detailing the design of bore profiles for an APMSPD with the TPGA. For the sake of making the performance that can be achieved via TPGA-generated profiles comparable to what is achievable via the type of profiles presented in the previous chapters, the first study utilizes the TPGA to design profiles for the 75 cc stock unit simulated in Chapters 6-8. The second study does the same for a 444 cc unit, but augments the simulated performance of the chosen profile with experimental validation.

9.3.1 75 cc Unit

As stated, this first study designs bore profiles for the 75 cc unit introduced in Ch. 6—specifically, for the modified version of this unit employed in the Set 1 baseline simulations described in that chapter. In order to ensure a satisfactory performance across as large a range of operating conditions as possible, the profile designs are generated for the high pressure, low speed operating condition, OC3. The value sets used in this study consist of all possible combinations of the values listed in Table 9.13.

Table 9.13. Values of δ_1 and δ_2 used to design bore profiles for a 75 cc unit.

δ_1/d_K [μm/mm]	δ_2/d_K [μm/mm]	δ_3/d_K [μm/mm]	γ_{1l}	γ_{1r}	γ_{2l}	γ_{2r}
0.36	0.36	0.097	0.8	0.8	0.5	0.5
0.483	0.483	0.24				
0.604	0.604					
0.725	0.725					

Of these combinations, three yield a maximum simulated contact stress under 20 N/m^2 at the end stage 2, after a single run through steps 2.2 and 2.3: Design W, X, and Y. The value sets of these designs are given in Table 9.14, and the corresponding profiles are plotted in Fig. 9.21. As can be seen, the three profiles are similar. This is advantageous, because it indicates that there is room for error during the machining process.

Table 9.14. Value sets of Design W-Y.

Design	δ_1/d_K [μm/mm]	δ_2/d_K [μm/mm]	δ_3/d_K [μm/mm]	γ_{1l}	γ_{1r}	γ_{2l}	γ_{2r}
W	0.604	0.604	0.097	0.8	0.8	0.5	0.5
X	0.725	0.604	0.097	0.8	0.8	0.5	0.5
Y	0.725	0.725	0.097	0.8	0.8	0.5	0.5

Fig. 9.22 shows how the performance of these profiles compares to that of the Ch. 6 baseline at OC4, allowing also for a comparison to the profile types explored in previous chapters. The plots show that designs W-Y eliminate the correction forces at this operating condition, i.e. they enable the piston-cylinder interface to provide full film lubrication. This is a drastic improvement to the baseline, which shows correction force magnitudes of up to nearly 1,500 N at the case end control point, and over 500 N at the DC end control point. It also constitutes an improvement over the performance delivered by the concave bore and barrel piston profiles. In fact, it even outperforms the concave bore profile with the extended guide length presented in Ch. 8.

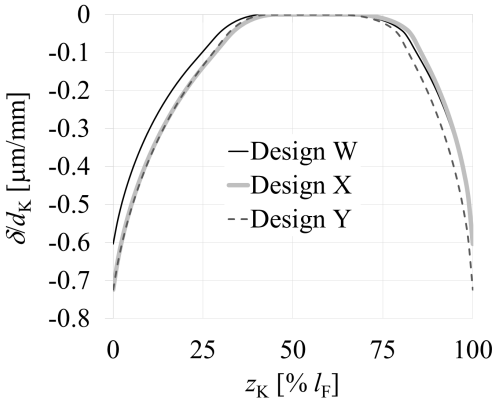

Figure 9.21. Design W-Y.

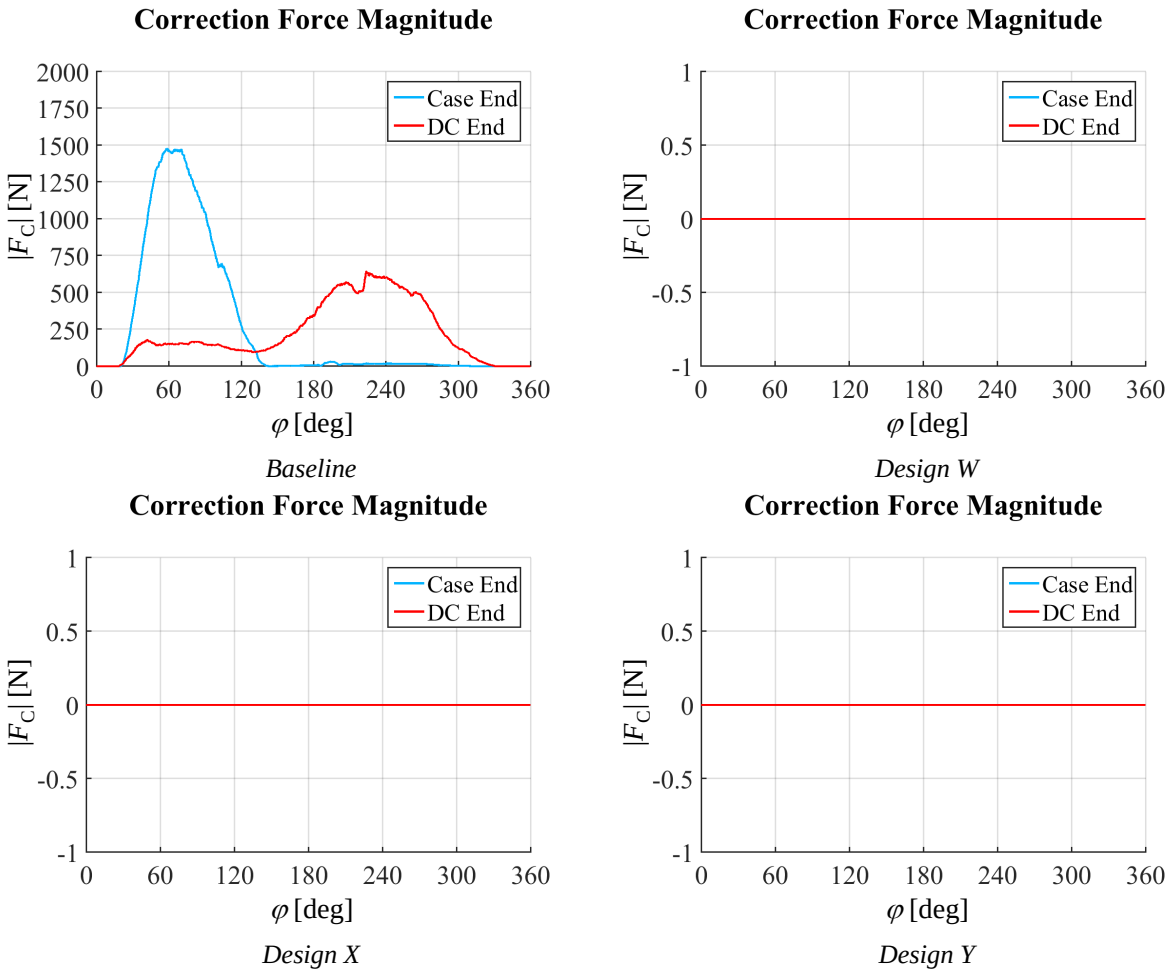

Figure 9.22. Comparison of correction force magnitudes at C_A and C_B for Design W-Y to the baseline at OC4.

The performance of designs W-Y at all four corner operating conditions, OC1-4, is summarized by Fig. 9.23. From Fig. 9.23 (a)-(b), it can be seen that these designs provide full load support at *all four operating conditions*. Such an improvement in load support does come at a price: Fig. 9.23 (c) shows that the power loss will be higher than that of the baseline. However, as already noted in Ch. 8, this is only the power loss due to viscous flow. For designs W-Y, the power loss due to mixed/solid friction is zero, because these profiles move the interface into the full film lubrication regime— for the baseline, by contrast, the high correction forces indicate that this loss will be significant.

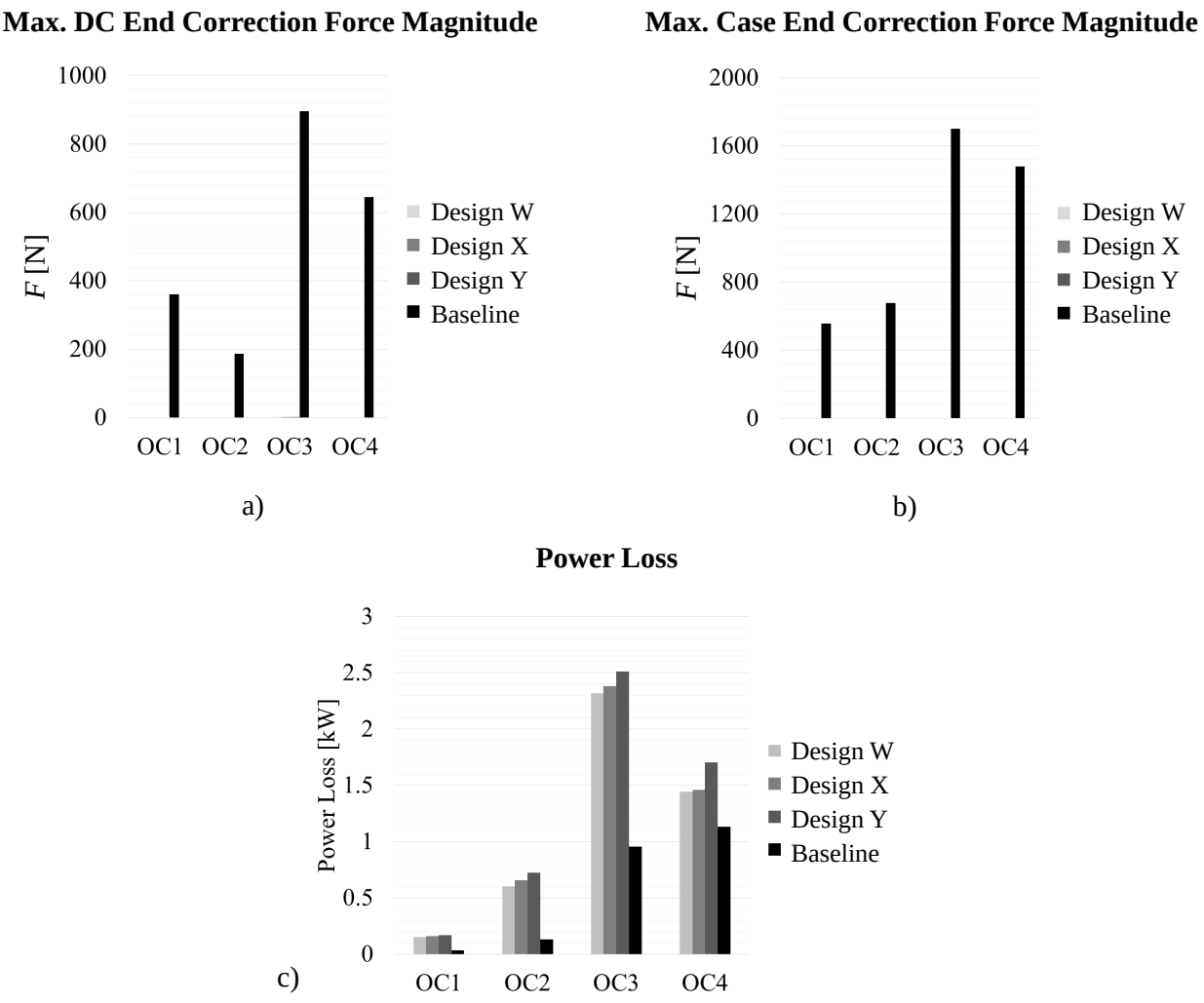

Figure 9.23. Load support comparison of Design W-Y to the baseline at OC1-4.

The TPGA can therefore be utilized to provide more (or even full) load support at the piston-cylinder interface, and to diminish/eliminate losses due to mixed/solid friction. In doing so, it can also allow units to be manufactured with larger piston/bore clearances. As an example, a new study was conducted, designing bore profiles for the same 75 cc unit, at the same operating condition, with the same value sets as before— but with the clearance doubled. Fig. 9.24 plots one of the resulting designs, and its corresponding correction forces: even with twice the clearance, metal-to-metal contact can be still prevented by a TPGA-generated design!

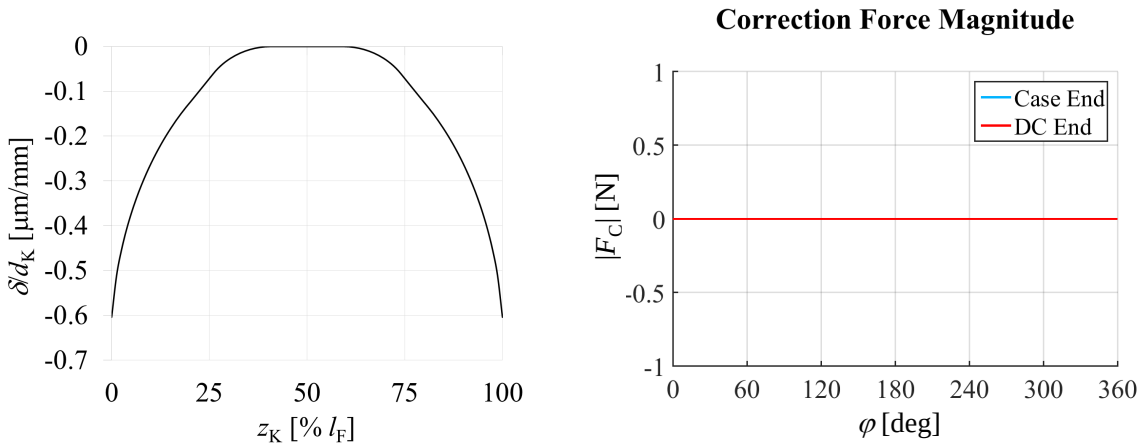

Figure 9.24. Correction force magnitudes at C_A and C_B for Design Z, at OC3.

In aim of testing the limits of the TPGA even further, the next section examines the design of a bore profile for a much larger unit, with a displacement nearly six times that of the machine simulated in this section.

9.3.2 444 cc Unit

In this study, the TPGA is employed to design a bore profile for a virtual prototype, Unit 1 [2]. In collaboration with the Danfoss High Pressure Pump Division, a physical prototype, Unit 2, is then constructed, and the output of the TPGA is tested experimentally at Danfoss facilities. Both prototypes (Unit 1 and Unit 2) are based on the geometry of a 444 cc commercial pump: the Danfoss unit 180B3071 [66]. The differences between this stock unit, Unit 1, and Unit 2, are summarized in Table 9.15.

The virtual prototype, Unit 1, is designed to have a higher swash plate angle than the stock unit, allowing for a larger displacement [2]. Furthermore, unlike the stock unit, Unit 1 has a shape imposed on the surfaces of its cylinder block bushing bores— the shape designed by the TPGA, which will be denoted Profile I (more details on this shortly). In order enable a more consistent performance from that shape, the length of the cylinder block bushings in Unit 1 is reduced from that of the stock unit to the point of achieving a fixed guide length. The material of the bushings has also been changed from that of the stock unit to brass,

Table 9.15. Comparison of the stock unit, Unit 1, and Unit 2 [2].

Feature	*Stock Unit*	*Unit 1*	*Unit 2*	
			RKA	*RKB*
Swash plate angle	β_s	$\beta_1 > \beta_s$	$\beta_{2A} = \beta_s$	$\beta_{2B} = \beta_s$
Shaping of bore surface	None	Profile I	None	Profile II
Bushing length	$l_{b,s}$	$l_{b,1} < l_{b,s}$	$l_{b,2A} = l_{b,s}$	$l_{b,2B} = l_{b,1}$
Bushing material	Stock unit matl.	Brass	Polymer	Polymer
Diametrical piston/ bore clearance	$h_{cl,s}$	$h_{cl,1} < h_{cl,s}$	$h_{cl,2A} = h_{cl,s}$	$h_{cl,2B} < h_{cl,s}$
Piston grooves	Yes	No	Yes	Yes

based on both its success in the previous studies, and on the material modeling capabilities of FSTI. Furthermore, in order to lower leakage through the piston-cylinder interface, the diametrical clearance between the pistons and bushing bores of Unit 1 has been reduced from that of the stock unit ($h_{cl,s}/d_K$=1.6 μm/mm, whereas $h_{cl,1}/d_K$=1.1 μm/mm). Lastly, the stock unit can have a circumferential groove in the running surface of its pistons, which has been eliminated from Unit 1 in the interest of lowering leakage and wear.

The physical prototype, Unit 2, is intended to serve as a proof-of-concept for the surface shaping of Unit 1 [2]. For this reason, its geometry is closer to that of the stock unit: it has the same swash plate angle, the same grooves on its pistons, and similar cylinder block bushing material. The prototype is tested with two rotating kits, RKA and RKB, each comprised of a cylinder block, complete with bushings, and nine piston-slipper assemblies. RKA is the baseline representing the stock unit, while RKB is designed with the bore profile to be tested. RKA therefore has diametrical piston/bore clearance as the stock unit, its cylinder block bushings have the same length, and no surface shaping on their bores. RKB is the rotating kit with the design changes that are to be assessed in measurement.

This kit differs from RKA in that it has surface shaping on the cylinder block bushing bores, the length of its cylinder block bushings is the same as that of Unit 1 (i.e. shorter than that of RKA), and its diametrical piston/bore clearance is smaller than that of RKA (the surfaces of five pistons and bores were measured, and found to have a maximum clear-

ance of h_{cl}/d_K=1.2 μm/mm). In order to ensure that the bore surface shape performs as expected with achievable machining tolerances, a sensitivity study was conducted to assess the effect of small changes in the slope at either end of the profile on load support in the piston-cylinder interface. The surface shape implemented on RKB is Profile II, a slightly modified version of Profile I that resulted from this sensitivity study.

Surface Shape Design for Unit 1

As stated, the bore surface shape for Unit 1 is designed using the TPGA. As in the previous study, the TPGA profiles are for a high-pressure, low-speed operating condition: $\triangle p$=117.5 bar, 700 rpm, and T_{in}=20°C [2]. The value combinations used as inputs to the TPGA are all possible combinations of the values listed in Table 9.16. The listed values of the critical dimension, δ_1, extend just past the radial piston-bore clearance, $h_{cl,r}/d_K$=0.55 μ/mm. Those of the other critical dimension, δ_2, do not extend quite as far, because opening up the interface at its DC end can drastically drive up leakage. The remaining three dimensions, which tend to be less critical, are each assigned a single value, to be used in each value combination.

Table 9.16. Value combinations [2].

Parameter	*Values*							
δ_1/d_K [μ/mm]	0.20	0.271	0.338	0.406	0.474	0.542	0.609	0.677
δ_2/d_K [μ/mm]	0.20	0.271	0.338	0.406				
δ_3/d_K [μ/mm]	0.068							
$\gamma_{1l} = \gamma_{1r}$	0.5							
$\gamma_{2l} = \gamma_{2r}$	0.6							

The profile chosen from those generated by the TPGA using the Table 9.16 value combinations is shown in Fig. 9.25 (a). This, is Profile I. The magnitudes of the correction forces calculated by FSTI when Profile I is implemented in Unit 1 for the final step of the TPGA's Stage 2 are plotted against shaft angle in Fig. 9.25 (b) [2]. As can be seen, with Profile I, the correction forces are practically zero. For comparison, Fig. 9.25 (c) shows the correction

force magnitudes that result when the surface shaping is taken away: they are thousands of Newtons higher than with the shaping. Lastly, Fig. 9.25 (d) shows the correction forces corresponding to the stock unit (without piston grooves). On account of the stock unit's lower swash plate angle and longer bushing length, these correction force magnitudes are lower than those shown for Unit 1 in Fig. 9.25 (c)— but still reach circa 1,000 N. That is, Profile I is able to deliver a better load support performance than the stock unit despite being implemented in a pump that has a higher swash plate angle, and a shorter guide length.

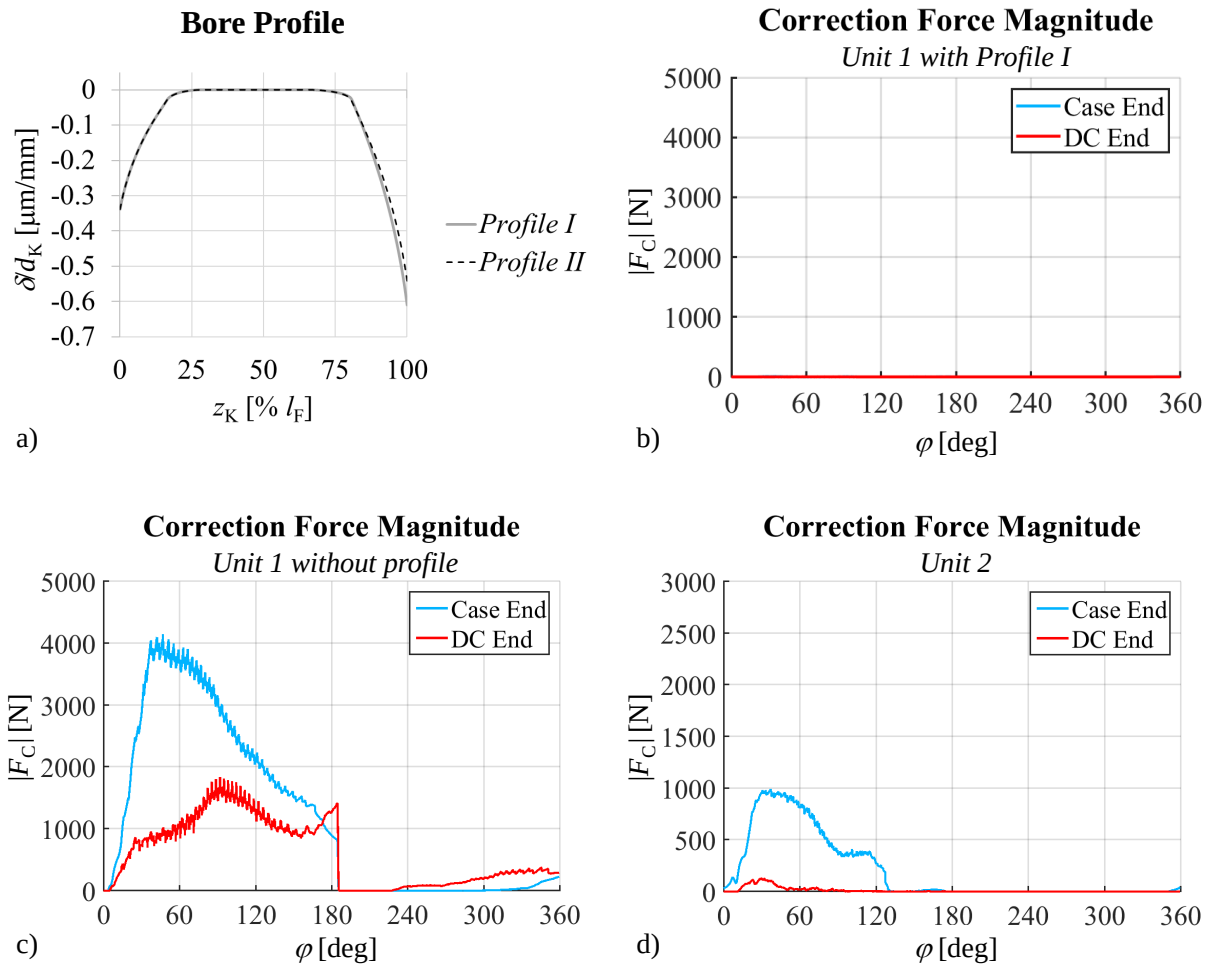

Figure 9.25. a) TPGA profile, and b)-d) simulation results at 700 rpm, $\triangle p$=117.5 bar, and T_{in}=20°C (image based on [2]).

Experimental Validation

Unit 2 is tested in three phases [2]:

Table 9.17. Test Phases.

Phase	*Objective*
1	Run in all non-rotating kit components
2	Run each rotating kit at the operating conditions in Table 9.18, and measure: p_{in}, the pressure at the pump inlet p_{out}, the pressure at the pump outlet Q_{out}, the outlet flow n, the pump speed τ, the torque on the axle Surface wear on the pistons and bushings
3	Test the long-term performance by re-taking the measurements for OC6 after 500 hours of operation

Table 9.18. Measured operating conditions [2].

OC	*1*	*2*	*3*	*4*	*5*	*6*
T_{in} [°C]	20	20	20	20	20	20
p_{in} [bar]	2.5	2.5	2.5	2.5	2.5	2.5
p_{out} [bar]	60	60	60	100	90	90
n [rpm]	700	1100	1500	700	700	1100

The experimental setup is shown in Fig. 9.26: an electric motor with variable frequency drive controls the speed of the test pump, the inlet and outlet pressures of that pump are measured by pressure transmitters on either side of it, and the setup is equipped with two flow meters, of two different ranges, to enable measurements for units of different sizes [2]. From the

parameters measured in Phase 2 and 3 using this test rig, the volumetric, mechanical, and total efficiency of the pump, η_v, η_m and η_t, can be calculated [2]:

$$\eta_\mathrm{v} = \frac{Q_\mathrm{out}}{nV_\mathrm{theo}}, \quad \eta_\mathrm{t} = \frac{Q_\mathrm{out}p_\mathrm{out}}{n\tau p_\mathrm{in}Q_\mathrm{in}}, \quad \eta_\mathrm{m} = \frac{\eta_\mathrm{t}}{\eta_\mathrm{v}}, \tag{9.80}$$

where Q_in is taken to be the product of pump speed and theoretical displacement. Years of testing and validating the results against real power consumption with customers by Danfoss HPP has shown that the described test rig can measure the total efficiency to within $\pm 1\%$ [2]. Furthermore, from the surface measurements taken at each operating condition, the wear-in process of the pistons and bushings can be observed. Together, these parameters serve as a solid basis for assessing the differences in performance between RKA and RKB.

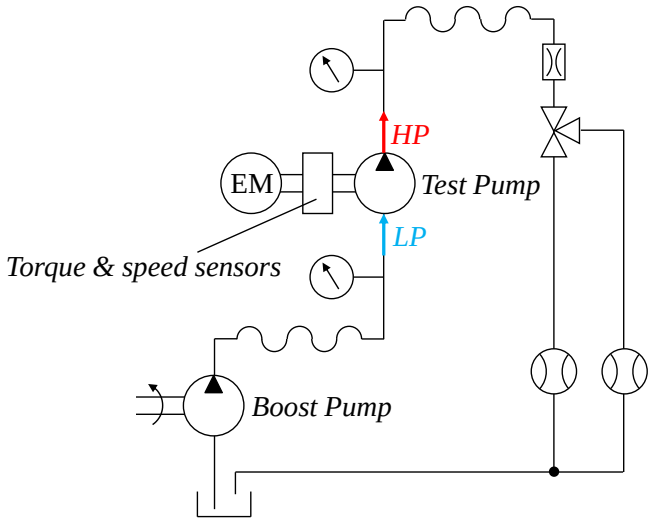

Figure 9.26. Test rig circuit supplied by Danfoss [2].

The volumetric, mechanical, and total efficiency measured for RKA and RKB during Phase 2 at OC1 is shown in the left column of Fig. 9.27; in order to show the trend of the data in each plot more clearly, it has been overlaid with a 9th degree polynomial fit [2]. As can be seen, the volumetric efficiency of RKB is visibly higher than that of RKA; the mechanical efficiency of RKB, by contrast, starts off lower than that of RKA, but then increases enough for the total efficiency of RKB to be close to that of RKA. The change in the mechanical efficiencies visible in this figure are most likely due to the wear-in process.

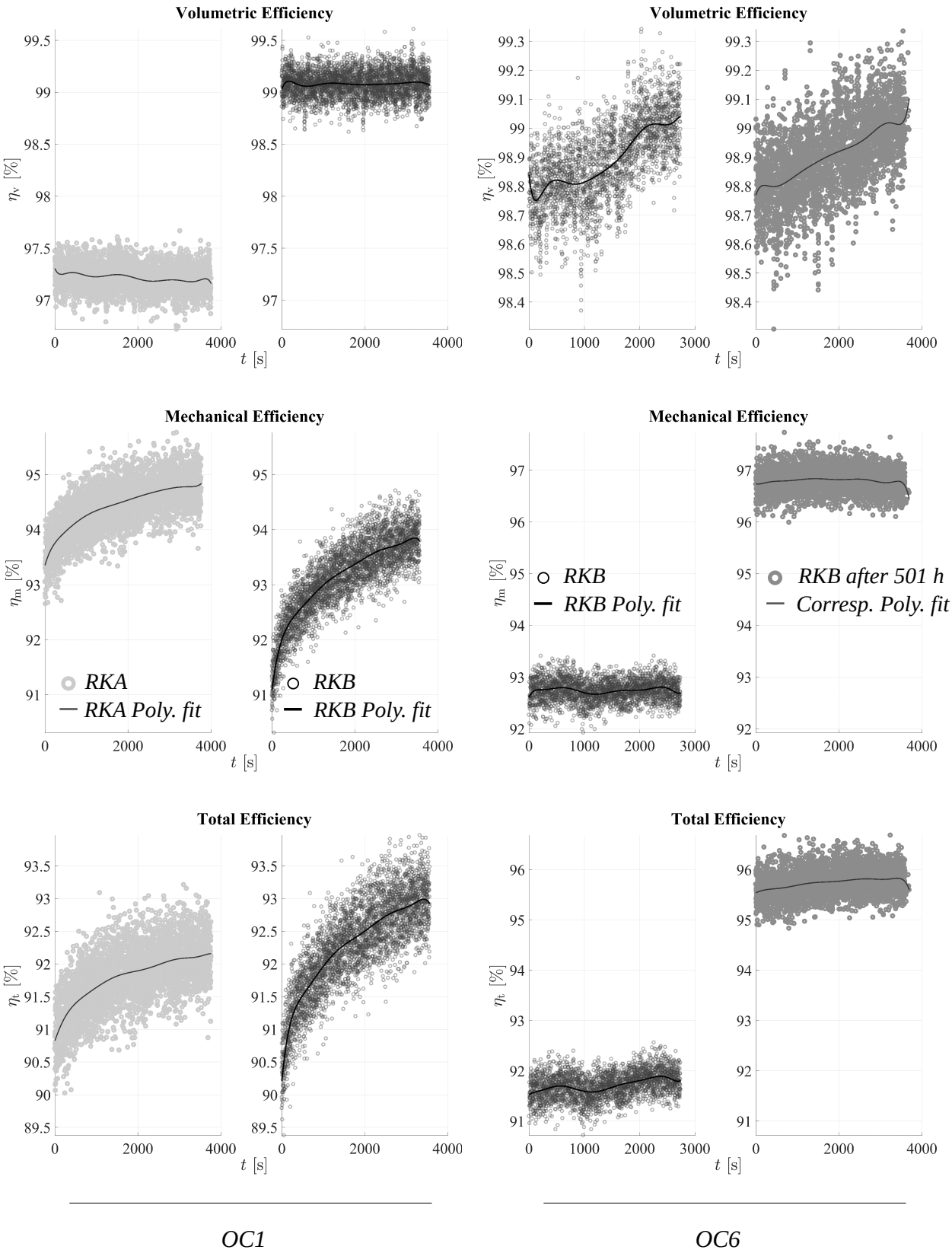

Figure 9.27. Measured volumetric, mechanical, and total efficiency at OC1, and at OC6 [2].

The efficiencies at the end of the OC1 measurements can be more rigorously compared via Fig. 9.28. These plots respectively show the average of the volumetric, mechanical, and total efficiencies calculated from the last 300 s of data for each measured operating condition (omitting outliers outside (70%-100%]), along with bars indicating one and two standard deviations from that average [2]. The normality of the data was verified using a Sharpio-Wilk test. From the results in Fig. 9.27, it can be seen that at OC1, the average volumetric efficiency of RKB is significantly higher than that of RKA. When comparing the mechanical efficiencies of these rotating kits at the same operating condition, the core of the data, within one standard deviation of the average, is higher for RKA than for RKB; however, if two standard deviations are taken into account, there is overlap between the two. For the total efficiency, the core of the data is higher for RKB, but taking into account two standard deviations, the data overlaps.

The next operating condition tested is OC2: identical to OC1, except that the speed is 400 rpm higher. At this speed, the volumetric efficiency of RKB is still higher than that of RKA, though the difference between the two is less [2]. The mechanical efficiency of RKA is clearly higher at this speed. For the total efficiency, even considering only the data one standard deviation from the average, there is overlap between the two. At OC3 (400 rpm faster), the difference in the volumetric efficiency diminishes more, though RKB retains its lead. The difference in mechanical efficiency diverges more, with RKA retaining its lead. The total efficiency for this operating condition is clearly higher for RKB. The difference in mechanical efficiency between the two rotating kits is most likely due to significant wear on RKB (to be discussed in more detail shortly).

The subsequent operating condition, OC4, is a high-pressure, low-speed operating condition [2]. While RKB was able to complete the full Phase II test at this operating condition, RKA began to exhibit excessive vibrations, and had to be shut down. On account of this, RKB was measured at OC5 instead, i.e. at a lower operating pressure. The results in Fig. 9.28 show that despite running at an operating pressure 10 bar higher than RKA, RKB is on par with the total efficiency of RKA. Finally, RKB was re-run at OC5. Comparing RKA

and RKB at OC5, it can be seen that the total efficiency data within one standard deviation of the average is higher for RKB, but, taking into account two standard deviations, there is overlap with RKA.

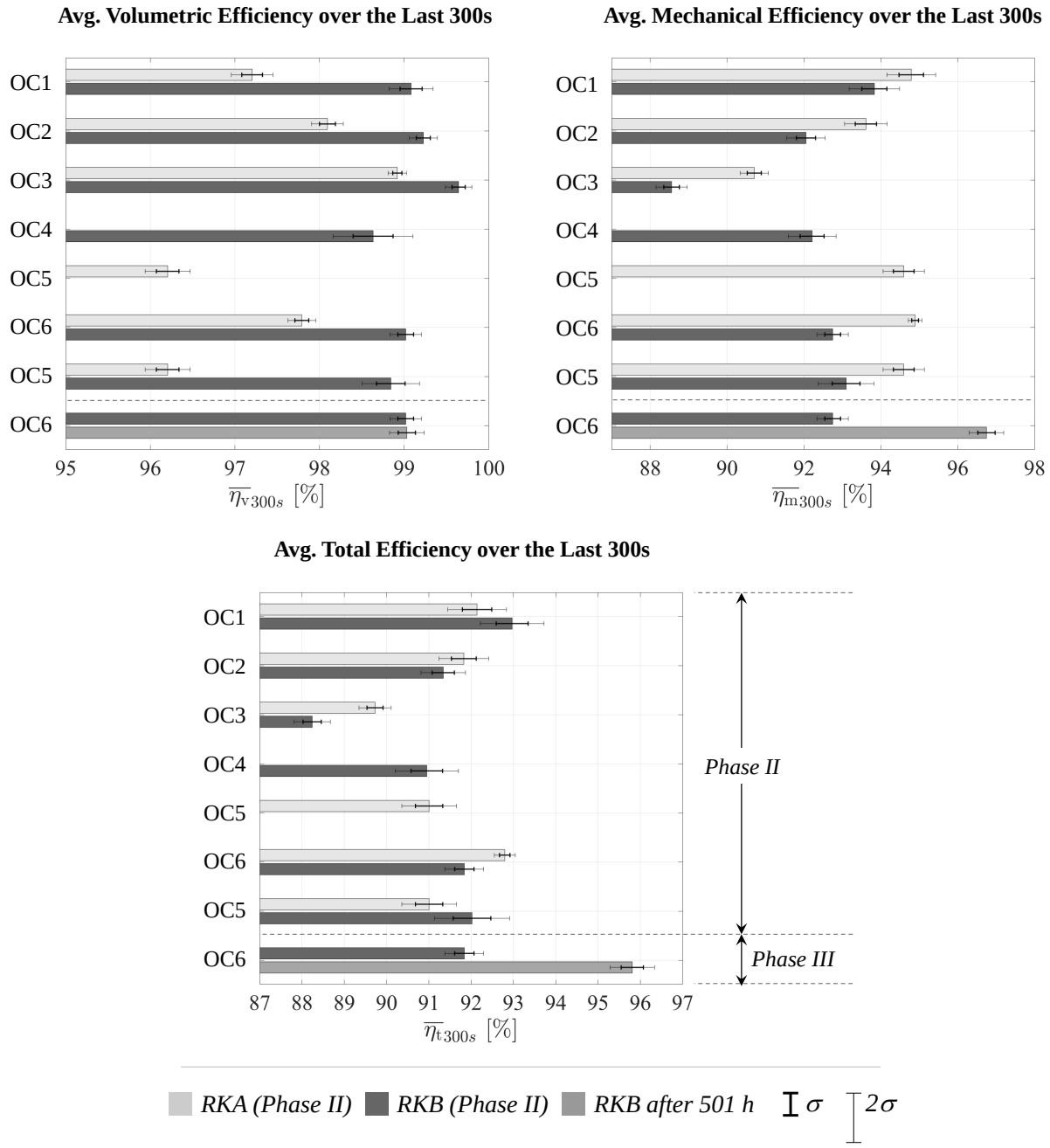

Figure 9.28. Average of the volumetric and total efficiencies over the last 300 s measured [2].

With Phase II complete, RKB was then run 501 h at OC6 [2]. This constitutes Phase III of the measurement procedure. Comparing the results from RKB during Phase II, versus at the end of Phase III, in Fig. 9.28, it can be seen that while the volumetric efficiency barely changes, the mechanical efficiency undergoes a significant increase. Consequentially, the total efficiency also undergoes a significant increase over Phase III, reaching an average value of 95.8%, with a standard deviation of 0.26%— higher than the 92% reached by the product line corresponding to the stock unit [3].

The change in mechanical efficiency from Phase II to the end of Phase III is most likely the result of wear-in [2]. This phenomenon can be seen more clearly when examining the surface measurements of the RKA and RKB bores taken over the course of these measurement phases. For a given bore, these measurements were taken by recording the location of the center of a zirconia sphere as it traveled along a pre-defined path over the bore surface. Contact between the sphere and the surface was assured by force feedback sensors.

Fig. 9.29 shows bore surface measurement traces taken at two representative circumferential locations for RKA, and two for RKB, where l_T is the length of the longest trace taken at each respective location [2]. The traces shown were taken prior to Phase I, after each operating condition tested in Phase II, and at the end of Phase III. They have been lined up using cross-correlation, and are stacked up in the order in which they were measured, with the earliest measurement at the bottom, and the last measurement at the top. The plots for RKB also show the nominal profile (Profile II), which has been lined up with the case end of the profile (the region near z_K/l_T=100%). As can be seen, while there is a significant difference between the nominal and manufactured profiles, and further development of the manufacturing approach would certainly be beneficial, the critical slope of the profiles nearest the case end of the bushing matches fairly well between the two. It should also be noted that for RKB, the measurements do not quite reach the DC end of the bushing.

Nevertheless, it can be seen that there is substantial wear at the end of the measurement traces nearest the DC (z_K/l_T=0%) [2]. This wear is most likely the result of the piston

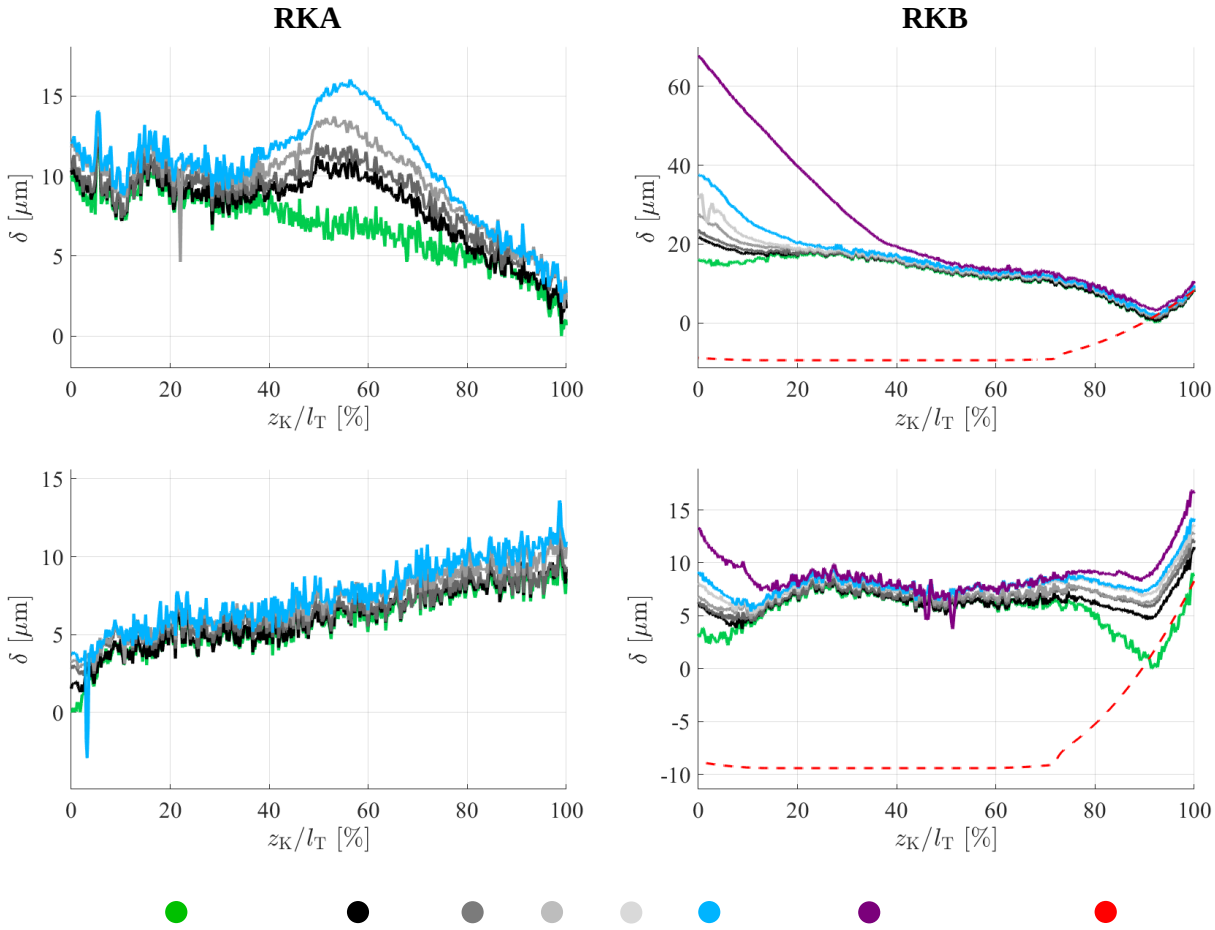

Figure 9.29. Surface traces for the bushing bores in RKA and RKB [2].

grooves scraping over the edge of the bushing. Eliminating these grooves could therefore significantly improve the performance of the piston-cylinder interface, and lessen the wear near z_K/l_T=0%. On the other end of the trace (z_K/l_T=100%), while there is also some wear, the slope of the profile remains fairly consistent. Furthermore, in comparing the results of the two rotating kits, it can be seen that for RKB, wear mainly occurs at the ends of the measurement traces, but for RKA, a deep divot is carved out near the middle of the measurement trace (z_K/l_T=50%). This is significant because the APMSPD being simulated is a desalination unit, and typically runs with seawater. If there is a deep divot in the bushing surface, sand particles, or other abrasive particles in the seawater, can collect in the divot, and effectively turn that bushing surface into sand paper, which then wears away at the

piston. For this reason, the nature of the wear in the piston-cylinder interfaces of RKB is more favorable than that of RKA.

9.4 Summary/Conclusions vis-á-vis Bore Profile Design via the TPGA

An algorithm has been developed to shape the surface of the bores through which the pistons move in axial piston machines. The proposed algorithm tailors the shape of the bores to the tilt and deformation of the pistons, in order to achieve a degree of piston-bore surface conformity conducive to building hydrodynamic pressure where it is needed in order to prevent solid contact between the two components. Two case studies have been conducted using this algorithm, one to design a bore profile for the same 75 cc unit simulated in the previous chapters, and one to design a profile for a 444 cc unit. The first study yielded three profiles that, in simulation, produce negligible correction forces (full load support) at all four of the operating conditions from Ch. 6— including the operating condition simulated in the previous chapters.

The second study encompassed the design of a bore profile for a virtual prototype, a slightly modified version of which was then tested on a physical prototype as a proof-of-concept. Both prototypes are based on the geometry of a commercial 444 cc unit. The virtual prototype has a higher swash plate angle than the commercial unit in order to enable a larger displacement. In simulation, the proposed algorithm was able to design a profile producing negligible correction forces for this unit. Since the physical prototype is only intended as a proof-of-concept, it has the same swash plate angle as the commercial unit. It was tested with two rotating kits, one representing the commercial unit, and one with several design changes, including changes to the clearance and bushing length, and the implementation of the designed bore profile. The second rotating kit (with the described design changes) was able to achieve a total efficiency higher than that of the commercial unit. However, surface measurements made show that the bores of this rotating kit did suffer significant wear, most likely due to a groove in the pistons scraping over the edge of the bushing. The elimination of this groove, and advances in the manufacturing technique used to produce the bore shaping, could enable the achievement of even higher efficiencies in the future.

10. CONCLUSIONS/ORIGINAL CONTRIBUTIONS

Green, cheap, non-toxic: water appears the ideal hydraulic fluid. However, its low viscosity detracts from the ability of lubricating interfaces in positive displacement machines to perform their load bearing and sealing functions at challenging operating conditions. This is a key obstacle to designing APMSPD running on water for the high-pressure regime—especially the piston-cylinder interfaces in these machines, which are responsible for carrying a heavy side load that increases with operating pressure. The performance of this interface type is decisive to the life of the components it separates, and to the overall efficiency of the machine, but it cannot be hydrostatically balanced, thus rendering its design for use with a low-viscosity fluid a particularly demanding task.

The present work is an investigation of micro-surface shaping design for this interface, in address of the aforementioned problems. Shaping the surface of the pistons, and/or their corresponding bores, is effective because it changes the thickness of the interface fluid film, which, in turn, changes the pressure field of that film, and, consequentially, the load support capacity of the interface, as well as the power loss that it incurs. Since the construction of physical prototypes for such surface shaping is expensive and time-consuming, the present work assesses the effect of this type of shaping by simulating the behavior of the piston-cylinder interface using FSTI, the APMSPD lubricating interface model of the Maha Fluid Power Research Center, and restricts experimental validation with a physical prototype to a single surface shape. The piston-cylinder module of FSTI, developed by Pelosi [10], Shang [15], and Mizell [14], outputs two metrics paramount for comparing the performance of different surface shape designs: correction forces imposed at two control points (one at either end of the interface), whose magnitude indicates the severity of predicted metal-to-metal contact, and power loss due to viscous flow. If full load support is achieved by the interface, the correction forces are zero. The objective of the present work is therefore to identify design trends in surface shaping that lead to zero correction forces, and minimal power loss.

The investigation conducted makes the following original contributions to the field of fluid power:

- *Contributions of Hydrostatic and Hydrodynamic Pressure to Load Support.*
  In order to study the unique nature of the piston-cylinder interface with regards to load support, a methodology has been developed to calculate the hydrostatic and hydrodynamic components of fluid pressure in the lubricating interfaces of APMSPD [1]. A case study comparing the contributions of these two components to load support in the three main lubricating interfaces of APMSPD has been conducted, using the geometry of a commercial 75 cc pump. The study examines three operating conditions: 100 bar pressure difference across the pump at a speed of 1,000 rpm and 3,000 rpm, and 300 bar pressure difference at 1,000 rpm. Since this is a topic of interest to the fluid power community at large, the study uses HLP-32 as the working fluid. However, as the use of a low-viscosity fluid, e.g. water, diminishes hydrodynamic pressure, this case study is highly relevant to the present work.

  The results of the study show that over the high-pressure stroke, the force from hydrostatic pressure in the piston-cylinder interfaces of this machine becomes so large that it not only counters the load force on the pistons, but surpasses it to such an extent that in order to balance the forces on the piston without metal-to-metal contact, the hydrodynamic pressure must generate a force larger than the original load [1]. By contrast, hydrostatic pressure carries more than half the load on the slipper and block. Moreover, nearly all of the load moment on the piston is carried by hydrostatic pressure, whereas less than half of the load moment on the block is carried by hydrostatic pressure, and the moment on the slipper is negligible. While the case study examines only one pump, it nevertheless demonstrates the degree to which the piston-cylinder interface can depend on hydrodynamic pressure, and how the design challenges associated with this interface differ from those of the other two.

- *Design Studies.*

  Two extensive design studies have been conducted to investigate the effects of a shape that gives the lubricating interface surface on which it is imposed the profile (lengthwise cross-section) of a circular arc, defined by a radius, R, and a shift, l_s. The first study imposes this shape on the bore through which a piston moves, and the second, on the running surface of the piston itself. Both studies simulate the piston-cylinder interfaces of the aforementioned 75 cc unit (designed to run on oil) with such surface shaping, with the diametrical piston-bore clearance reduced to circa 35% of that in the stock unit, and with water as the hydraulic fluid. The simulated pump runs at 3,000 rpm, with a 300 bar pressure difference between the inlet and outlet ports. In a baseline simulation, it is found that when the bore and piston surfaces are unshaped (perfectly cylindrical), the correction forces calculated by FSTI rise to over 1,000 N at this operating condition. The design studies conducted investigate how the magnitudes of R and l_s change load support and power loss at the piston-cylinder interface.

  The first study shows that imposing the circular arc shaping can reduce the maximum and average correction forces at both control points by more than 50%. The correction force at the case end of the interface (the end nearest the piston head) is reduced most by bore profiles whose apex is located within the half of the maximum guide length closest to the DC, whereas the DC end correction force is reduced most by profiles whose apex is located in the other half. This is because, over the high-pressure stroke, moving the apex towards the DC increases piston-bore surface conformity near the case end of the interface, thus increasing the generation of hydrodynamic pressure there. Simultaneously, it opens the interface up wider to the pump case, allowing more of the pressure that contributes to the force and moment causing contact at the case end of the interface to drain away. Moving the apex towards the case end of the interface has the opposite effect. The manner in which the piston deforms causes shapes that move the apex towards the DC to be more effective in increasing load support. However, they generate more power loss due to viscous flow. The shift should therefore be just far enough towards the DC to achieve for full load support— not further.

The second study compares the performance of the piston-cylinder interface resulting from the imposition of this profile on the bores, versus on the pistons. The results show that the maximum and average case end correction forces to exhibit the same basic trends for both shapes. However, in the region of the design space where the case end correction forces are lowest for both profiles— small radii, large apex shift towards the DC— the piston profile exhibits a much higher DC end correction force than the bore profile. This is because the piston profile only aids piston-bore surface conformity near the DC end of the interface while the profile apex is located within the fluid film. Once the apex exits into the DC, i.e. once the part of the piston running surface converging with the bore at the DC end of the fluid film is on the side of the profile apex closest to the piston head, the profile takes away from the surface conformity there, rather than contributing to it.

- *PCID RSA (Piston-Cylinder Interface Design Response Surface Algorithm).*
  A response surface algorithm specifically for piston-cylinder interface design based on a multi-physics model of the fluid film that requires extensive run time, such as FSTI, has been developed: the PCID RSA. The algorithm constructs a radial basis function model for every objective function, and then locally refines these models based on new function evaluations with every iteration until convergence. This enables a more reliable modeling of the load support and power loss trends over a given design space than a simple design study, and concentrates the costly function evaluations in regions of the design space where the objective function is most detailed: it averts the need to save computation time by making compromising simplifications in the interface model. Furthermore, the RSA features a DOE algorithm capable of covering elaborate design spaces, including the often intricately shaped regions over which the objective function models have not achieved convergence. It allows the user to specify the resolution to which a design space should be described by the objective function models, and even allows for design spaces consisting of discrete points.

Case Study:

Using the PCID RSA, a multi-objective optimization of the dimensions R and l_s for the bore profile from the previously described design studies has been conducted, with the same hydraulic fluid, and pump geometry, operating condition, piston-bore diametrical clearance, etc.— but with the length of the bushings in the cylinder block bores extended 11% from the original. The objective functions include the power loss due to viscous flow, maximum contact stress, maximum and average correction force magnitudes at both control points, and the area taken up by the largest patch of film thickness at or below $0.1\mu m$. The objective function surrogate models generated by the RSA exhibit the same basic trends as those seen for the simpler design study with the shorter guide length; however, the function evaluations more completely fill the design space under study, especially at its borders, revealing that although a drastic reduction in correction forces can be achieved, they are again not brought to zero. An algorithm has been developed to generate such a profile for this, and any other unit for which the studied bore profile does not suffice: the TPGA.

- *TPGA (Tailored Profile Generator Algorithm).*

  The TPGA generates bore profiles conducive to producing hydrodynamic pressure buildup that prevents metal-to-metal contact by tailoring the bore surface to conform with the piston, taking into account both piston tilt and deformation [2]. Given user-supplied values for the axial length along the fluid film over which the bore and piston surfaces should conform at either end of the interface, the TPGA determines the slope of the bore surface in those regions that is required to achieve the desired surface conformity. Establishing the profile slope on either end of the interface based on piston tilt and deformation significantly reduces the available design space, thus enabling the efficient generation of profiles with a desirable performance.

  Case Studies:

  Two case studies have been conducted to demonstrate the potential of this algorithm. In the first, the TPGA is employed to design bore profiles for the same 75 cc unit

used in the previously described design studies, with the same piston-bore diametrical clearance, with the original bushing length, and, again, with water as the working fluid. The design process is completed at an operating condition of 1,000 rpm, full displacement, and 300 bar pressure difference across the pump. Of the designs generated, three result in negligible correction forces— not only at the operating condition they are designed for, but also when the pump speed is increased to 3,000 rpm, and at both 1,000 rpm and 3,000 rpm when the pressure difference across the pump is 50 bar. At the high-pressure operating conditions, the TPGA design does incur significantly more power loss than the commercial unit when simulated with oil as the working fluid— but, for the pump speed of 3,000 rpm, still significantly less than the profiles with the lowest correction forces in the PCID RSA case study.

The second case study employs the TPGA to design a bore profile the virtual prototype Unit 1, a slightly modified version of which is then tested on the physical prototype Unit 2 [2]. Both prototypes are based on a 444 cc commercial unit. Unit 1 differs from the stock unit in that its swash plate angle is over 10% higher, its bushing length has been shortened so that the piston-cylinder interface has a fixed, rather than a variable, guide length, and its piston-bore diametrical clearance is smaller. Using the TPGA, a bore profile has been generated for Unit 1 that results in negligible correction forces in simulation. This profile was slightly adjusted based on a sensitivity study of the slope at either end of the profile, to ensure that small changes in that slope due to manufacturing error would not result in poor performance.

In collaboration with Danfoss High Pressure Pumps, the resulting profile was then tested on the physical prototype, Unit 2 [2]. The testing of this unit serves as a proof of concept— for this reason, the swash plate angle is the same as that of the 444 cc commercial unit. After 501 h, the Unit 2 rotating kit, with the aforementioned profile implemented on its cylinder block bushing bores, its bushing length the same as that of Unit 1, and its piston-bore clearance, significantly smaller than that of the stock unit, is able to achieve an average total pump efficiency of 95.8% over the last 5 min-

utes of measurement, with a standard deviation of 0.26%: significantly higher than the product line of the stock unit [3]. Surface measurements show that significant wear has occurred on the bushing, which is most pronounced near the DC end of the interface [2]. This wear is most likely due to the grooves in the pistons of the unit scraping against the edge of the bushing, and suggests that the elimination of these grooves might enable the achievement of even higher efficiencies. While there is also wear at the case end, the slope of the profile in this region is fairly well retained.

Through the design studies presented, and the design tools developed, the present work represents a significant step in enabling the construction of piston-cylinder interfaces in axial piston machines of swash plate design using water as their working fluid for the high-pressure regime.

REFERENCES

[1] M. Ernst and A. Vacca, "Hydrostatic vs. hydrodynamic components of fluid pressure in the tribological interfaces of axial piston machines," *Tribology International*, p. 106 878, 2021, ISSN: 0301-679X. DOI: https://doi.org/10.1016/j.triboint.2021.106878. [Online]. Available: http://www.sciencedirect.com/science/article/pii/S0301679X21000268.

[2] M. Ernst, A. Vacca, M. Ivantysynova, and G. Enevoldsen, "Tailoring the bore surfaces of water hydraulic axial piston machines to piston tilt and deformation," *Energies*, vol. 13, 22 2020.

[3] Danfoss, *Making fresh water possible in a sustainable and energy-efficient way*, Online Brochure. [Online]. Available: https://assets.danfoss.com/documents/DOC298456256052/DOC298456256052.pdf.

[4] J. Ivantysyn and M. Ivantysynova, *Hydrostatic Pumps and Motors*. New Delhi: Tech Books International, 2003.

[5] E. Trostmann and M. Clausen, "Hydraulic components using tap water as pressure medium," SICFP, Ed., ser. Proceedings of the Fourth Scandinavian International Conference on Fluid Power, SICFP'95, SICFP, Tampere, Finland, Sep. 1995, pp. 942–954.

[6] G. W. Krutz and P. S. K. Chua, "Hydraulic fluid power - a historical timeline," ser. Workshop on Water Hydraulics, Agricultural Equipment Technology Conference 9AETC '04, Louisville, KY, USA, Feb. 2004.

[7] M. P. Schneider, "Review: Plant-oil-based lubricants and hydraulic fluids," *Journal of the Science of Food and Agriculture*, vol. 86, pp. 1769–1780, 12 2006. DOI: 10.1002/jsfa.2559.

[8] L. R. Ruble, "The expanded focus, use, and future of water powered rotary actuators," NCFP, Ed., ser. Proceedings of the 48th National Conference on Fluid Power, NCFP'2000, NCFP, Chicago, Il, USA, 2000, pp. 567–574.

[9] M. Rokala, "Analysis of slipper structures in water hydraulic axial piston pumps," Ph.D. dissertation, Tampere University of Technology, 2012.

[10] M. Pelosi, "An investigation on the fluid-structure interaction of piston/cylinder interface," Ph.D. dissertation, Purdue University, 2012.

[11] M. Zecchi, "A novel fluid structure interaction and thermal model to predict the cylinder block/valve plate interface performance in swash plate type axial piston machines," Ph.D. dissertation, Purdue University, 2013.

[12] M. Pelosi and M. Ivantysynova, "Heat transfer and thermal elastic deformation analysis on the piston/cylinder interface of axial piston machines," *Journal of Tribology*, vol. 134, 4 2012. DOI: 10.1115/1.4006980.

[13] M. Pelosi and M. Ivantysynova, "The impact of axial piston machines mechanical parts constraint conditions on the thermo-elastohydrodynamic lubrication analysis of the fluid film interfaces," *International Journal of Fluid Power*, vol. 14, pp. 35–51, 3 2013.

[14] D. Mizell, "A study of the piston cylinder interface of axial piston machines," Ph.D. dissertation, Purdue University, 2018.

[15] L. Shang, "A path toward an effective scaling approach for axial piston machines," Ph.D. dissertation, Purdue University, 2018.

[16] L. Shang and M. Ivantysynova, "Thermodynamic analysis on compressible viscous flow and numerical modeling study on piston/cylinder interface in axial piston machines," *JFPS INternational Journal of Fluid Power System*, vol. 11, pp. 117–123, 2019. DOI: 10.5739/jfpsij.11.117.

[17] T. Kim, P. Kalbfleisch, and M. Ivantysynova, "The effect of cross porting on derived displacement volume," *International Journal of Fluid Power*, vol. 15, pp. 77–85, 2 2014. DOI: 10.1080/14399776.2014.923605.

[18] P. Kalbfleisch, "Computational valve plate design," M.S. thesis, Purdue University, 2015.

[19] U. Wieczorek and M. Ivantysynova, "Caspar— a computer-aided design tool for axial piston machines," ser. Proceedings of the Bath Workshop on Power and Motion Control, University of Bath, Bath, UK, 2000, pp. 113–126.

[20] B. Hamrock, S. Schmid, and B. O. Jacobson, *Fundamentals of Fluid Film Lubrication*. New York: Marcel Dekker, Inc., 2004.

[21] M. Ernst, "Design solutions for piston machines with high operating pressures and water as a working fluid," M.S. thesis, Purdue University, 2015.

[22] U. Wieczorek and M. Ivantysynova, "Computer aided optimization of bearing and sealing gaps in hydrostatic machines - the simulation tool caspar. international journal of fluid power," vol. 3, pp. 7–20, 1 2002.

[23] L. Shang and M. Ivantysynova, "Thermodynamic analysis on compressible viscous flow and numerical modeling study on piston/cylinder interface in axial piston machine," ser. Proceedings of the 10th JFPS International Symposium on Fluid Power, JFPS, Fukuoka, Japan, 2017, pp. 475–481.

[24] T. Zloto, "Simulation of the hydrostatic load of the valve plate-cylinder block system in an axial piston pump," *Procedia Engineering*, vol. 177, pp. 247–254, 2017, XXI Polish-Slovak Scientific Conference Machine Modeling and Simulations MMS 2016.September 6-8, 2016, Hucisko, Poland.

[25] E. Koç and C. Hooke, "Investigation into the effects of orifice size, offset and overclamp ratio on the lubrication of slipper bearings," *Tribology International*, vol. 29, no. 4, pp. 299–305, 1996. [Online]. Available: http://www.sciencedirect.com/science/article/pii/0301679X95000445.

[26] S. Dhar and A. Vacca, "A novel cfd – axial motion coupled model for the axial balance of lateral bushings in external gear machines," *Simulation Modelling Practice and Theory*, vol. 26, pp. 60–76, 2012.

[27] A. Schenk and M. Ivantysynova, "An investigation of the impact of elastohydrodynamic deformation on power loss in the slipper swashplate interface," ser. Proceedings of the 8th JFPS International Symposium on Fluid Power, JFPS, Okinawa, Japan, Oct. 2011.

[28] A. Schenk, "Predicting lubricating performance between the slipper and swashplate in axial piston hydraulic machines," Ph.D. dissertation, Purdue University, 2014.

[29] M. Zecchi and M. Ivantysynova, "Cylinder block/valve plate interface - a novel approach to predict thermal surface loads," ser. Proceedings of 8th IFK International Conference on Fluid Power, IFK, Dresden, Germany, 2012.

[30] A. Schenk and M. Ivantysynova, "A transient thermoelastohydrodynamic lubrication model for the slipper/swashplate in axial piston machines," *Journal of Tribology*, vol. 137, no. 3, Jul. 2015.

[31] A. Busquets, "An investigation of micro-surface shaping on the piston/cylinder interface of axial piston machines," Ph.D. dissertation, Purdue University, 2018.

[32] R. Chacon and M. Ivantysynova, "Virtual prototyping of axial piston machines: Numerical method and experimental validation," *Energies*, vol. 12, 2019. DOI: 10.3390/en12091674.

[33] E. Trostmann, *Water Hydraulics Control Technology*. New York: Marcel Dekker, Inc., 1996.

[34] X. He, B. Zhu, Y. Liu, and Z. Jiang, "Study on a seawater hydraulic piston pump with check valves for underwater tools," *Proceedings of the Institution of Mechanical Engineers Part A: Journal of Power and Energy*, vol. 226, pp. 151–160, 2012.

[35] Danfoss, *Series 90 axial piston pumps*, Online Brochure. [Online]. Available: https://assets.danfoss.com/documents/53497/BC152886483413en-000907.pdf.

[36] Y. Huayong, Y. Jian, and Z. Hua, "Research on materials of piston and cylinder of water hydraulic pump," *Emerald Insight*, vol. 55, pp. 38–43, 1 2003, [30 June 2015]. [Online]. Available: http://www.emeraldinsight.com/doi/pdfplus/10.1108/00368790310457124.

[37] L. Yinshui, D. Wu, X. He, and L. Zhuangyun, "Materials screening of matching pairs in a water hydraulic piston pump," *Industrial Lubrication and Tribology*, vol. 61, pp. 173–178, 3 2009.

[38] S. Nie, G. Huang, Y. Zhu, Z. Li, and Y. Li, "Sewhapm: Development of a water hydraulic axial piston motor for underwater tool systems," *Proceedings of The Institution of Mechanical Engineers Part C-journal of Mechanical Engineering Science - PROC INST MECH ENG C-J MECH E*, vol. 219, pp. 639–655, Jul. 2005. DOI: 10.1243/095440605X31409.

[39] G. Kim, B. Kim, and S. Lee, *High-speed wear behaviors of crsin coatings for the industrial applications of water hydraulics*, [30 June 2015], 2005. [Online]. Available: http://www.sciencedirect.com/science/article/pii/S0257897205008807.

[40] A. Zhang, S. Nie, and L. Yang, "Evaluation of tribological properties on peek + ca30 sliding against 17-4ph for water hydraulic axial piston motor," *Proceedings of the Institution of Mechanical Engineers, Part C: Journal of Mechanical Engineering Science*, vol. 228, no. 13, pp. 2253–2265, 2014. DOI: 10.1177/0954406213518746. [Online]. Available: https://doi.org/10.1177/0954406213518746.

[41] W. Dong, S. Nie, and A. Zhang, "Tribological behaviour of peek filled with cf/ptfe/graphite sliding against stainless steel surface under water lubrication," *Proceedings of the Institution of Mechanical Engineers, Part J: Journal of Engineering Tribology*, vol. 227, pp. 1129–1137, Oct. 2013. DOI: 10.1177/1350650113481416.

[42] B. C. Majumdar, R. Pai, and D. Hargreaves, *Analysys of water- lubricated journal bearings with multiple axial grooves*, [25 April 2015], 2004. [Online]. Available: http://pij.sagepub.com/content/218/2/135.full.pdf.

[43] R. Mallya, S. B. Shenoy, and R. Pai, "Steady state characteristics of misaligned multiple axial groove water-lubricated journal bearing," *Proceedings of the Institution of Mechanical Engineers, Part J: Journal of Engineering Tribology*, vol. 229, no. 6, pp. 712–722, 2015. DOI: 10.1177/1350650114560833. [Online]. Available: https://doi.org/10.1177/1350650114560833.

[44] A. Yamaguchi, "Motion of pistons in piston-type hydraulic machines : 3rd report, exponential function-type piston," *Transactions of the Japan Society of Mechanical Engineers.*, vol. 41, no. 348, pp. 2413–2421, 1975. DOI: 10.1299/kikai1938.41.2413.

[45] M. Ivantysynova, "The piston cylinder assembly in piston machines- a long journey of discovery," *Ventil*, pp. 374–386, 2012.

[46] R. Lasaar, *Eine Untersuchung zur mikro- und makrogeometrischen Gestaltung der Kolben- /Zylinderbaugruppe von Schraegscheibenmaschinen*. Duesseldorf: VDI Verlag GmbH, 2003.

[47] T. Park, "Lubrication analysis between piston and cylinder in high pressure piston pump considering circumferential grooves and viscosity variation with pressure," ser. Proceedings of the 9th Biennial ASME Conference on Engineering Systems Design and Analysis, Haifa, Israel, 2008.

[48] S. Gels and H. Murrenhoff, "Simulation of the lubricating film between contoured piston and cylinder," *International Journal of Fluid Power*, vol. 11, no. 2, pp. 15–24, 2010. DOI: 10.1080/14399776.2010.10781003. [Online]. Available: https://doi.org/10.1080/14399776.2010.10781003.

[49] M. Ivantysynova, R. A. Garrett, and A. A. Frederickson, "Positive displacement machine piston with wavy surface form," US 20120079936 A1, 2012.

[50] Wondergem, A., and M. Ivantysynova, "The impact of the surface shape of the piston on power losses," ser. Proceedings of the 8th FPNI Ph.D Symposium on Fluid Power, FPNI, Lappeenranta, Finland, 2014, pp. 1–12.

[51] A. Wondergem, "Piston/cylinder interface of axial piston machines- effect of piston micro-surface shaping," M.S. thesis, Purdue University, 2014.

[52] A. Wondergem and M. Ivantysynova, "The impact of micro-surface shaping on the piston/cylinder interface of swash plate type machines," ser. Proceedings of the 2015 ASME/Bath Symposium on Fluid Power & Motion Control, Chicago, IL, 2015.

[53] M. Ernst and M. Ivantysynova, "Micro surface shaping for the high-pressure operation of piston machines with water as a working fluid," ser. Proceedings of the 2015 ASME/Bath Symposium on Fluid Power & Motion Control, Chicago, IL, 2015.

[54] A. Wondergem and M. Ivantysynova, "The impact of micro-surface shaping of the piston on the piston/cylinder interface of an axial piston machine," ser. Proceedings of the 10th IFK International Conference on Fluid Power, vol. 2, Dresden, Germany, 2016, pp. 289–300.

[55] H. Berthold, "Axial piston machine having a cooling circuit for the cylinders and pistons," US 5971717 A, 1999.

[56] I. Yoshimura, R. Nomura, H. Wada, and R. Sakai, "Piston of axial piston pump motor, cylinder block of axial piston pump motor, and axial piston pump motor," US 2015/0219215 A1, 2015.

[57] E. Varandili, "Properties of tap water as a hydraulic pressure medium," SICFP, Ed., ser. Proceedings of the Sixth Scandinavian International Conference on Fluid Power, SICFP'99, SICFP, Tampere, Finland, May 1999, pp. 113–127.

[58] M. Ernst and M. Ivantysynova, "Cylinder bore micro-surface shaping for high pressure axial piston machine operation using water as hydraulic fluid," ser. Proceedings of the ASME/BATH 2017 Symposium on Fluid Power and Motion Control, (FPMC 2017), ASME, Sarasota, FL, USA: ASME, Oct. 2017, ISBN: 978-0-7918-5833-2.

[59] M. Ernst and M. Ivantysynova, "Axial piston machine cylinder block bore surface profile for high-pressure operating conditions with water as working fluid," ser. Global Fluid Power Society PhD Symposium. 2018. (GFPS 2018), GFPS, vol. 1, Samara, Russia: IEEE, Jul. 2018, ISBN: 9781538647868.

[60] Y. Özgür, "Comparative study of algorithms for response surface optimization," *Computational Applications*, vol. 19, no. 1, pp. 93–104, 2014.

[61] A. Giunta, S. Wojtkiewicz, and M. Eldred, "Overview of modern design of experiments methods for computational simulations (invited)," in *41st Aerospace Sciences Meeting and Exhibit*. DOI: 10.2514/6.2003-649. eprint: https://arc.aiaa.org/doi/pdf/10.2514/6.2003-649. [Online]. Available: https://arc.aiaa.org/doi/abs/10.2514/6.2003-649.

[62] B. S. Morse, T. S. Yoo, P. Rheingans, D. T. Chen, and K. R. Subramanian, "Interpolating implicit surfaces from scattered surface data using compactly supported radial basis functions," in *Proceedings International Conference on Shape Modeling and Applications*, 2001, pp. 89–98.

[63] S. Sarra and E. Kansa, "Multiquadric radial basis function approximation methods for the numerical solution of partial differential equations," *Advances in Computational Mechanics*, vol. 2, Jan. 2009.

[64] D. Forti, "Comparison of shape parametrization techniques for fluid-structure interaction problems," M.S. thesis, Politecnico di Milan, 2012.

[65] L. Brinkschulte, J. Mattes, and M. Geimer, "An approach to wear simulation of hydrostatic drives to improve the availabiility of mobile machines," ser. 11th IFK Conference Proceedings, RWTH Aachen University, Aachen, Germany, Mar. 2018.

[66] Danfoss, *Pump, app 38 180b3071*, Online Brochure. [Online]. Available: https://store.danfoss.com/en/High-Pressure-Pumps/Pumps/Pumps-for-Sea-Water/Pump%2C-APP-38/p/180B3071.

[67] M. Ernst and M. Ivantysynova, "Cylinder bore micro-surface shaping for high pressure axial piston machine operation using water as hydraulic fluid," ser. Proceedings of the ASME/BATH 2017 Symposium on Fluid Power and Motion Control, (FPMC 2017), ASME, Sarasota, FL, USA: ASME, Oct. 2017, ISBN: 978-0-7918-5833-2.

VITA

Meike Ernst was born in Stuttgart, Germany, but moved to the United States with her family in 2000, at the age of nine. In 2013, she received her B.S.E. in Aerospace and Mechanical Engineering from Case Western Reserve University in Cleveland, Ohio. She then joined the Maha Fluid Power Research Center at Purdue University, earning her M.S.E. from the School of Mechanical Engineering in 2015, and subsequently pursuing her PhD at the same facility. Her research centers on the design of micro surface shaping at the piston-cylinder lubricating interfaces in axial piston machines of swash plate design that run with water as the hydraulic fluid.

PUBLICATIONS

M. Ernst and M. Ivantysynova, "Cylinder bore micro-surface shaping for high pressure axial piston machine operation using water as hydraulic fluid," ser. Proceedings of the ASME/BATH 2017 Symposium on Fluid Power and Motion Control, (FPMC 2017), ASME, Sarasota, FL, USA: ASME, Oct. 2017, ISBN: 978-0-7918-5833-2.

M. Ernst and M. Ivantysynova, "Axial piston machine cylinder block bore surface profile for high-pressure operating conditions with water as working fluid," ser. Global Fluid Power Society PhD Symposium. 2018. (GFPS 2018), GFPS, vol. 1, Samara, Russia: IEEE, Jul. 2018, ISBN: 9781538647868.

M. Ernst, A. Vacca, M. Ivantysynova, *et al.*, "Tailoring the bore surfaces of water hydraulic axial piston machines to piston tilt and deformation," *Energies*, vol. 13, 22 2020.

M. Ernst and A. Vacca, "Hydrostatic vs. hydrodynamic components of fluid pressure in the tribological interfaces of axial piston machines," *Tribology International*, p. 106 878, 2021, ISSN: 0301-679X. DOI: https://doi.org/10.1016/j.triboint.2021.106878. [Online]. Available: http://www.sciencedirect.com/science/article/pii/S0301679X21000268.